Low Frequency Dielectric Spectroscopic Analysis of Reverse Microemulsions

Beckford, Elaine Susan

Awarding institution:
King's College London

Low Frequency Dielectric Spectroscopic Analysis of Reverse Microemulsions

A thesis submitted for degree of

DOCTOR OF PHILOSOPHY

in

Faulty of Life Sciences & Medicine
of
Kings College London

Elaine Beckford

November 2016

Department of Pharmacy and Forensic Science
King's College London

Abstract

Low frequency dielectric spectroscopy in the MHz down to 0.1 mHz range, was used to investigate and characterise ternary reverse microemulsions, micellar systems and their individual components. Anionic surfactant sodium bis (2-ethylhexyl) sulfosuccinate (AOT), oil isopropyl myristate (IPM) and deionised water were chosen as they readily form reverse microemulsions and have been investigated with other physicochemical techniques.

Low frequency dielectric spectroscopy is a non-invasive technique, able to probe the electrical properties of materials without isotopic labelling.

The dielectric response of the microemulsions stabilised with 20% w/w AOT displayed a small anomalous increase in the conductance and a decrease in the capacitance to negative values at frequencies below the characteristic intracluster frequency ω_1, but above the commencement Maxwell-Wagner interface charging process. Spectroscopic measurements of the individual components showed IPM exhibited similar anomalous characteristics at frequencies below 1Hz.

Increases in conductance are indicative of structural change, and negative capacitances have been reported to occur in animal cells such as neurons undergoing changes in membrane potential during ion flux. Hence the response of IPM displayed characteristics of biological membranes able to undergo structural changes resulting in an increased conductance in specific frequency ranges.

The response of the anomalous features were fitted using the Dissado-Hill cluster model adapted to include the linearised frequency dependant conductance term $G(\omega)$. This term replaced the static conductance component in the bulk parallel conductance–capacitor pair of bulk–barrier series circuit model of the samples investigated.

The anomalous features, together with the changing intracluster relaxation time τ_1 were used to track the micellar to microemulsion transition as the molar concentration ratio $W_0=[H_2O]/[AOT]$ was increased $0<W_0<26$. The presence of microemulsion aggregates

indicated by the slowing down of the τ_1 response time at $W_0>9$ was confirmed by the detection of particles with radii 12 to 29 nm using light scattering.

Acknowledgments

I would like to thank my supervisor Professor Jayne Lawrence for her support and guidance during the course of my research. I'd also like to thank Dr Richard Harvey for stepping in as my second supervisor after the sad death of my mentor Professor Robert Hill.

I also want to acknowledge the help provided by Professor Len Dissado in identifying potential sources for some of the dielectric features observed in my research.

I also want to acknowledge the support received from the workshops and research technicians for sourcing the materials and building replacement sample cells to my specifications and the timely loan of equipment when needed.

I'd also like to thank my members of family Jonathan, Donna, David and Ingrid for proof reading this thesis.

And finally thanks to Christine and the next generation Annaliese, Nathanael and Benjamin for making me smile.

List of Abbreviations and Symbols

2Dx	potential energy difference between alternative orientations
2-n	Maxwell-Wagner dispersion index
A	area
a_0	area occupied by polar head group
$Å^2$	area at interface
$Å^3$	volume occupied by alkyl chains
ac	alternating current
AOT	Aerosol OT, bis(2-ethylhexyl) sulfosuccinate
c(0)	dielectric increment
C(ω)	complex capacitance
c0	dielectric increment
C_0	magnitude of the capacitance
C_0	spontaneous curvature of interface
C_∞	high frequency bulk capacitance
C_b	barrier capacitance
C_{bar}	barrier capacitance
C_{bulk}	high frequency bulk capacitance
CDI	Chelsea Dielectric Interface
C_{inf}	high frequency bulk capacitance
CMC	critical micelle concentration
CPA	constant phase angle
CPP	critical packing parameter
C_s	number of surfactant molecules per unit volume

D	Debye unit
d	electrode spacing
D_2O	Deuterated water
dc	direct current
d_f	fractal dimension of the self-similar hierarchy
DH	Dissado-Hill - referring to the Dissado-Hill cluster model
DLS	dynamic light scattering
DOC	disordered open connected model
d_w	charge walk dimension
E	electric field
E (ω)	alternating electric field E
EC	ethyl caprylate
eV	electron volt
F	farad
f	frequency Hz
FCS	fluorescence correlation spectroscopy
FRA	Frequency Response Analyser
G	conductance
G	Gibbs free energy G = H-TS
g	Kirkwood correlation factor
H	enthalpy term from Gibbs free energy G = H-TS
HLB	hydrophilic-lipophilic balance
HOD	Deuterated water
Hz	Hertz
i	square root of -1

I	Type I Winsor system
II	Type II Winsor system
III	Type III Winsor system
IPM	isopropyl myristate
IV	Type IV Winsor system
K	kelvin
k_B	Boltzmann's constant
L2	reverse microemulsion
l_c	length of alkyl chain
m	reorientable component of a dipole moment
μF	micro farad
n	loss index
n_c	close to but less than the number of carbon atoms per alkyl chai
nm	nanometres
NMR	nuclear magnetic resonance
ns	nanosecond
O/W	oil-in-water
o/w	oil-in-water
p	low frequency dielectric index for quasi dc responses
P	the polarisation at time, t
P_0	maximum magnitude of the polarisation at time, t = 0
PCS	photon correlation spectroscopy
pF	picofarad
PG	propylene glycol
q_{CRC}	scattering vector

qdc	quasi-dc
$q_{observed}$	scattering vector
R	charge displacement distance
R	radius
rad	radian
S	entropy term from Gibbs free energy G = H-TS
s	second
S	siemens
SANS	small angle nuclear scattering
SAXS	small angle x-ray scattering
T	temperature
t	time
t_1	fast process relaxation time (ms)
t_1	intracluster relaxation time
t_2	intercluster relaxation time
t_2	slow process relaxation time (ms)
tan(d)	tan delta of constant phase angle C'(w)/C"(w)
Temp	temperature
V	volt
V	volume
V_w/V_o	water / oil volume fraction
w/o	water-in-oil
W/O	water-in-oil
w/w	% w/w percentage weight per total weight
W_0	molar ratio of water to molar ration of surfactant in the micellar system

$Y(\omega)$	complex admittance
$Z(\omega)$	complex impedance
ε_0	permittivity of free space is the a $8.854 \times 10^{-12} (Fm^{-1}$
$\boldsymbol{\varepsilon}_\infty$	high frequency permittivity
ε_k	persistence length of film for non-spherical micelles
ε_r	relative permittivity
ε_s	static permittivity
μm	micrometer
Σ	area per surfactant molecule
λ	wavelength
φ_d	volume fraction of the dispersed phase
φ_o	volume fraction of the oil phase
φ_p	percolation volume fraction
φ_w	volume fraction of water
$\chi(w)$	dielectric susceptibility
χ'	real component of the complex dielectric susceptibility
χ''	imaginary component of the complex dielectric susceptibility
Ω	ohm
σ	conductivity
ω	radian frequency 2pf
ω_c	cross over frequency

Table of Contents

List of Figures

Chapter 1 Introduction

Chapter 3 Materials and Methods

Results & Discussion

Chapter 4 Microemulsion Phase Behaviour Characterisation and Particle Sizing

Chapter 5 Dielectric Characterisation of Polar, Oil & Surfactant Components

Chapter 6 Dielectric Characterisation of the Surfactant Dispersed in Oil

Appendix

List of Tables

Chapter 1

Introduction

1. Introduction

Microemulsions, micelles and indeed emulsions and other colloidal systems have been the subject many studies to determine their size, structure or shape using a range of techniques such as small angle nuclear scattering (SANS) [Barlow *et al.* 2000], dynamic light scattering (DLS) [Rouch *et al.* 1989], high frequency dielectric spectroscopy [Feldman *et al.* 1995, Antalek *et al.* 1997, Feldman *et al.* 1997] and photon correlation spectroscopy (PCS) [Zulauf and Eicke 1979, Kantaria 1998].

Danielsson and Lindman [1981] and Langevin [1985] defined the microemulsion as two immiscible liquids, oil and water mixed with a surfactant to form a single phase, optically transparent or translucent (aggregates are smaller than the wavelength of visible light 400 nm $< \lambda <$700 nm) and thermodynamically stable liquid. The definition was further refined to include constraints on the structure of the microemulsion in that it must contain definite microstructure and a definite boundary or interface between the oil and water phase.

Emulsions are another type of colloid which consists of surfactant, oil and polar components. However unlike microemulsions they are not thermodynamically stable systems and do not form spontaneously. Emulsions require mechanical and thermal energy to be applied to a system containing the constituent components before the emulsions is created. They generally contain large aggregates (sizes of order μm) dispersed within the bulk continuum and can have a cloudy or opaque appearance. The emulsion readily separates into its constituent components as the added energy dissipates over a relatively short period of time (typically days). The rate of breakdown of the emulsion can also be speeded up by exposing it to cycles of extreme thermal conditions [Hill *et al.* 1990].

Interest in the application of microemulsions has grown significantly since the 1980's where the number of publications per year has increased from around 150 to over 1000 in 2009. The majority of the more recent publications cover applications in nano-particle production, drug delivery, polymerisation and reaction media research [Salager *et al.* 2005]. The number of publications retrieved using the key words "microemulsions" and "drug delivery" or "cosmetic" since 1980 and categorised under

biology, life sciences, chemistry, engineering, computing science, medicine, pharmacology and physics is displayed in Figure 1-1.

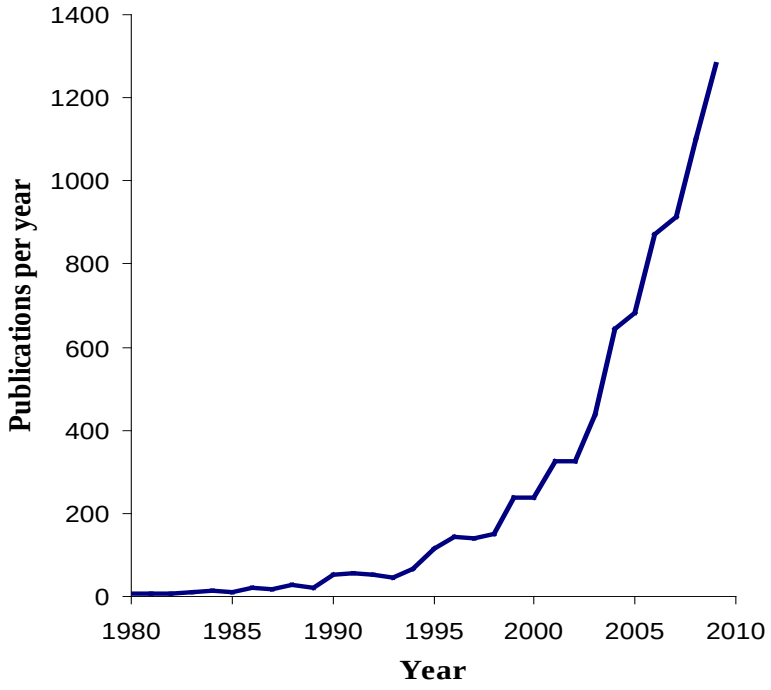

Figure 1-1 Number of publications per year containing the key words "microemulsions" and "drug delivery or cosmetic" updated from [Salager *et al.* 2005]

Probe techniques frequently used to examine the structure of samples, such as dynamic light scattering (DLS), photon correlation spectroscopy (PCS) and small angle neutron scattering (SANS) require the sample to be either diluted or be modified to render it visible to the probe. In the case of neutron scattering and infrared spectroscopy, deuterated forms of water D_2O and HOD have also been used to distinguish the OH stretching modes within a single molecule [Thompson and Gierasch 1984]. Dielectric spectroscopy possesses the advantage of not requiring the sample to be diluted or specially prepared for analysis.

There have been relatively few studies of colloidal systems using low frequency dielectric spectroscopy [Hill and Lawrence 2002, Hill *et al.* 1990, Craig *et al.* 1993, Hill 2001, Cooper and Hill 1996, and Hill and Cooper 1992] in comparison to the afore mentioned probe techniques. Unlike high frequency dielectric spectroscopy, low frequency dielectric spectroscopy remains a largely unexploited tool. One reason for this under exploitation is the Maxwell-Wagner or interface polarisation [Barsoukov and

Macdonald 2005] and electrode polarisation (also known as a barrier effect) which is the simplest form of interfacial polarisation [Jonscher 1983] where charged particles build up at the electrode, membrane or system interface. These charged particles form a layer at the interface which reduce or block the flow of current (Figure 1-2), and occurs at low frequencies in the range 10^6 Hz down to 10^{-5} Hz. It is these types of polarisation, but particularly the interface polarisation, which is of interest in this present study. It should be noted however that measurements of single points at the lowest frequencies can take over 24 hours.

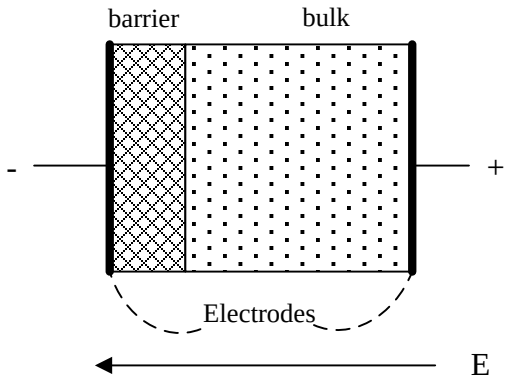

Figure 1-2 Electrode barrier layer. The sample is polarised by the action of the applied electric field. The polarised aggregates are attracted to the oppositely signed electrode and migrate to form a barrier layer on the electrode. The barrier layer is less conducting than the bulk hence reduces the apparent conductivity of the sample [Jonscher 1983].

Schwan [1992, 1960] consider that the dielectric dispersion due to electrode polarisation is a nuisance which must be reduced or eliminated, either experimentally or mathematically. Other researchers [Hill and Lawrence 2002, Hill *et al.* 1990, Hill 2001, Hill and Cooper 1995] however believe that the electrode polarisation is due to a thin barrier layer of the sample on the surface of the electrodes. The barrier layer is believed by Hill and Lawrence [2002] and Hill *et al.* [1990] to contain information related to the structure of the sample. General interface polarisation can be described as the build-up of charged particles at the boundaries between cells, aggregates or clusters of aggregates [Dissado 1987]. It is anticipated that examining the Maxwell-Wagner effect [Barsoukov and Macdonald 2005, Jonscher 1983] (Figure 1-2), will reveal information about the structure of the aggregates as well as the positioning of any drug that is solubilised within the microemulsion.

1.1 Amphiphilic Compounds and Surface Active Agents

Amphiphilic compounds are dual natured molecules which contain both polar head groups which have an affinity to water, and non-polar water hating tail groups [Tanford 1973] (Figure 1-3). The polar head group has a strong attraction to polar solvents whilst the non-polar component has an aversion to polar solvents.

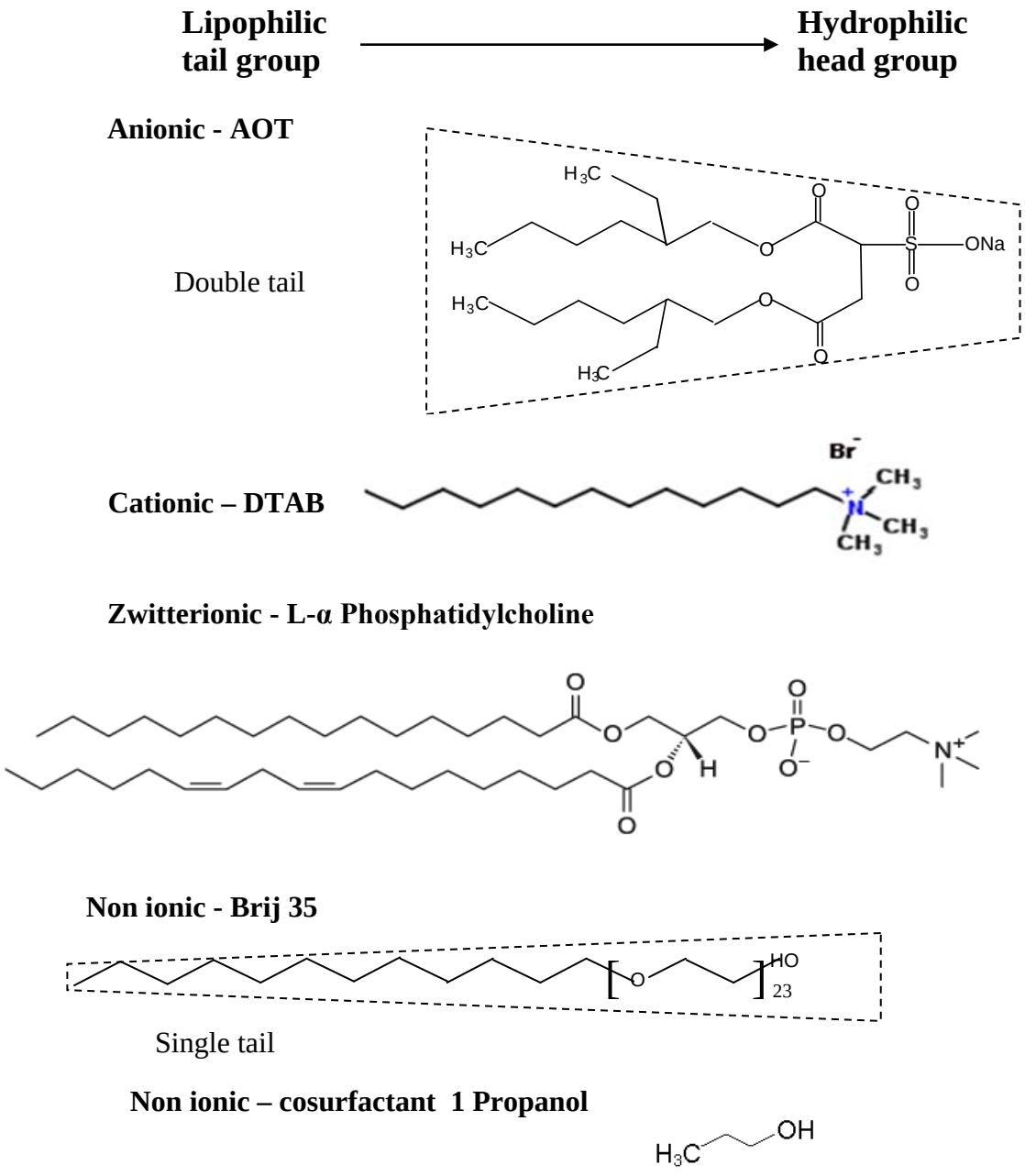

Figure 1-3 Representation of single tail and double tail surfactants

Surface active agent or surfactant, [Salager 1999] is the term used to describe the subgroup of amphiphilic molecules that have a tendency to migrate to, and locate themselves at liquid/liquid interface when added to a mixture of two immiscible (polar

and non-polar) liquids, or at the liquid/gas interfaces. The surfactant monomers orientate themselves with polar group facing the polar or aqueous solutions and the non-polar hydrocarbon tail groups facing the non-polar solution or gas (Figure 1-4a). The change in the nature of the interface between the immiscible liquids due to the presence of the surfactant is of considerable importance to the pharmaceutical, detergent, as well as other industries [Binks 1993]. Above the critical micelle concentration point (CMC) all additional surfactant monomers migrate from the gas/water interface and form micelles. This is exemplified by the creation of oil–water emulsions and the dispersion of particles in the suspension via the adsorption of the surfactants to the particles.

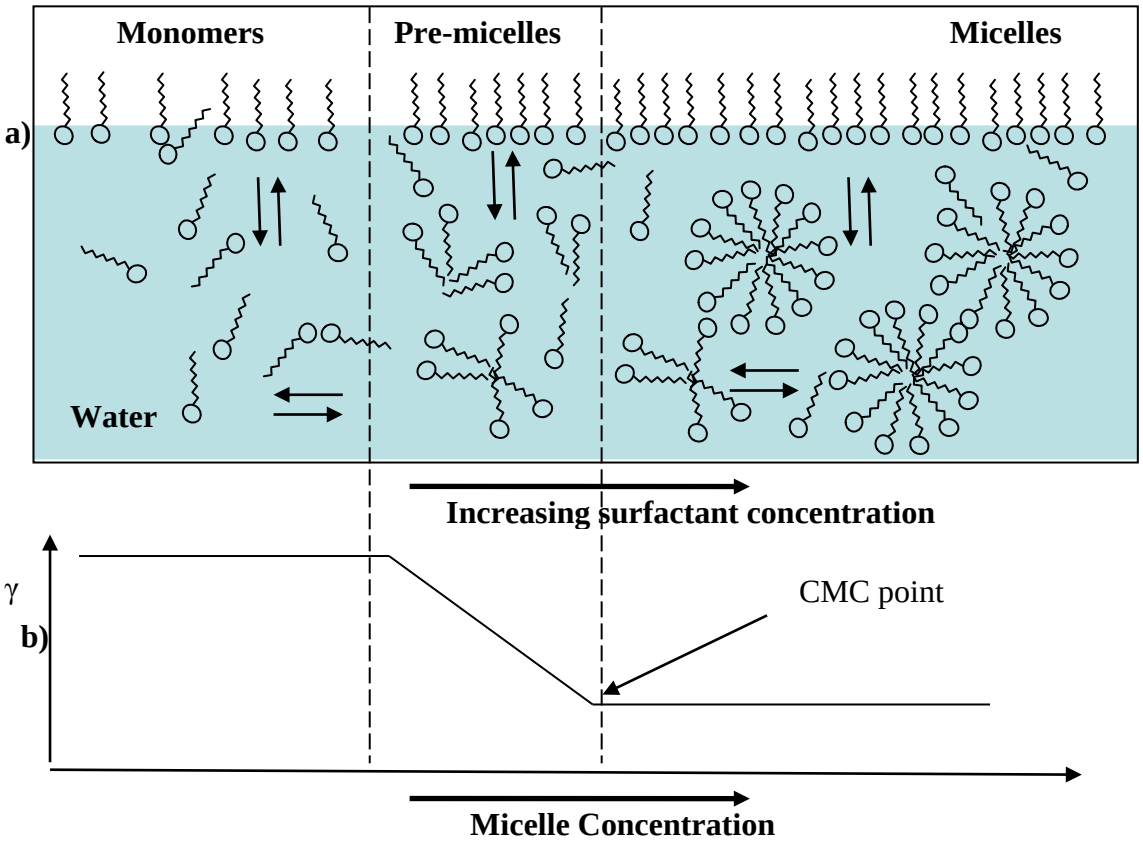

Figure 1-4 a) A schematic of the equilibrium that exists between surfactant monomers at surface and in the bulk and micellar aggregates [Durbut 1999]. b) Surface tension γ decreases as surfactant monomer concentration increases.

There are several types of surfactants and their classification is determined by the ionic nature of the head group, anionic, cationic, zwitterionic and non-ionic (Fendler and Fendler [1975], Oldenhove de Guertechin [1999]). Anionic head groups are negatively charged with a neutralising, positive counterion. The functional head groups are typically comprised of carboxylate ($RCOO^-$), sulphate (SO_4), sulfonate (SO_3), phosphate (PO4), or nitrate (NO_3). Anionic surfactants are the most common type and

have a wide range of applications from detergents used to remove soiling through to viscous self-thickening products. Similarly cationic head groups are positively charged with a neutralising negative counterion. The functional head groups are typically comprised of either quaternary ammonium (NR_4) or pyridinium (C_5H_5NH). Cationic surfactants are used in applications ranging from fabric conditioners, hair conditioners and bactericide and fungicide products.

Surfactants with zwitterionic or amphoteric head groups contain both anionic and cationic components. Some of these surfactants such as those based on amino acids are pH sensitive. Others such as the lecithin phosphatidylcholine are pH insensitive and are used in personal care products e.g. eye irritation and hair conditioner products.

Nonionic surfactants are second to the anionic group of surfactants in their industrial production market share. Nonionic surfactants do not become ionised in aqueous solutions because the hydrophilic head group cannot dissociate hence they are compatible all types of surfactants. Examples of this type of surfactant include Brij 35 ($C_{12}E_{23}$) and sugar esters which have low toxicity such as Span 80 sorbitan monooleate. Co-surfactants are alcohols such as propanol, and are usually classified under nonionic surfactant type. The apolar groups are so short that they are completely soluble in water or polar solutions or else the polar group is so small that its effects are overridden by the hydrophobic chain.

1.2 Critical Packing Parameter (CPP) and Hydrophilic-Lipophilic Balance HLB

There have been attempts to rationalise the behaviour of surfactants in terms of the hydrophilic-lipophilic balance (HLB) [Griffin 1949] and the critical packing parameter (CPP) [Israelachvili *et al.* 1976]. Both CPP and HLB are empirical methods used as a guide in the selection of and surfactants for particular fields of study. The surfactants used in this study are highly surface active compounds which are capable of forming reverse micellar aggregates [Eicke & Kvita 1984, Fletcher *et al.* 1984] and this capability varies for each surfactant and solvent mixture.

1.2.1 Hydrophilic-Lipophilic Balance Approach

The ability of a particular surfactant to form micelles are generally determined by the combined properties hydrophilic head group and hydrophobic tail group of the

surfactant and is known as hydrophilic-lipophilic balance (HLB). The HLB is defined by a number that ranges between 0 and 40. Surfactants with a HLB value < 10 generally have a low solubility in water or aqueous solutions and tend to form water in oil w/o microemulsions. Surfactants with a HLB value ranging from 10 to 20 generally have good solubility in water and can be used to form oil-in-water (o/w) microemulsions (Table1-1). Surfactants with HLB values in excess of 20 require the presence of a co-surfactant to improve its ability to reduce surface tension and form a microemulsion (Figure 1-4b). Other ranges of HLB values have been categorised as wetting agents, detergents and solubilisers with HLB values of 7-9, 13-15 and 15-18 respectively [Becher 1977].

Table 1-1 Surfactant HLB ranges including those able to form direct and reverse micelles

HLB range	**Microemulsion type**
3-6	w/o reverse microemulsion
7-9	Wetting agent
8-18	o/w microemulsions
13-15	Detergents
15-18	Solubilisers
>20	Such surfactants e.g. SDS need co-surfactant SDS to reduce the HLB for Microemulsion formation

1.2.2 Critical Packing Parameter (CPP) Approach

The CPP relates the ability of a surfactant to form a particular aggregate to its geometry. The CPP is calculated using equation

$$CPP = \frac{V}{a_0 l_c} \qquad \text{Eqn. 1-1}$$

where V = volume occupied by the alkyl chains ($Å^3$), a_0 = area occupied by the polar head group at the interface ($Å^2$) and l_c = length of the alkyl chain (Å).

Values of V and l_c can be calculated from Tanford [1980] and Israelachvili *et al.* [1976].

$$V = 27.4 + 26.9 n_c \qquad \text{Eqn. 1-2}$$

$$l_c = 1.5 + 1.265 n_c \qquad \text{Eqn. 1-3}$$

where n_c = close to but less than the number of carbon atoms per alkyl chain and l_c = 70>80% of the fully extended hydrocarbon chain length.

Calculated values of CPP for surfactant shapes ranging from conical to cylindrical surfactant shapes have been reproduced by Israelachvili *et al.* [1976] and are shown in (Figure 1-5). For values of CPP < 1 oil-in-water structures dominate. Spherical structures are formed for CPP < 1/3, cylindrical structures for 1/3 < CPP <1/2 and bilayers are formed 1/2 < CPP < 1. For values CPP < 1, inverted water in oil structures are formed.

AOT, a surfactant with relatively short hydrocarbon twin tails and a small polar head group, has an inverted truncated cone shape and readily forms reverse micro emulsions without the presence of a co-surfactant. Epikuron 200, E200 is twin long tail surfactant, but contains a zwitterionic head group. This cone shaped surfactant also forms reverse microemulsions, but requires the presence of a co-surfactant.

CPP shape	CPP	Surfactant	Structures formed
Cone 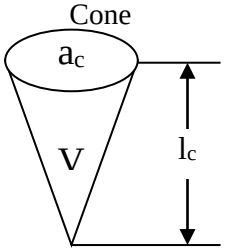	< 1/3	Single chain surfactant with large head group areas: NaDS in low salt some lysophospholipids	Spherical micelles 
Truncated cone or wedge 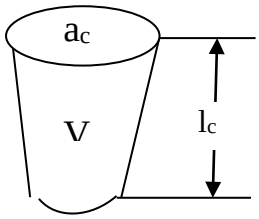	1/3 > 1/2	Single chain surfactant with small head group areas: NaDS in high salt, non-ionic surfactants lysolecithin	Globular or cylindrical micelles 
Truncated cone 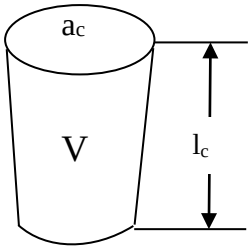	1/2 > 1	Double chain surfactant with large head-group areas, fluid chains: lecithin, sphingomyelin phosphatidylglycerol Some single chain surfactants with very small head groups	Flexible bilayer vesicles 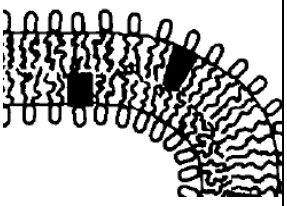
Cylinder 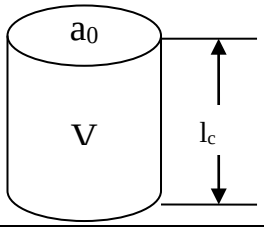	~ 1	Double chained surfactants with small head group areas: anionic surfactants in high salt, saturated frozen chains: phosphatidylethanolamine, phosphatidylserine + Ca^{2+}	Planar bilayers 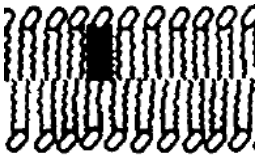
Inverted truncated cone 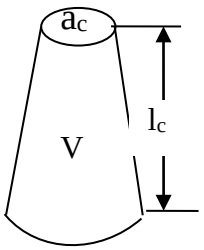	> 1	Double chained surfactants with small headgroup areas, nonionic surfactants, unsaturated phosphatidylethanolamine cardiolipin + Ca^{2+} phosphatidic acid + Ca^{2+} monosugardigglycerides cholesterol	Inverted micelles 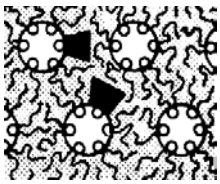

Figure 1-5 Packing parameters of surfactants and the aggregate structures they form. [Reproduced from Israelachvili *et al.* 1976]

1.3 Aggregate Formation and Structure- Micelles or Microemulsions

Microemulsions contains aggregates or droplets that consist of a surfactant shell or monolayer encapsulating either an oil or aqueous pool in the case of oil in water (o/w) or water in oil (w/o) microemulsions respectively. Any aggregates present in the dispersed phase are not visible to the eye because the sizes of such aggregates are less than the wavelength of visible light (400 nm < λ < 750 nm) and are of order 75 to 140 nm [Prince 1977]. In order to form a microemulsion, the surfactant has to reduce the interface tension between the hydrophobic oil and water to such a low value that it is virtually zero [Tanford 1973]. Microemulsions are thermodynamically stable systems which form spontaneously when the components are mixed in the required ratios. In addition, to the droplet aggregate structure, clusters of droplet and bicontinuous structures which form interfaces with both water and oil domains are also found in microemulsions.

The concept of micelle formation was introduced by McBain in 1913 when he concluded that soaps formed large aggregate or micelles in aqueous solution. The concept although initially opposed has now gained universal acceptance. Hartley described the spherical micelle, aggregate model in 1936 which is still generally accepted [Stenius 1984]. The term microemulsion was first coined by Schulman *et al.* in 1959 to describe the microemulsion spherical aggregate microstructure. Authors such as Zulauf and Eicke [1979] refer to the aggregate structures as swollen micelles in that the cavity within the surfactant aggregate contains varying volumes of the second immiscible components, oil in the case of oil-in-water (o/w) microemulsions or water in the case of water-in-oil (w/o) reverse microemulsions.

Winsor [1948] presented a qualitative classification and theory for ternary mixtures of water and oil stabilised by a surfactant or mixtures of surfactants. The Winsor microemulsion classifications theory was put forward to supplement theories put forward by McBain and Hartley. The Winsor classification denotes microemulsions of type I to type IV. Winsor type I, oil-in-water (o/w) and Winsor type II water-in-oil (w/o) two phase microemulsions (Figure 1-6) are formed when a relatively narrow range surfactant is added to varying ratios of water (in the presence of salt) and oil (Figure 1-7). As the ratio of surfactant is increased for relatively equal ratios of oil and water, the Winsor type III multiphase system is created. The type III systems contain a

range of structures which include the bicontinuous structures proposed by Scriven in 1976. The type IV phase is classified as a single phase o/w or w/o microemulsions.

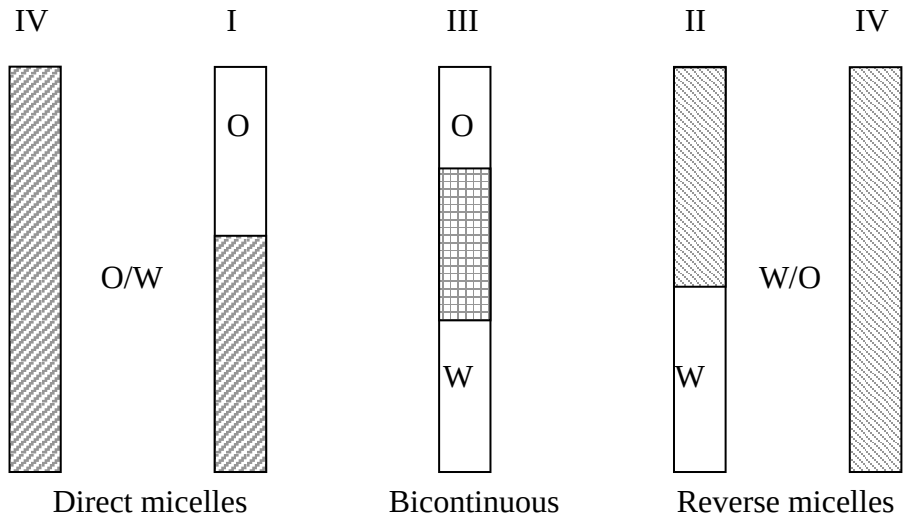

Figure 1-6 Schematic of the appearance of Winsor type I –IV microemulsion system

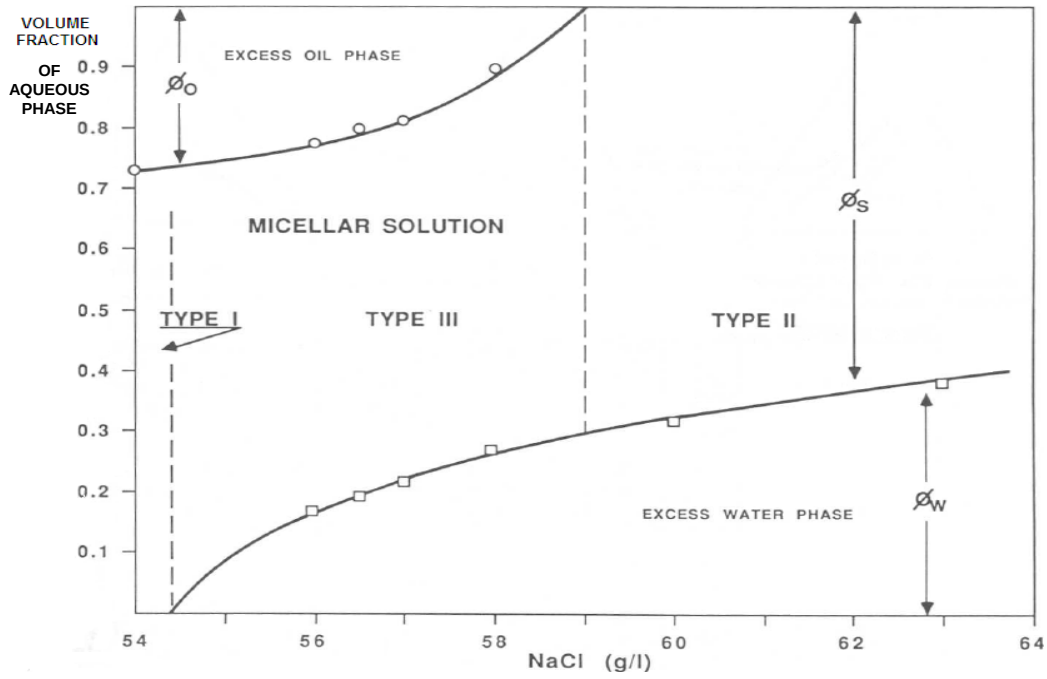

Figure 1-7 Change in Winsor type phases as volume fraction of the aqueous phase increases Bourrel & Schechter [1988]

Biologists and chemists have also considered the structure of micelles to be similar to cells or organelles [El Seoud 1984, Bru *et al.* 1995; Martinek *et al.* 1989] and hence can be used to model the transport of guest molecules through membranes using in vitro tests. The use of micelles as model systems for membranes has very important biological implications. The importance of micelles in the physiological transport and adsorption of lipids solubilisers has been generally recognised. Self-association and multi association of hydrophobic molecules is of great importance for many physiological molecules, food constituents and drug delivery.

1.3.1 Micellization – Normal or Direct Micelles

Normal or direct micelles are oil in water (o/w) aggregates dispersed within a water or polar continuum. The micellization process is the spontaneous aggregation or self-assembly of surfactants in within an aqueous solution. Surfactant monomers tend to adsorb at the surface (air/water interface) with the hydrophobic tails oriented towards the air and the polar head group immersed within the water or polar medium. As the concentration of the surfactant is increased and the surface is saturated with adsorbed monomers, the surface tension begins to reduce until the critical micelle concentration (CMC) point is attained (Figure 1-4) where all additional monomers aggregate into micelles. At surfactant concentrations above the CMC, micelles are dispersed in the aqueous continuum and are in dynamic equilibrium with the monomers both in the bulk and adsorbed at the surface. Surface tension remains relatively constant above the CMC (Tanford [1973], Burrell & Schechter [1988], Durbut [1999], Danov *et al.* [1999]).

Aggregates formed in aqueous solution have a spherical shape when the surfactant average aggregation number <n> is in the range of approximately 100. As the aggregation number increases disk and rod like micelles shapes tend to form (Figure 1-8). However, for surfactant concentrations lower than the CMC point, some monomers form micellar or premicellar aggregates and exist in dynamic equilibrium with the monomer. Studies by Hadgiivanova and Diamant [2007], Cui *et al.* [2008], Drennan *et al.* [1998], using ^{1}H NMR spectra, NMR self-diffusion, stopped-flow rate coefficients techniques have given indications of premicellar structures which exist well before the CMC. The authors concluded that micelle formation is a multi-step process up to and beyond the CMC point in aqueous solutions. The application of fluorescence correlation spectroscopy (FCS) has been used as an alternative method of characterising

the premicellar and micellar self-aggregation behaviour of surfactants (Zettl *et al.* [2005], Barnadas & Estelrich [2009]).

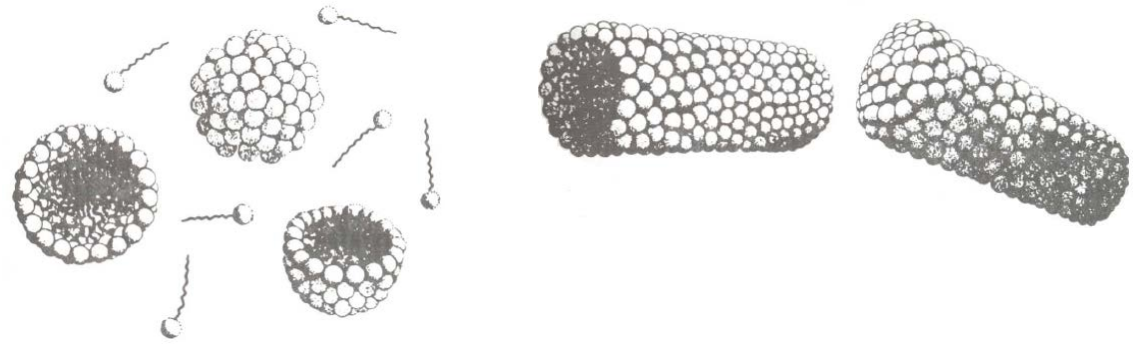

a) Spherical micelles b) Rod like micelles

Figure 1-8 Pictorial representation of spherical and rod like micelles Reproduced from Bourrel and Schechter [1988]

In addition to the reduction in surface tension with increasing surfactant concentration, a number of physio-chemical properties also vary with the change in concentration of the surfactant (Figure 1-9). These properties show dramatic changes in magnitude or gradient in the surfactant concentration region associated with the CMC and it is agreed that these changes coincide with the formation of aggregates.

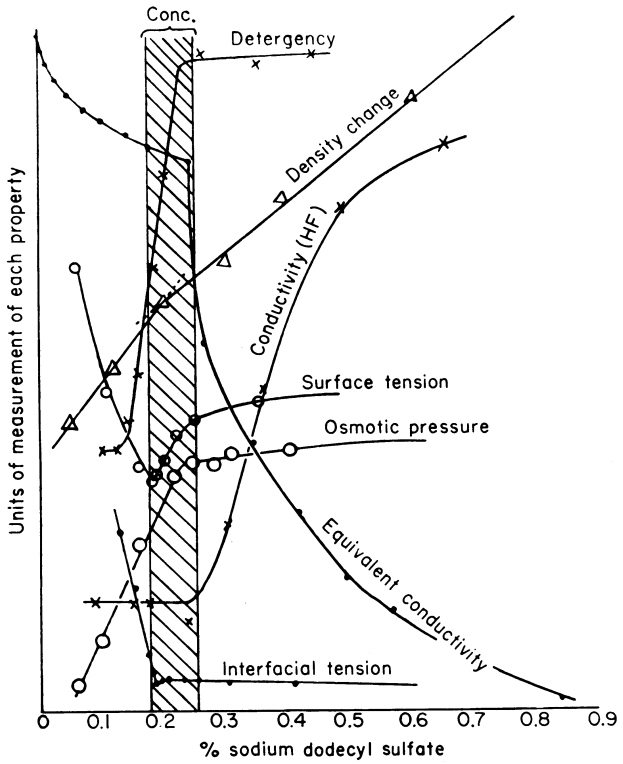

Figure 1-9 Changes in the concentration of a wide range of physio chemical quantities in the neighbourhood of the critical micelle concentration (Reproduced from Bourrel and Schechter [1988] original source Preston [1948])

1.3.2 Reasons for Micellar Aggregation in Aqueous Solutions

When surfactants are dissolved in water, or polar solvents, the hydrophobic effect causes surfactant monomers to achieve segregation of their hydrocarbon tails from the polar solvent by; self- aggregation to form micelles and/or by the adsorption of the monomer at the surface interface with hydrocarbon tails re-oriented away from and out of the solvent. The ability of a particular surfactant to form micellar aggregates is governed both by the attractive and repulsive electrostatic forces between polar – polar head groups and polar head group – water molecular interactions. The force of attraction facilitates the aggregation growth process whilst the repulsive force limits the size of the aggregate (Tanford [1977], Israelachvili *et al.* [1976]). In aqueous solution, a minimum number of monomers have to become associated with each other before an effective elimination of the hydrocarbon-water interface and the consequential shielding of surfactant hydrocarbon tails from the aqueous solvent by the polar head groups can be achieved. Thus micelle formation is a cooperative process requiring many monomers to simultaneous participate in the formation of a single micelle.

The premicellar aggregates are short lived structures as the hydrophobic screening of the surfactant hydrophobic tail is ineffective as the number of screening monomers are too low (Hadgiivanova & Diamant, [2009]).

1.3.3 Micellization – Indirect or Reverse Micelles

Reversed or water in oil (w/o) microemulsions consist of aggregates of surfactants containing water or a polar core which are dispersed with in an oil continuum. Reverse micelles are structurally the reverse of the normal micelle having a surfactant shell with the head group orientated towards the interior of the shell and the hydrocarbon tail group directed toward the oil continuum. El Seoud [1984] and Luisi *et al.* [1988] put forward a pictorial representation of a reverse micelle comprising of a surfactant shell sodium bis(2-ethylhexyl) sulfosuccinate (AOT) and containing water. The micelle contains regions of tightly bound water located near the anionic head group at the shell interface, and a pool of unbound water in the centre of the spherical shell (Figure 1-10) indicated by dark and light grey shading, respectively.

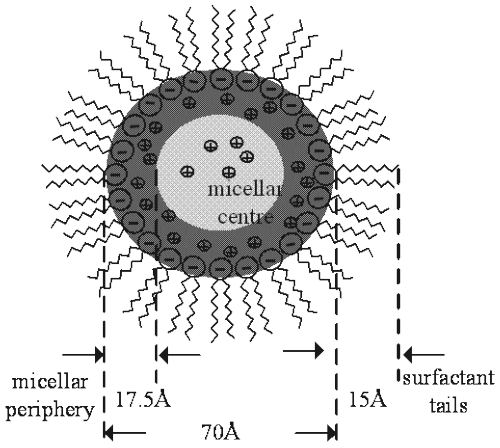

Figure 1-10 Pictorial representation of the interior of a reverse micelle showing the different regions of the water pool.

1.3.4 Reasons for Reverse Micellar Aggregation

Surfactants solubilised in apolar solvents do not experience a hydrophobic effect (Bourrel and Schechter [1988], Ruckenstein & Nagarajan [1980]). The surfactant tail group remains relatively unchanged prior to and post aggregation in the apolar solvent. The forces responsible for association are directly attributed to the attractive ionic or dipole-dipole interaction of the surfactant head groups. The aggregates formed within the apolar solvent contain a relatively small number of surfactant monomers as it is sterically constraining to arrange the surfactants so that their head groups are in close proximity. Hence there is no apparent CMC for apolar systems. The addition of water to the reverse micelles enables the size of the aggregates to grow (Martinek *et al.* [1989], Eicke, and Zulauf [1979]) via hydration of the head groups, swelling and the eventual pooling of free water in the interior of the aggregate at which point the aggregate is described as a microemulsion Figure 1-11 to Figure 1-16.

The size and structure of micelles with varying levels of hydration have been studied using many techniques. Researchers (Zulauf & Eicke [1979], Kantaria [1998], Hauser [1989], Kaler [1991]) using techniques such as photon correlation spectroscopy (PCS), ^{2}H NMR, electron spin resonance (ESR) spin labelling authors have reported differences between the structures with respect to the variation in the levels of hydration. It is considered that reverse aggregates containing low ratio of $W_0 = [H_2O]/[\text{surfactant}]$ have no detectable free water, any water present is considered to be strongly bound to the surfactant head group and the aggregate is described as a micelle. As the ratio W_0

increases, unbound water accumulates in the core of the aggregate and the aggregate is described as a reversed microemulsion.

Photon correlation spectroscopy was used by Zulauf and Eicke [1979] to examine hydration levels of reverse micelles and microemulsions comprises of water, the surfactant aerosol-OT (AOT), and the oil, isooctane. Zulauf and Eicke found that despite their effort to purify and remove any water contaminant from the supplied surfactant and oil, reversed micelles with no added water had a radius of 15.0 ± 0.3 Å. This was larger than expected as the AOT molecule has a length of 12 Å. When water was added to a molar concentration ratio, $W_0 = [H_2O]/[AOT] < 10$ in the temperature range 0-50°C the micelles radius size increased to around 35 Å. The size of the micelle radius was found to be temperature independent up to $W_0 = 10$ (Figure 1-11). The micelles behave as a rigid structure which also indicated that the water is bound or highly structured. The size of the aggregates begin to exhibit strong temperature dependent characteristics when $W_0 > 10$. The water within the core of the aggregate is considered to be unbound and sensitive to variations to external temperature when $W_0 > 10$ (Figure 1-11).

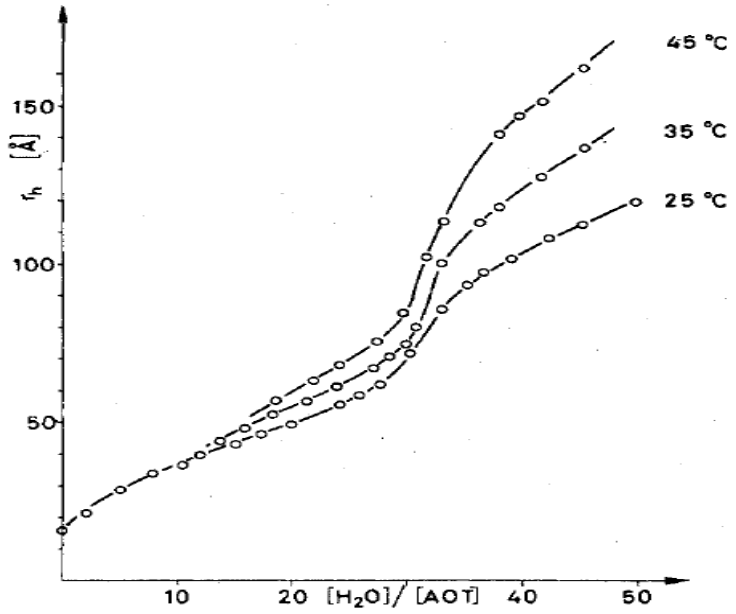

Figure 1-11 Measurements of the Stokes radii r_h of microemulsions formed by water and AOT in isooctane as a function of molar ratio $[H_2O]/[AOT]$ for three temperatures. (Reproduced from Zulauf and Eicke [1979])

Infrared spectroscopy studies have also provided evidence of water exhibiting different natures within the interior of the reverse microemulsion aggregates. Thompson and

Gierasch [1984] have reported a single absorption band occurring at a wavelength of 1400 nm when the examining a reverse micelle with a low W_0 ratio of ~ 1.5. This absorption band is attributed to water that is tightly bound to the polar head group of the surfactant. When $W_0 > 8.3$ the absorption band shifted to a wavelength of 1420 nm and a second band appeared at wavelength 1670 nm. The intensity of the second absorption band increased as W_0 was increased to 21.6. The second absorption band is believed to be due to the accumulation of free water within the aggregate (Figure 1-12).

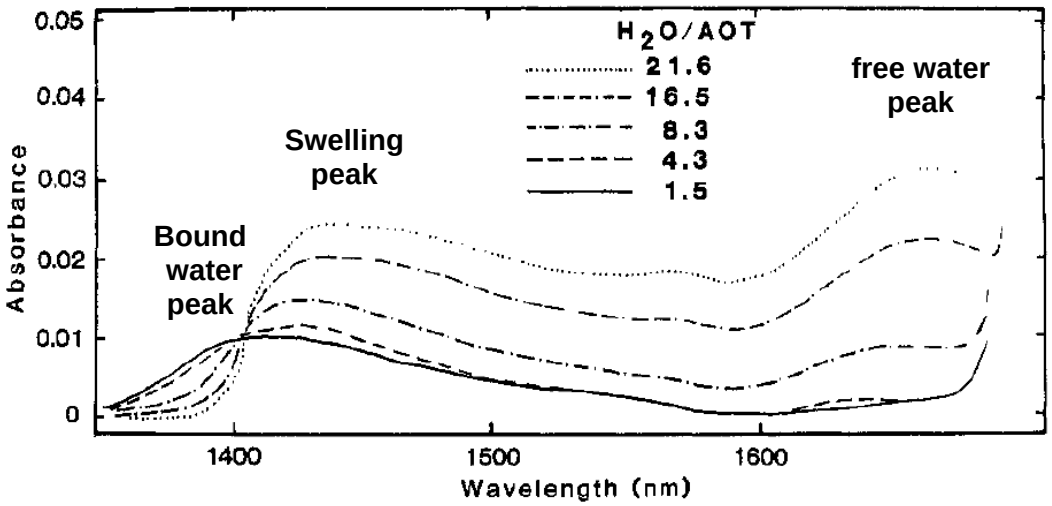

Figure 1-12 Near–IR spectra of water in AOT reverse micelles as a function of water content. (Note the appearance of a second band at 1670 nm and a shift from ca. 1400 nm to 1420 nm with increasing water content. Reproduced from [Thompson and Gierasch 1984].

Martinek *et al.* [1989] described the variation in the size and structure of a reverse micelle as concentration ratio of water and surfactant W_0 is varied. The addition of water has a dramatic effect on the solubility of surfactants and their aggregation in solvents. The initial water added serves to hydrate the head groups and this water is considered to be bound. Water added subsequently can be visualised as forming a pool in the interior of the reverse micelle and results in a dramatic increase the aggregation as well as the reduction in the number of micelles. The reduction in the number of micelles is due to micelle growth via the coalescence of smaller micelles (Figure 1-13). The transition between the head group hydration process (bound water) and the forming of pools of free water has been shown to be dependent on the charge to mass ratio of the surfactant counterion and occurs at around $W_0 = 10$ for sodium bis-(2ethylhexyl) sulfosuccinate [Eicke and Kvita 1984] (Figure 1-14 to Figure 1-16).

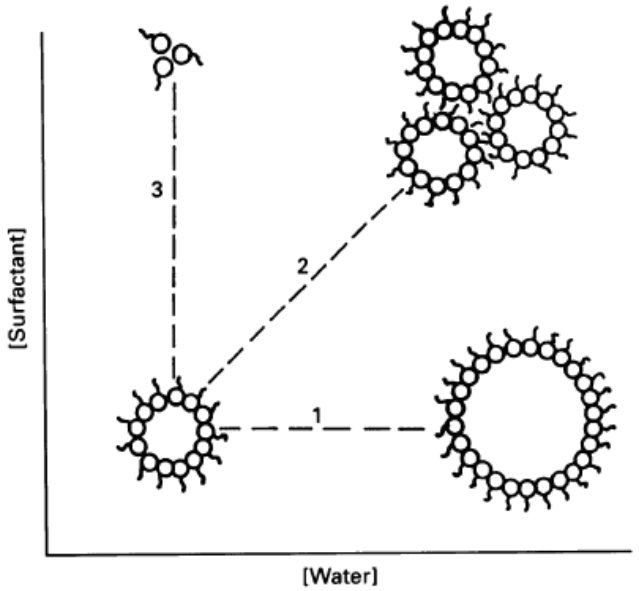

Figure 1-13 Path 1-Increasing water concentration leads to an increase in micelle size for fixed surfactant/oil concentration ratios. Path 2- An equal increase in the concentration of both water and surfactant leads an increase in micelle concentration but no increase in micelle size. Path 3- An increase in surfactant concentration leads to a decrease in size of micelles but the concentration of these smaller micelles increases. (Reproduced from Martinek *et al.* [1989])

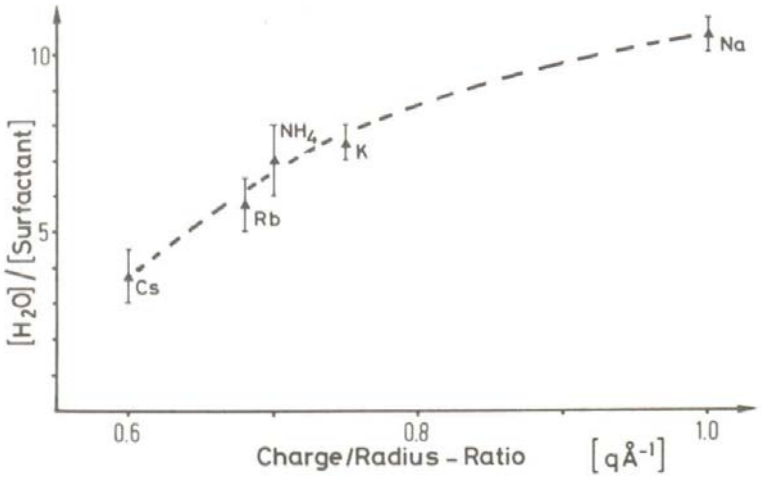

Figure 1-14 Ratios of water to surfactant $[H_2O]/[Surfactant]$ which induce the transition between micellar and microemulsion phase states in iso-octane against the charge/radius ratio. Surfactants: alkali and ammonium bis-(2-ethylhexyl) sulfosuccinates (reproduced from Eicke and Kvita [1984])

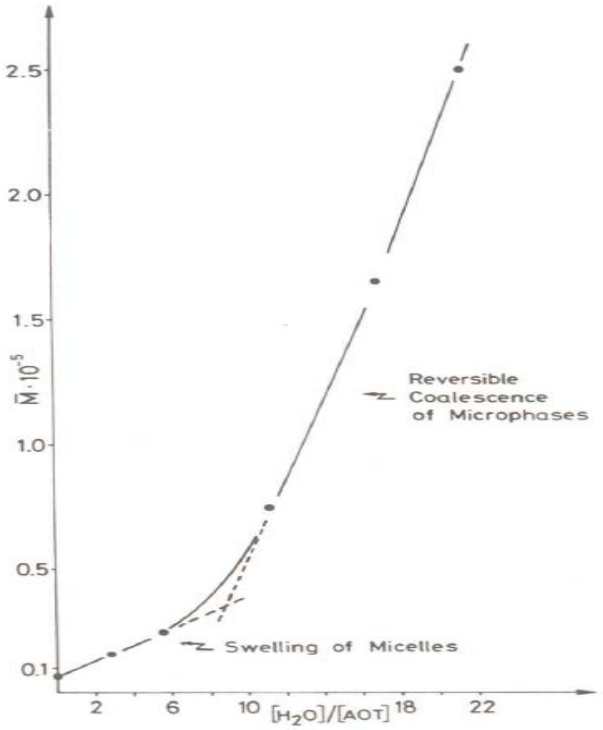

Figure 1-15 Mean weight average of sodium bis-(2-ethylhexyl) sulfosuccinate (AOT) as a function of the ratio of water to AOT at constant temperature (298K) (reproduced from Eicke and Kvita [1984])

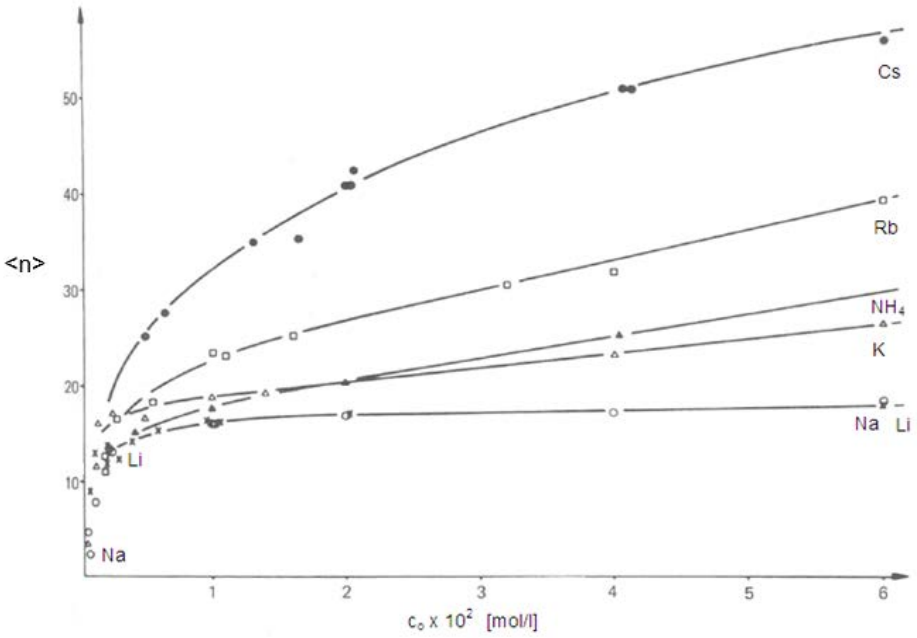

Figure 1-16 Average aggregation number <n> of Li (x); Na (○); K (Δ); NH4 (▲); Rb(□); Cs (●) di-2-ethylhexylsulfoccinate (AOT) in iso-octane at 298K based on vapour pressure osmometry (Reproduced from Bourrel and Schechter [1984])

1.3.5 Solubilisation and Drug Delivery

Some drugs are soluble in water while others are insoluble in water. The interior of the microemulsion droplets are able hold the drug when solubilised in either a hydrophilic or hydrophobic medium. The microemulsion is able to carry small packets of the drug to the target area. The size and the structure of the microemulsion droplet are important. A large droplet with a large interior has the potential to hold a greater amount of a drug. Kantaria [1998] reported that the PCS technique detected a reduction in the particle size of the aggregate when a 10% w/w solution of the drug sodium salicylate was added to the aqueous phase of a microemulsion comprising of 25% w/w AOT, oil isopropyl myristate (IPM) and water. In addition to this size reduction, aggregates with <10-12.5% w/w aqueous phase were no longer detectable using PCS. This is due to the aggregates being smaller with the presence of a co-solvent, as co-solvents such as sodium salicylate also need to be hydrated. Once both the surfactant head group and the co-surfactant are hydrated, additional water added to the mixture is available to pool within the interior as the aggregate swell to a size that is detectable using PCS.

It is important to determine the bound nature of the water inside the core of the micelle aggregate. The selection of the reverse microemulsion aggregate as a medium for drug delivery is dependent on how much drug can be solubilised within the water within the core. If the water is bound to the surfactant, then it is not free to be used as a medium to disperse a drug.

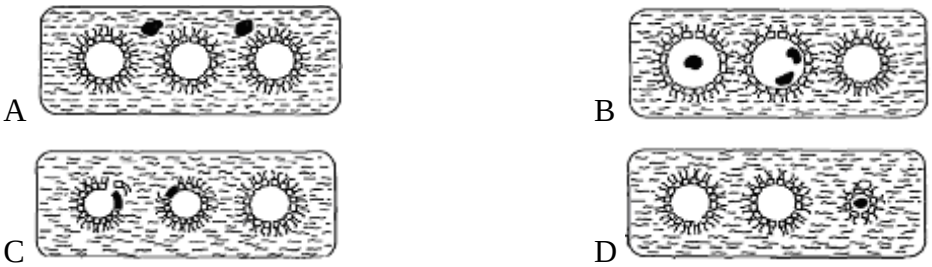

Figure 1-17 Geometrical models for solubilisation. The model suggests changes to the size of the reverse micelle based on the site of the solute A: Solute within bulk phase, B: Solute within the water core, C: Solute located at the interface, D: Solute segregated. (Pileni *et al.* [1985])

Pileni *et al.* [1985] have used small angle x-ray scattering (SAXS) to examine the structure of reverse microemulsions comprised of the surfactant AOT, oil isooctane and water to determine the sites of a solubilised drug. The team used solutes that were expected to be solubilised at various sites represented by models A-D (Figure 1-17).

The sizes of the aggregates were found to be affected the addition of the solute (Kantaria [1998]) for models A-C however the model D configuration could not be confirmed.

1.4 Rates of Micellar Aggregate Formation

1.4.1 Direct Micelles

In aqueous micellar solutions, aggregates are dynamic and transient structures (Winsor [1968]) in that an individual amphiphile is only present in a particular aggregate for a finite lifetime, τ_1, as there are rapid exchanges of monomers with the bulk aqueous solution. Also the structure of the whole micellar aggregate breaks down over a longer time interval, τ_2. The slow process τ_2, is thought to take place through a sequence of increasingly smaller aggregates. These two processes have been characterised by two relaxation times where, $\tau_1 << \tau_2$ and τ_1 the fast exchange of single monomers has been reported by Lang *et al.* and Aniansson *et al.* [1976] to be in the order of microseconds and τ_2 the slow complete dissociation of the micelle has been found to have a relaxation time in the order of milliseconds (Figure 1-18).

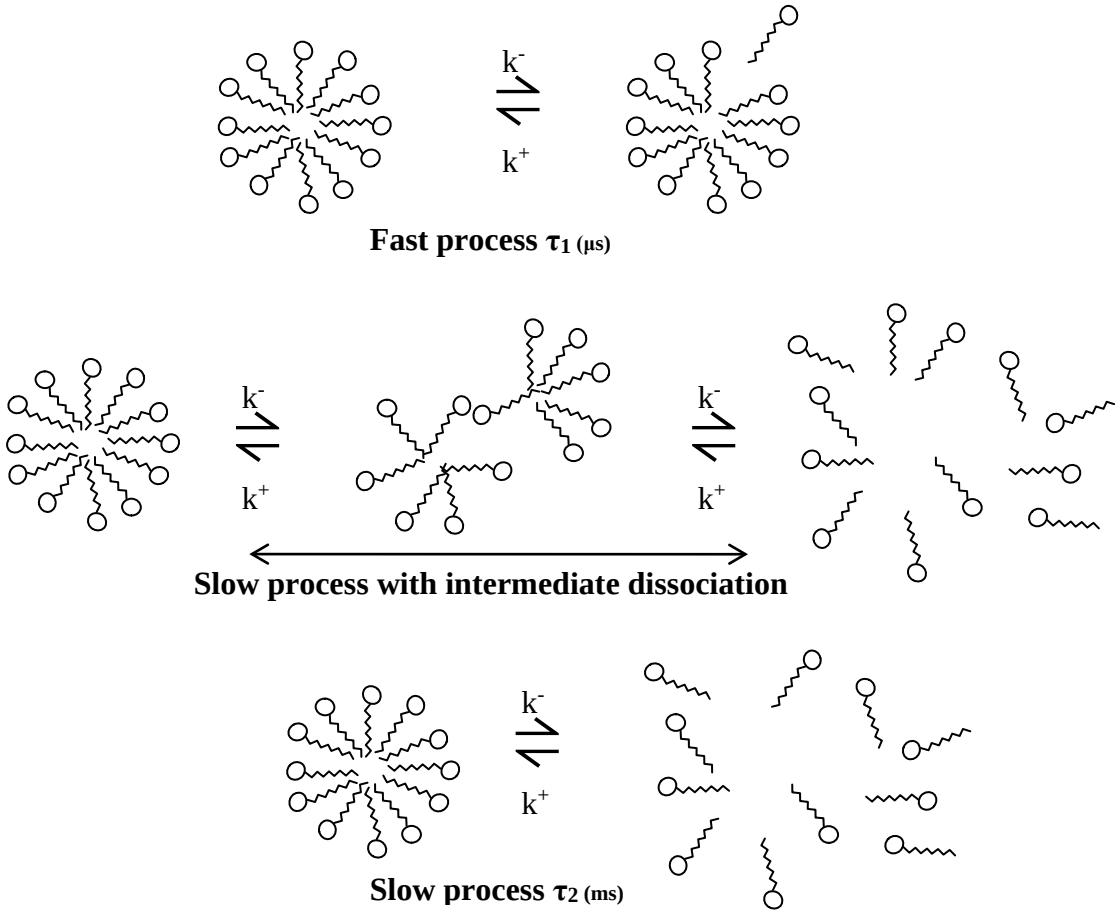

Figure 1-18 The relaxation mechanisms proposed for dilute micellar solutions of pure surfactants. (Adapted from Bourrel and Schechter [1988])

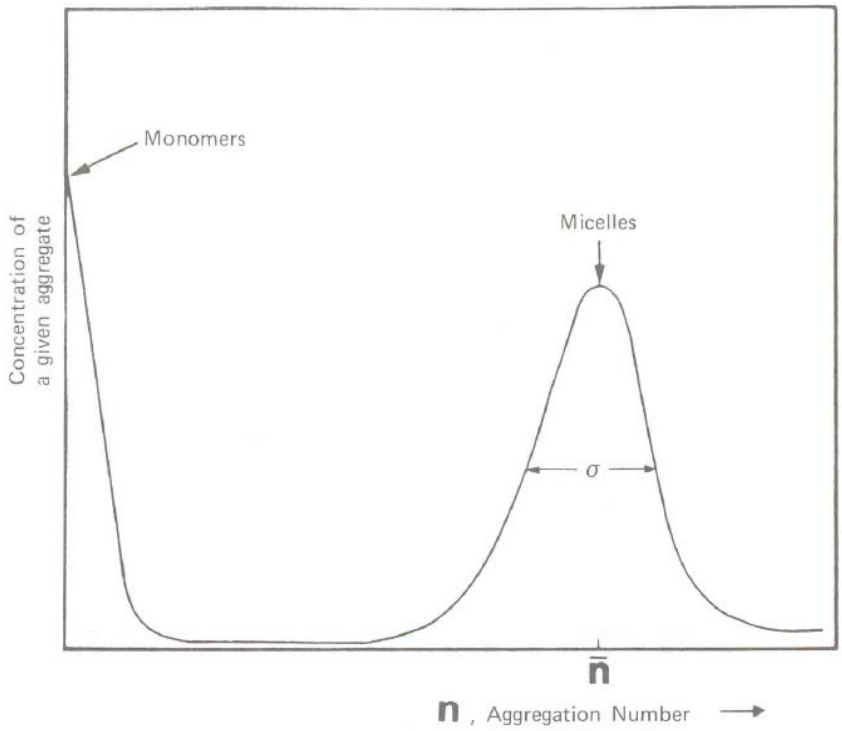

Figure 1-19 Form of distribution curve for aggregates which is responsible for the existence of the two relaxation times: τ_1 and τ_2. (Reproduced from Bourrel and Schechter [1988])

A number of researchers (Hadgiivanova and Diamant, [2007], [2009], Barnadas-Rodreguez *et al.* [2009], Brinch *et al.* [2009]) have reported the presence of aggregates described as premicellar aggregates which exist well before and after the CMC point depicted in Figure 1-9. The micelle aggregation number distribution curve (Figure 1-19) is dominated by two species indicating that the intermediate aggregate species do not either exist in large enough populations or are too unstable to be observed with the techniques previously mentioned.

1.4.2 Reverse Micelles

Eicke *et al.* [1989] used conductivity measurement of AOT stabilised reverse microemulsions to show that rate of droplets charge fluctuations ranged from 0.1 μs to 1 μs and was due to surfactant ions joining and leaving aggregate, and ions such as counter-ions moving through water channels. North *et al.* [1986] described the process of droplet fusion and subsequent separation as pool communication (Figure 1-20). This communication process can only proceed if a channel is opened in the surfactant droplet shells resulting in a fused droplet containing an excess of surfactant due to the change in the surface to volume ratio. The fusion process also results in an increase in the viscous interfacial forces from the surrounding medium which must be reduced. This reduction

in energy is achieved by expelling surfactants from the interfacial region resulting in separation of the fused droplets.

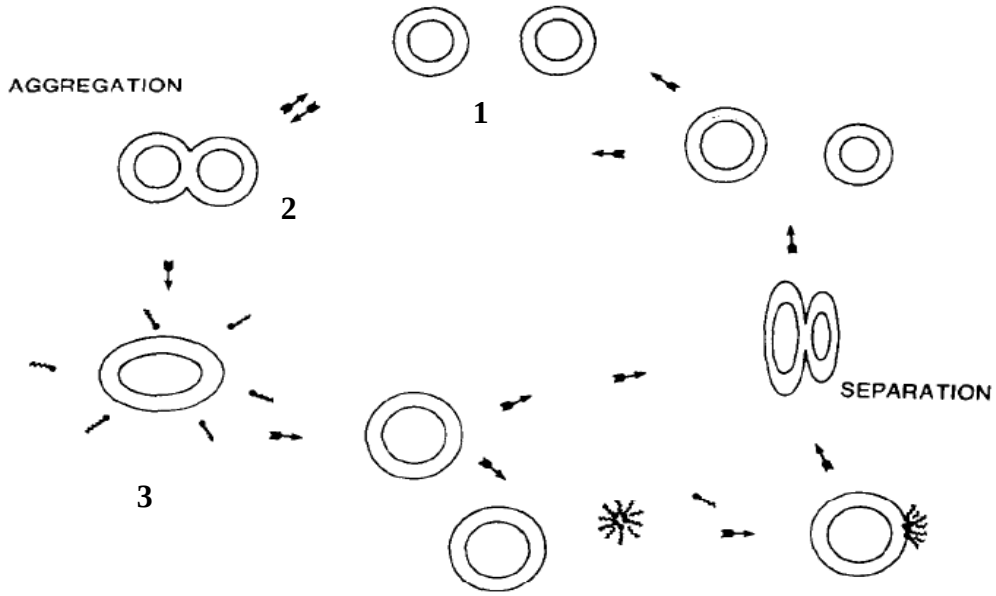

Figure 1-20 Mechanism of aggregation and separation of individual droplets due to attractive interactions in microemulsion system (reproduced from North *et al.* [1986])

1.4.3 Solubilisate Exchanges in Reverse Micelles

Particulates encapsulated within reverse micelles droplets pools as well as those adsorbed at the interfaces have been observed to pass rapidly to other droplets within the sample. The rate of exchange was found to be independent of the size and of the charge of transferred the particulate (Bru *et al.* [1995], Fletcher *et al.* [1987]). Particulate exchange is facilitated via the formation of a transient dimer (Figure 1-21 a) for those particles that are hosted within droplet pools. Other exchange pathways can be employed when particles are not confined to the droplet pool such as exchange by interface contact (Figure 1-21 b) or via passage through the apolar region (Figure 1-21 c). Process b) and c) are faster than a) as this process requires the formation of dimer.

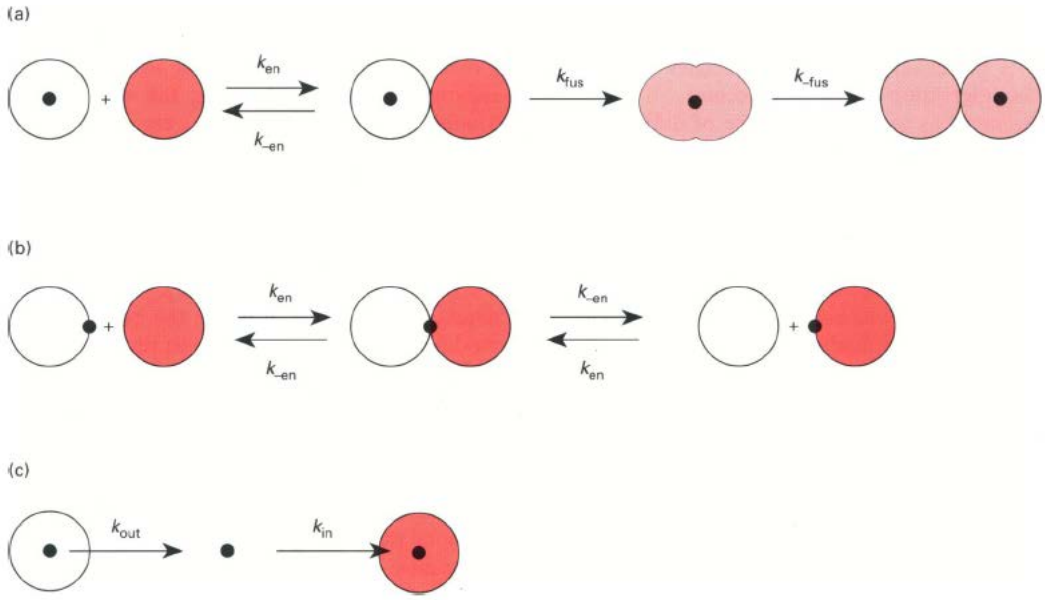

Figure 1-21 a) Exchange of hydrophilic molecules: fusion of reverse micelles and formation of a transient dimmer is compulsory: b) exchange of amphiphilic or interface-bound molecules: micelle collision is sufficient for exchange, and so fusion is not compulsory; c) exchange of oil-soluble molecules through interfacial transport: collision is not even required. Subscripts en and fus denote encounter and fusion, respectively (Bru *et al.* [1995])

1.5 Structure of Bicontinuous and other Colloidal Microstructures

Scriven [1976] compiled a hypothetical ternary phase diagram (Figure 1-22) from multiple authors covering the structures observed in mixtures classified as Winsor type III systems. The ternary diagram contained spherical micelle phases for direct, S1, and reverse, S2, phases. More ordered structures such as hexagonal, rod like structures appear in the middle phase M1 and M2 at higher surfactant concentrations or lower temperatures. Large multilayer lamellar structures have a gel like appearance, G1, and, G2. The bicontinuous structures are classified as viscous cubic systems V1, and V2. Schematic representations of possible bicontinuous structure are depicted in Figure 1-23.

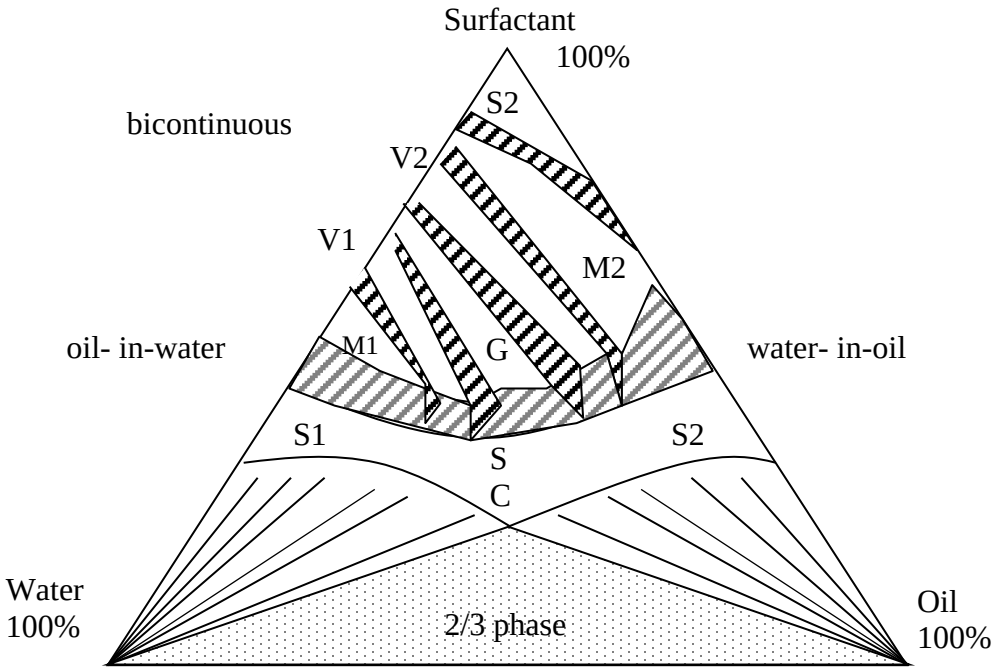

Figure 1-22 Hypothetical water-oil-surfactant ternary phase diagram generated from Winsor's phase schemes and other sources. [Scriven 1976]

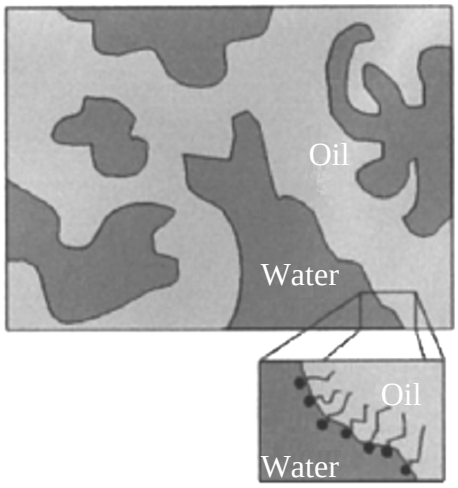

Figure 1-23 Schematic representation of non-cubic bicontinuous microstructures present in surfactant rich Winsor III system reproduced from Lawrence and Rees (2000)

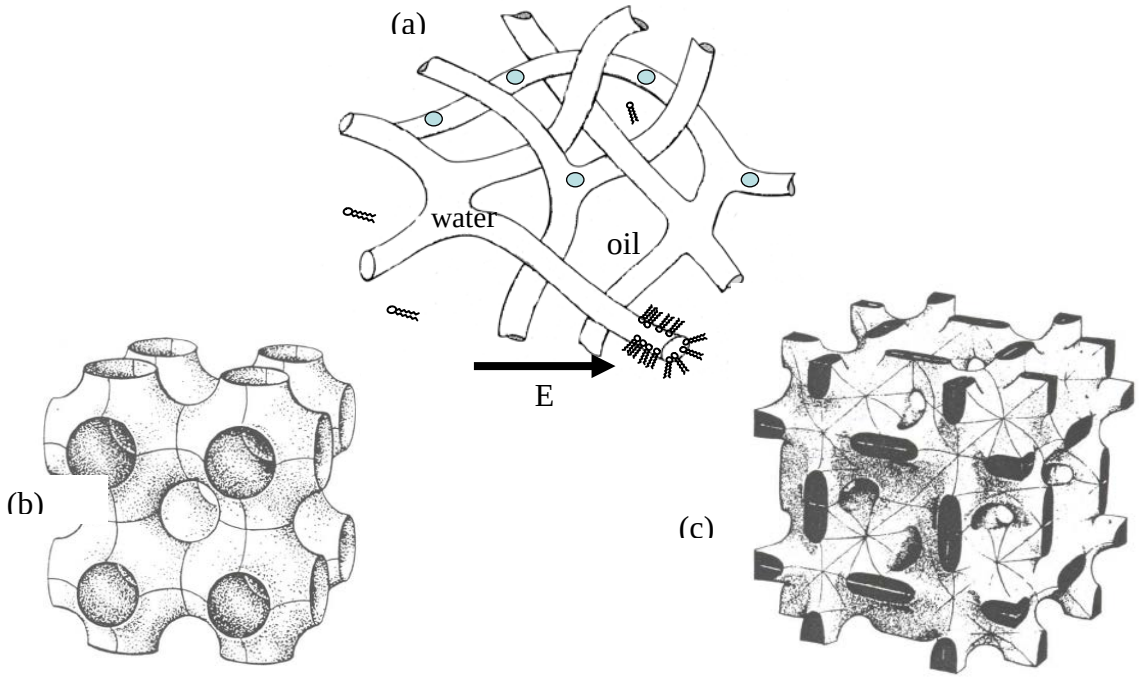

Figure 1-24 (a) Bicontinuous interconnecting conduits [adapted from Chen *et al.* 1986] (b) & (c) cubic symmetry structures [Scriven 1977]

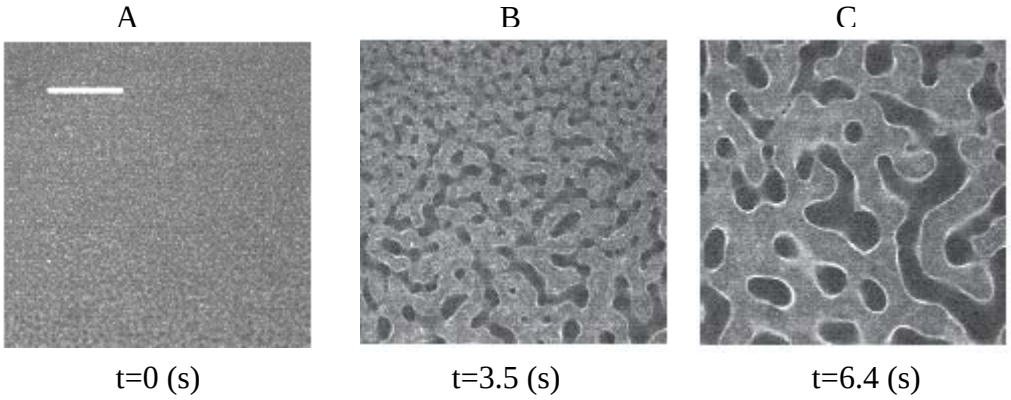

Figure 1-25 Formation of bijel via phase separation – Time series of fluorescence confocal microscopy images [adapted from Herzig *et al.* 2007]

1.5.1 Liquid Crystal Structures

Liquid crystal phase or mesophase are formed when the surfactant ratio is intermediate to high. This phase can contain either lamellar or hexagonal, rod like structures [Lawrence and Rees 2000]. The presence of the liquid crystal phase can be confirmed if polarised light appears as birefringent after passing through a sample with the crystalline structure.

1.5.2 Bicontinuous Structures

Bicontinuous structures contain both water and oil domains separated by an amphiphile interfacial layer of minimal surface or no mean curvature. The interface takes the form of saddle shape for periodic structures with cubic symmetry forms as described by Scriven [1977] (Figure 1-24 b and c). Birefringence is not observed when these structures are examined using plane polarised light hence the cubic structures are not thought to be macroscopically ordered and considered to be some type of molten cubic phase [Chevalier and Zemb 1990].

Bicontinuous structures with a more chaotic irregular form are observed to have the form described by Lawrence and Rees [2000] and imaged experimentally by Herzig *et al.* [2007] (Figure 1-25).

1.5.3 Percolating Micelle Cluster Structure

The transport of charged species or increase in electrical conductivity (percolation) in the w/o microemulsion, can be used for characterising morphological clustering and bicontinuous structural transformations within microemulsions. The onset of percolating phenomena has been shown to be dependent on temperature, volume fraction of the dispersed phased or electrical field strength. Eicke *et al.* [1986] and Langevin [1986] and is believed to be due to van der Waals force of attraction.

Langevin [1986] describes possible mechanism for the increased conductivity where by water cores of clustered droplets become connected during percolation and/or the conductivity of the interfacial layer becomes high enough to produce a steep increase in conductivity across the whole sample. Figure 1-26 shows the possible structural evolution in microemulsions as the volume fraction of the dispersed phase is increased above the percolation threshold, φ_p.

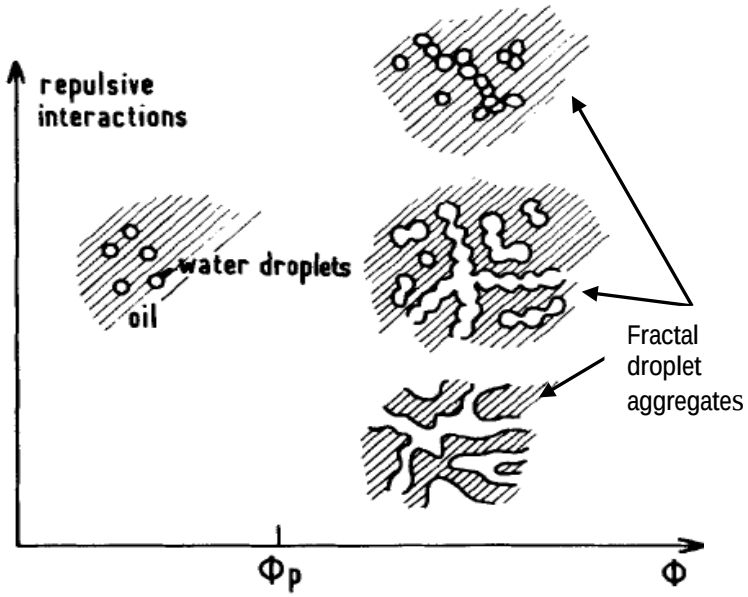

Figure 1-26 Possible structural evolution of w/o microemulsion with increasing droplet volume fraction for hard sphere like attractive droplets

Antalek *et al.* [1997] in examining the percolation phenomenon in reverse microemulsion described the phases of microemulsions as dispersed, continuous and pseudo phase, where the pseudo phase is attributed to fractal droplet aggregates undergoing percolation also described as percolating clusters. The authors analysis of temperature, volume fraction and cosurfactant (chemical potential) percolation, concluded that static percolation was probably the dominant mechanism for charge transport. Leading to the suggestion from NMR self-diffusion experiments that bicontinuous structures do not contribute significantly to static charge transport rather, that charge transport must be due to cluster (strings) of droplets. A simple two-state diffusion model for this conclusion suggests a mixture droplets, clusters and bicontinuous structures existing in equilibrium (Figure 1-27).

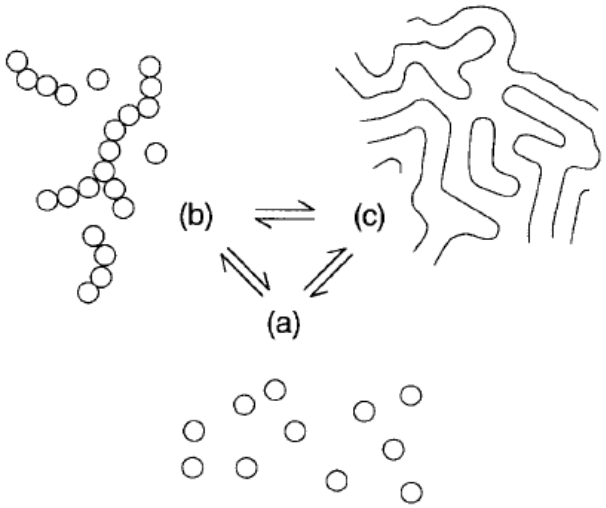

Figure 1-27 Equilibria between (a) separated reverse microemulsion droplet, (b) percolating fractal clusters of microemulsion droplets, and (c) bicontinuous structures of low to zero mean curvature [Antalek *et al.* 1997]

1.6 Structure Models for Microemulsions

1.6.1 Surfactant Film Curvature

The shape of the dispersed microemulsion aggregate is dependent upon the spontaneous curvature, C_0, of the surfactant layer or film. The surfactant molecule is represented as cone, truncated cone or cylinder (Figure 1-5). Where $C_0 > 0$ the interface curves towards the water continuum (direct micelles) and $C_0 < 0$ the interface curves towards the oil continuum. When the mean spontaneous curvature approaches zero, bicontinuous structures can be formed. This occurs when the surfactant geometry is either cylindrical or the surfactant mixtures possess a mean curvature equal to zero (Figure 1-28).

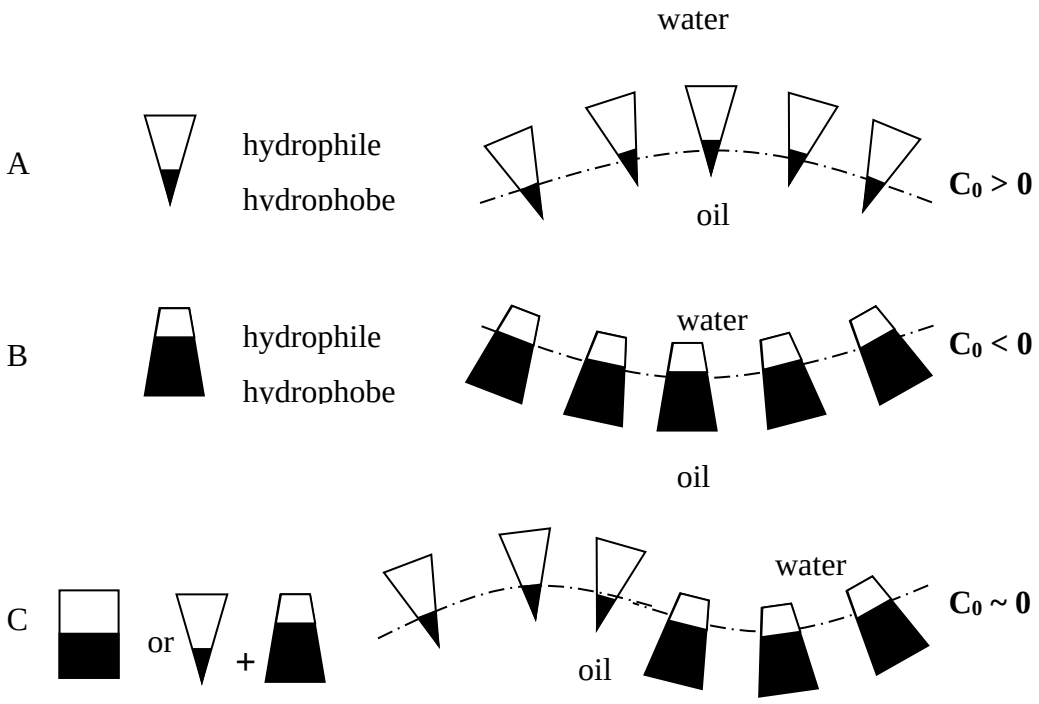

Figure 1-28 Relationship between the amphiphile molecular shape and the spontaneous curvature of the interface Langevin [1986]

1.6.2 Spherical Droplets

The earliest structural model of the three component microemulsion was based on the spherical or droplet structure. The droplet structure was composed of either O/W or W/O microemulsion containing relatively low concentrations of the surfactant. Albillon *et al*, [1988] proposed Equation 1-4 to estimate the radius and size of the droplet for Winsor type I and II systems stabilised by cationic surfactants.

$$R = \frac{3\varphi_d}{C_s \Sigma} \qquad \text{Eqn. 1-4}$$

where φ_d is the volume fraction of the dispersed phase, Σ is the area per surfactant molecule and C_s is thenumber of surfactant molecules per unit volume. The droplet size depends mainly upon the composition of the microemulsion. The area per surfactant molecule is fairly static hence as the surfactant concentration decreases and or the internal phase increases, the radius increases until it attains a maximum value equivalent to the inverse of the spontaneous curvature C_0 (Figure 1-13) [Martinek *et al*, 1989].

1.6.3 Bicontinuous and Non Spherical Structures

Talmon and Prager [1978] proposed a model to describe non spherical microemulsion structures which occur in Winsor III systems. The model uses a lattice based on a set of random Voronoi polyhedra. The model is constructed using a set of random Poisson points which define a complete tessellation of space belonging to a random lattice (Figure 1-29 a). Each point in space belongs to a cell centred at the closest Poisson point, and which has 13.4 nearest neighbours (Figure 1-29 b). The Voronoi lattice model allows the each distributed component to be connected to a maximum of 13 spheres via cylindrical structures.

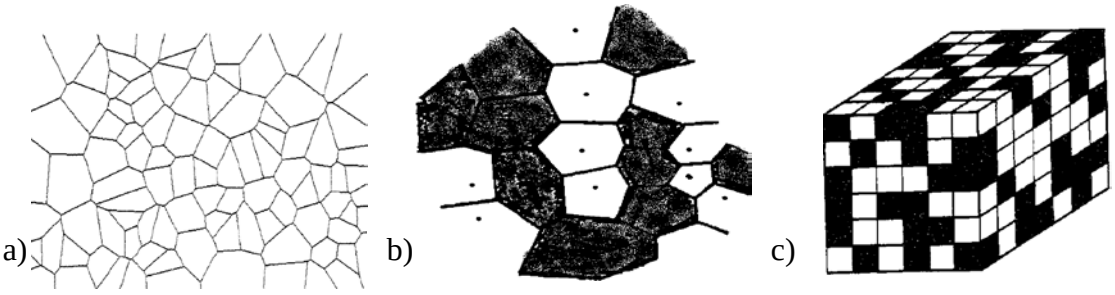

Figure 1-29 a) & b) Two dimensional partitioning of space with Voronoi polygons: centre points chosen at random and Voronoi cells are defined as the set of points closest to a given centre point. c) Simplified representation of bicontinuous microemulsion. Reproduced from Chevalier and Zemb [1990]

The Voronoi cells represent the oil or water filled cells with a surfactant interface. If the volume fraction of water φ_w is less than a specific value φ_p (about 0.185 [Langevin 1986]), the oil phase is continuous and the water forms finite sized cells or droplets surrounded by the oil (i.e. droplets) w/o. For higher water volume fractions there exists a continuous water path spanning from one side of the sample to the other (Figure 1-29b). The transition occurs at the percolation volume fraction, φ_p. When $\varphi_w = 1- \varphi_p$ the oil polygons are no longer connected and the microemulsion becomes an o/w type. The medium becomes bicontinuous when the volume fraction is between φ_p and $1- \varphi_p$.

De Gennes and Taupin [1982] simplified the Talmon and Prager model with the introduction of the cubic random cell model (CRC). The CRC model proposed a characteristic size of the Voronoi polyhedra cells defined by a persistence length, ε_k, of the interfaces. The random polyhedra is replaced by cubic cells filled at random with oil and water dependent on the volume fraction of the oil and water components (Figure 1-29c). The persistence characteristic length is given by equation 1-5 and is related to the film bending energy for spontaneous average curvature equation 1-6:

$$\varepsilon_k = \frac{6\varphi_o\varphi_w}{C_s \Sigma} \qquad \text{Eqn. 1-5}$$

where ε_k is the persistence length of film, φ_o is the volume fraction of the oil phase and φ_w is the volume fraction of the water phase.

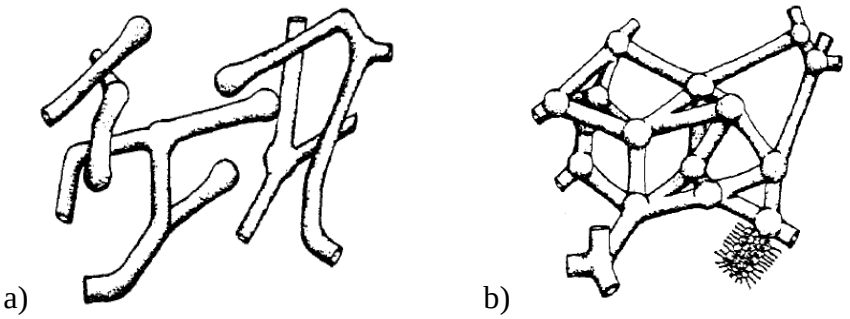

a) b)

Figure 1-30 Schematic diagram of a typical microemulsion structure without cosurfactant according to the DOC model a) connectivity Z=2; b) connectivity Z=4

$$\varepsilon_k = a\exp\left(\frac{-4\pi K_0}{kT}\right) \qquad \text{Eqn. 1-6}$$

where ε_k is the spontaneous average curvature, K_o is the film elasticity, a is the molecular size, k is the Boltzmann constant, T is the Temperature.

1.6.4 The Disordered Open Connected (DOC) Model

The Talmon-Prager and CRC models were designed to describe Winsor type III microemulsions with equal volume fractions of oil and water and negligible surfactant concentration. These models are unable to characterise the structures observed in microemulsions using scattering techniques. Talmon-Prager cannot account for any peak in scattering and the predicted position of scattering peak in the CRC model (Equation 1-7) is twice that observed experimentally in real systems (Equation 1-8).

$$q_{CRC} = \frac{2\pi}{\varepsilon} \qquad \text{Eqn. 1-7}$$

$$q_{Observed} = \frac{\pi}{\varepsilon} \qquad \text{Eqn. 1-8}$$

The Disordered Open Connected (DOC) model proposed by Zemb *et al.* (1987) to provide a low resolution picture of the structure of micelles and microemulsions. The model was introduce specifically to explain the behaviour of ternary systems and

provides a relatively good model for the bicontinuous structures observed experimentally. The basic assumption of the DOC model is that the surfactant can be described as two phases (oil and water) separated by an interface of constant non-zero curvature. The structure is macroscopically disordered and has local constraints given by the available volume fraction and specific area. The DOC model takes into account that there is more interfacial area for a given structure than expected from other structural models.

The DOC model allows the following structures: a) connectivity z = 0, spherical droplets which represent the hard sphere model with occasional coalescence when droplets are in contact (Figure 1-31(a)); connectivity z = 2, DOC cylinders connected to two adjacent spheres (Figure 1-31(b)). Figure 1-31b; connectivity z = 4, DOC lamellar model connected to four adjacent spheres and Figure 1-31(b). Figure 1-31(c), (d).

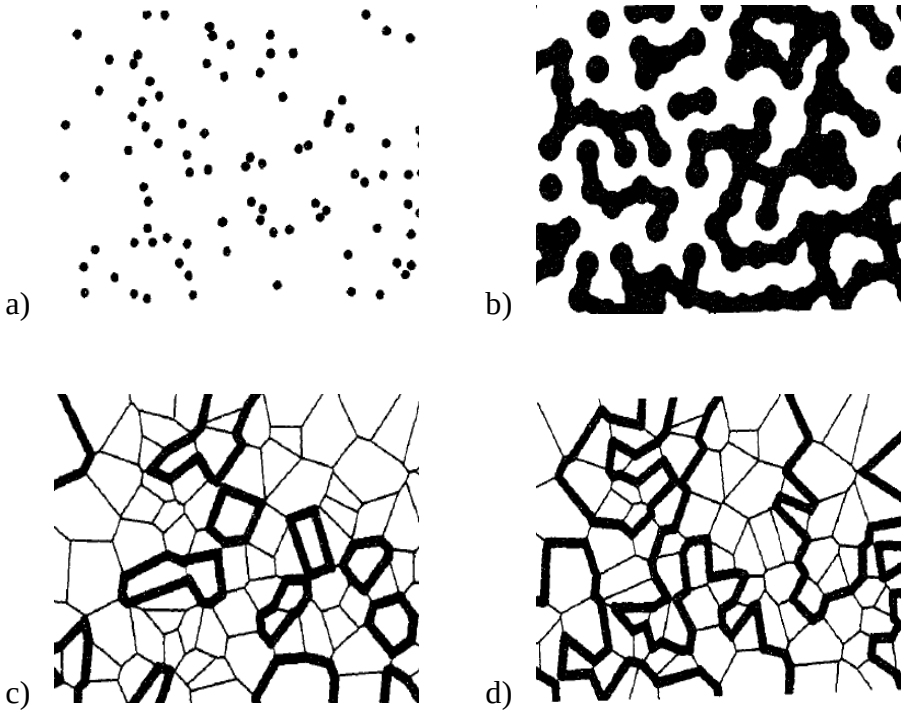

Figure 1-31 Examples of DOC model structures built from the same Voronoi lattice a) connectivity Z = 0 reduces to a set of hard spheres. b) DOC cylinder with connectivity Z = 2: each centre is bond to the two nearest neighbours on average. c) DOC lamellar with pseudo-volume 2.5% is a dispersion of vesicles. d) DOC lamella with pseudo-volume 50% is a random dispersion of flexible bilayers.

1.7 Techniques Used to Investigate Microemulsions

1.7.1 Phase Characterisation

Microemulsions are created when two immiscible liquids, oil and water are mixed with a surfactant to form a single phase clear liquid also known as Winsor type IV microemulsion [Winsor 1948]. Other Winsor classifications are types I, II and III. Type I consists of a two phase system where the water soluble surfactant forms o/w microemulsions which coexist with an oil phase. Type II consists of a two phase system where oil soluble surfactants forms w/o microemulsions that coexist with the water phase. Type III consists of a three phase system where a surfactant rich middle phase exists in equilibrium with both excess oil and excess water. Winsor also described the type I system as a type IV system in equilibrium with excess oil; a type II system as a type IV system in equilibrium with excess water and a type III system as a type IV system in equilibrium with both excess oil and excess water (Figure 1-32).

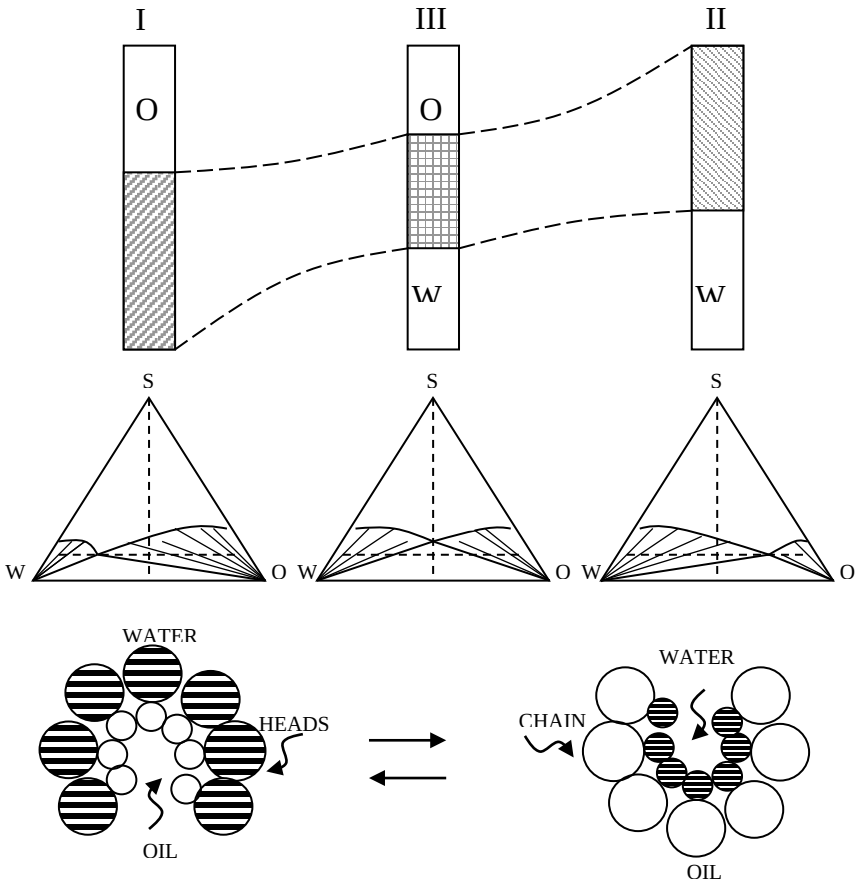

Figure 1-32 Phase behaviour of microemulsions – Winsor type I↔II↔III transition; appearance of equilibrated system (top), representation of ternary phase diagram (centre) and interfacial curvature [Robins 1977])

1.7.2 Conductivity Measurements

Measuring the electrical conductivity of microemulsion samples under varied conditions or composition is another technique used to examine microemulsions. A phenomena known as percolation is observed if an increase in electrical conductivity is exhibited by a reverse microemulsion whilst either the temperature of the sample of fixed composition is varied or the ratio of water to surfactant W_0 = [H_2O]/[surfactant] is varied for a fixed temperature. Potential structural changes are identified by a notable increase in conductance or percolation of the reverse microemulsions. Chen, *et al.* [1990] described microstructure observed in SANS experiments (Figure 1-33) of the transformation from W/O microemulsion droplets to clusters of droplets to a bicontinuous structure as the weight ratio α = oil: water increase from α = 10 through to α = 90 whilst also increasing the temperature of the sample. Chen, *et al.* [1986] describes bicontinuous interconnecting conduits (Figure 1-24) A through which charged particles are able to pass easily.

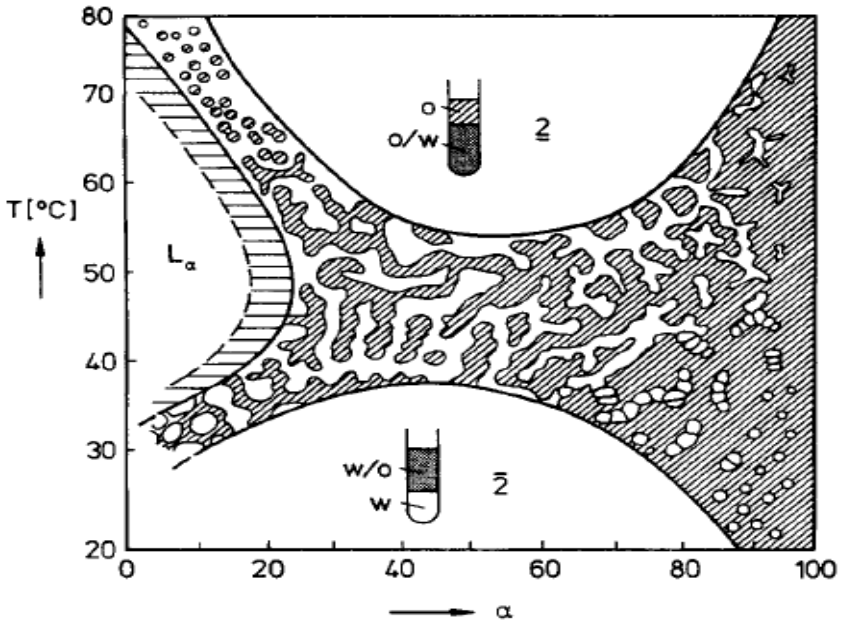

Figure 1-33 Conceptual view of microstructure transitioning from a single phase through to a bicontinuous structure which is deduced from SANS data analysis.

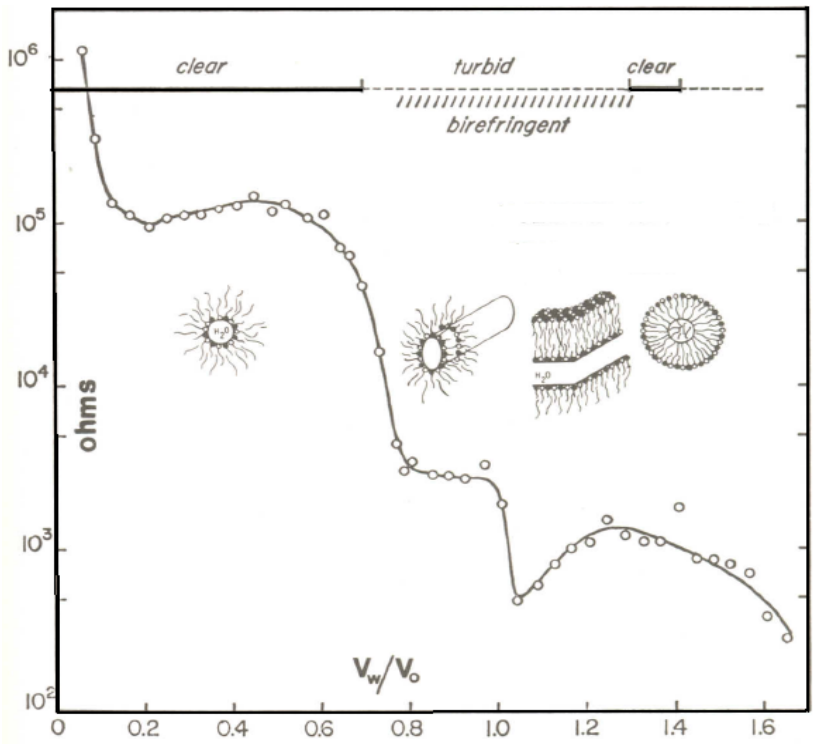

Figure 1-34 Variation in electrical resistance, optical appearance, birefringence as the volume ratio of water: oil is increased for a fixed volume of surfactant [Prince 1977]

O/W microemulsions are expected to have higher magnitudes of conductivity than W/O microemulsions as the volume fraction of the W/O is increased for a fixed volume of surfactant as the composition moves from Winsor type I > III > II microemulsions. Figure 1-34 shows the change in magnitude resistance $\Omega=1/\sigma$ as the volume fraction V_w/V_o increases.

Chapter 2

Dielectric Spectroscopy Theory and Models

2. Dielectric Spectroscopy Theory and Models

2.1 Dielectric Spectroscopy - Background

Dielectric materials have few or no charges that are free to move through the medium hence they are poor conductors of electricity as compared to metals or ion rich materials. Such materials are able to respond to an applied electric field by the induction of dipoles. The induced and permanent dipoles in the material are able to align with the electric field and whilst free charges migrate towards the attracting electrode or diffuse through the medium and thus the medium is described as being polarised. When the applied field is removed the induced dipoles disappear and the displaced charges and permanent dipoles attempt to return to their original location or rotational alignment state. This process is described as dielectric relaxation.

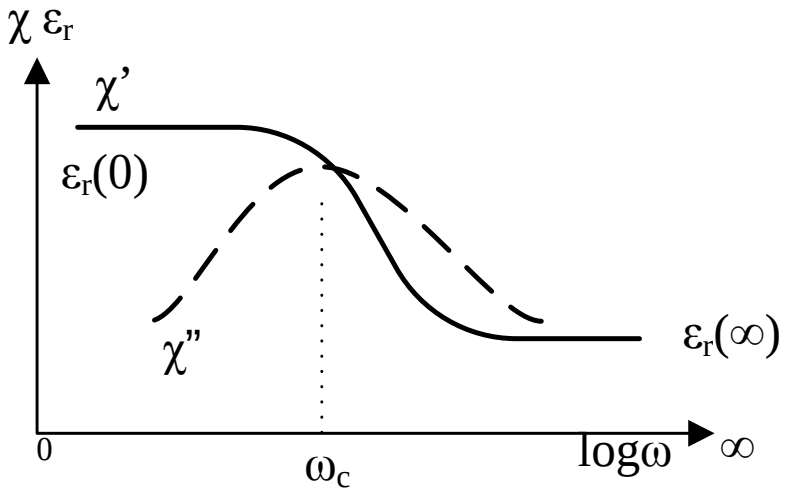

Figure 2-1 A representation of a linear dielectric dispersion of the real and imaginary components of the dielectric susceptibility χ' and χ'' over a log frequency range. The static permittivity ε_s is measured at the lowest frequency and the high frequency permittivity ε_∞ is measured at higher frequencies. The characteristic relaxation frequency $\omega_c = 1/\tau$ for the process is the reciprocal of the relaxation time τ.

The polarisation and relaxation of a particular medium or the species within the medium can occur over a stimulated field frequency range of several decades on a log frequency scale. The average time taken for a polarised material to relax to its original, non-polarised state once the external electrical stimulus is removed is known as the relaxation time. Figure 2-1 shows the dielectric susceptibility $\chi(\omega) = \varepsilon_r - 1$ and dielectric permittivity $\boldsymbol{\varepsilon_r}$ which is a measure of polarisation, plotted as the angular frequency, ω**,** is varied.

Dielectric spectroscopy is the study of the polarization and relaxation processes that occur within a dielectric medium when an alternating electric field frequency ranging from 10^{12}Hz to 10^{-6}Hz (where the magnitude of the polarization peaks at the lowest frequencies) is applied. There are various polarisation processes which participate in, and contribute to, the total polarisation Figure 2-2(4); including electronic/atomic (Figure 2-2(1) occurs at the higher frequency range), induced dipole/ionic and orientation (Figure 2-2(2, 3) occurs in the lower frequency range).

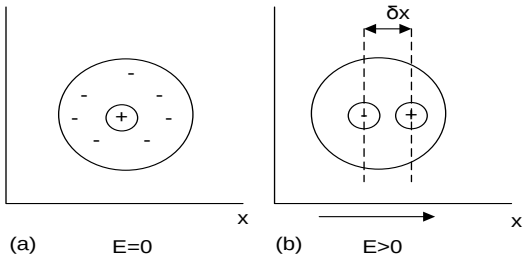

(1) Atomic polarisation.

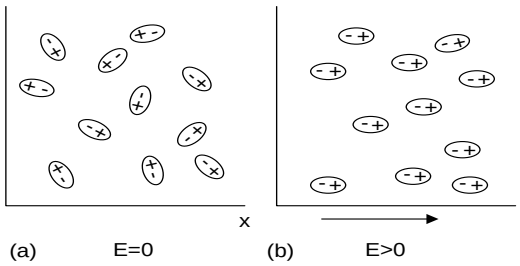

(2) Dipole polarisation.

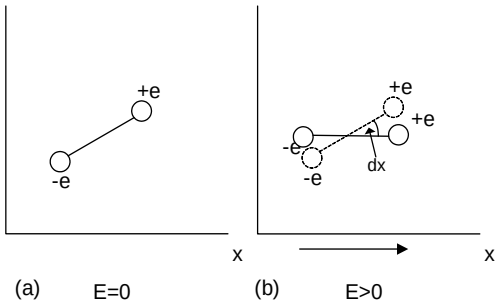

(3) Orientation polarisation.

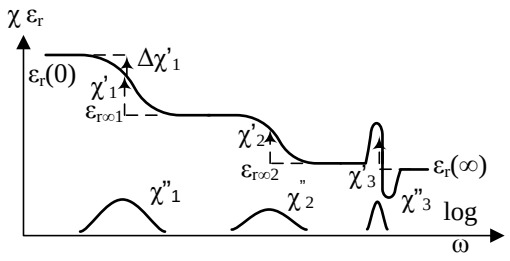

(4) Idealised polarisation.

Figure 2-2 (1) The electron cloud surrounding the nucleus with a centre of charge coincident. The nucleus is displaced and a dipole is induced when the field is applied. (2) When the dipoles within the material align with the applied field and the material is said to be polarised. (3) Charged molecules or permanent dipoles rotate to orientate with the applied field. (4) The magnitude of the relative permittivity ε′ increases as frequency ω of the applied filed decreases to zero. (Types of polarisation [Jonscher 1983])

Dielectric materials can also experience molecular dipole re-orientation, interface polarisation, and/or charge transport processes ([Jonscher [1983], Martinsen *et al.* [2002]) as the frequency of the applied ac field is reduced to zero. The individual responding species within the dielectric material such as dipolar molecules, local groups or clusters of molecules and /or semi mobile charges will respond to the field at, or within, specific frequency ranges.

When a high frequency alternating field is applied to the sample, small particles such as electrons and atoms are able to respond and are displaced by the applied field (Figure 2-2(1), (Figure 2-2(2)). The centre of charge in the neutral atom is displaced and a dipole is induced. When the field is removed the particles attempt to return to their original positions and the induced dipole vanishes. Larger molecules are unable to respond to the higher field frequencies and hence make no contribution to any measured polarisation in this frequency range. However small dipolar molecules or larger molecular structures that contain groups of atoms, such as a polar head group, have permanent dipoles that are able to move, or reorientate, under the influence of the applied field.

As the frequency of the applied field is reduced, then larger particles and structures are able to respond to the applied field, and are displaced from their rest positions. In addition to displacement of the electrons, the particles are also re-orientated to line up with the field and migrate towards the electrodes (Figure 2-2(2) Figure 2-2(3)). The sum of all the different types of polarisation forms the idealised dispersion pattern (Figure 2-2(4)) (Martinsen *et al.* [2002], Schwan [1957]), and the maximum polarisation or dielectric increment, $\chi(0) - \chi(\infty)$, is proportional to the square of the permanent dipoles, μ^2.

2.2 Low Frequency Measurement Description and Theory

The low frequency dependent dielectric spectrum is obtained by applying an ac voltage across a sample between a pair of parallel electrodes (Figure 2-3) and measuring the resultant ac current and phase difference between the voltage and current. The dielectric response typically presented in this study, is in the form of complex capacitance, $C(\omega)$, as a function of the radian frequency, ($\omega=2\pi f$ Hz), of the applied voltage. However the response can also be presented in the related form of complex impedance, $Z(\omega)$, and admittance, $Y(\omega)$, where $C(\omega) = (i\omega)^{-1}Y(\omega) = (i\omega Z(\omega))^{-1}$.

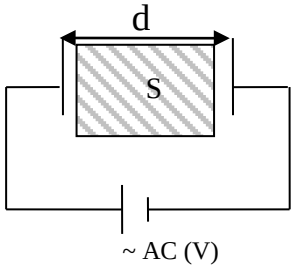

Figure 2-3 Capacitance of a sample S measured with a parallel electrode configuration. The electrodes are separated by a distance d (mm).

The frequency dependent complex capacitance consists of the, in phase, (real C′) and out of phase, (imaginary or loss C″) of the response.

$$C(\omega) = C'(\omega) - iC''(\omega)$$

$$= C(\omega) = \varepsilon_r \varepsilon_0 \frac{A}{d}\{\cos(\omega t) - i\sin(\omega t)\} = \varepsilon_r \varepsilon_0 \frac{A}{d}\{\exp(-i\omega t)\} \quad \text{Eqn. 2-1}$$

where, A is the area of the electrodes in contact with sample, d is the a distance between the electrodes, ε_0 is the permittivity of free space is the a 8.854×10^{-12}(Fm^{-1}), ε_r is the dimensionless relative permittivity of the sample, ω is the frequency of the applied voltage in radians per second (2πf (Hz), t is the time and i is $\sqrt{-1}$.

The magnitude of the capacitance, C_o is dependent on the permittivity of free space ε_0, measuring cell geometry and thus is frequency independent:

$$C_o = \varepsilon_0 \frac{A}{d} \quad \text{Eqn. 2-2}$$

Hence equation 2.1 can be re-expressed as frequency dependent permittivity:

$$C(\omega) = \varepsilon_r C_0 \{\cos(\omega t) - i\sin(\omega t)\} \quad \text{Eqn. 2-3 (a)}$$

$$= C_0 \varepsilon(\omega) \quad \text{Eqn. 2-3 (b)}$$

Or as a sum of frequency dependent susceptibility:

$$C(\omega) = C_0 \left\{ \sum_{\omega}^{\infty} \chi(\omega) + 1 \right\} \quad \text{Eqn. 2-3 (c)}$$

where

$$\varepsilon(\omega) = \left\{ \sum_{\omega}^{\infty} \chi(\omega) + 1 \right\} \quad \text{Eqn. 2-3 (d)}$$

The complex capacitance Eqn. 2.1 can now be expressed as:

$$C(\omega) = C_0\{\varepsilon'(\omega) - i(\varepsilon''(\omega))\} \quad \text{Eqn. 2-4 (a)}$$

Adding the low frequency dc conductivity component σ

$$C(\omega) = C_0\left\{\varepsilon'(\omega) - i\left(\varepsilon''(\omega) + \frac{\sigma}{\varepsilon_0\omega}\right)\right\} \quad \text{Eqn. 2-4 (b)}$$

or

$$C(\omega) = C'(\omega) - i\frac{G}{\omega} \quad \text{Eqn. 2-4 (c)}$$

where ε′ is the relative permittivity, ε″ is the loss, σ is the dc conductivity, G is the conductance and χ is the susceptibility.

The real and imaginary components of the complex capacitance together contain information about the interaction of the applied electric field with the sample under examination. Equation 2.4(a) represents an ideal dielectric material whose response to an applied electric field is due to the rotation of charges. Equation 2.4(b) represents a dielectric material that also contains charges that are mobile and contribute a dc conductivity element to the loss term of the complex capacitance.

2.3 Debye's Relaxation Simple Model

Debye [1945] reported that applying a dc voltage to an insulating sample (configured as in Figure 2-3) resulted in current flow. The current continued to flow until equilibrium was established and maximum polarisation was achieved when the current flow ceased. When the dc voltage was removed, the magnitude of polarisation began to decay. The residual polarisation at time, t, after the dc voltage was removed is given by:

$$\frac{dP(t)}{dt} = -\frac{P(t)}{\tau} \quad \text{Eqn. 2-5}$$

where, P, is the polarisation at time, t, τ, is a constant with units of time and the negative sign is used for decay.

Integrating Equation 2-5

$$\int\frac{dP}{P} = -\int\frac{dt}{\tau} \qquad = \ln[P(t)] = -\frac{t}{\tau} \quad \text{Eqn. 2-6}$$

$$P(t) = P_0\exp(-t/\tau) \quad \text{Eqn. 2-7}$$

where P_0 is constant and is the maximum magnitude of the polarisation at time, t = 0. Equation 2-7 describes the exponential decay of the polarisation at time (t) after the

driving force is removed, where the relaxation time, τ, is the time at which the magnitude of the polarisation has decayed to e^{-1} = 0.36788 of the original polarisation.

In this study we are interested in the polarisation as a function of frequency. Hence we transform the time domain Equation 2-7 to the frequency domain by making a Fourier transformation [Abramowitz and Stegun, 1972], resulting in the frequency dependant dielectric polarisation, P(ω).

$$P(\omega) = \int_0^\infty P_0 \exp-(t/\tau) * \exp-(i\omega t)dt = \int_0^\infty P_0 \exp-(i\omega + \frac{1}{\tau})tdt \qquad \text{Eqn. 2-8}$$

$$P(\omega) = \left[\frac{P(t)}{(\frac{1}{\tau} + i\omega)} \exp-(i\omega + \frac{1}{\tau})t \right]_0^\infty = \frac{P_0}{(\frac{1}{\tau} + i\omega)} \qquad \text{Eqn. 2-9 (a)}$$

$$P(\omega) = \frac{P_0}{(1 + i\omega\tau)} \qquad \text{Eqn. 2-9 (b)}$$

The frequency dependence of dielectric polarisation is represented by the dimensionless complex susceptibility, χ, which is a measure of how easily a material polarizes in response to an alternative electric field, E (ω).

$$P(\omega) = \varepsilon_0 \chi(\omega) E(\omega) \qquad \text{Eqn. 2-9 (c)}$$

Hence the dielectric susceptibility can be written as

$$\chi(\omega) = \frac{\chi_0}{1 + i\omega\tau} = \chi_0 \frac{1 - i\omega\tau}{1 + (\omega\tau)^2} \qquad \text{Eqn. 2-10}$$

and is separated into the real and imaginary components, χ′, and, χ″, respectively:
real component χ’

$$\chi'(\omega) = \frac{\chi_0}{1 + (\omega\tau)^2} \qquad \text{Eqn. 2-11 (a)}$$

imaginary component χ’’

$$\chi''(\omega) = -\frac{i\omega\tau\chi_0}{1 + (\omega\tau)^2} \qquad \text{Eqn. 2-11 (b)}$$

The dielectric permittivity ε(ω) is related to the sum of the individual susceptibilities of all the dielectric species dispersing at a given frequency.

$$\varepsilon(\omega) = \sum_\omega^\infty \chi(\omega) + 1 \qquad \text{Eqn. 2-12}$$

The complex permittivity

$$\varepsilon(\omega) = \varepsilon'(\omega) - i\varepsilon''(\omega) \qquad \text{Eqn. 2-13}$$

Separating the real and imaginary components

real component ε'

$$\varepsilon'(\omega) = \varepsilon_\infty + \frac{(\varepsilon_s - \varepsilon_\infty)}{1+(\omega\tau)^2} \qquad \text{Eqn. 2-14}$$

imaginary component ε''

$$\varepsilon''(\omega) = \frac{(\varepsilon_s - \varepsilon_\infty)(\omega\tau)}{1+(\omega\tau)^2} \qquad \text{Eqn. 2-15}$$

where ε_s is the static permittivity which occurs at low frequency and for values of frequency much less than the relaxation frequency, $\omega_c = \tau^{-1}$ and ε_∞ is the infinite permittivity which occurs at high frequency and for values of frequency much greater than the relaxation frequency $\omega_c = \tau^{-1}$.

As shown in Figure 2-4, when the frequency, $\omega=\tau$, the real component ε' is equal to $(\varepsilon_s + \varepsilon_\infty)/2$ and the imaginary component ε'' is equal to $(\varepsilon_s - \varepsilon_\infty)/2$. As the frequency ω approaches zero $\varepsilon' \rightarrow \varepsilon_s$ and $\varepsilon'' \rightarrow 0$. At frequencies, $\omega>\tau$ the magnitude of the real component of the complex permittivity decreases, $\varepsilon' \rightarrow \varepsilon_\infty$, as the frequency increases. The loss component ε'' is inversely proportional to the driving frequency of the ac field, $\varepsilon'' \propto \omega^{-1}$ and approaches zero and depicted in figure 2-4.

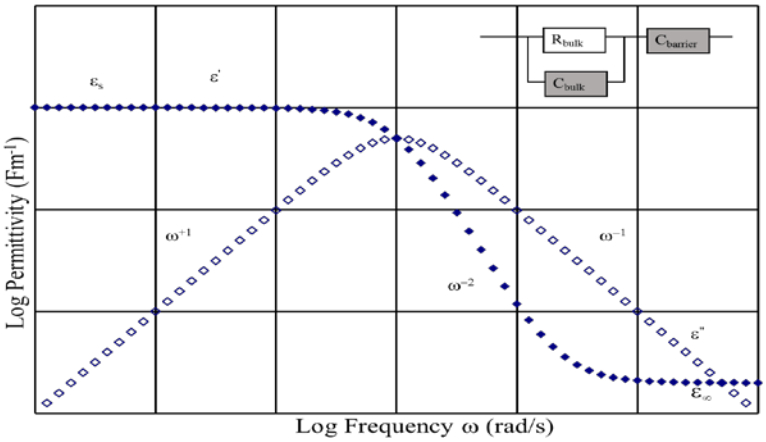

Figure 2-4 Plot of the real and imaginary components of the complex permittivity obtained using the Debye Equation 2-14 and 2-15. The plot shows a single dispersion normalised at $\omega\tau=1$ where τ is the characteristic relaxation time for this system. Insert Circuit representing the Debye equation comprising of a resistor and capacitor ($R_{bulk}C_{barrier}$) series circuit in parallel with a high frequency bulk capacitor.

In the series circuit represented by Figure 2-4 insert, the resistor element is responsible for the bulk charge transport (conductance, G=1/R). This charge transport is blocked by the series capacitor circuit element. The characteristic time constant, τ, for this circuit configuration is $\tau = R_{bulk}C_{barrier} = C_{barrier}/G_{bulk}=1/\omega$. A specific feature of the Debye model is that it requires the gradients of the wings of both the real and imaginary frequency independent components of the complex permittivity to be whole numbers 0, +1, -1 and -2.

In practice, there are few materials apart from gases or very dilute systems that can be modelled using circuits containing frequency independent capacitance and resistors as is the case for the simple Debye model. Indeed the majority of the published experimental data has reported half height widths being broader than the Debye value and obeying a fraction power law dependency which can only be characterised with two parameter functions. Table 2-1 contains a summary of the one and two parameter empirical models that have been used to characterise experimental data with varying degrees of success.

Table 2-1 Summary of various spectral functions and their power law exponents [Jonscher 1983]

Processes	Susceptibility functions	Exponent for $\omega << \omega_p$		Exponent for $\omega >> \omega_p$	
One parameter		$\Delta\chi'(\omega)$	$\chi''(\omega)$	$\chi'(\omega)$	$\chi''(\omega)$
Debye	$\left(1+i\frac{\omega}{\omega_p}\right)^{-1}$	2.0	1.0	-2.0	-1.0
Cole-Cole (1941)	$\left(\left\{1+i\frac{\omega}{\omega_p}\right\}^{1-\alpha}\right)^{-1}$	1-α	1-α	α-1	α-1
Fuoss-Kirkwood (1941)†	$2\left(\frac{\omega}{\omega_p}\right)^{\gamma}\left(1+\left\{\frac{\omega}{\omega_p}\right\}^{2\gamma}\right)^{-1}$	γ	γ	- γ	- γ
Davidson-Cole (1951)	$\left(1+i\frac{\omega}{\omega_p}\right)^{-\beta}$	2.0	1.0	-β	-β
Williams-Watts (1970)	$\sum_{s=1}^{\infty}\frac{\Gamma(\Delta s)}{(s-1)!}\left\lvert\frac{\exp(-i\Delta\pi/2)}{\omega^{\Delta}\omega_p^{-\Delta}}\right\rvert^{s}$	2.0	1.0	-Δ	-Δ
Two parameter					
Havriliak-Negami (1966)	$\left(\left\{1+i\frac{\omega}{\omega_p}\right\}^{1-\alpha}\right)^{-\beta}$	1-α	1-α	-β (1-α)	-β (1-α)
Jonscher (1975)	$\left(\left\{\frac{\omega}{\omega_1}\right\}^{-m}+\left\{\frac{\omega}{\omega_2}\right\}^{1-n}\right)^{-1}$	m	m	n-1	n-1
Hill (1978)	$\omega^{m}\left(\omega_p^{2s}+\omega^{2s}\right)^{-(m+1-n)/2s}$	m	m	n-1	n-1
Dissado-Hill (1979)	$\left(1+i\frac{\omega}{\omega_p}\right)^{n-1} {}_2F_1\left(1-n,1-m;2-n;\frac{\omega_p}{\omega_p+i\omega}\right)$	m	m	n-1	n-1

2.4 Fractional Power Law Relaxation Model

In practice the charge blocking barrier capacitance is rarely constant or frequency independent [Jonscher, 1983]. The barrier capacitance in the RC circuit depicted in Figure 2-4 can be written as:

$$C_b(\omega) = C_b(i\omega)^{n-1}$$

$$= C_b(\omega)^{n-1}\{\sin n\pi/2 - i\cos n\pi/2\} \qquad \text{Eqn. 2-16}$$

where the parameter n ranges between zero and one $0 < n < 1$ and is a measure of the disorder in the barrier [Hill 2001] with $n = 1$ representing the perfect non-dispersive, charge blocking barrier (Debye circuit) (Figure 2-5). When n approaches zero, the barrier blocking properties is poor, turning the circuit into a perfect charge conductor (Figure 2-5 (b)).

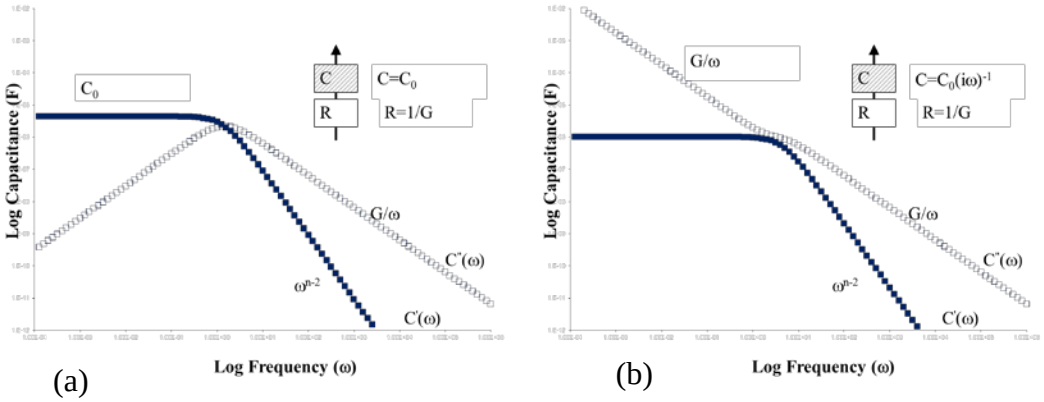

Figure 2-5 (a) Series RC circuit with dispersive barrier capacitance where parameter $n = 1$, recreates the non-dispersive barrier Debye response. (b) Series RC circuit with dispersive barrier capacitance where parameter $n = 0$, a dc conductance response results.

The calculated power law model requires only three parameters to generate the dispersions displayed in Figure 2-5 and Figure 2-6. The magnitude of the conductance, G, and the barrier capacitance, C_b, and the dispersion parameter, $0 < n < 1$. The calculated dispersions plotted in Figure 2-6 (a) and (b) are a more generic form of the Maxwell-Wagner interface response and shows that the effects of the barrier capacitance continues to influence the dispersion at frequencies above the frequency corresponding to the crossover of the bulk conductance and the barrier capacitance. In addition, at frequencies below the cross over frequency the dispersive barrier capacitance dominates and the phase angle $\tan(\delta) = C'(\omega)/C''(\omega)$ is constant.

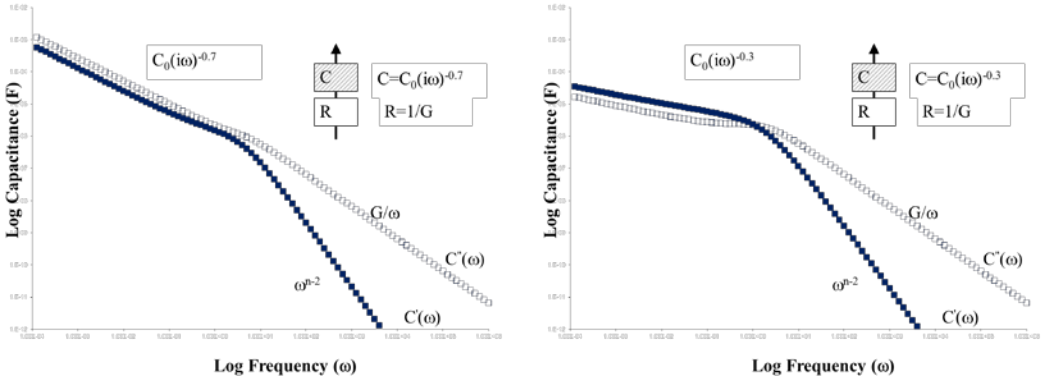

(a) (b)

Figure 2-6 (a) Series RC circuit with dispersive barrier capacitance where parameter, n = 0.3. For values of $0 < n < 0.5$ the magnitude C˝ is greater than C˙ below the cross over frequency. (b) Series RC circuit with dispersive barrier capacitance where parameter, n = 0.7. For values of $0.5 > n > 1$ the magnitude of C˝ is less than C˙ below the cross over frequency.

When the dispersive barrier parameter, n = 0.5 a diffusive dispersion response is obtained, where the real and imaginary components of the capacitance are equal and parallel below the cross over frequency.

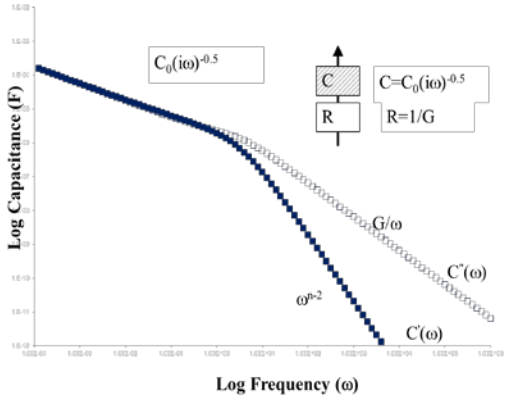

Figure 2-7 Series RC circuit with dispersive barrier capacitance where parameter, n = 0.5. For values of n = 0.5 the magnitude of C˝ is equal to C˙ below the cross over frequency.

The ideal Debye, Maxwell-Wagner, power law models are three of a number of models can be used to characterise dielectric responses which have been observed experimentally [Cole-Cole 1941, Davidson-Cole 1951]. However, applications of each of these models are limited as they either cover specific response forms or are valid only over a limited frequency range. Dissado and Hill [1983] proposed a cluster model which covered responses for coupled species or many bodies interactions above and below some characteristic frequency as well as simple Debye single species and a direct current or near direct current (quasi-dc) responses. It is this cluster model that will be

applied to the responses obtained for the microemulsions and their constituents examined in this study.

2.5 Dissado – Hill Cluster Model Approach

Dissado and Hill [1983] proposed a theory based on a cluster approach to model the structure of the material and charge transport through imperfect materials using dielectric relaxation spectroscopy. The Dissado-Hill cluster model incorporated the both the Debye relaxation for ideal materials such as gases or dilute systems, cluster structures with both strongly and weakly bound charge species characterised using power law indices, and the perfect conducting crystal material Figure 2-8.

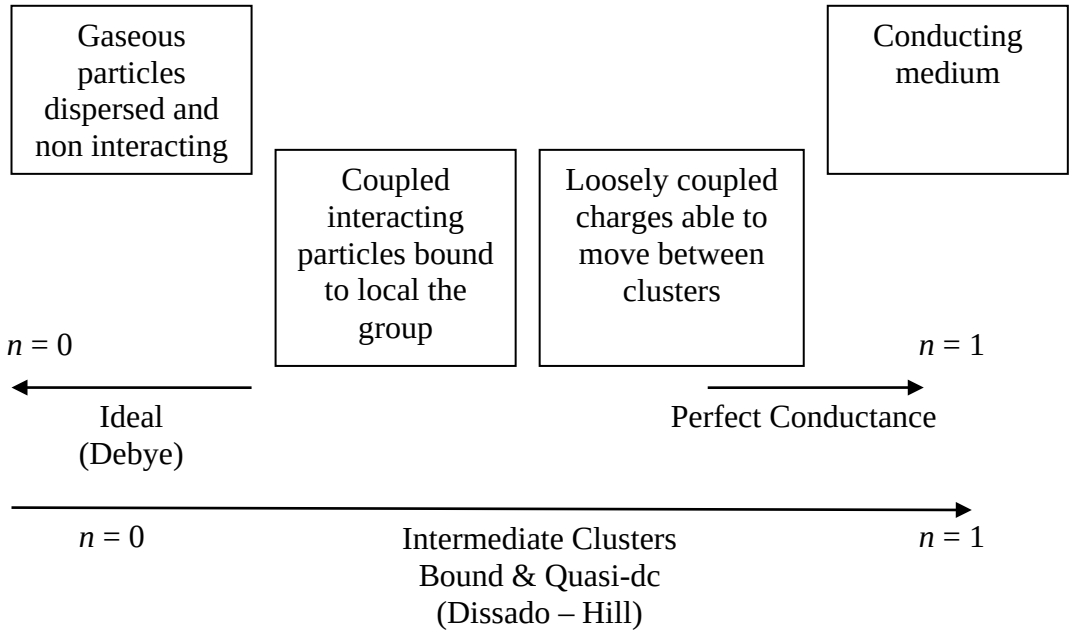

Figure 2-8 Dielectric models used for characterising dilute and condensed samples [Dissado and Hill, 1983]

The dielectric cluster is defined as a local group of particles that are coupled and have short ranged interactions with neighbouring particles. Polarisation and relaxation of a dipole within the cluster has an impact on neighbouring dipoles. The complex susceptibility for the cluster model takes the general form of the Gaussian hyper geometric function ${}_2F_1(,;;)$ Equation 2-17.

$$\chi(\omega) = \chi'(\omega) - i\chi''(\omega) = \chi_0\left(F_0^{-1}(1+ix)^{n-1} *_2 F_1\left(1-n,1-m;2-n;\frac{1}{1+ix}\right)\right) \quad \text{Eqn. 2-17 (a)}$$

$$\chi'(\omega) \propto \chi''(\omega) \propto \omega^{n-1}, \omega > \omega_c \quad \text{Eqn. 2-17 (b)}$$

$$\chi''(\omega) \propto \chi'(0) - \chi'(\omega) \propto \omega^{-m}, \omega < \omega_c \quad \text{Eqn. 2-17 (c)}$$

where the cross over frequency, ω_c, from high frequency and low frequency behaviour limit is given by Equation 2-17 (b) and (c). The frequency term, x, is normalised with respect to the characteristic relaxation frequency rate ω_c, x = ω/ω_c, F_0, is the normalising function ${}_2F_1(1-n,1-m;2-n;1)$ and the value of the indices range between $0 < n, m < 1$. Hence the broadened loss peak power law response which is found experimentally in the majority of condensed materials (liquids and solids) can be modelled (Figure 2-9 (a(i))).

The quasi-dc charge transport response observed experimentally (Figure 2-9 (b(i))) and described as responses where low frequency loss peaks are obscured by a near dc dispersion of the loss component with a gradient close to -1 (ω^{-1}) but less than -1 [Dissado and Hill, 1984]. The quasi-dc process results in an increase, rather than a decrease, in the magnitude of the low frequency loss component hence the magnitude of the dispersion exponent 'm' is negative resulting in the signage alteration to Equation 2-18. To avoid confusion as to whether a loss peak process Equation 2-17 or a quasi-dc process Equation 2-18 is under discussion, the exponent '*m*' is replaced with exponent '*p*' Equation 2-19 when the quasi-dc process is the subject of discussion.

$$\chi(\omega) = \chi_0 F_0^{-1}(1+ix)^{n-1} *_2 F_1\left(1-n,1+m;2-n;\frac{1}{1+ix}\right) \quad \text{Eqn. 2-18}$$

$$\chi(\omega) = \chi_0 F_0^{-1}(1+ix)^{n-1} *_2 F_1\left(1-n,1+p;2-n;\frac{1}{1+ix}\right) \quad \text{Eqn. 2-19 (a)}$$

$$\chi'(\omega) \propto \chi''(\omega) \propto \omega^{n-1}, \omega > \omega_c \quad \text{Eqn. 2-19 (b)}$$

$$\chi''(\omega) \propto \chi'(0) - \chi'(\omega) \propto \omega^{-p}, \omega < \omega_c \quad \text{Eqn. 2-19 (c)}$$

The cross over frequency, ω_c, from high frequency and low frequency behaviour limit is given by Equation 2-19(b) and Equation 2-19(c).

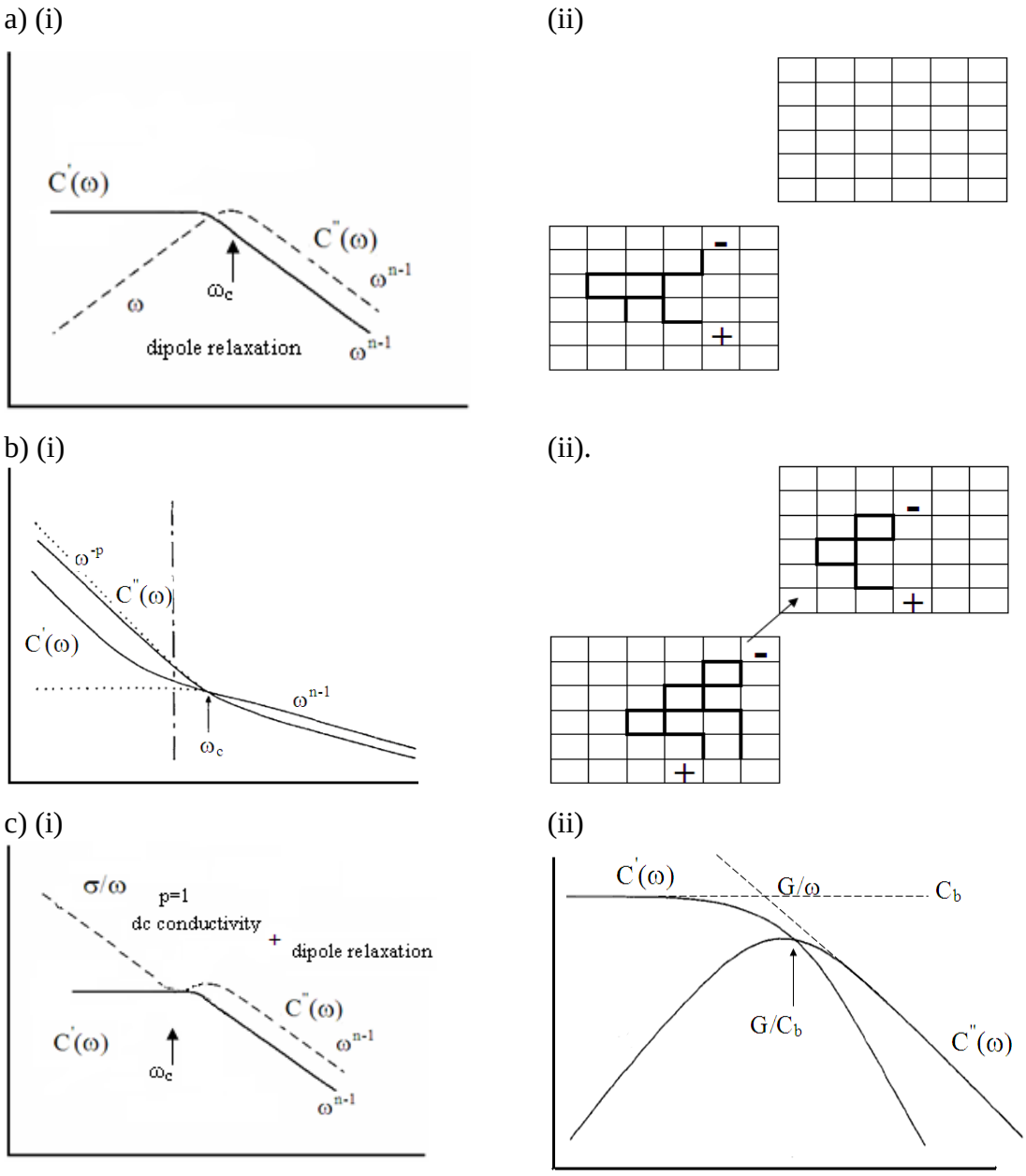

Figure 2-9 Plots reproduced from Dissado *et al.* [1987]
a) (i) Loss peak or relaxation response for cluster bound charges and dipoles. a) (ii) representation of a charge species site hopping journey within the cluster. b) (i) Quasi-dc transport response for charges weakly bound to clusters and able to move to neighbouring clusters $p < 1$. b) (ii) Representation of a charge species site hopping journey within the cluster and eventual site hop to a neighbouring cluster at a specific distance (quasi-dc). c) (i) A charge becomes free at a specific point resulting in dc conduction and a relaxation response. $p = 1$. c) (ii) Maxwell-Wagner response for a series combination of constant barrier capacitance and bulk conductance with magnitudes C_b and G.

2.5.1 Relaxation Processes Description

Hill and Cooper [1992] described the characteristic frequency dependent processes associated with the points of crossover of the capacitance and loss elements of the complex capacitance when modelled by a series pair of parallel capacitance, C and conductance, G electrical circuits (Figure 2-10). Process descriptions of an elementary unit in an emulsion, capacitance C_p and conductance G_p and a single barrier between particles capacitance, C_b and conductance, G_b from Hill and Cooper [1992] will be used throughout the present study to describe the general characteristic relaxation times τ_c associated with crossover frequencies ω_c processes. Where $\omega_1^{-1} = \tau_1 = C_p/G_p$, the relaxation time of particles or clusters within a material; $\omega_2^{-1} = \tau_2 = C_b/G_b$, the relaxation time of charges whose transport is blocked by the capacitance of a single barrier layer. $\omega_3^{-1} = \tau_3 = C_b/G_p$, the barrier charging relaxation time associated with the charging of a single barrier layer at the interface between two particles, two clusters or with the electrode. This last process is also known as the Maxwell-Wagner interface or the barrier charging process.

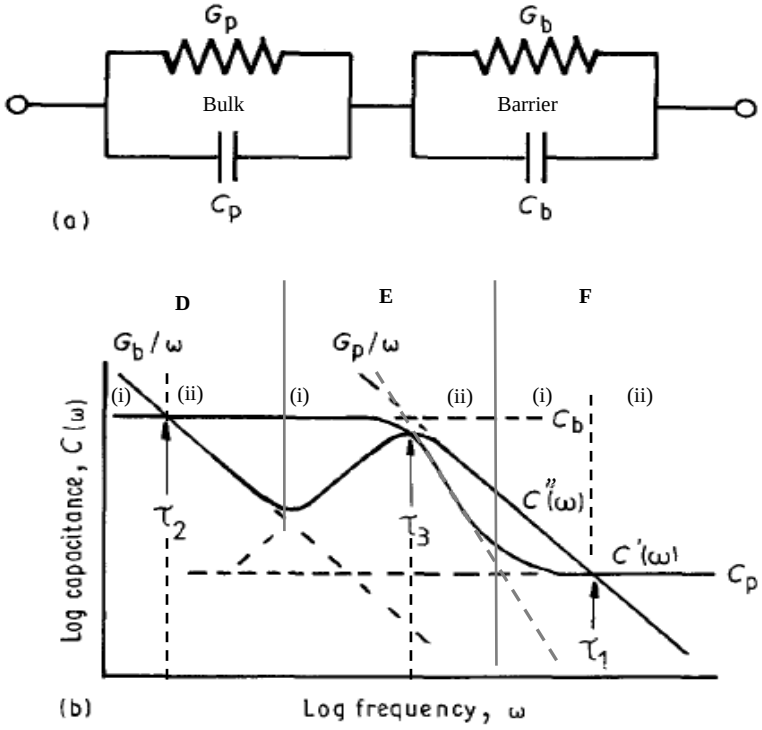

Figure 2-10 Representation of a single particle and barrier between two particles. (a) Pair of parallel bulk capacitance C_p and conductance G_p circuit, in series with barrier parallel C_b and G_b circuit and (b) the characteristic dielectric response of the circuit. The relaxation times τ_1, τ_2 and τ_3 are associated with intracluster, barrier polarisation and interface charging are indicated [reproduced from Hill and Cooper 1992]

The total impedance or total magnitude of the dielectric response of the circuit depicted in Figure 2-10 region D is dominated by the barrier conductance G_b of the parallel barrier circuit $G_b = C_b$ at the lower frequencies where $\omega < 1/\tau_2 = (C_b/G_b)^{-1}$; but is dominated by the barrier capacitance C_b at higher frequencies. In the transition frequencies Figure 2-10 region E, where the Maxwell-Wagner barrier charging the response is dominated by dominated by the barrier capacitance C_b at the lower frequencies, then dominated by the bulk conductance G_p as the frequency increases.

The intracluster response in Figure 2-10 region F is dominated by the bulk conductance G_p then by the bulk capacitance $C_\infty = C_p$ at higher frequencies. It should be noted that total capacitance for the series circuit Figure 2-10 (a) is $C = (C_p*C_b)/(C_p+C_b)$, and the descriptions above assumes the lower frequency barrier capacitance $C_b >> C_p$ is much greater than the higher frequency particle capacitance $C_p = C_\infty$, and the barrier conductance $G_b < G_p$ particle conductance.

2.5.2 Intracluster Polarisation Bound Charges (τ_1)

The intracluster or sub-cluster polarisation occurs at frequencies above the cross over frequency, $\omega > \omega_c$, where relaxation processes characterised by Equation 2.19(b). The processes typically occur above a frequency of 1 KHz and are associated with the polarisation of particles within clusters of self-similar clusters. Charges, permanent dipoles and induced charges bound to a specific cluster and can only move within that cluster.

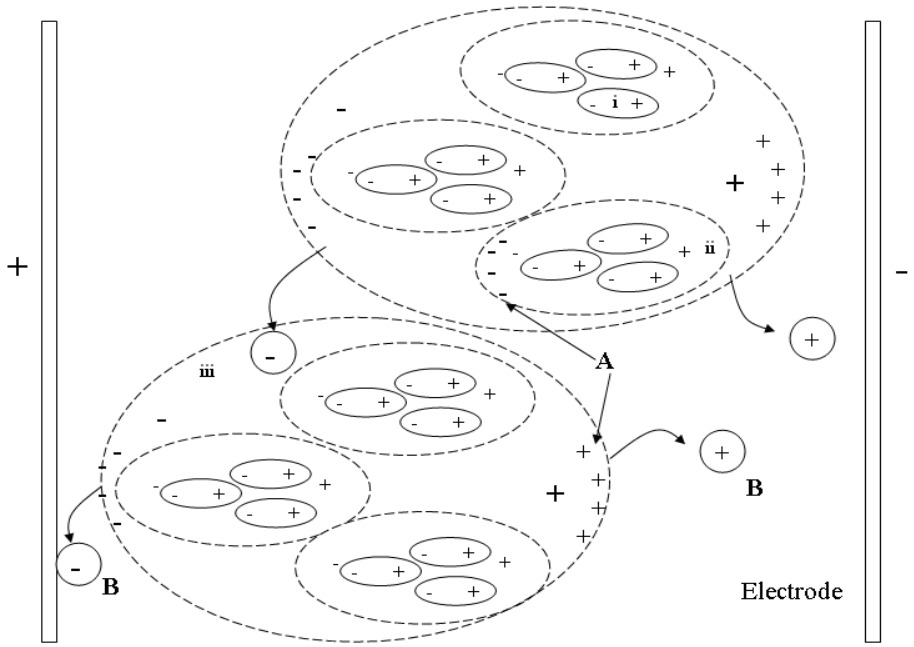

Figure 2-11 Representation of self-similar scaling of (i) aggregates, (ii) clusters of aggregates and (iii) clusters of clusters and the polarisation of each length scale which contributes to the total polarisation. Charges, (A), migrate to and charge the interface boundary between the clusters. Charges, (B), leaking from the interface and establishing a quasi-dc conductance.

This movement can be visualised as a charge hopping from site to site within the cluster. In the case of micellar or microemulsion aggregates, a cluster of aggregates coalesce or simply being in contact with another aggregate, allows the charge, polarised monomer or ions to be exchanged. However, the bound charges cannot migrate beyond the local cluster hence can only travel small distances. The intracluster polarisation process is illustrated in Figure 2-11 (i, ii, and iii), where it can be seen that the cluster of aggregates scale in to larger groups of clusters. For frequencies greater than the characteristic frequency $\omega > \omega_c$, the susceptibility derived from Equation 2-19 for the intracluster polarisation gives the expressions Equation 2-20.

$$\chi(\omega) \propto \chi_0 (i\omega/\omega_c)^{n-1} \quad \text{Eqn. 2-20 (a)}$$

$$= \chi_0 (i\omega/\omega_c)^{n-1} \{\sin(n\pi/2) - i\cos(n\pi/2)\} \quad \text{Eqn. 2-20 (b)}$$

The parameter '*n*' (Equation 2.19b) represents the degree to which a charge or dipole is bound or coupled to other particles within the cluster. It is considered to be a measure of the structural order of the cluster. As $n \rightarrow 0$ charges or dipoles within the cluster become decoupled and the characteristic response becomes Debye like, i.e. the relaxation of a charge has no impact on other polarised species within the medium (Figure 2-9 (c(ii))).

2.5.3 Maxwell-Wagner Barrier or Interface Charging (τ_3)

The Maxwell-Wagner interface charging occurs when charges within a polarised medium migrate to the interface between structures within the medium. The process is evidenced by a large dispersion in the capacitance as the frequency is reduced (when the complex capacitance is plotted in a log/log form) and occurs in the frequency range between the τ_1 and τ_2 relaxation processes, where the capacitance increases from the bulk to the barrier response magnitudes. The Dissado-Hill cluster theory fractional power law exponent for dispersive barrier layers provides information on the effectiveness of energy transport through the Maxwell-Wagner barrier [Dissado and Hill (1983), (1984)]. Figure 2-11 (A) represents the charges accruing at the interface between the aggregates and clusters of material and the electrode. The dispersive barrier has also been described as a leaky barrier due to imperfect packing of material in the barrier layer, which allows some charge to leak through the barrier to establish a constant conductance but of a lower magnitude than the bulk conductance. If the barrier is non-dispersive then it is effective at blocking the current flow.

2.5.4 Barrier or Interface Polarisation (τ_2)

The individual aggregates, clusters and clusters of clusters have a surface or barrier that defines the boundaries of their local grouping. The effectiveness of this barrier is determined by its ability to block the transport of charges from outside the grouping process, and is typically manifested below a frequency of 10^{-2} Hz. Figure 2-11 (A) shows the interface boundary blocking the transport of charges. The barrier process

also describes the build-up of charges at the material-electrode interface, and which again results in a reduction of current flow, and is manifested by a decrease in the recorded conductance.

2.5.5 Intercluster, Mobile Charge Transport, Quasi-dc and Barrier Leakage Current

Quasi-dc fractional power law theory (Dissado and Hill [1983], [1984]) describes the polarisation process where charges are transported through interface or barrier layers. Weakly bound charges are able to break free and to move to neighbouring, clusters and cluster of clusters outside of their local cluster group establishing a quasi-dc current. The charges are not completely free to move between each scaling group hence the path way traversed by the charge on its journey may require more than one hop in the desired direction to establish conduction.

$$\chi(\omega) = \chi_0 (i\omega/\omega_c)^{-p} \qquad \text{Eqn. 2-21 (a)}$$

$$= \chi_0 (i\omega/\omega_c)^{-p} \{\cos(p\pi/2) - i\sin(p\pi/2)\} \qquad \text{Eqn. 2-21 (b)}$$

Equation 2-21 is the susceptibility form of the complex capacitance for a dispersive barrier and the charge transport character occurs in the lower frequency range $\omega < \omega_c$. The exponent 'p' represents the degree to which a cluster affects other clusters in its neighbourhood and defines the extent to which different disturbed clusters remain isolated from one another during relaxation. When p approaches zero isolated identical clusters result. When p approaches unity an exponential distribution of decreasing cluster sizes is formed. A near dc or quasi-dc response is observed and the system can be described as percolating as the conductance has increased. Hence the efficiency of charge transport between clusters ranges $0 < p < 1$.

If $2/3 < p < 1$ the response is described as quasi-dc as the charges being not completely free require more than one step to find a path that leads to a neighbouring cluster. If $p = 1$ perfect DC conductivity is establish and the maximum efficiency for energy transfer is achieved. Figure 2-9 b(ii) and 2-12 B illustrate the journey of a charge as it moves through clusters and to neighbouring clusters outside the local group.

2.6 Anomalous Negative Dispersions

There are some anomalous dielectric responses that have been observed by Fishman *et al.* [1979] and Dissado [1987] that cannot be modelled with the general Dissado-Hill cluster model, in these cases it is necessary to adapt the complex capacitance form of the model.

2.6.1 Frequency Dependent Bulk Conductance Characteristics

Non biological materials and biological tissue such as squid axons (Fishman *et al.* [1979]) that have exhibited a time dependent increase in the magnitude of the bulk conductance. This increase in conductance results in a corresponding decrease in the magnitude of the capacitance which can be sufficient to generate negative capacitances. The bulk conductance term of the complex capacitance restated in Equation 2-21 is replaced by a linearised conductance term in Equation 2-22, which contains up to three frequency dependent elements. The frequency dependent conductance contains a constant component which dominates at high frequency and a component that varies as the frequency of the applied field varies. The linearised form of the frequency dependent conductance introduces incremental changes in the magnitude of the conductance (m = 0, 1, 2).

$$C^{*}_{bulk}(\omega) = C^{'}(\omega) - i\left(\frac{G(\omega)_{bulk}}{\omega}\right) \qquad \text{Eqn. 2-22}$$

$$G(\omega) = G_{\infty} + \left(\frac{G_m}{1+i\omega\tau}\right) = \left(G_{\infty} + \left(\frac{G_m}{1+\omega^2\tau_m^2}\right) - \left(\frac{i\omega\tau G_m}{1+\omega^2\tau_m^2}\right)\right) \qquad \text{Eqn. 2-23}$$

Figure 2-12 shows the effect of the capacitance response replacing the constant bulk conductance element with linearised time dependent bulk conductance element in the series parallel circuit. The resultant anomalous negative capacitance displayed in Figure 2-12 in the frequency range 10^6 Hz < f < 10^4 Hz occurs as a consequence of the differences in magnitude of the linearised conductance and the characteristic times, τ_{G0}, τ_{G1}, and τ_{G2}.

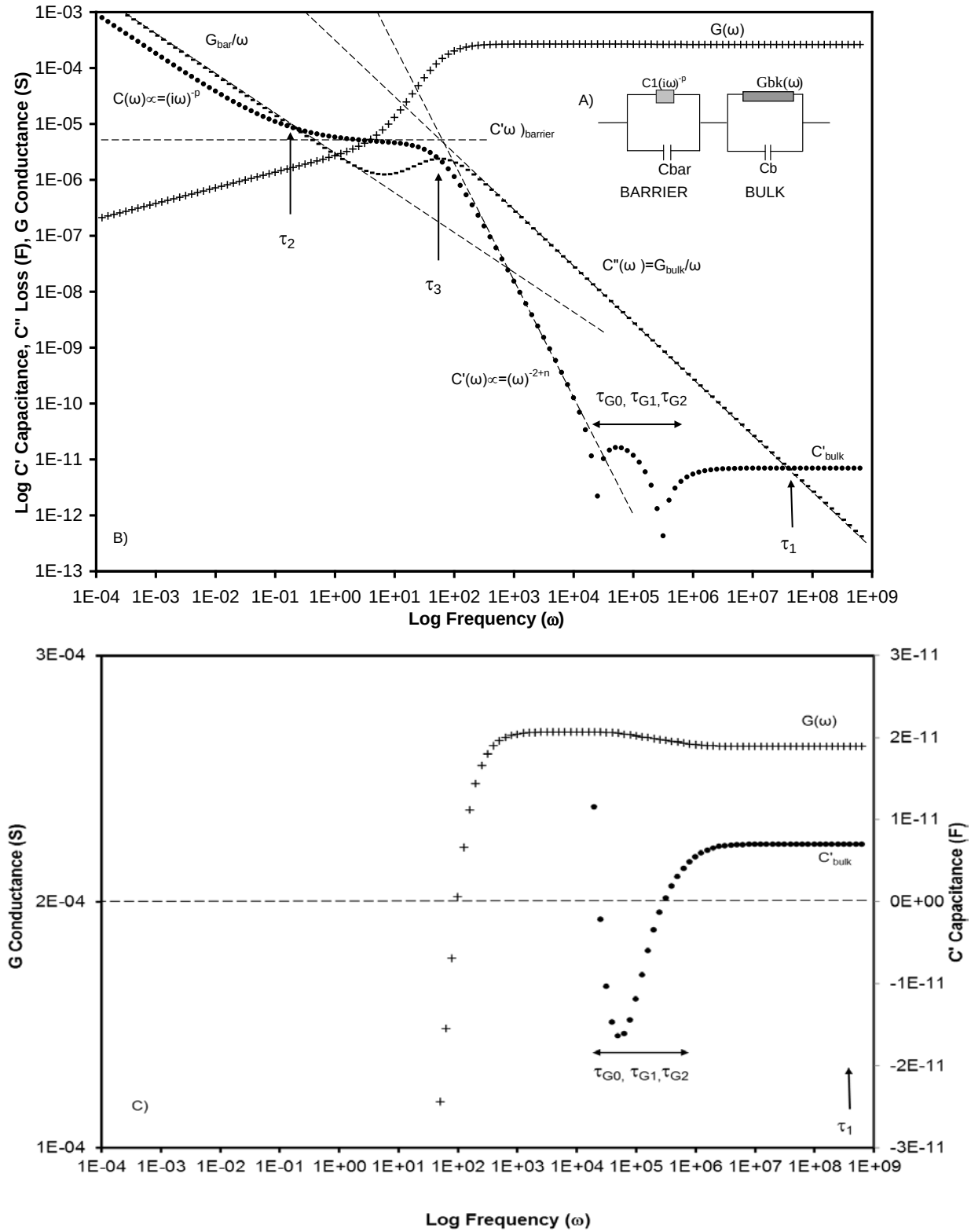

Figure 2-12 (A) Series-parallel circuit containing parallel time dependent bulk conductance and constant capacitance elements in series with a parallel dispersive and constant barrier capacitance elements. (B) Plot of circuit (A) showing the anomalous frequency dependent negative capacitance dispersion in the bulk capacitance generated as a consequence of the time dependent bulk conductance element. The characteristic relaxation features intracluster τ_1, barrier τ_3, and intercluster τ_3 are indicated together with the characteristic times for the time dependent increase in the conductance τ_{G0}, τ_{G1} and τ_{G3}. (C) Lin / Log plot of circuit (A) showing the modelled increase in conductance and corresponding decrease in capacitance.

2.6.2 Anomalous Negative Low Frequency Dispersion

Negative capacitances have been observed in many types of samples ranging electrochemical systems involving electrolyte /electrode interfaces, batteries to biological tissue such as membranes, squid nerve axons and muscle [Jonscher, 1986 and Dissado, 1987]. The capacitance of a sample can become negative if there is a time dependent increase in conductance of the system. Examples of negative capacitance have been attributed to either artefacts of the measuring instrumentation [Craig *et al.* 1993], homocharge injection at electrodes or the time dependent gating and release of built up charge reservoirs at membrane interfaces [Fishman *et al.* 1979].

2.6.3 Reasons for Negative Capacitance - Homocharge Injection at Electrode Model

In the case of an electron being injected in the negative electrode, the flow of charge is limited by the resulting space charge. An additional hetrocharge or positive ion migrates to negative electrode hence rate of current flow or conductance is increased. The time delay for the increase in conductance to occur is dependent on the transit time which is dependent on the geometry of the system.

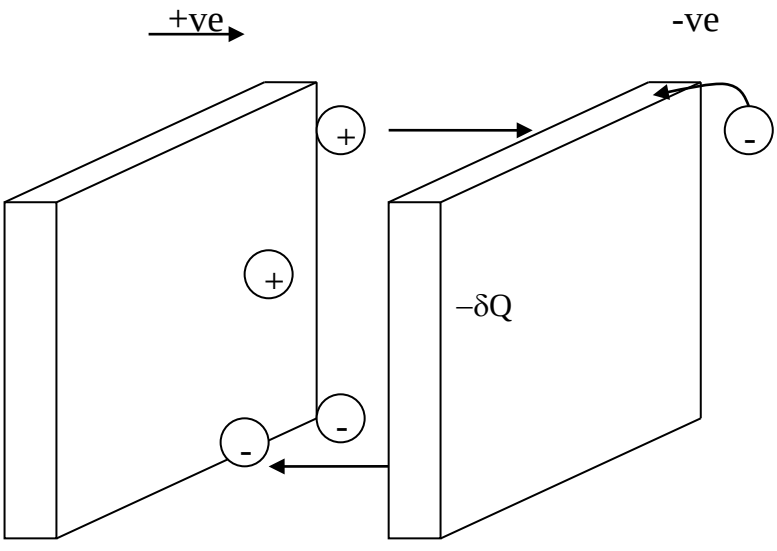

Figure 2-13 Homocharge injection at the negative electrode

2.6.4 Reasons for Negative Capacitance – Gating of Interface Charge Reservoirs Model

In the case of biological systems such as squid axon (Fishman *et al.* [1979]), plant leaves (Hill *et al.* [1987]), mouse muscle [Dissado 1987], charges pass through channels or pores in the semi permeable membranes of cells or nerve walls. The flow of charges through the cell membrane is dependent on the translocation of bound charges or dipoles to open then close gates when a voltage is applied to the membrane. The nature of the gating process falls in to one of two categories: a) The gating physically opens and closes pores within the structure of the membrane, hence controlling the flow of ions in either a solvated form or via ion specific carrier molecules. This process is frequency independent electrical conductance. b) The gating takes place via ion specific transport paths across the membrane surface of bridging molecules or via embedded proteins with ion specific absorption sites confined to potential valleys in the membrane surface. The formation of the transport paths and the access of ions to them are controlled through the adoption of the appropriate conformation by the protein. This mechanism constitutes gating as is frequency dependent as the total path length of the ion crossing the membrane is much greater than the thickness of the membrane.

The frequency dependent gating mechanism can be modelled by the quasi-dc Dissado-Hill cluster model Equation 2-19 however dielectric responses observed for squid axons exhibit ranges of negative values for both capacitance and conductance components. These negative features have been modelled (Fishman *et al.* [1979]) by utilising frequency dependent linear conductance increments to account for the opening and closing of gates enabling the increase of conductance due to the passage of potassium and sodium ions through the axon membrane.

2.6.5 Fractals – A Hierarchy of Self Similar Structures

Dissado and Hill [1989] reviewed the various relaxation models (Table 2-1) based on power law and noted that all models contain hierarchy of self-similar or fractal-like processes (Figure 2-14). Most models identify only one region of fractal behaviour which crosses over at low frequencies to a non-fractal behaviour. In the two distinct classes of materials that can be identified i.e. those with bound dipoles and those with potentially mobile charges, these models predict a crossover of random relation process and uniform dc transport respectively. Experimental observations have suggested that

the relaxation of bound dipolar systems involves a cross over to a different form of self-similarity at low frequencies. A similar behaviour has also been found to occur when mobile charges face irregular interruptions of their transport paths. This identification of two different fractal regions in the observed dielectric relaxation is strengthened by the analytical derivation of simple fractal circuit models (Dissado [1990]).

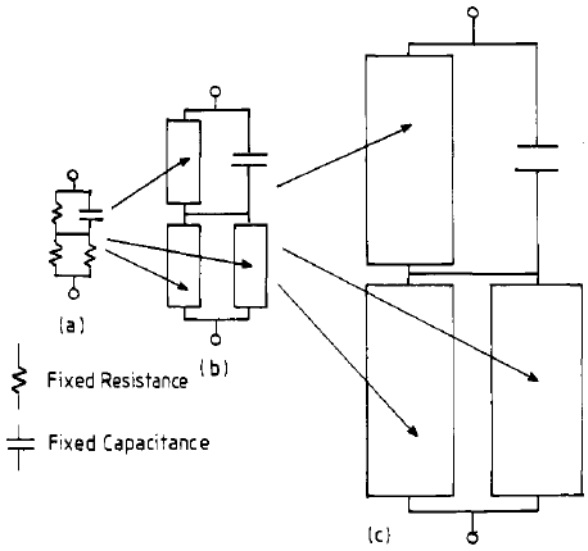

Figure 2-14 Fractal Circuits (Dissado [1990])

2.6.6 Potentially Mobile Charge Movements

The fractional power law identified in dielectric relaxation experimental observations have been attributed to the charging process of capacitive type membranes within cellular tissue or interfaces boundaries (Dissado [1990], Dissado *et al.* [1995]), and takes the form $\varepsilon'(\omega) \propto \omega^{n-1}$ and $\varepsilon''(\omega) \propto \omega^{n-1}$ for the permittivity and loss components of the dielectric response. This relationship, where the same power law applies to both the real and loss component has been termed a constant phase angle (CPA) response as the phase difference between the driving ac voltage and the relaxation current is independent of frequency, ω. Lui [1985 & 1986] related the CPA to the fractal dimensions of a self-similar system and it provides information on the conducting properties of percolating clusters because, the sub-circuits on different levels contribute in a self-similar way to the relaxation response of the hierarchy (Figure 2-14).

Dissado *et al.* [1995] suggested a simple way to envisage the relaxation response is to regard the charging of the cell's outer membrane or cluster interface to be the result of a

charged particle making a random walk on the self-similar internal structure. In time, t, the particle is displaced a distance, R, with

$$t \propto R^{d_w} \qquad \text{Eqn. 2-24}$$

Here the walk dimension is d_w and the number of unique sites of the fractal that have been charged within the range R is

$$R^{d_f} \propto t^{\frac{d_f}{d_w}} \qquad \text{Eqn. 2-25}$$

where d_f is the fractal dimension of the self-similar hierarchy and is purely geometrical in origin.

The polarisation of the system at time t is proportional to, R^{d_f} the polarisation of the percolation structure in a driving ac field of frequency, ω, which is proportional to the capacitance and is given by

$$C(\omega) \propto R^{d_f} \propto t^{\frac{d_f}{d_w}} \propto \omega^{-\frac{d_f}{d_w}} \qquad \text{Eqn. 2-26}$$

$$\omega^{-\frac{d_f}{d_w}} \propto \omega^{n-1} \qquad \text{Eqn. 2-27}$$

Leading to the relationship between CPA index '*n*' and the fractal dimension for the frequency range $\omega > \omega_c$:

$$n = 1 - \frac{d_f}{d_w} < 1 \qquad \text{Eqn. 2-28}$$

The fractal walk, d_w, Equation 2-26 is usually large implying the charge requires a lot of steps or hops to go a given distance because it is held by the counter charge.

Equation 2-25 also leads to the relationship between CPA index '*p*' and the fractal dimension for the frequency range $\omega < \omega_c$:

$$p \approx \frac{d_f'}{d_w'} \longrightarrow 1 \qquad \text{Eqn. 2-29}$$

Information about the fractal hierarchy arrangement is contained within the CPA index '*n*' and '*p*' in the frequency range $\omega > \omega_c$ and $\omega < \omega_c$ respectively. The indices can be been related to self-similar, scaling sub-clusters (Equation 2-26) and supra-clusters (Equation 2-27) (Lui [1985], [1986]).

Inside the cluster, the paths of the charges are easy but they are bound i.e. they are blocked at the capacitive ends of the sub percolation clusters Figure 2-9 a(ii). Outside a cluster, the low frequency index is less than unity $p < 1$ and the paths of the charge are weak resulting in the movement of the charges between clusters being similar to that of a charge moving on a structure with its original counter charge. The charge moves over much larger distances and almost every step counts for separation and it eventually moves to a neighbouring cluster at a specific distance. The charge is not completely free Figure 2-9 b(ii) and a quasi-dc conductance is achieved.

When $p = 1$, charges become free and is able to escape from a cluster at the characteristic frequency, ω_c. For frequencies below ω_c, dc conduction occurs and dipoles relaxation response occurs (Figure 2-9 c(i)).

2.7 Dielectric Characterisation and Modelling

Characterising the spectra produced from the dielectric measurements begins with comparing the general shape of the experimental response spectra with those contained within the susceptibility column, $\chi(\omega)$, of Figure 2-15 (Jonscher [1983]). The equivalent ideal and simple circuit can then be located in the circuit column and is used as the basis to build a representative circuit model of sample under examination.

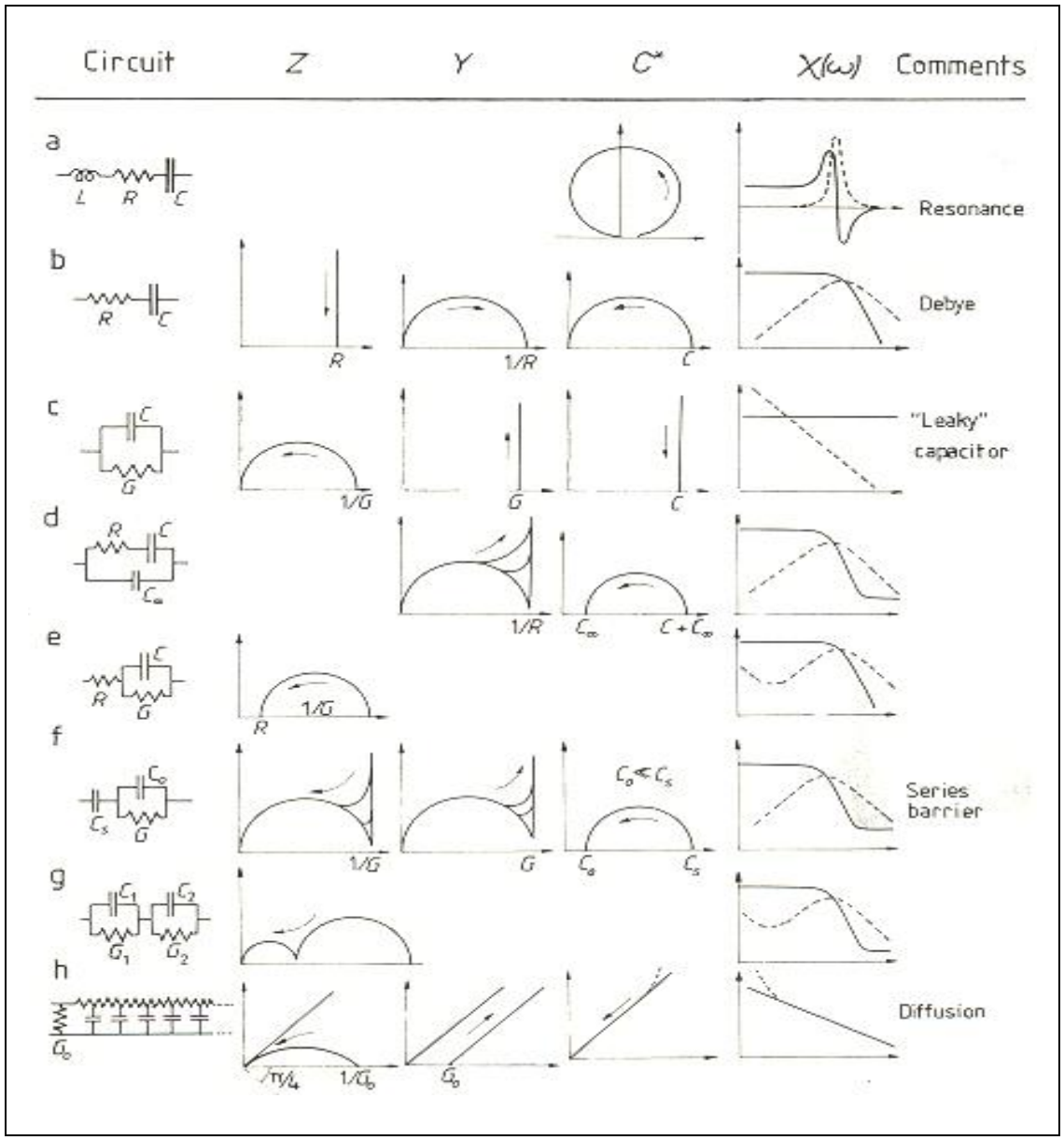

Figure 2-15 Schematic representations of simple circuit combinations of ideal frequency–independent elements of capacitance C, conductance G or resistance R and inductance L as shown in the first column. The fifth column gives the corresponding plots of log C'(ω) (solid lines) and log C" (ω) (dotted lines) against log ω. [Reproduced from Jonscher [1983]]

The circuits contained within Figure 2-15 are comprised of capacitance, C, conductance, G, or resistance, R, elements of constant and frequency independent values. It has been shown experimentally (Jonscher [1983]) that a wide range of dielectric materials exhibit a more complex dielectric relaxation response of the fractional frequency power law frequency form. This power law form of response can be represented by a universal capacitor Equation 2-30.

$$C_n(\omega) = B(i\omega)^{n-1} + C_\infty \qquad \text{Eqn.2-30}$$

$$C_n(\omega) = B\left\{\cos(\frac{(n-1)\pi}{2}) + i\sin(\frac{(n-1)\pi}{2})\right\}(\omega)^{n-1} + C_\infty \qquad \text{Eqn.2-30(a)}$$

$$C_n(\omega) = B\left\{\sin(\frac{n\pi}{2}) - i\cos(\frac{n\pi}{2})\right\}(\omega)^{n-1} + C_\infty \qquad \text{Eqn.2-30(b)}$$

The term B is the magnitude of the capacitance, and the exponent $0 < n < 1$ defines the power law frequency dependence. The universal capacitor is unique in that the real and imaginary components are the same functions of frequency and have a constant frequency independent ratio.

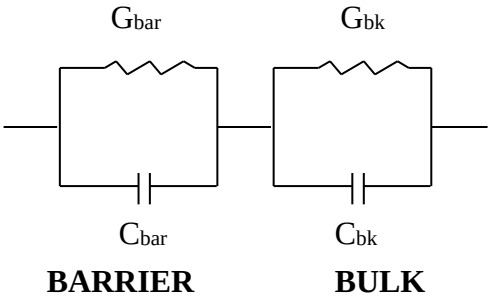

Figure 2-16 Circuit representing the series barrier physical arrangement

Many of the dielectric response spectra observed in this study have the general appearance of a form similar to Figure 2-15(g) equivalent to a series barrier arrangement circuit (Figure 2-16). Although similar, the spectral form requires further refinement in the shape of the barrier response. The calculated response (Hill *et al.* 1990]) in Figure 2-17 replaces the constant barrier capacitance value with a power-law dispersive capacitance.

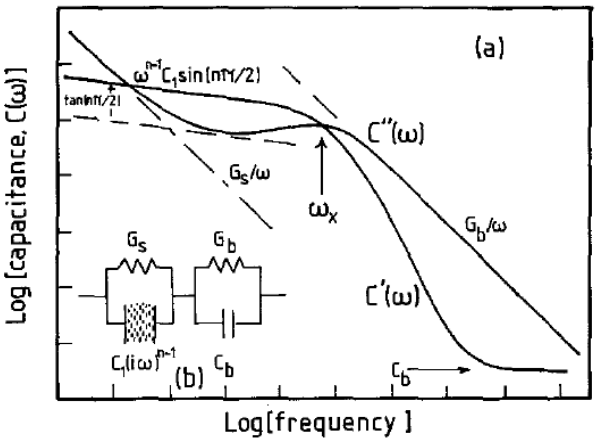

Figure 2-17 The calculated frequency response (a) for the circuit shown in insert (b). G_b and C_b refer to the low-magnitude conductance and capacitance of the bulk of the sample; the power-law dispersive capacitance $C_l\ (i\omega)^{n-1}$ blocks the bulk conductance at frequencies below ω_x and is in parallel connection with the barrier leakage conductance G_s. Reproduced from Hill *et al.* (1990).

2.7.1 Circuit Alterations for Non Linear Responses

In addition, the characteristic spectra of the samples measured showed indications of frequency dependent conductance, G(ω), in the bulk frequency region. More complex circuits such as those described and applied by the authors [Hill (2001), Dissado (1987), Dissado & Hill (1984), Fishman *et al.* (1979) and Dissado, Hill (1989)] are required to model these responses. The barrier-bulk series pair of parallel resistor/ capacitor circuits Figure 2-17(b) is further adapted by 1) replacing the constant bulk conductance G_b with the frequency dependent element $G_{bk}(\omega)$ and replacing the barrier conductance with a large capacitor (Figure 2-18).

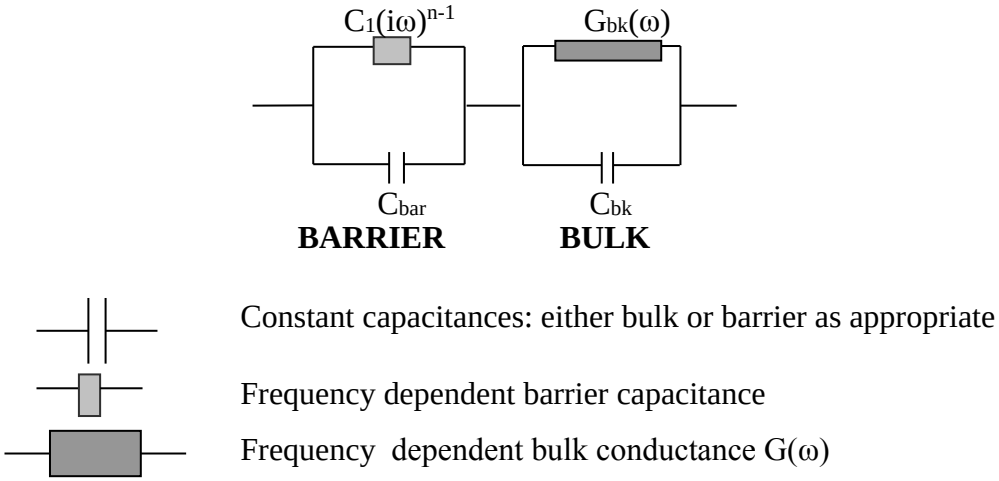

Figure 2-18 Circuit containing a time dependent bulk conductance element in series with power law dispersive barrier capacitance

The series pair of parallel circuits depicted in Figure 2-18 describes the bulk parallel capacitor and frequency dependent conductance circuit in series with a dispersive capacitor in parallel with a constant capacitor. The complex bulk parallel circuit is represented by:

$$C^*_{bulk}(\omega) = C'(\omega) - i\left(C''(\omega) + \frac{G(\omega)_{bulk}}{\omega}\right) \qquad \text{Eqn.2-31}$$

Where the loss term is dominated by the inverse frequency term is dominated by the conductance, eqn 2-30a can be written in the form:

$$C^*_{bulk}(\omega) = C'(\omega) - i\left(\frac{G(\omega)_{bulk}}{\omega}\right) \qquad \text{Eqn.2-32}$$

The frequency dependent conductance contains a constant component (which dominates at intermediate frequency (Figure 2-19)) and a component that varies as the frequency of the applied field varies. The linearised form of the frequency dependent conductance can be represented by Equation 2-33 and introduces discrete incremental steps in the magnitude of the conductance (m = 0, 1, 2) at characteristic frequencies of ω_m=0, 1, 2, associated with the discrete conductance G_m step changes.

$$G(\omega) = G_\infty + \left(\frac{G_m}{1 + i\omega\tau}\right) = \left(G_\infty + \left(\frac{G_m}{1+\omega^2\tau^2}\right) - \left(\frac{i\omega\tau G_m}{1+\omega^2\tau^2}\right)\right) \qquad \text{Eqn. 2-33}$$

Noting that conductance, capacitance and admittance are related via:

$$G(\omega) = i\omega C(\omega) = Y(\omega) \qquad \text{Eqn. 2-34}$$

Eqn 3-4 can be re-written

$$C^*_{bulk}(\omega) = \left(C_\infty - \frac{\tau G_m}{1+\omega^2\tau^2}\right)_{Real} - \frac{i}{\omega}\left(G_\infty + \frac{G_m}{1+\omega^2\tau^2}\right)_{Imag} \qquad \text{Eqn. 2-35}$$

Where m = 0, 1 or 2

The complex barrier parallel circuit is represented by:

$$C^*_{barrier}(\omega) = B(i\omega)^{n-1} + C_{bar}$$
$$= \left(C_{bar} + B(\omega)^{n-1} Cos\frac{(n-1)\pi}{2}\right)_{Real} - i\left(B(\omega)^{n-1} Sin\frac{(n-1)\pi}{2}\right)_{Imag} \qquad \text{Eqn. 2-36}$$

The total capacitance of the series pair of parallel circuits is given by:

$$C^*_{total}(\omega) = \left(\frac{C^*_{barrier} * C^*_{bulk}}{C^*_{bulk} + C^*_{barrier}} \right) \qquad \text{Eqn. 2-37}$$

2.7.2 Parameters Used to Model the Experimental Responses

The microemulsion samples in the study were modelled using the circuit depicted in Figure 2-18 and Equation 2-35, 2-36 and 2-37. The terms contained in the total complex capacitance Equation 2-37 for the circuit were separated into real and imaginary components and were incorporated into a spreadsheet enabling the values for the complex capacitance to be calculated and plotted over the frequency range 10^6 Hz to 10^{-5} Hz. The intermediate steps for separating the real and imaginary components of the total complex capacitance are stated in Equations 2-38 to 2-47:

$$\text{Let } A(\omega) = \left(\frac{G_m}{1 + \omega^2 \tau^2} \right) \qquad \text{Eqn. 2-38}$$

Substituting equation 2-38 into 2-35, the complex bulk capacitance term becomes:

$$C^*_{bulk}(\omega) = \left(C_\infty - \tau A(\omega)\right)_{Real} - \frac{i}{\omega}\left(G_\infty + A(\omega)\right)_{Imag} \qquad \text{Eqn. 2-39}$$

$$\text{Let } D = \left(C_\infty - \tau A(\omega)\right)_{Real} \qquad \text{Eqn. 2-40}$$

$$\text{Let } E = \frac{\left(G_\infty + A(\omega)\right)}{\omega}_{Imag} \qquad \text{Eqn. 2-41}$$

$$C^*_{bulk}(\omega) = D - iE \qquad \text{Eqn. 2-42}$$

Substituting H and J for the real and imaginary components of the complex barrier capacitance equation 2-36.

$$\text{Let } H = \left(C_{bar} + B(\omega)^{n-1} Cos \frac{(n-1)\pi}{2} \right)_{Real} \qquad \text{Eqn. 2-43}$$

$$\text{Let J} = \left(B(\omega)^{n-1} Sin \frac{(n-1)\pi}{2} \right)_{Imag} \qquad \text{Eqn. 2-44}$$

$$C^*_{Barrier}(\omega) = H - iJ \qquad \text{Eqn. 2-45}$$

Substituting equations 2-42 and 2-45 into the total complex capacitance equation 2-37, the real and imaginary components can be written as equations 2-46 and 2-47.

$$\text{Let } C^{*}_{\mathrm{Re}\,al} = \left(\frac{(HD - JE)(D + H) + (JD + EH)(E + J)}{(D + H)^2 + (E + J)^2} \right) \qquad \text{Eqn. 2-46}$$

$$\text{Let } C^{*}_{\mathrm{Im}\,ag} = \left(\frac{(HD - JE)(E + J) - (JD + EH)(D + H)}{(D + H)^2 + (E + J)^2} \right) \qquad \text{Eqn. 2-47}$$

Modelling was carried out using a minimum of three parameters, bulk capacitance C_∞, bulk conductance G_∞ and barrier capacitance B, which were extracted from plots of the raw experimental data. However up to eleven parameters were usually required to model the results over ten decades on a log frequency scale (Table 2-2).

Table 2-2 Modelling Parameters

Parameter	Description	Dominant response region
$C_{bulk,,}(C_\infty)$	High frequency constant capacitance	Bulk
$G_{bulk\ ,}(G_\infty)$	High frequency constant conductance	Bulk
G_0	Linearised frequency dependent bulk conductance	Bulk
G_1	Linearised frequency dependent bulk conductance	Bulk
G_2	Linearised frequency dependent bulk conductance	Bulk
ω_{g0}	Conductance G_0, characteristic frequency	Bulk
ω_{g1}	Conductance $G_{1,}$ characteristic frequency	Bulk
ω_{g2}	Conductance G_2,characteristic frequency	Bulk
ω_c	High to low frequency characteristic crossover frequency	Crossover
C_{bar}	Barrier capacitance	Barrier
B	Magnitude of dispersive barrier capacitance	Barrier
p	Low frequency power law indices	Barrier

The parameters describing the bulk characteristics of the sample are utilised for frequencies above the cross over frequency, ω_c, whilst the parameters describing the barrier characteristics dominate at frequencies below ω_c. Figure 2-19 A) contains a plot of a modelled complex capacitance C' ●, loss C" –, conductance G +, superimposed on the measured response sample comprised of surfactant AOT 25%, oil IPM 62.5% and water 12.5%, indicating the frequency regions where the parameters were applied. The absolute value of the negative capacitance values were used on log/log plots.

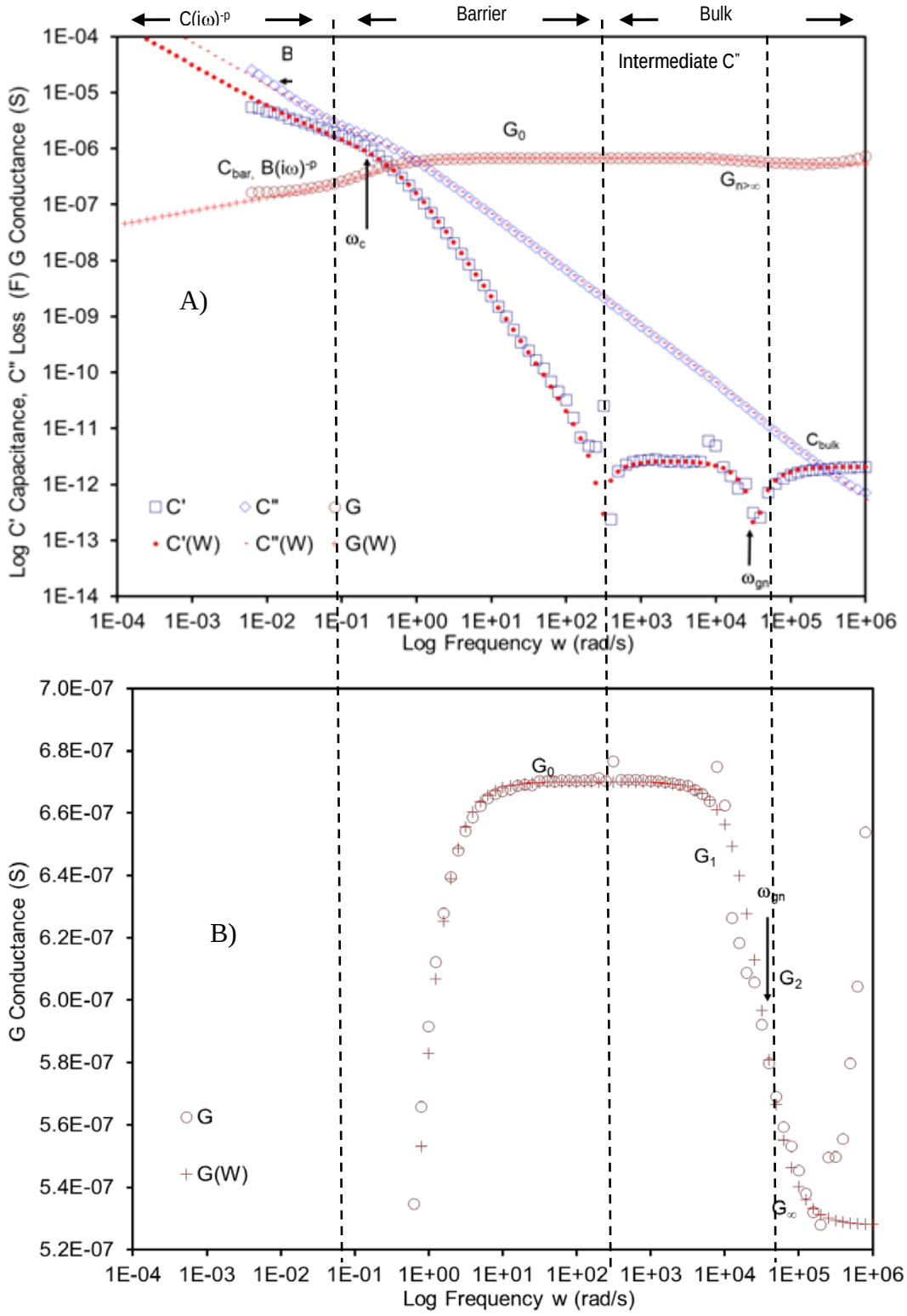

Figure 2-19 Sample comprised of AOT 25%, IPM 62.5% and water 12.5% A) Model of complex capacitance superimposed on experimental response. The modulus of the negative capacitance is plotted on a logarithmic scale. B) Example of modelling of the linearised bulk conductance

The magnitude and frequency range duration of the frequency dependent conductance component had a significant impact on the sign, shape and magnitude of the modelled bulk capacitance. The magnitudes of linearised conductance parameters were

determined by detailed examination of linear/log plot of the high frequency increase in conductance (Figure 2-19 (B)).

2.7.3 Impedance plot of experimental data

An example of the characteristics responses of reverse microemulsions in this study is represented in the form of an impedance plot in Figure 2-20 and is similar to series pair of parallel RC circuits depicted in Figure 2-15g. However this example plot shows the anomalous negative capacitance appears in an overlapping region between the bulk and barrier response.

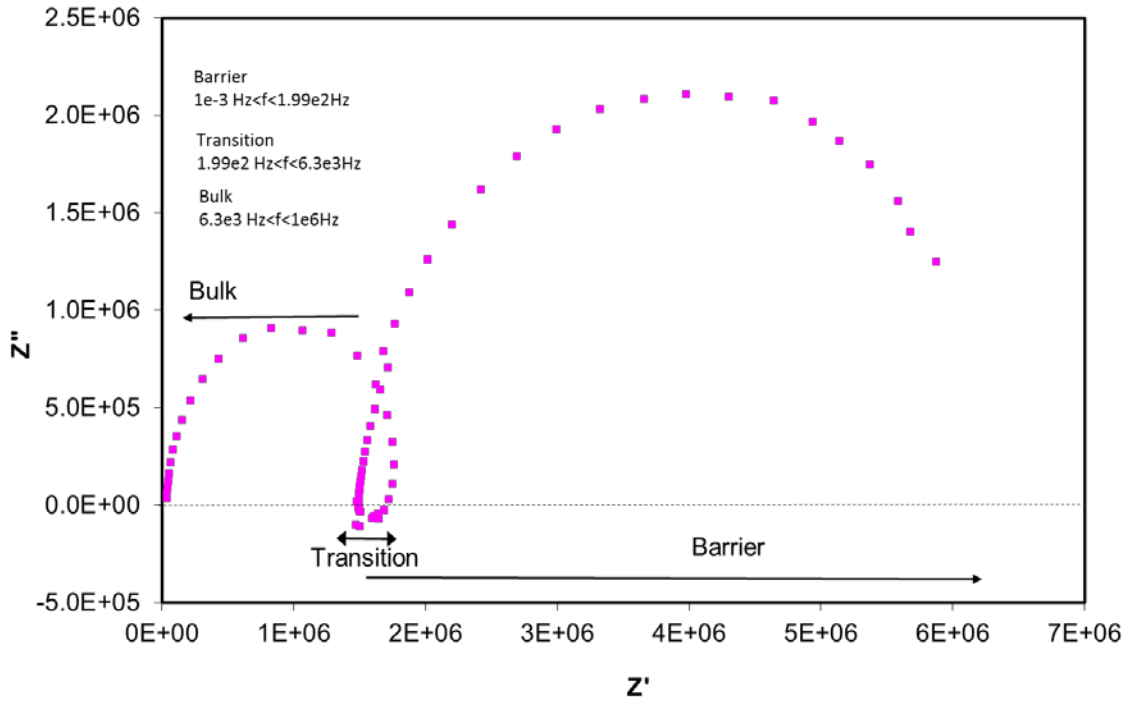

Figure 2-20 Example of an impedance plot of a sample comprised of AOT 25%, IPM 62.5% and water 12.5%

2.8 Aim of the Present Study

The aim of the present study is to determine if low frequency dielectric spectroscopy characterisation of ternary mixtures, including single, dual and tertiary components of reverse microemulsions, could be used to predict the characteristic response of more complex ternary reverse microemulsion mixtures.

2.8.1 Objectives

The objectives of the study are to create and identify single phased mixtures which contain reverse microemulsions aggregates; then using low frequency dielectric spectroscopy to characterise samples that contain single components, mixtures of two components, and ternary compositions that contain reverse microemulsion aggregates and those that do not.

Chapter 3

Materials and Methods

3. Materials and Methods

3.1 Materials

3.1.1 Surfactants and Co-Surfactants

The anionic surfactant sodium bis(2-ethylhexyl) sulfosuccinate (AOT) was purchased from Fluka (UK). The zwitterionic surfactant, Epikuron 200 (E200), was supplied by Lucas Myer (Germany). The non-ionic surfactant, polyoxyethylene (23) lauryl ether ($C_{12}E_{23}$, Brij 35), was obtained from Aldrich (UK). The cosurfactant, 1-propanol, was purchased from Sigma-Aldrich (UK).

3.1.2 Oil

Isopropyl myristate (IPM) and ethyl caprylate were supplied by Sigma Aldrich (UK).

3.1.3 Hydrophilic Components

De-ionised water was used throughout to the prepare the microemulsions. Propylene glycol (PG) was suplied Lancaster (UK). Sodium salicylate was purchased from Fluka (UK).

Table 3-1 Components used to prepare the microemulsion

Component	Type	Details
Isopropyl myristate (**IPM**) 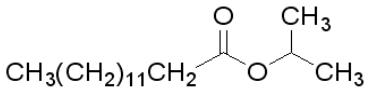 ($C_{17}H_{34}O_2$)	Oil	Supplier: Sigma Aldrich CAS: [110-27-0] Purity: > 98% (99.8%) Molecular weight: 270.46 Density: 0.850 g/mL at 25ºC
Ethyl caprylate (**EC**) 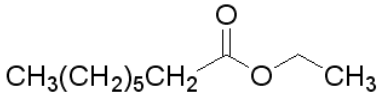 ($C_{10}H_{20}O_2$)	Oil	Supplier: Sigma Aldrich CAS: [106-32-1] Purity: ≥99% Molecular weight: 172.26 Density: 0.867 g/mL at 20ºC
Sodium bis(2-ethylhexyl) sulfosuccinate **(AOT)** 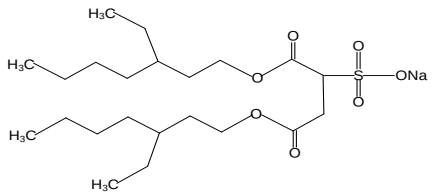 **($C_{20}H_{37}NaO_7S$)**	Surfactant	Supplier: Fluka CAS: [577-11-7] Purity: >96% (TLC) $H_2O \leq 2\%$ Molecular weight: 444.57 Density: 1.21 g/mL at 25ºC HLB = 10.2

Table 3-1 Components used to prepare the microemulsion

Component	Type	Details
Epikuron 200 (**Lecithin**) 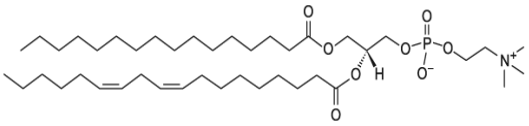 ($C_{42}H_{80}NO_8P$)	Surfactant	Supplier: Lucas Meyer Phosphatidylcholine > 95% Lyso- Phosphatidylcholine <3% Moisture, oil <3% Molecular weight: 758.07 HLB=8>14
Polyoxyethylene (23) lauryl ether **(Brij 35**, $C_{12}E_{23}$**)** 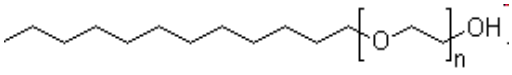 ($C_{58}H_{118}O_{24}$)	Surfactant	Supplier: Sigma–Aldrich CAS: [9002-92-0] Molecular weight: 1198 Batch No 127K0101 HLB = 16.9
1-propanol 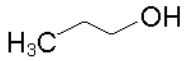 (C_3H_8O)	Co-surfactant	Supplier: Aldrich CAS: [71-23-8] Purity: > 99% (99.8%) Molecular weight: 60.10 Density: 0.804 g/mL at 25ºC
Water  (H_2O)	Polar solvent	Deionised – on tap Molecular weight: 18.02 Density : 0.997 g/mL at 25 ºC
1,2 propanediol **(**propylene glycol, **PG**) 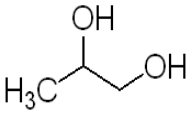 ($C_3H_8O_2$)	Polar solvent	Supplier: Lancaster CAS: [57-55-6] Purity: >98% (99.8%) Molecular weight: 76.10 Density: 1.036 g/mL at 25ºC
Sodium salicylate 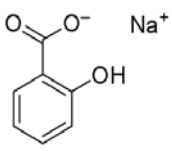 (C7H5O3Na)		Supplier: Fluka CAS: [54-21-7] Lot: 1135193 Purity: > 99.0% Molecular weight: 160.10

3.1.4 Reasons for Component Selection

The surfactant, AOT, was selected as the basis for characterising w/o microemulsions as it a relatively simple model as it does not require the presence of a cosurfactant to form microemulsions. W/O microemulsions stabilised by AOT have been the subject of numerous studies using a wide variety of techniques which include small angle neutron scattering (SANS) and photon correlation spectroscopy (PCS) hence there is a wealth of available data that can be used to support results obtained using the low frequency dielectric technique. Epikuron 200 was chosen as it is a pharmaceutical safe lecithin and like AOT has been the subject of numerous studies using a wide range of techniques. E200 requires a cosurfactant to be present in order for w/o aggregates to form spontaneously. Systems containing E200 are dielectrically more complex than AOT by virtue of requiring a cosurfactant to form microemulsions. Hence results obtain from AOT studies will be used as a guide to analysing E200/cosurfactant systems.

Isopropyl myristate (IPM) was selected as it is a pharmaceutical grade excipient used in topical and cosmetic products such as skin lubricants, creams and bath oils. IPM is classified as a penetration enhancer however its mechanism of action is not fully understood (Mortazavi and Aboofazeli [2003], Singh *et al.* [2005]). It is anticipated that this study will reveal information on how IPM interacts with the surfactants dispersed in the microemulsion.

3.2 Preparation of Microemulsions

Microemulsions and corresponding micelles, formed in the absence of water were prepared by mixing the required amount by weight of each component in the following order, surfactant, oil and polar component (either water or propylene glycol). The samples were then vigorously mixed and heated to a temperature of 343 K ± 5 K. Once the samples were clear or had been heated for 20 minutes they were removed from the heat and stirred until cool. The samples were then stored in screw to vials, covered in Parafilm to stop the ingress of moisture, at room temperature until needed. The appearance of all samples were checked through cross polaroids to ensure that they were not birefringent, and therefore not liquid crystalline in nature. Figure 3-1 shows an example of the appearance of birefringence. Samples which were clear, one phase, non-birefringent liquids after one month were denoted as microemulsions.

Figure 3-1 Appearance of a birefringent sample through cross polaroids

3.3 Dielectric Equipment

The low frequency dielectric measurements were made using an experimental set up consisting of a sample cell, a Solartron Frequency Response Analyser (FRA) model 1255a (Solartron Analytical [2001]) and a Chelsea Dielectric Interface (CDI) daisy chained together and connected to a personal computer (PC). The Solartron Impedance measurement software which controls the FRA and CDI and records the output from the sample was installed (Figure 3-2). The sample cells, the FRA and CDI are connected via BNC connectors. In a few of the investigations the CDI was replaced by the Solartron 1296 Dielectric Interface, however unless otherwise indicated the CDI was used.

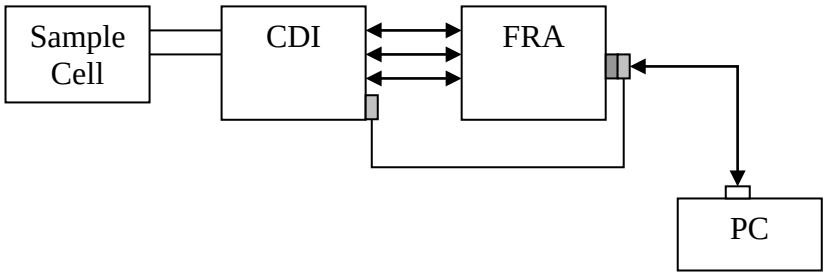

Figure 3-2 Experimental set up for low frequency dielectric measurements

3.3.1 Frequency Response Analyser (FRA) – Generator

The FRA acts as the generator (Figure 3-3) and provides a sinusoidal (AC) voltage at a frequency of between 100 μHz and 20 MHz and a voltage ranging between 0.05 V and 3V. The ac voltage is applied to the sample under investigation held in the sample cell via the CDI. The signal arising from the sample is returned, via the CDI to the FRA which measures the phase angle and amplitude of the sample signal.

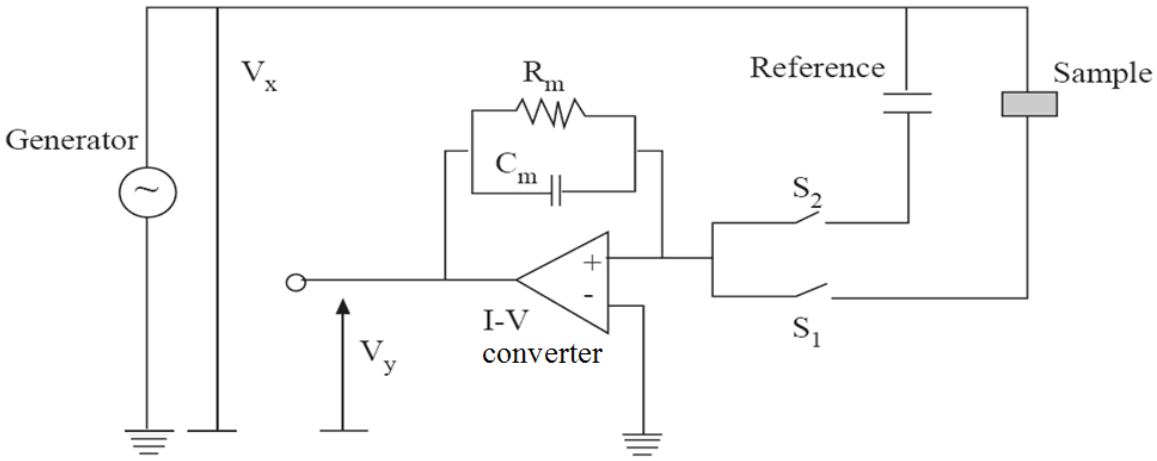

Figure 3-3 FRA – CDI- sample measurement circuit [Pugh (1988)]

3.3.2 Chelsea Dielectric Interface (CDI)

The CDI via means of the impedance software, controls the output from the FRA. The CDI functions as a high impedance buffer between the output signal from the FRA and the sample under study. The inclusion of the CDI in the experimental set-up extends and improves the measuring range of the FRA.

3.4 Dielectric Sample Cells

3.4.1 Small Dielectric Sample Cell

The measuring cell (Figure 3-4) was required to contain the liquid microemulsion sample without reaction and to limit the exposure of the sample to the environment. The cell design was adapted from the cell used by Hill *et al.* [1990] and was hand crafted in the laboratory works shop (Appendix B). The inner cell (internal volume 4052.0 ± 0.5 mm^3) in which the sample was directly contained was composed of Teflon. The inner Teflon cell was placed into an outer copper cell. A PTFE lid (ε_r = 2.1), through which the electrodes were passed, fitted securely onto both the inner and outer cells. Once in place, the lid was tightly sealed with Parafilm to ensure no ingress of moisture into the sample being measured. The electrodes, which were immersed in the sample, consisted of two platinum wires of 1.04 ± 0.03 mm diameter and of 20.02 ± 0.07 mm length giving an effective area of 33.44 mm^2. For the present study the area of the electrodes was small so that the magnitude of the dielectric response from samples with high polar molecule content was small enough to be within the measuring range of the equipment (Pugh [1988]).

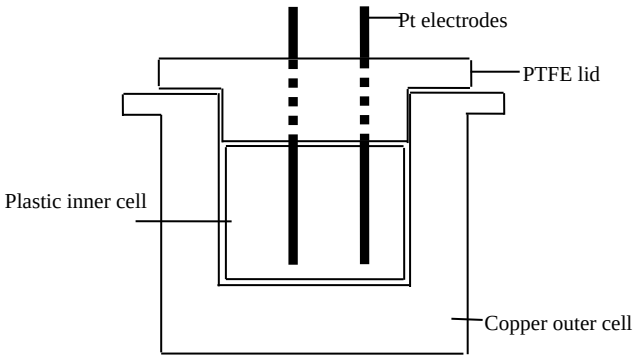

Figure 3-4 Small Dielectric Sample Cell

In order to interpret the experimental data it was necessary to determine the value the cell constant, C_0. The value of the cell constant is a consequence of the materials from which the cell is made, the geometry of the cell and the separation of the electrodes. The value of the cell constant varies inversely proportionally to the electrode separation. The cell constant was determined experimentally by measuring the dielectric response of the empty cell (the relative permittivity of the air in the cell ε_r = 1 at all frequencies). The cell constant (or the permittivity) was calculated using Equation 3-1.

$$C(\omega) = \varepsilon_r \varepsilon_0 \frac{A}{d}\left\{\exp^{-i(\omega t)}\right\} = \varepsilon_0 \frac{A}{d}\left\{\exp^{-i(\omega t)}\right\} = C_0\left\{\exp^{-i(\omega t)}\right\} \qquad \text{Eqn. 3-1}$$

where 'C(ω)' is the frequency dependent capacitance, 'ε_0' is the permittivity of free space, 'A' is the area of the electrodes in contact with the sample, 'd' is the separation of the electrodes.

The cell constant, C_0, for this small cell was also calculated to be 0.7 pF at an electrode separation of 1 mm. As the electrodes are removed from the cell as part of the cleaning process which can result in a variation of the separation of the electrodes, the electrode separation is measured and the cell constant recalculated after each cleaning process.

3.4.2 Large Dielectric Sample Cell

A limited number of experiments were carried out using a commercially available liquid sample cell (Figure 3-5) to check the calibration of measurements made using the small (in-house built) cell. Thereby the accuracy of the value cell constant obtained from the small cell. This cross calibration was possible because the large commercial cell

possessed the ability to more accurately control electrode separation than was possible in the small cell. This control was obtained by means of a micrometer which was used to adjust electrode separation by altering the separation of the upper electrode – the position of the lower electrode was fixed. Unfortunately however, the large cell was found to be unsuitable for routine use in the current study as there appeared to be a reaction between the AOT surfactant and the brass electrodes (Figure 3-6). In addition the large, commercial cell suffered from the disadvantage that it was not possible to securely seal or close the cell to ensure that there was no ingress of moisture into the sample being measured, due the presence of a micrometer used to adjust electrode separation.

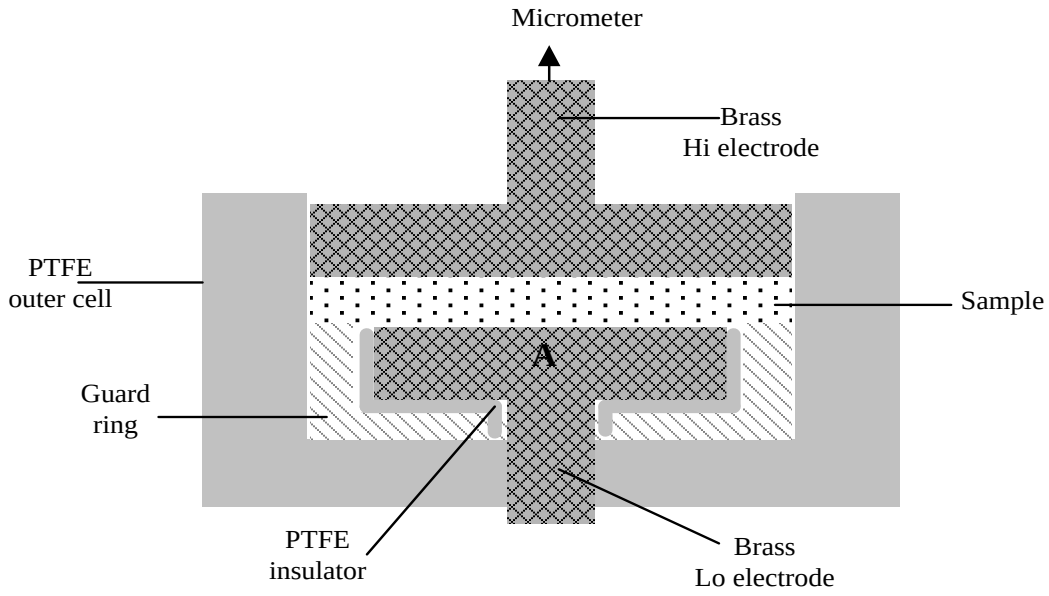

Figure 3-5 Large dielectric sample cell

The cell constant, C_0, for this large cell was calculated to be 0.7 pF with an effective electrode area of 78.54 mm^2 and an electrode separation of 2 mm.

Figure 3-6 Large sample cell brass electrode discolouration showing signs of a reaction.

3.5 Methods

3.5.1 Low Frequency Dielectric Measurement

3.5.1.1 Frequency Sweep

The purpose of a frequency sweep was to obtain the general characteristic response of the sample over the whole of the available frequency range. The spectrum is required to establish whether the sample under study displays any variation in dielectric response over the frequency range of the experiment.

A frequency sweep was performed by varying the frequency of the fixed ac voltage over the frequency range of the equipment. Each point was measured three times using the auto signal integration analyser mode. This mode averages the signal over three cycles which narrows the signal bandwidth thus narrowing the noise to signal ratio. The more a signal is averaged, the longer it takes to get a result for each point however the level of accuracy is increased. The auto integration averages the signal until it stabilises. The parameters used in the frequency sweep experiment are listed in Table 3-2.

Table 3-2 Parameters used for a frequency sweep measurement cycle

Parameter	Description
Voltage ac	A fixed ac voltage point ranging between 0.05 and 1.0 V
Frequency	Frequency sweep range starting at the lowest frequency up to the maximum available frequency i.e. 10^{-4} Hz to 10^{6} Hz.
Measurement points per frequency decade	Ranging between 4 and 10 points
Cycle repeat	Single frequency sweep cycle
Temperature	Room Temp 293 K ± 1 K

The dielectric spectra obtained using the frequency sweep method are presented in the form of log/log plots of the complex capacitance and conductance as function of frequency. The frequency, f, will be reported in hertz (Hz) or radians per second ($\omega = 2\pi f$). The real and imaginary (also referred to as capacitance and loss) components of the complex capacitance will be represented by solid and line symbols respectively (♦◊, ▲Δ, ■□, ●○). The conductance property will be presented solid triangle ▲when displayed with the capacitance and loss properties.

3.5.1.2 Voltage Sweep

This method was used to determine the sample sensitivity to changes in the magnitude of the applied ac electric field. The method is employed if the general characterising spectra, obtained via the frequency method indicates that they may be a frequency range which the sample is particularly sensitive to strength of the applied electric field. Alternatively the method may be used to examine the sensitivity of the characteristic relaxation frequencies where the real and imaginary components coincide also known as cross over points. The parameters used in measuring the sample and value range are listed in Table 3-3.

Table 3-3 Parameters used for a voltage sweep measurement cycle

Parameter	Description
Voltage ac	Set sweep ac voltage range from 0.05 V and 1.0 V
Frequency	A fixed frequency, selected from features observed in the fixed ac voltage, frequency sweep spectra.
Measurement points per decade	Ranging between 10 and 20 points
Repeat	Voltage sweep cycle is repeated 10 times
Temperature	Room Temp 293 K ± 1 K

The sample was measured beginning at lowest ac voltage and ending at the highest in the selected range. The sample is re-measured 10 times to determine the reproducibility of the characteristic within the ac voltage range selected.

3.5.1.3 Sample Cell Cleaning

Between sample measurements, the dielectric sample cell was dismantled (Figure 3-7) in order to clean all the parts and reduce the risk of any residue contaminating subsequent samples. The used inner cell (Figure 3-7(d)) was discarded and replaced with new Teflon cell for each new sample. The individual cell parts are washed with detergent rinsed thoroughly with deionised water then dried. The platinum electrodes were flamed with a Bunsen burner until they glowed. The electrodes are then cooled before the cell is reassembled.

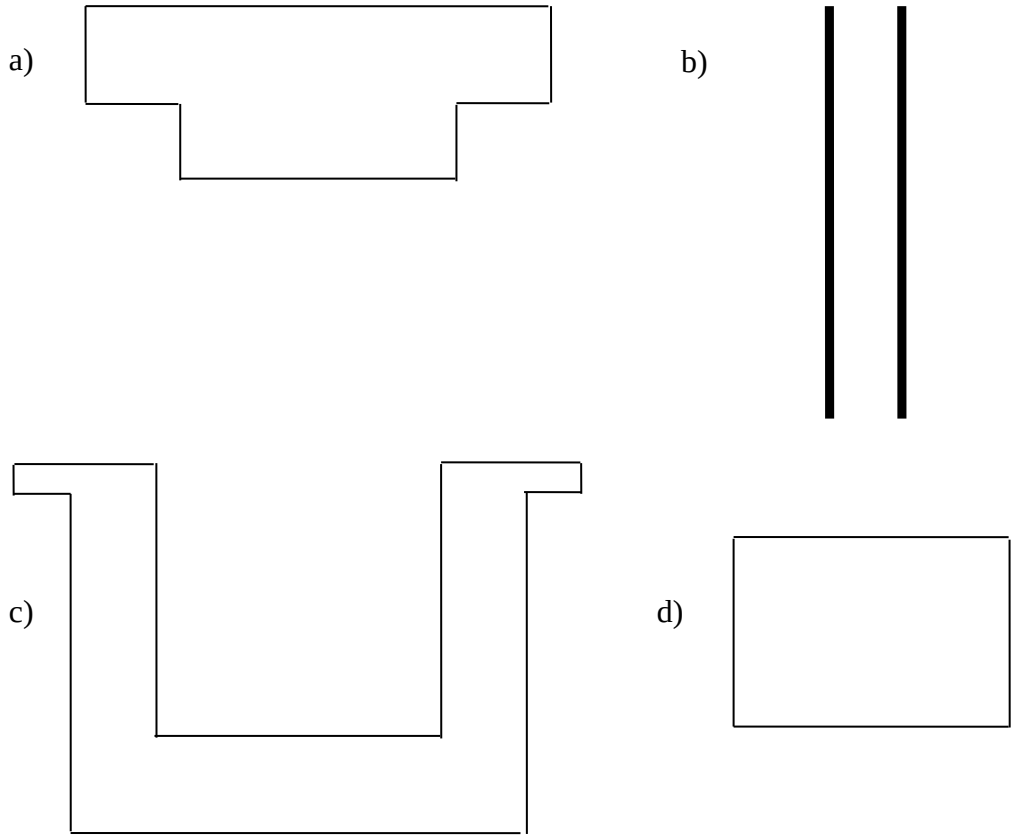

Figure 3-7 Disassembled dielectric small sample cell a) PTFE top, b) platinum electrodes c) outer copper cell, d) inner Teflon cell

The dielectric response of the empty sample holder was measured in order to establish the cell constant for each set of measurements. Measuring and checking the response of the empty cell reduces the chances of subsequent samples being contaminated by residue from a previous sample.

Results & Discussion

Results and Discussion

The reverse micelles and microemulsions reviewed within this study comprise three or four distinct components; oil, water, surfactant and cosurfactant. Different ratios of components were mixed and measured to determine if differences in their response could be observed.

The primary focus of this study was to examine the dielectric properties of the single phase water-in isopropyl myristate oil continuum (water-in-oil, w/o) stabilised by the anionic surfactant, sodium bis(2-ethylhexyl) sulfosuccinate (AOT). All samples were required to be classified as microemulsions which contained reverse micellar or microemulsion aggregates or bicontinuous structures, but excluded liquid crystalline structures.

The results are presented in the following section:

Chapter 4: Microemulsion Phase Behaviour Characterisation and Particle Sizing

Chapter 5: Dielectric Characterisation of Polar, Oil & Surfactant Components

Chapter 6: Dielectric Characterisation of the Surfactant Dispersed in Oil

Chapter 7: Dielectric Characterisation of Ternary Systems

Chapter 4

Microemulsion Phase Behaviour Characterisation and Particle Sizing

4. Microemulsion Phase Behaviour Characterisation and Particle Sizing

4.1 Introduction

The objective of phase behaviour characterisation study was to identify clear single phase non-birefringent samples composed of a range of weight ratios of surfactant, (AOT), oil (IPM), and water which could be used in the dielectric spectroscopy study. Also to identify the phase transition boundary where clear, single phase mixtures transformed to multiphase liquids. The objective of the particle sizing study was to determine if microemulsion aggregates were present in the single phase samples targeted for examination by dielectric spectroscopy.

4.2 Phase Behaviour

Samples comprised of a range of weight ratios of AOT, IPM and water were mixed and the appearance of the resultant mixture was observed over a period one month. The sample appearance was classed as clear single phase **(■)** and cloudy or multiphase (●) liquids and plotted in Figure 4-1.

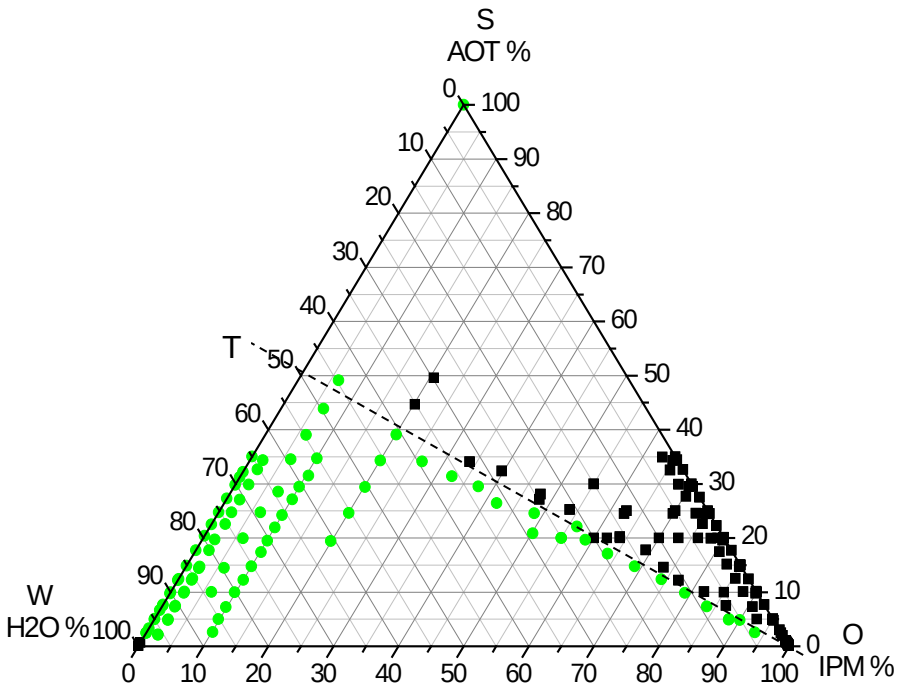

Figure 4-1 Ternary phase diagram for IPM, AOT and H_2O compositions. ■ single phase/clear, ● cloudy or multi-phase appearance, phase transition boundary dashed line T.

Mixtures where the percentage water content was high and greater than that of the oil, although clear became increasingly viscous. Some mixtures which had a cloudy

appearance shortly after mixing became, either clear with a single phase or clear with two discernable phases over several days of observation. The transition between a single phase clear and a cloudy appearance is indicated by the dashed line labelled "T" Figure 4-1, where the percentage weight ratio H_2O/AOT=1.

4.3 Birefringence

The samples were checked for birefringence using plane polarised light and the results showing clear single phase (■) and birefringence (•) liquids were plotted in Figure 4-2. It was noted that for oil dominant compositions where, the percentage weight of AOT w/w was greater than 20% and the weight ratio H_2O/AOT > 1 was just less than 1, birefringence was observed. Where the weight ratio H_2O/AOT was less than one, no birefringence was observed.

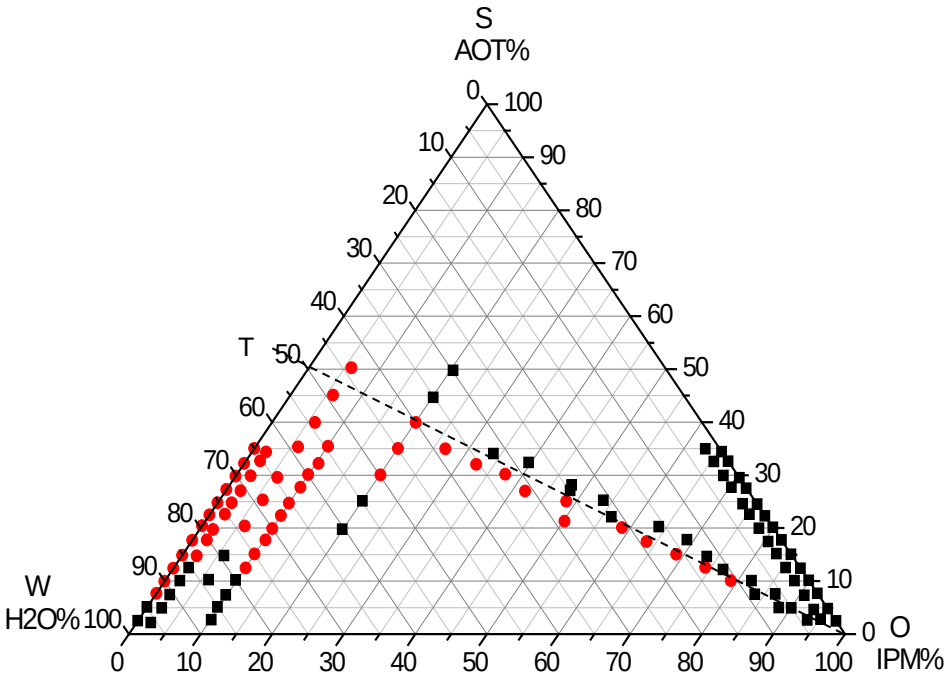

Figure 4-2 Birefringence ternary diagram for IPM, AOT and H_2O compositions. Samples exhibiting birefringence(•) and no birefringence (■)

4.4 AOT, IPM and H2O Samples Selected for Dielectric Study

Using the results of the phase behaviour and birefringence studies, three groups of oil dominant, water-in-oil (w/o) mixtures of AOT, IPM and water samples were selected for low frequency dielectric characterisation. Group 1, anhydrous samples where no water was added to mixtures of AOT and IPM (Table 4-1); group 2, 20 % AOT w/w

samples containing IPM, 20% w/w AOT and water percentage weights ranging between 0<water%<20 (Table 4-2); and group 3, a small group of samples containing a 50% water/surfactant ratio with $W_0 = [H_2O]/[AOT] = 13\pm1$ (Table 4-3).

Table 4-1 Group 1 - Anhydrous reverse micelles (no added water)

	% By weight	Molar ratio	Effective permittivity
Ref	AOT	[AOT]/[IPM]	ε_{eff} IPM=3.4 (IPM=3.2)
D01	0.23	0.0014	3.25 (3.25)
D02	1.01	0.0062	3.27 (3.26)
D03	5.00	0.032	3.33 (3.32)
D04	10.01	0.0677	3.42 (3.40)
D05	15.01	0.1074	3.50 (3.47)
D06	20.00	0.1521	3.58 (3.54)
D07	24.96	0.2023	3.66 (3.61)
D08	*30.13	0.2624	3.75 (3.69)

Table 4-2 Group 2 - Microemulsions containing 20% w/w AOT by weight

	% By weight			Molar ratio			Effective permittivity
Ref	IPM	AOT	H_2O	$\frac{[H_2O]}{[AOT]}$	$\frac{[AOT]}{[IPM]}$	$\frac{[IPM]}{[AOT]}$	ε_{eff} IPM=3.4 (IPM=3.2)
T01	80.00	19.60	0.400	0.4934	0.1521	6.57	3.58 (3.54)
T02	79.07	19.61	1.323	1.6321	0.1540	6.50	4.28 (4.24)
T03	75.96	19.58	4.456	5.5038	0.1600	6.25	6.65 (6.61)
T04	72.94	19.60	7.453	9.1668	0.1668	5.99	8.92 (8.88)
T05	70.00	19.60	10.399	12.8323	0.1738	5.75	11.15 (11.11)
T06	63.97	19.61	16.409	20.2335	0.1903	5.25	15.70 (15.66)
T07	61.82	19.56	18.618	23.0226	0.1964	5.09	17.37 (17.33)
T08	59.99	19.58	20.422	25.2206	0.2027	4.93	18.73 (18.69)

Table 4-3 Group 3 - Microemulsions containing in weight ratio H_2O/AOT ~ 50%

	% By weight			Mol	Molar ratio			Effective permittivity
Ref	IPM	AOT	H_2O	[AOT]	$\frac{[H_2O]}{[AOT]}$	$\frac{[AOT]}{[IPM]}$	$\frac{[IPM]}{[AOT]}$	ε_{eff} IPM=3.4 (IPM=3.2)
T08	62.43	24.98	12.59	0.001965	12.9288	0.2434	4.1076	13.19 (13.14)
T09	69.99	20.00	10.01	0.001575	12.8323	0.1738	5.7534	11.15 (11.11)
T10	92.29	4.99	2.72	0.000393	13.9237	0.0329	30.3872	5.39 (5.38)

The effective dielectric permittivity for each sample mixture, was derived using Equation 4-1 [Cooper and Hill 1996] and is listed in Tables 4-1, 4-2 and 4-3. The permittivity of IPM = 3.4 reported and measured (IPM = 3.2) hence two values for the effective permittivities are estimated. The effective permittivity of water = 78.90 and AOT = 3.2. The effective permittivities of the anhydrous samples listed in Table 4-1 were plotted in Figure 4-3 and show that the change in permittivity is relatively linear.

$$\varepsilon_{eff} = (\varepsilon_{rAOT} * AOT\%) + (\varepsilon_{rIPM} * IPM\%) + (\varepsilon_{rH_2O} * H_2O\%) \qquad \text{Eqn. 4-1}$$

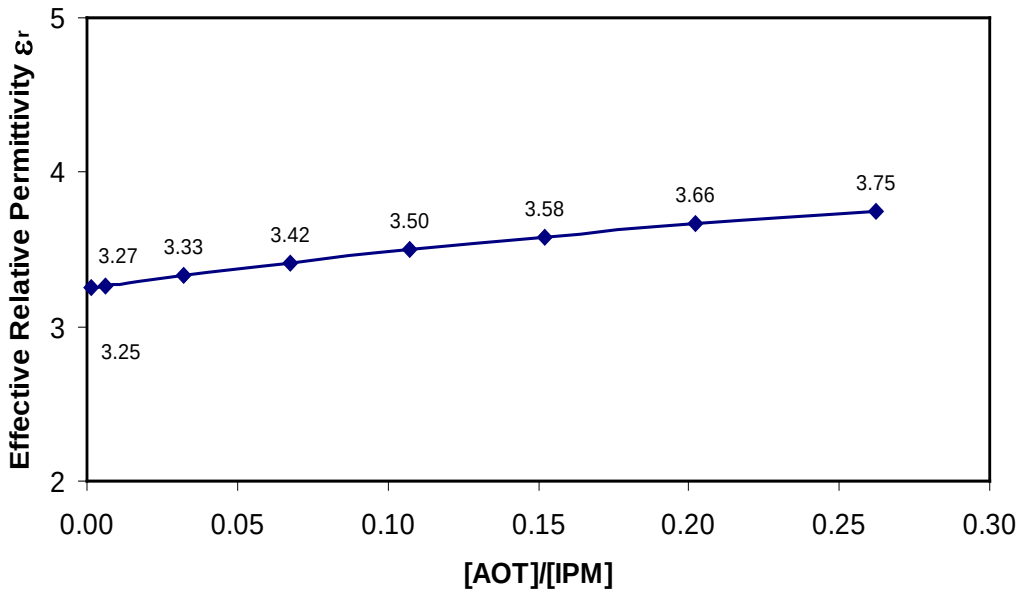

Figure 4-3 Effective permittivity of anhydrous AOT-IPM mixtures

4.5 Particle Sizing

Particle sizing experiments were carried out with Brookhaven Instruments Particle Sizer and the ZetaPlus particle sizing software using a laser of wavelength 677 nm.

The anhydrous samples, D01-D08, listed in Table 4-1 were examined but no particles were detected. The hydrated samples, T01-T08 based on 20% AOT percentage weight listed in Table 4-2 were examined, however no particles were detected in samples where the molar ratio $W_0 = [H_2O]/[AOT] < 10$. Where the molar ratio ranged from $10 < W_0 < 26$, particles with average radii sizes ranging from 12 nm to 29 nm were detected.

Group 2, the 20% w/w AOT samples were examined 1 day, 6 weeks and 3 years after they were originally mixed. The average size and number of the detected particles were reduced for the aged samples and are listed in Table 4-4 plotted in Figure 4-4.

Table 4-4 Particle sizes for AOT- IPM-H2O mixtures measured 1 day, 6 weeks and 3 years after mixing

Percentage ratio	Percentage by weight			Particle size (nm)			Average no of particles (kcps)		
H_2O /AOT	AOT	IPM	H_2O	Days after mixing			Days after mixing		
				1	41	1,075	1	41	1,075
1	20	60	20	28.9	30.3	13.3	75.2	27.6	3.8
0.9	20	62	18	21.4	20.7	17.8	35.0	12.6	9.2
0.8	20	64	16	15.7	15.6	13	4.1	6.1	3.7
0.625	20	67.5	12.5	12.7	10.1		5.9	2.0	
0.5	20	70	10	12	10.2	7.6	3.0	0.9	0.7
0.35	20	73	7	-	-	0	-	-	0

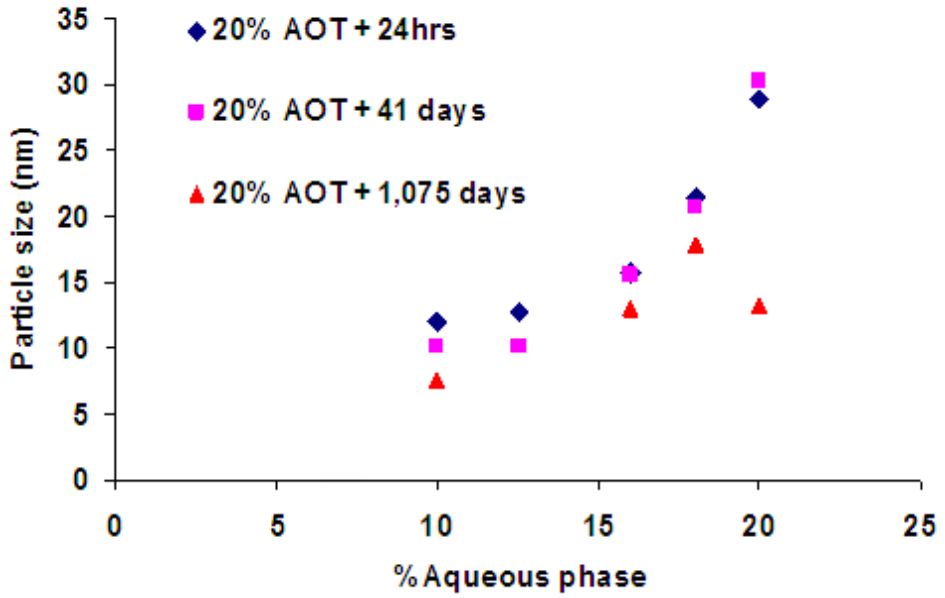

Figure 4-4 Particle sizes for AOT- IPM-H_2O mixtures (20% AOT) Samples measured 1 day, 6 weeks and 3 year after being created

4.6 Discussion

4.6.1 Phase Behaviour Characterisation

The oil dominant (w/o) microemulsions selected for further studies were identified from the phase diagrams Figure 4-1 and Figure 4-2. The single phase liquid samples are found in the region where the percentage weight ratio water/AOT $\leq$ 1 and the percentage weight ratio of AOT < 35%.

4.6.2 Particle Sizing

No particles were observed below W_0 = 10 using the Brookhaven Particle Sizer. However Thompson and Gierasch [1984], using the near infrared (780 nm – 3000 nm) technique reported the presence of tightly bound water in aggregates with low levels of hydration with a small pool of free water increasing in size as the levels of hydration increased to W_0 = 8.3.

The length of the surfactant AOT was reported as 1.2 - 1.5 nm [Zulauf and Eicke 1979] hence there is minimum possible diameter of 3 nm for an anhydrous micelle. However no particles with sizes below 7.6 nm were detected.

4.6.3 Sample Aging

The samples were stored at room temperature 293 K ± 2 K over the 3 year period of the study. The visual appearance of the single phase samples listed in Table 4.2 remained unchanged during the study. As the samples aged, the detectable size and number of particle sizes reduced by 15-20% for $W_0 < 20$ samples at 6 weeks old and reduced by 37% when sample was 3 years old. It should be noted that the stored samples were not agitated prior to particle sizing measurements.

4.7 Further Work

It is recommended that a sample aging study of the changes in both particles sizes and the number of particles detected be conducted over a period.

Chapter 5

Dielectric Characterisation of Individual Polar, Oil & Surfactant Components

5. Dielectric Characterisation of Polar, Oil & Surfactant Components

5.1 Introduction

The dielectric polarisation and relaxation process are able to characterise the individual elements within a mixture as well as interfaces between the components. For many dielectric materials, several characteristic relaxation processes respond at similar frequencies when subjected to an ac field. This overlapping of responses may result in some features being masked or be barely discernable on plots of the response data. It is there for necessary that spectrums are obtained for the individual base components in order for multi-component micellar or microemulsion sample responses to be analysed.

The objectives of the following investigations are to characterise the response spectra for individual components to be used in reverse micellar and microemulsion studies. Then to determine if the responses of the more complex binary and ternary systems can be predicted from the response of the individual components, together with knowledge of the structure of the dispersed and continuous phases of microemulsions.

5.2 Characterisation of the Polar Components Water and Propylene Glycol (PG)

The frequency dependant response characteristic of water and PG were measured with fixed voltages in the range 0.05 V through to 1.00 V (Figure 5-1 and Figure 5-2). The magnitude of the bulk response was found to be sensitive to variations in electrode separation, but insensitive to the magnitude of the applied voltage. The electrode area/separation ratio was set to $A/d = 7.07 \times 10^{-03} \pm 0.71 \times 10^{-03}$ m for related results reported in Table 5-1. The magnitude of the bulk capacitance and conductance response of the polar components are the largest of all the components measured. PG, $\varepsilon_r = 32$, was chosen as an alternative to water as the relative permittivity is less than that of water $\varepsilon_r = 80$ and magnitude of the dielectric response expected to be well within the limits of the equipment used in the present study.

Table 5-1 Dielectric properties of the individual components

Property		IPM	EC	Soya Oil	Castor Oil	AOT	E200	Brij 97	PG	H_2O	H_2O reverse sweep	AOT: 20 IPM: 60 H_2O: 20	E200:30 IPM: 40 H_2O: 30
Effective permittivity		3.25	-	-	4.5	3.2	5	-	32	78.9	78.9	18.41	26.47
Capacitance Cbulk	(pF)	1.32	1.49	1.39	1.71	1.37	1.26	2.45	9.9	11.8	11.8	3.68	5.88
Conductance Gbulk	(pS)	1.79	29	0.853	1.32	316	101	1.06E6	1.18E6	2.38E6	1.55E6	5.96E5	6.86E5
Intracluster Frequ. ω	(Rad/s)	1.12	15.6	0.628	0.873	250	156	4.33E5	1.12E5	1.99E5	9.96E4	1.58E5	1.12E5
Intracluster Relaxation time τ_1	(s)	0.89	0.064	1.59	1.15	4.00E-3	6.43E-3	2.31E-6	8.93E-6	5.03E-6	1.00E-5	6.33E-6	8.93E-6
Maxwell-Wagner $\omega^{-(2-n)}$		-	-	-	-	1.5	1.3	1.68	1.59	1.72	1.68	1.78	1.69
Index n		-	-	-	-	0.5	0.7	0.32	0.41	0.28	0.32	0.22	0.31
Interface charging Frequency ω	(mRad/s)	-	-	-	-	0.02	0.2	4.24E-2	95	56.4	35	62.8	62.8
Interface charging Relaxation time τ_3	(s)	-	-	-	-	5.00E4	5.00E+3	23.58	10.5	17.7	28.6	15.9	15.9
Capacitance Cbarrier	(μF)	-	-	-	-	15.8	0.505	25	12.4	42.2	44.3	9.49	10.9
Dielectric Increment Cbulk/ Cbarrier		-	-	-	-	8.67E-8	2.50E-6	9.80E-8	7.97E-7	2.79E-7	2.66E-7	3.88E-7	5.38E-7
Intermediate dispersion index		-	-	-	-	0.45	-	0.50	-	-	-	-	-

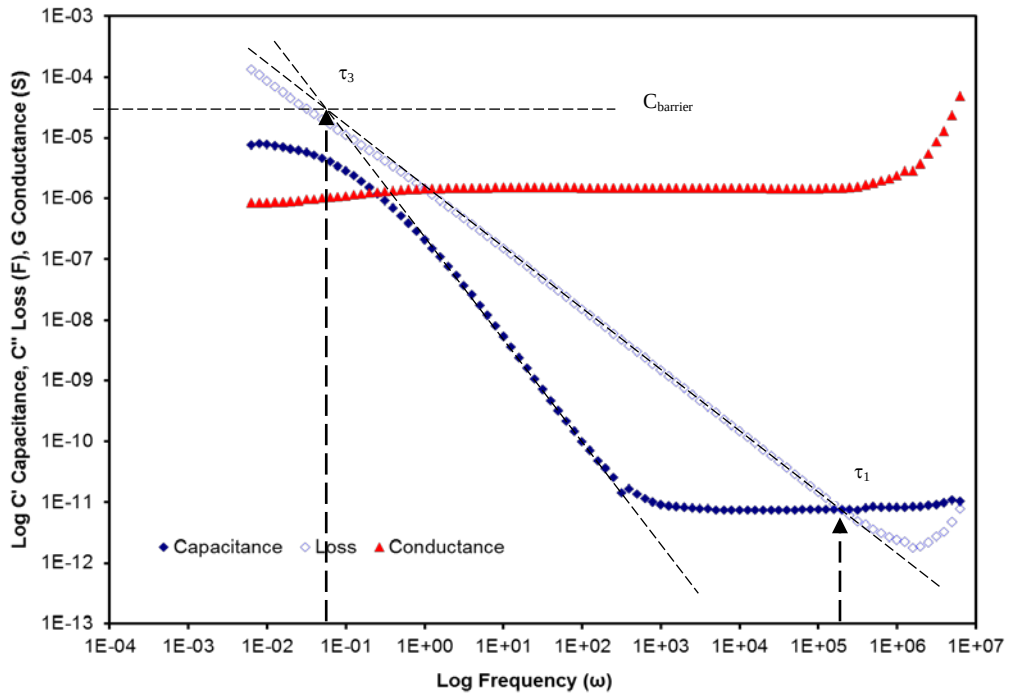

Figure 5-1 Dielectric response of deionised water showing the intracluster, Maxwell-Wagner interface charging and barrier processes. Capacitance ♦, loss ◊ and conductance ▲

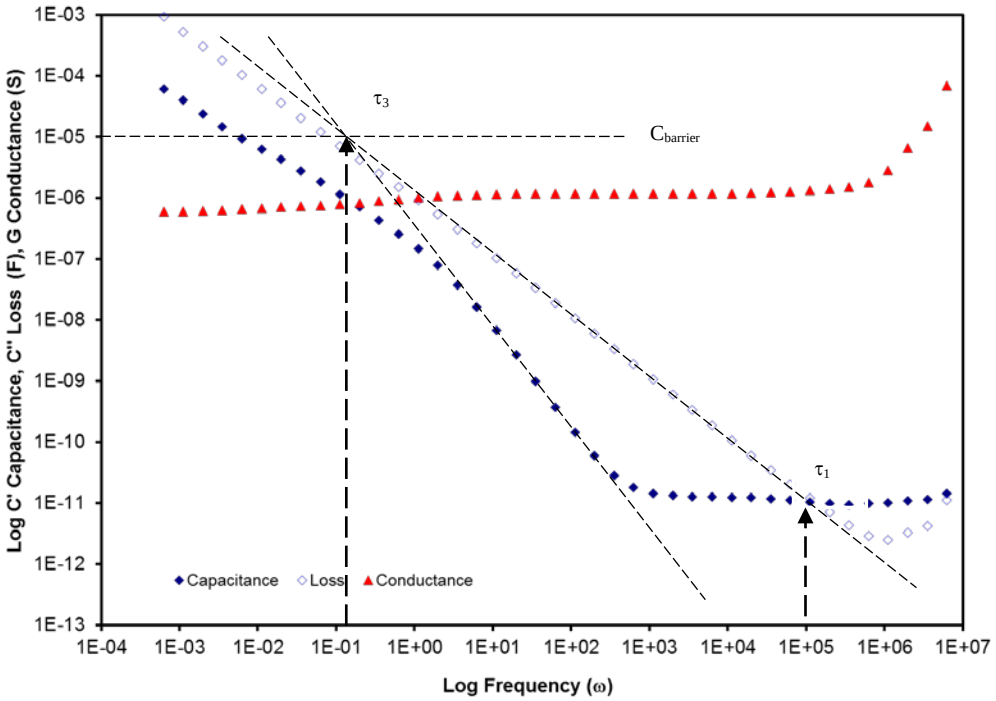

Figure 5-2 Dielectric response of PG showing the intracluster, Maxwell-Wagner interface charging, barrier and quasi-dc processes below $\omega<10^{-1}$ Rad/s. Capacitance ♦, loss ◊ and conductance ▲

5.2.1.1 Intracluster Relaxation

The crossover of the loss and capacitance responses in the frequency range $10^{+5} < \omega$ 10^{+6} yields the characteristic relaxation time of τ_1 for the cluster bound charge hopping process, which was found to be of the order of 5-10 μs for water (Figure 5-1) and 9 μs for propylene glycol (PG) (Figure 5-2).

$$\tau_1 = (\omega_1)^{-1} = \left(\frac{1}{R_{bulk}C_{bulk}}\right) = \left(\frac{G_{bulk}}{C_{bulk}}\right)^{-1} = \left(\frac{\sigma A/d}{\varepsilon_r A/d}\right)^{-1} = \left(\frac{\sigma}{\varepsilon_r}\right)^{-1} \qquad \text{Eqn. 5-1}$$

Where τ_1 is given by Equation 5-1 and is a parallel resistor-capacitor (R_{bulk}-C_{bulk}) circuit composed of the conductance of the bulk continuous phase in parallel with the capacitance of the bulk phase.

This time constant, τ_1, provides information on both the microscopic and macroscopic processes as the magnitude of both the conductance and the capacitance are a sum of all the conductivities,σ and relative permittivities, ε_r, of the particles that make up the bulk.

5.2.1.2 Maxwell-Wagner Interface Charging Relaxation

As the frequency of the applied electric field is reduced ($\omega \rightarrow 0$), in the frequency range $10^{-1} < \omega < 10^{+3}$, the capacitance exhibits a large dispersion as the magnitude increase from a constant bulk value at high frequencies to constant barrier capacitance at lower frequencies. Simultaneously, the gradient of the loss component of the complex capacitance remains constant until the bulk conductance begins to decrease with the onset of the formation of a barrier layer. This process is associated with the Maxwell-Wagner barrier charging process. The gradient $\omega^{-(2-n)}$ of the dispersing capacitance was -1.72 and -1.59 ± 0.02 for water and PG, respectively. The value of the index n, the efficiency of charge transport [Hill 2001], was found to be n = 0.28 ± 0.02 for water and n = 0.41 ± 0.02 for PG.

The magnitude of the water and PG barrier response was approximately 6-7 orders of magnitude greater that that bulk, indicating that the barrier layer is 10^{-6} times thinner than the electrode spacing. As both water and PG samples are homogenous, the barrier thickness can be estimated. Taking the average electrode spacing to be 4.5 mm ± 0.5 mm and using the relationship Eqn 5-2 for a homogeneous material results in a barrier thickness of 12.5 Å ± 1.5 Å for water and 36.0 Å ± 4.0 Å for PG can be determined.

The estimated diameter of a liquid water molecule in a cluster at room temperature is 2.85 Å [Ludwig 2001] which gives a barrier layer for water comprised of 4 to 5 water molecules.

$$\left(\frac{C_{bulk}}{C_{bar}}\right)=\left(\frac{\varepsilon_{bulk}\varepsilon_0 A/d_{bulk}}{\varepsilon_{effbar}\varepsilon_0 A/d_{bar}}\right)=\left(\frac{d_{bar}*\varepsilon_{bulk}}{d_{bulk}*\varepsilon_{effbar}}\right)\rightarrow d_{bar}=d_{bulk}*\left(\frac{C_{bulk}}{C_{bar}}\right)*\left(\frac{\varepsilon_{effbar}}{\varepsilon_{bulk}}\right) \quad \text{Eqn. 5-2}$$

The characteristic relaxation time for the interface charging process, τ_3, is given by Equation 5-3 and is a series resistor capacitor circuit composed of, the conductance of the bulk or continuous phase material in series with the capacitance of an interface between two clusters of molecules. τ_3 for water and PG were found to be approximately 18 s and 11 s respectively.

$$\tau_3=(\omega_3)^{-1}=\left(\frac{G_{bulk}}{C_{bar}}\right)^{-1} \quad \text{Eqn. 5-3}$$

5.2.1.3 Intercluster Relaxation

PG exhibited quasi-dc characteristics at the lowest frequencies $\omega < 10^{-1}$ where the gradient of the loss component was close to unity but less than unity. The dispersion of water contains a well developed barrier. The development of the quasi-dc dispersion in the barrier capacitance is not visible in the measured frequency range. However using the universal lossy capacitor model [Jonscher 1983] an estimate for the values of the gradient $\omega^{-(p)}$ index is p =0.72 ± 0.02.

The magnitude of the barrier capacitance of PG is determined from the extrapolated crossover of C'/C" at $\tau_3 = 1/\omega_3$ but the barrier conductance G_{bar} is not easily discerned from the plot but a low frequency gradient of the q-dc dispersion in the capacitance was estimated to be 0.80 ± 0.02.

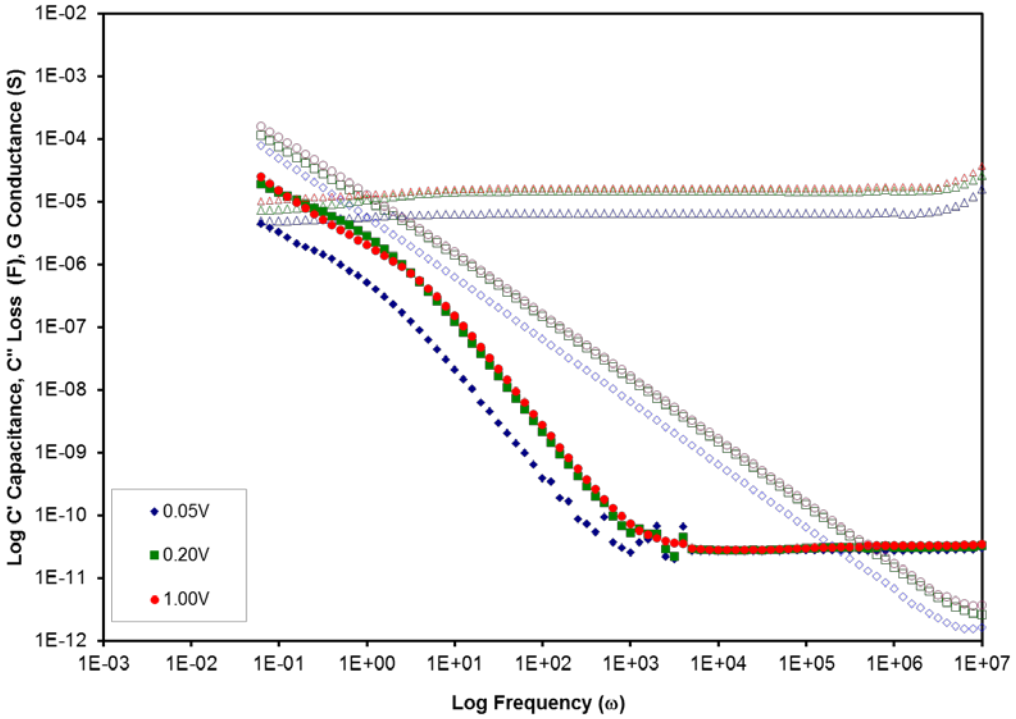

Figure 5-3 Dielectric response of PG for applied ac voltage range 0.05 V, 0.20 V and 1.00 V measured in the large sample cell. Capacitance ♦, ■, ●, loss ◊, □, ○ and conductance Δ, Δ, Δ.

5.2.1.4 Impact of Voltage Variation

For PG, the magnitude of the bulk capacitance in the frequency range above $x10^{+3}$ Hz is relatively insensitive to the magnitude of the applied ac voltage. The magnitude of the conductance exhibits a marked increase when the applied voltage was increased from 0.05 V to 0.20 V (Figure 5-3). A comparison of the equivalent energy stored and lost by the capacitance and loss components shows that changes to the magnitude of the capacitance is directly proportional to the applied voltage, whilst the energy loss is variable (Figure 5-4). The shape and magnitude of the capacitance displays significant differences at lower frequencies. This is due to the development of the Maxwell-Wagner interface barrier layer (Figure 5-3 and Table 5-1). The greater the magnitude of the applied voltage, the larger the local field $E = V/d_{barrier}$ is on the relatively thin barrier layer $d_{barrier}$. The barrier blocks or reduces the flow of charges hence above a given threshold the conductance is driven by the magnitude of the applied voltage.

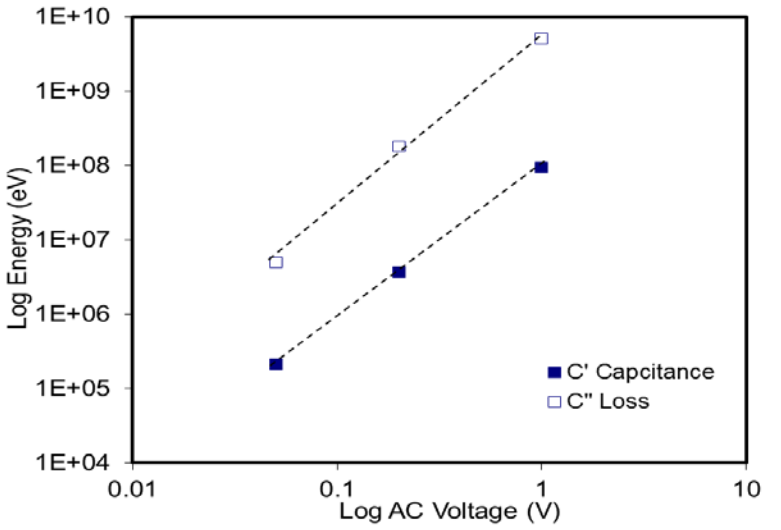

Figure 5-4 Rate of change of energy stored and lost for PG as the applied ac voltage is increased from 0.05 V to, 0.20 V and to 1.00 V. Values extracted for frequency $\omega = 10^{+4}$

Table 5-2 Capacitance and loss properties of PG as the voltage is increased from 0.05 V to 1.00 V

Properties		AC Voltage (V)		
		0.05	0.20	1.00
Bulk Capacitance	(pF)	27.2	29.3	29.9
Bulk Conductance (at ω=1E4 Rad/s)	(μS)	6.43	14.6	16.4
Intracluster Characteristic Frequency ω	(MRad/s)	0.236	0.498	0.548
Intracluster Relaxation time τ_1	(μs)	4.23	2.01	1.82
Maxwell-Wagner Gradient $\omega^{-(2-n)}$		1.67	1.61	1.72
Interface Charging Characteristic	ω	0.071	0.356	0.448
Frequency	(Rad/s)			
Interface Charging Characteristic Time	τ (s)	1.4.1	2.81	2.23
Barrier Capacitance	(μF)	90.6	41.1	36.6
Dielectric Increment C_{bulk} /C_{bar}	(μ)	0.300	0.713	0.816
Barrier thickness	Å	15.01	35.67	40.79
Stored Energy $(CV^2)/2$	(MeV)	0.212	3.66	93.3
Conductance energy $(GV^2)/2$	(MeV)	5.02	182	5,120

5.3 Characterisation of the Surfactant Components, AOT Sodium bis(2-ethylhexyl) sulfosuccinate, E200 Epikuron 200 and Brij 97

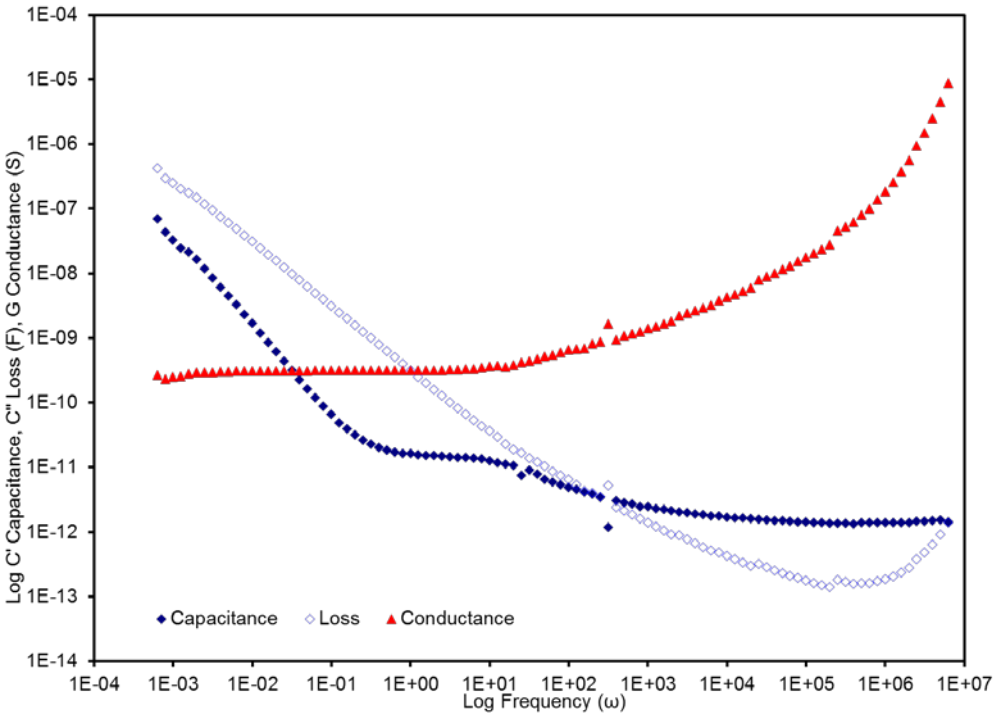

Figure 5-5 Dielectric response of sodium bis(2-ethylhexyl) sulfosuccinate (AOT).

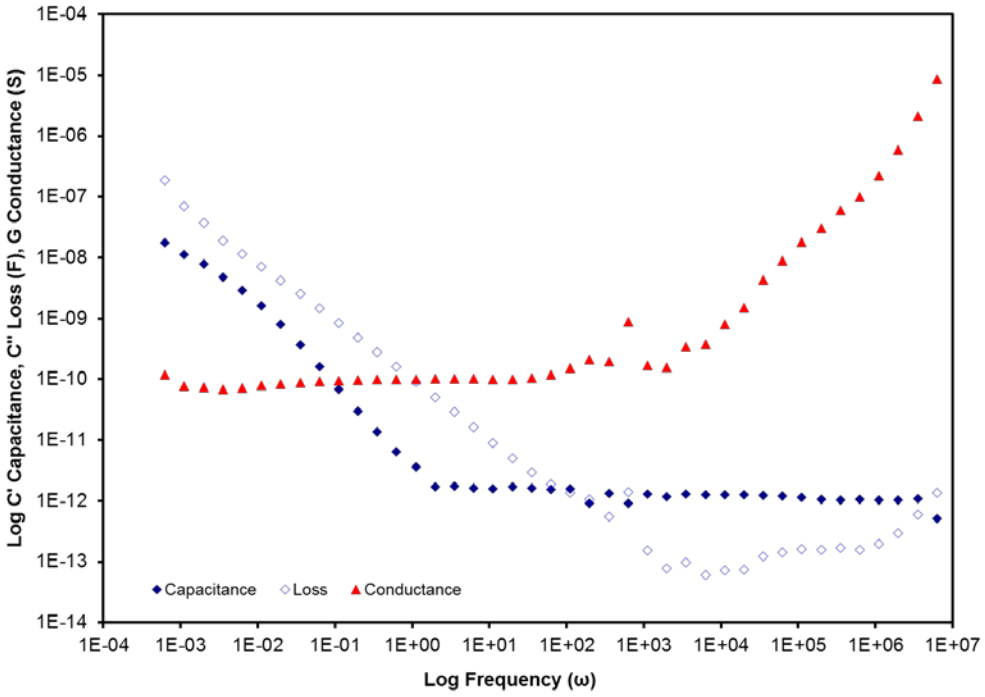

Figure 5-6 Dielectric response of Epikuron 200 (E200), measured after being stored in the measuring cell at 293 K for 24 hours.

Both AOT and E200 surfactants are solid at room temperature (293 K ± 1 K). E200 was stored in a domestic freezer prior to use hence measurements were taken after sample have been kept at room temperature for 24 hours. The characteristic responses for AOT and E200 are displayed in Figure 5-5, Figure 5-6 and bulk, Maxwell-Wagner and barrier, characteristics catalogued in Table 5-1.

5.3.1.1 Intracluster Polarisation and Characteristic Relaxation

The crossover of the loss and capacitance in the frequency range $10^{+1} < \omega < 10^{+3}$ yields the relaxation time of the cluster bound charge hopping process and was found to be of the order of 4 ms for AOT and 6.5 ms for E200. AOT is an anionic surfactant whose small counterion Na^+ is readily able to dissociate from the surfactant head group. It is reasonable to assume that the counterion is able more able to migrate through a cluster of AOT molecules hence contribute more to the polarisation response at higher frequencies than the zwitterionic, E200.

As the frequency ω of the electric field is reduced to zero, the capacitance of both surfactants exhibit large dispersions in the capacitance. AOT (Figure 5-5) also exhibited an intermediate dispersion of the capacitance in the frequency range $10^{+1} < \omega < 10^{+2}$ above the Maxwell-Wagner dispersion which begins below $\omega = 10^{-1}$ but below the intracluster polarisation processes. The gradients of the capacitance and loss associated to the intermediate process were 0.45 and 0.66 respectively, whist the magnitude of the capacitance plateau was 14.4 1pF. E200 did not exhibit a similar intermediate dispersion in the capacitance as the frequency ω was decreased below the cross over frequency when compared to the dispersion of AOT.

5.3.1.2 Maxwell-Wagner Interface Charging Relaxation

The Maxwell-Wagner gradient, $\omega^{-(2-n)}$, of the dispersing capacitance was found to be 1.50 ± 0.02, n = 0.50 for AOT which corresponds to that of one undergoing a diffusive process in the barrier region [Jonscher 1983]. The estimate obtained for the thickness of AOT barrier layer was 3.9 ± 0.4 Å, which is equivalent to the diameter of one sodium atom [Kaye & Laby 1995]. It is assumed that the sodium counter ions have dissociated from the surfactant head group and have diffused through the solid sample in a relaxation time of 50 Ks (approximately 14 hours).

The gradient of the dispersing capacitance of E200 was found to be $\omega^{-(2-n)} = 1.30 \pm 0.02$ resulting in the index n = 0.7 indicating that the E200 barrier layer was highly structured [Hill 2001]. The barrier layer thickness was estimated at 112 Å ± 12 Å.

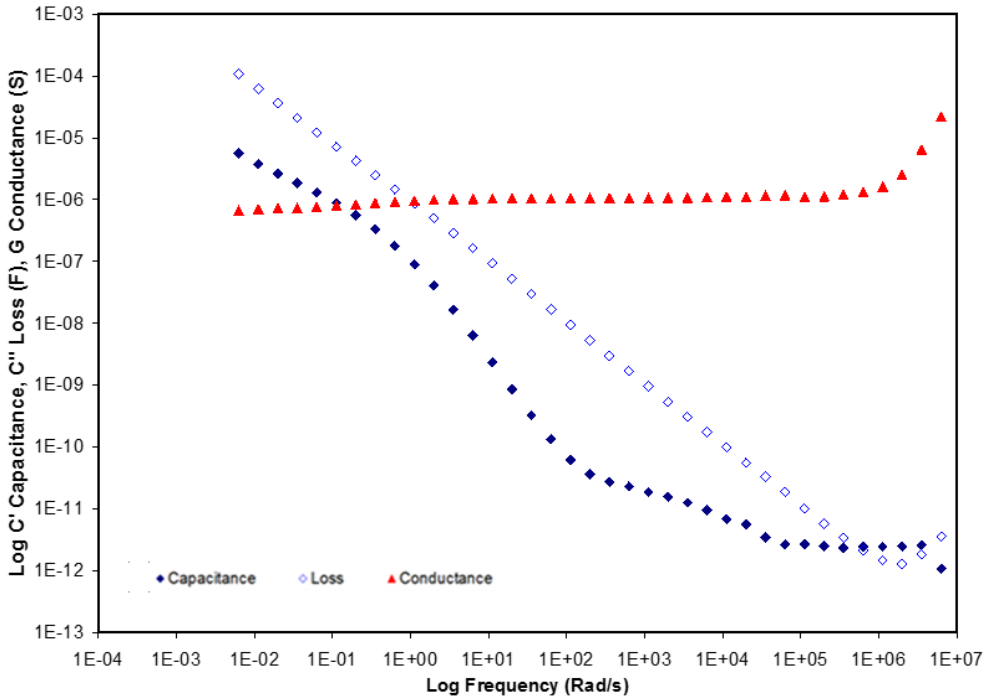

Figure 5-7 Dielectric response of Brij 97 3 days after solidifying and cooling to 293 K and repeated measurements.

The response of Brij 97 (Figure 5-7) has been included as an example of a non-ionic single tailed surfactant. The Brij 97 response displays intracluster τ_1=2.3 μs, Maxwell-Wagner interface charging index $\omega^{-(2-n)}$, (2-n) = 1.62, and an interface charging relaxation time τ_3=23 s. There is also evidence of a quasi-dc intercluster charge transport with index p estimated to be 0.65. The sample also exhibits an intermediate dispersion of the capacitance between the intracluster and Maxwell-Wagner interface charging processes with a gradient equal to 0.5.

5.4 Characterisation of the Non polar Components, IPM, Ethyl Caprylate, Caster and Soya Oil

5.4.1 Isopropyl Myristate (IPM)

Isopropyl Myristate is the main oil used to in the production of reverse micelles and microemulsions in this study.

The frequency dependant response characteristic of IPM was measured with fixed ac voltages in the range 0.05 V through to 1.00 V. However the responses were generally noisy when the applied ac voltage was less than 0.20 V. The magnitude and shape of the response was sensitive to the spacing of the electrode (Figure 5-8 and Figure 5-9) where the capacitance became negative at the lowest frequencies for wider electrode separations. The response of the samples were relatively insensitive to changes to the magnitude of the applied voltage above 0.20 V ac in the bulk frequency region above the crossover of the loss and capacitance ($\omega > 1$). It can also be seen from Figure 5-8 and Figure 5-9 that IPM is weakly conducting of the order of 10^{-12} S at low frequencies, and the onset frequency and magnitude of the conductance is dependent upon the geometry of the measuring cell.

An inspection of the capacitance dispersion below the cross over frequency, shows a decrease in magnitude whilst the magnitude of the conductance shows a small but anomalous increase in magnitude as the frequency $\omega \rightarrow 0$. The IPM sample was replaced with fresh samples from the same batch and two alternative batches, but the anomalous low frequency dispersion still occurred. Varying the electrode separation between 3 mm and 6 mm generated negative capacitances and a small increase in conductance as the electrode separation increases (Figure 5-10 to Figure 5-13). The occurrence of the negative capacitance is unusual and was unexpected. An increase in conductivity is usually a sign of a structural transition or onset of percolation. The frequency at which the magnitude of the capacitance was the lowest and the increase in conductance for a range of electrode separations are detailed in Table 5-3.

Table 5-3 Variation in magnitude of the anomalous capacitance and conductance of IPM as the electrode spacing is increased

Properties		Electrode spacing d (mm) ± 0.5 (mm)				
		3.15	4.37	5.67	5.96	2.00[1]
Capacitance bulk	(pF)	1.35	0.975	0.750	0.714	2.48
Conductance $G\infty$	(pS)	1.62	1.43	0.19	0.106	3.94
Conductance G_0	(pS)	1.79	1.73	0.429	0.193	6.46
$G_0/G\infty$		1.10	1.21	2.26	1.82	1.64
$\sigma_\infty=G_\infty d/A$	(nS/m)	0.153	0.187	0.032	0.019	0.100
$\sigma_0=G_0 d/A$	(nS/m)	0.169	0.226	0.073	0.034	0.165
Capacitance lowest magnitude	(pF)	0.792	0.3.03	-2.46	-2.96	1.90
Frequency at lowest Capacitance Magnitude	(ω)	0.112	0.0628	6.28E-3	9.96E-3	3.15E+2
Intracluster Relaxation time	(s)	0.83	0.68	3.95	6.74	0.46
Electric Field/Spacing E/d	(V/m)	317.46	228.99	176.24	167.79	100
Loss gradient		0.96	1.00	1.18	1.14	0.978
Frequency barrier charging begins	(ω)	19.8	11.7	0.20	1.98	79.1
Frequency constant conductance begins	(ω)	0.117	0.117	6.28E-3	1.98E-2	0.791

[1] The large sample cell Area=7.85E-05 m^2 was used in obtaining this response for comparison

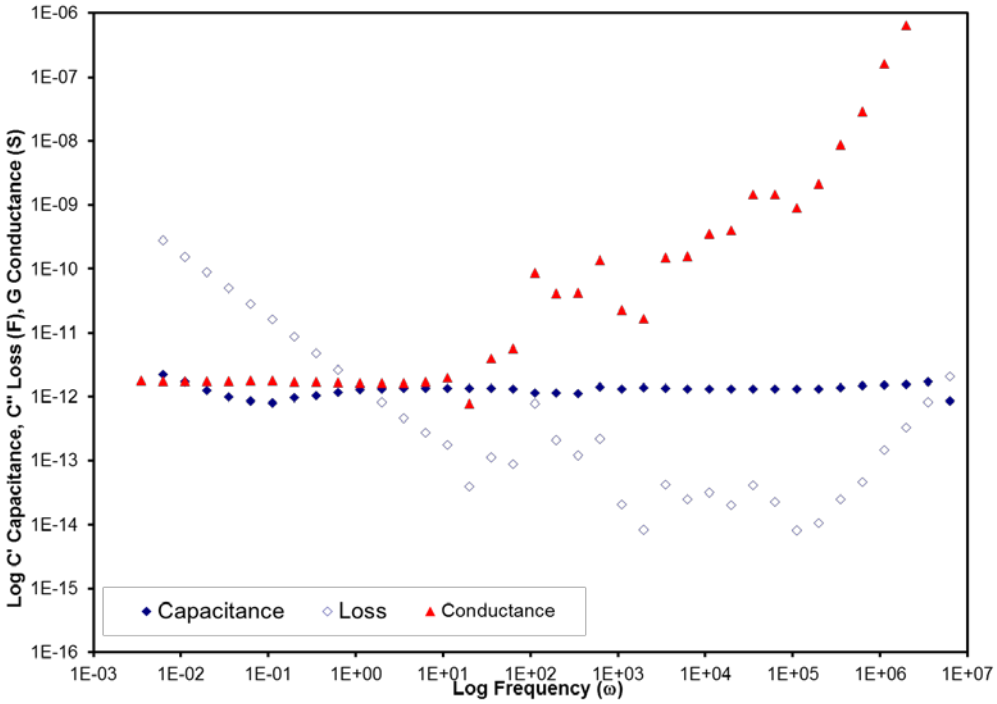

Figure 5-8 Dielectric response of IPM for electrode spacing ~3 mm.

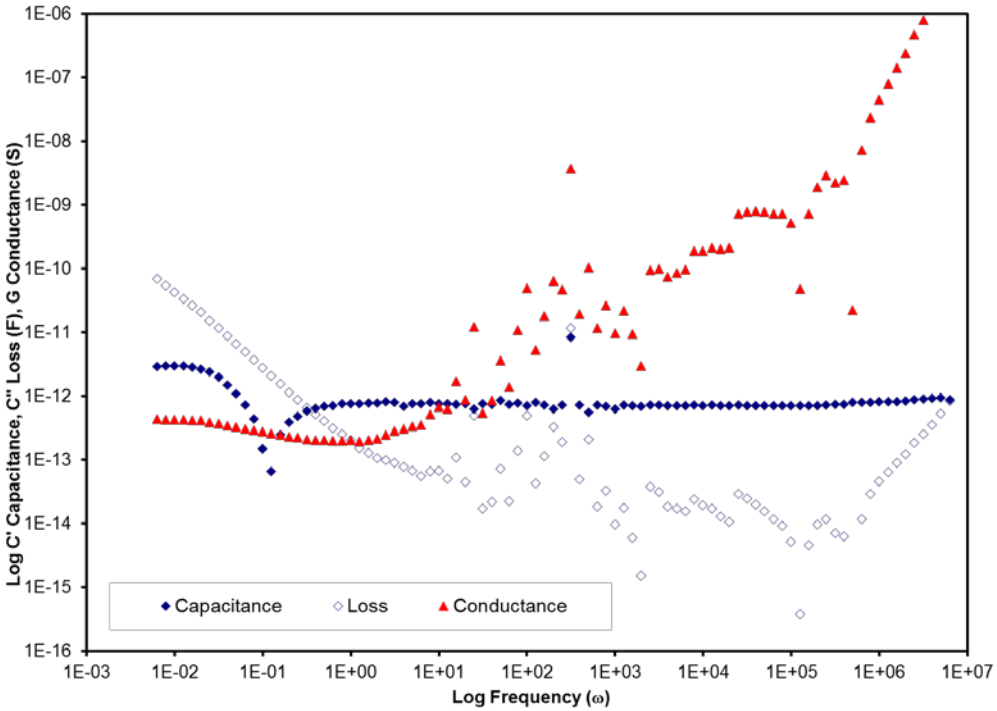

Figure 5-9 Dielectric response of IPM for electrode spacing ~6 mm.

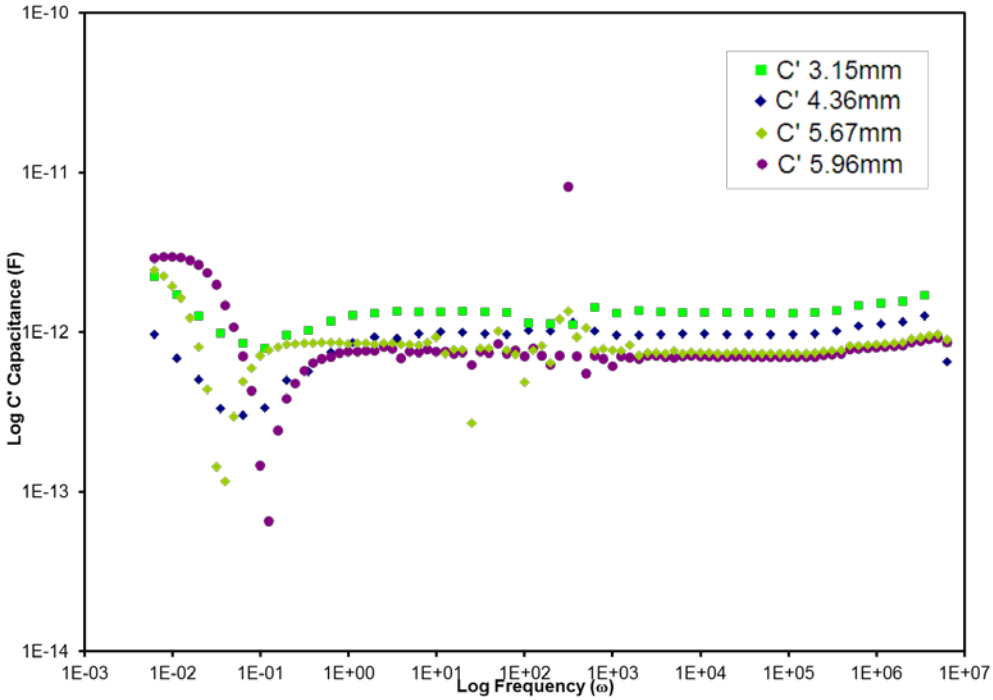

Figure 5-10 Capacitance response of IPM with electrode spacing ranging from 3 to 6 mm. The capacitance becomes negative for electrode spacing greater than 5 mm in the frequency range less than ω=1

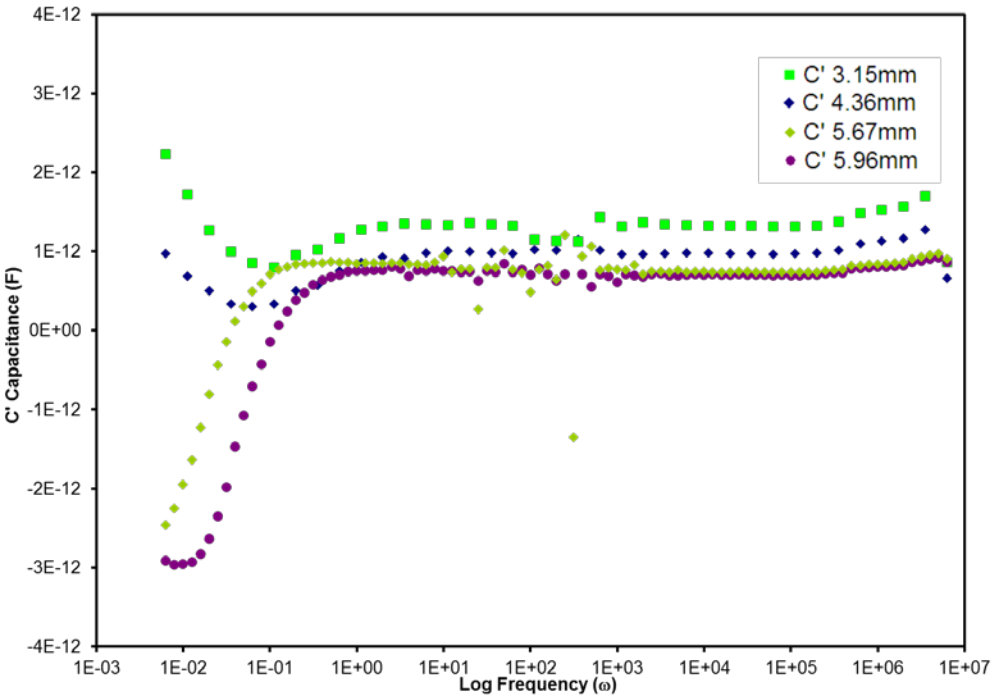

Figure 5-11 Negative capacitance of IPM re- plotted on a lin/log scale measured for with electrode spacing ranging from 3 to 6 mm

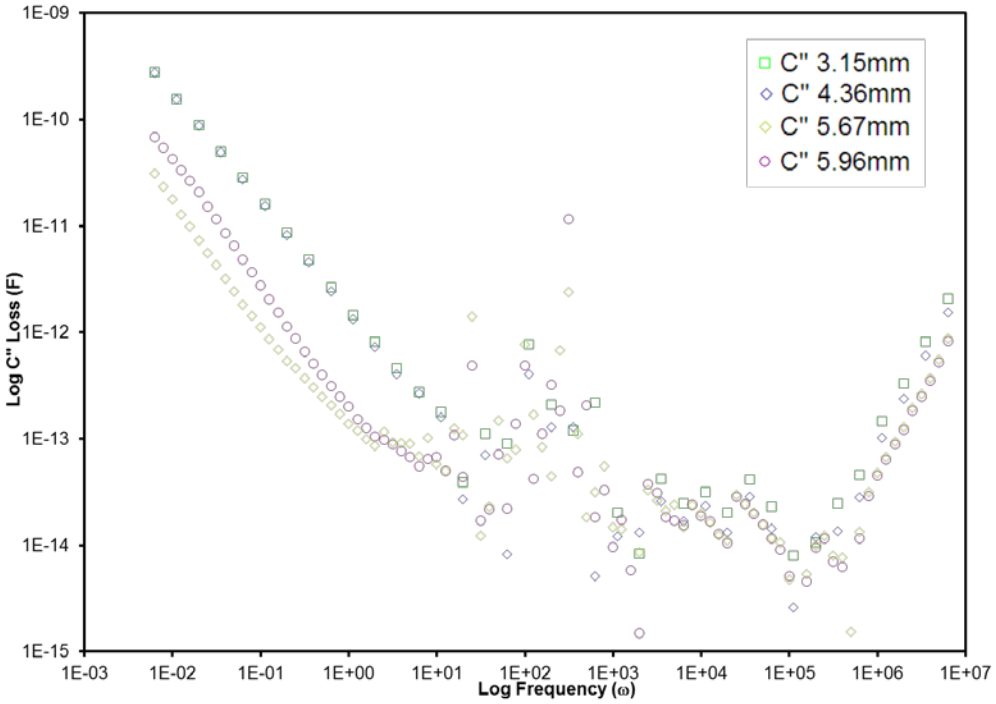

Figure 5-12 Loss response of IPM with electrode spacing ranging from 3 to 6 mm

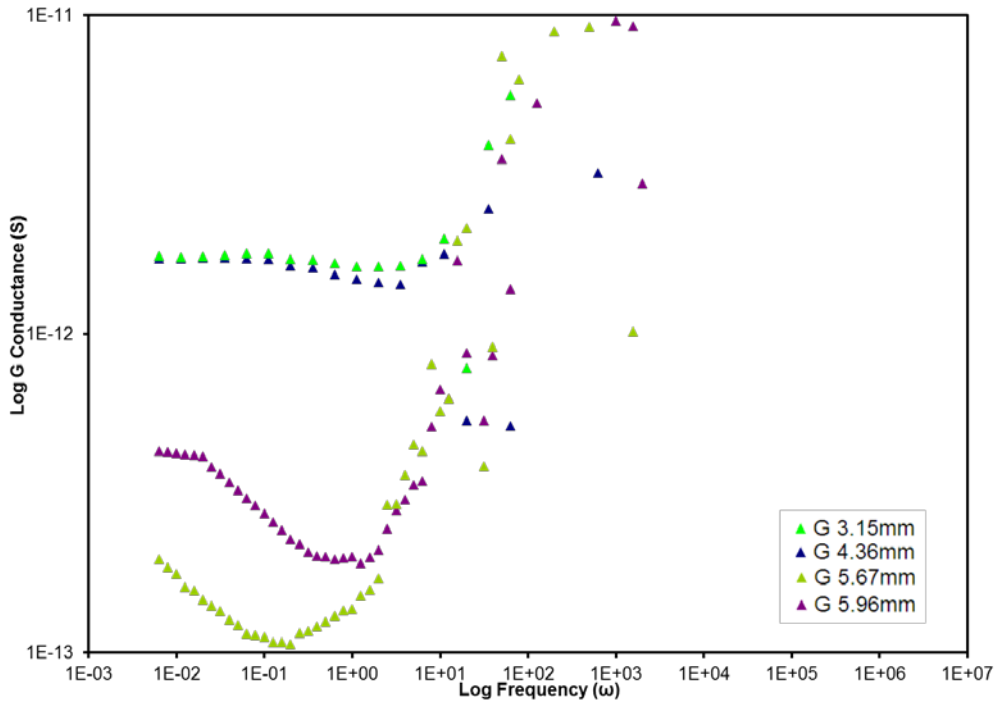

Figure 5-13 Conductance of IPM measured with electrode spacing ranging from 3 to 6 mm. All electrode spacing exhibit an increase in the magnitude of the conductance at frequencies $\omega < 1$

In order to verify whether the anomalous conductance and capacitance features were due to the sample and not an artefact of the measuring equipment, a fresh sample was measured using the large sample holder and Solartron 1296 dielectric interface described in section 3. Although negative capacitance values were eliminated, the magnitude of the conductance still experienced a small increase at frequencies below the crossover of the loss and capacitance (Figure 5-14).

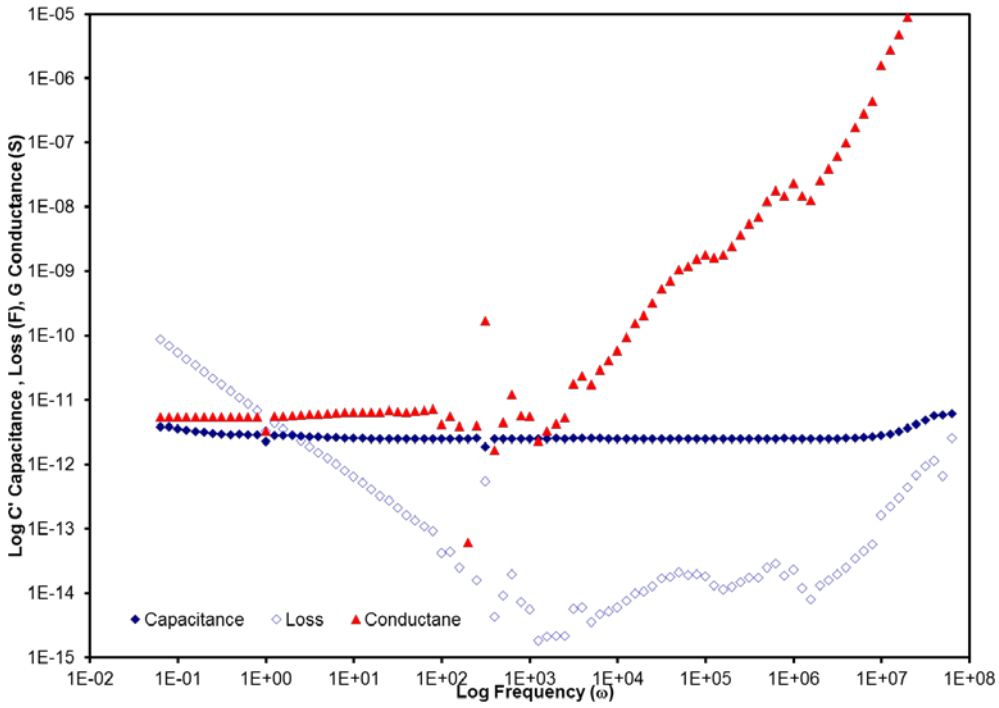

Figure 5-14 Response of IPM measured with the 1296 dielectric interface and large sample cell.

It can be seen in Figure 5-15 that there is a linear relationship between the bulk capacitance and the reciprocal of the electrode spacing. Hence if the electrode spacing "d" is increased the bulk capacitance is expected to decrease, or if the electrode spacing decreases, the bulk capacitance increases. Due to the flexibility of the wire electrodes (Figure 3-4) it was not possible to be certain electrode spacing measured before the sample cell was closed, stayed the same once the sample cell was sealed. Hence the linear relationship plotted in Figure 5-15 makes it reasonable to normalise the bulk responses of each component by applying a multiplier or divisor. This linear relationship did not extend to the low frequency conductance characteristics (Figure 5-16).

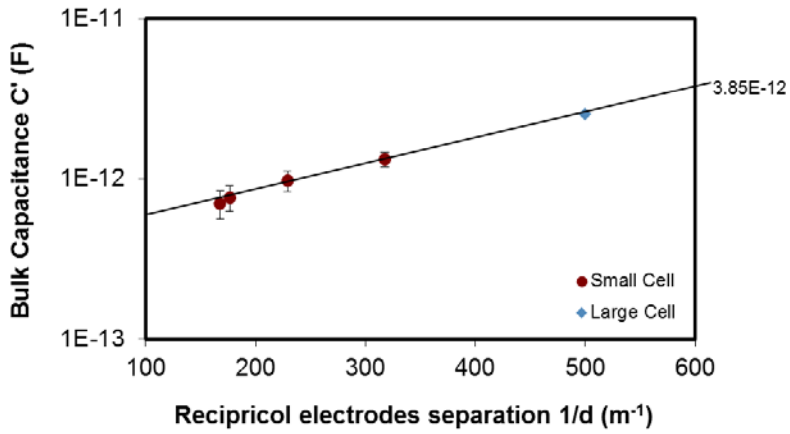

Figure 5-15 Log/lin Bulk capacitance verse the reciprocal of the electrode spacing for IPM oil.

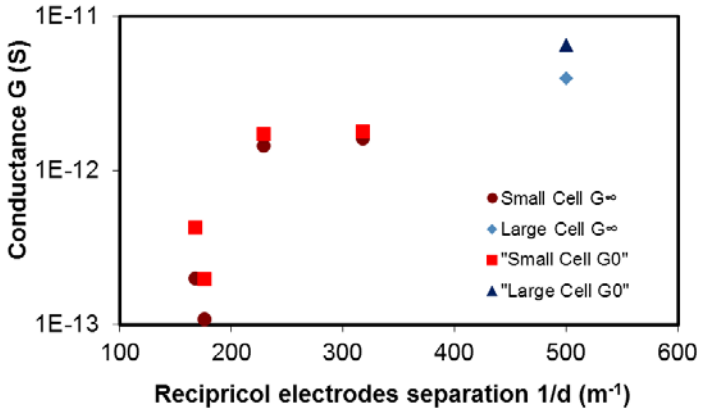

Figure 5-16 Log/lin plot of low frequency conductance verse the reciprocal of the electrode spacing for IPM oil.

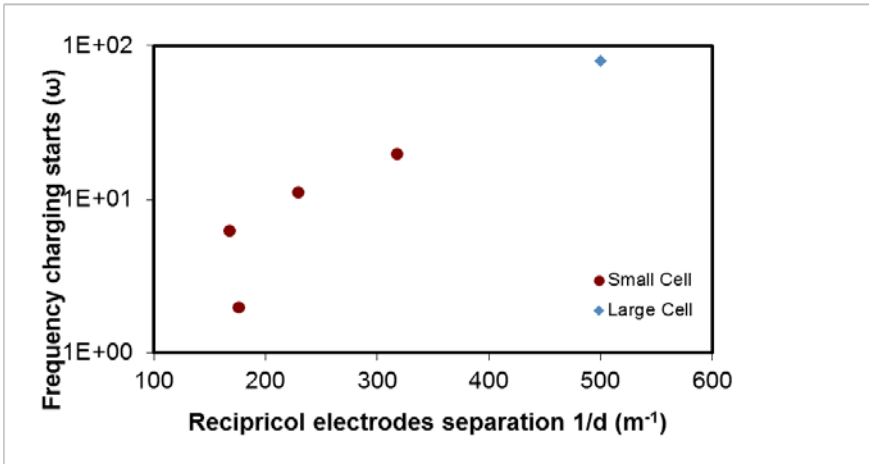

Figure 5-17 Log/lin plot of frequency at which the barrier charging begins verse the reciprocal of the electrode spacing for IPM oil.

5.4.1.1 Intracluster Relaxation

The crossing of the loss and capacitance in the frequency range 10^{-01} Hz < ω < 1 Hz yields the characteristic relaxation time of the cluster bound charge hopping process and was found to be of the range of 0.46 to 6.75 s depending on the electrode area and spacing.

5.4.1.2 Maxwell-Wagner Interface Charging Relaxation

A Maxwell-Wagner dispersion was not visible within the measuring frequency range. The low frequency negative values of the capacitance make it difficult to determine if and how a Maxwell-Wagner dispersion will develop. Hence the values of Maxwell-Wagner index n and the efficiency of charge transport cannot be determined for the IPM response.

5.4.1.3 Modelling of the Anomalous Negative Capacitance

The responses containing the anomalous negative capacitances were modelled with a modified quasi-dc cluster model, which replaces the constant bulk conductance term with a linearised frequency dependent term described in section 2.6.1. The modified equation is re-stated below in eqn 5-4 and 5-5.

$$C^{*}_{bulk}(\omega) = C^{'}(\omega) - i\left(\frac{G(\omega)_{bulk}}{\omega}\right) \qquad \text{Eqn. 5-4}$$

$$G(\omega) = G_{\infty} + \left(\frac{G_m}{1+i\omega\tau}\right) = \left(G_{\infty} + \left(\frac{G_m}{1+\omega^2\tau_m^2}\right) - \left(\frac{i\omega\tau G_m}{1+\omega^2\tau_m^2}\right)\right) \qquad \text{Eqn. 5-5}$$

An example of the modelled anomalous negative capacitance response is displayed in Figure 5-18A where the curve fit data capacitance ●, loss +, and conductance -, are plotted together with the experimental data capacitance □, loss ◊, conductance ○, to show the goodness of the curve fit data Table 5-4. The small increase in conductance which corresponds to the negative capacitance is displayed in Figure 5-18B.

A

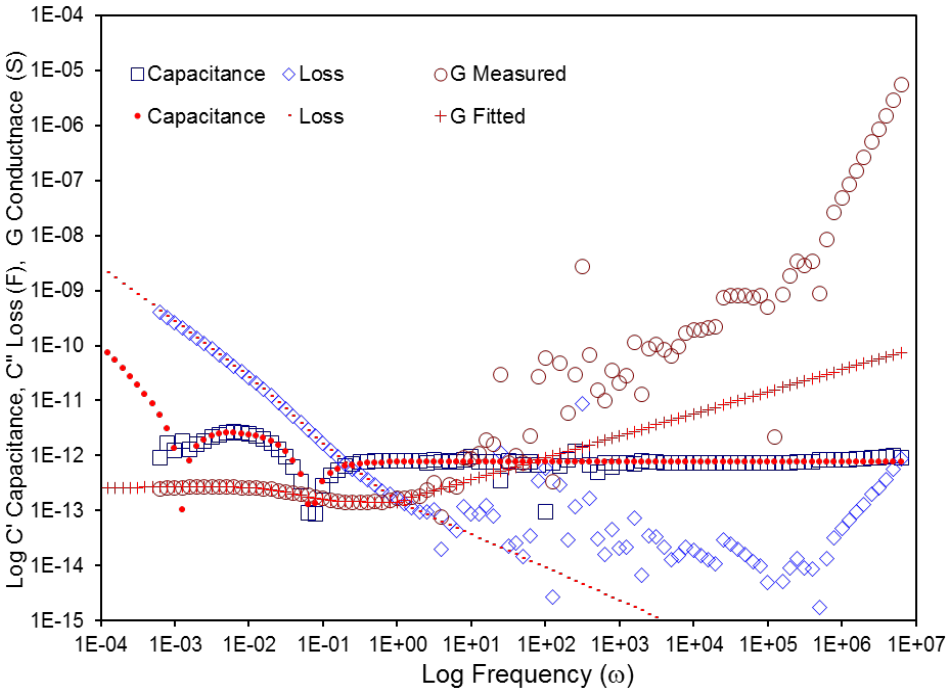

B

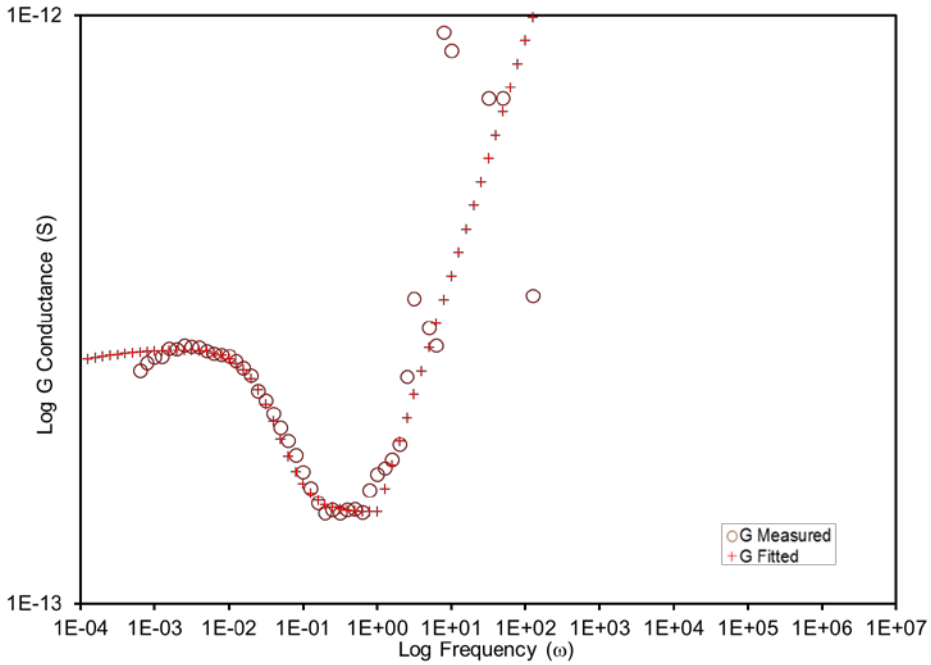

Figure 5-18 A) IPM dielectric response curve fit using Dissado-Hill quasi-dc cluster model with a linearised frequency dependent bulk conductance. The capacitance ●, loss +, and conductance **-**, are the curve fit data superimposed on the measured data capacitance □, loss ◊, conductance ○ using 1 V applied ac voltage and 5.0 ± 0.5 mm electrode spacing. B) A magnified view of the curve fit for the conductance increase.

Table 5-4 Modelling parameters for IPM linearised frequency dependent conductance response

Parameter			Description	Dominant response region
$C_{bulk,,}(C_{\infty})$	(pF)	0.764	High frequency constant capacitance	Bulk
$G_{bulk\ ,}(G_{\infty})$	(pS)	0.143	High frequency constant conductance	Bulk
G_0	(pS)	0.0110	Linearised frequency dependent bulk conductance	Bulk
G_1	(pS)	0.121	Linearised frequency dependent bulk conductance	Bulk
G_2	(pS)	-	Linearised frequency dependent bulk conductance	Bulk
ω_{g0}	(mRad/s)	9.96	Conductance characteristic frequency	Bulk
ω_{g1}	(mRad/s)	40.00	Conductance characteristic frequency	Bulk
ω_{g2}	(mRad/s)	620	Conductance characteristic frequency	Bulk
ω_c	(mRad/s)	187.00	High to low frequency characteristic crossover frequency	Crossover
C_{bar}	(pF)	185.00	Barrier capacitance	Barrier
B		1.50E-10	Magnitude of dispersive barrier capacitance	Barrier
p		0.60	Low frequency power law indices	Barrier

5.4.2 Ethyl Caprylate (EC)

Ethyl caprylate (EC) (Figure 5-19) which has a similar structure to IPM in that is and ester of a fatty acid, was measured for comparison purposes (Figure 5-20). The dielectric response of EC also exhibited a similar, low frequency increase in the magnitude of the conductance together with a corresponding negative capacitance. EC was found to have a conductance of magnitude 16 times greater than IPM and a characteristic intracluster relaxation time 13 times faster than IPM. The difference in the rate of the response is not unreasonable given the differences in the length of the carbon tails below the carbonyl group and with ratio of the molecular weight [IPM] / [EC] =1.57.

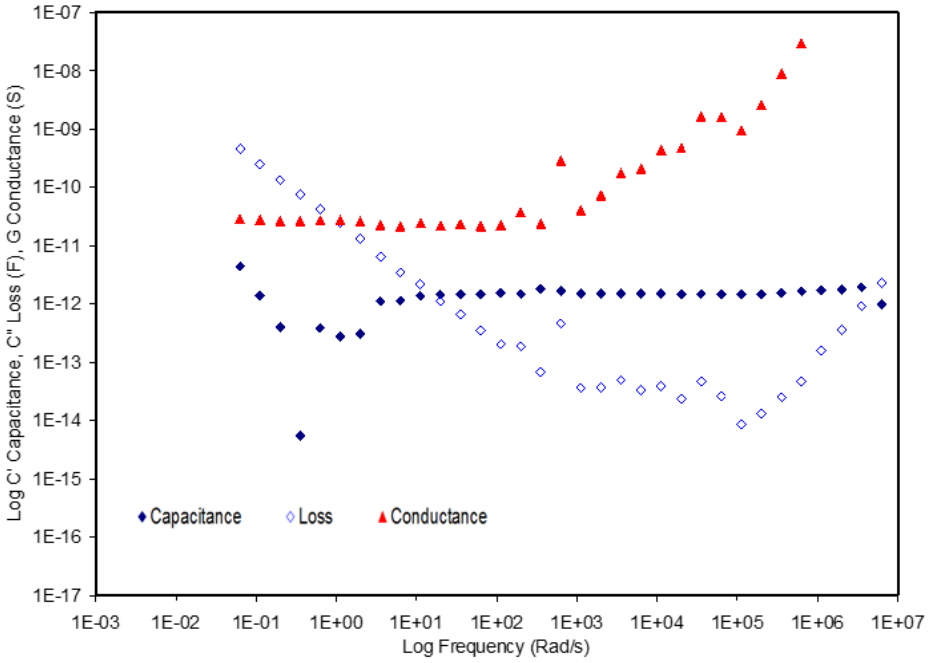

Figure 5-19 Response of ethyl caprylate using 1.0 V applied ac voltage and 5.0 ± 0.5 mm electrode spacing.

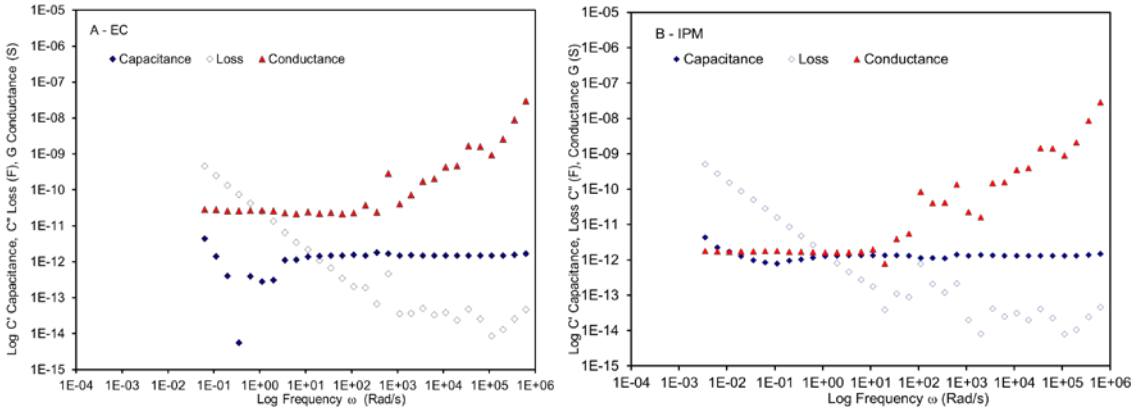

Figure 5-20 Responses of EC and IPM presented together for visual comparison. (A) Complex capacitance response of 100% EC. (B) Complex capacitance response of 100% IPM.

5.4.3 Soya Bean and Caster Oil

The dielectric spectra of soya bean and caster oil was measured for comparison with the ester oils, IPM and EC. Both oils were found to be weakly conducting however no dielectric measurements were carried out on surfactants dispersed in either oil as part of this study.

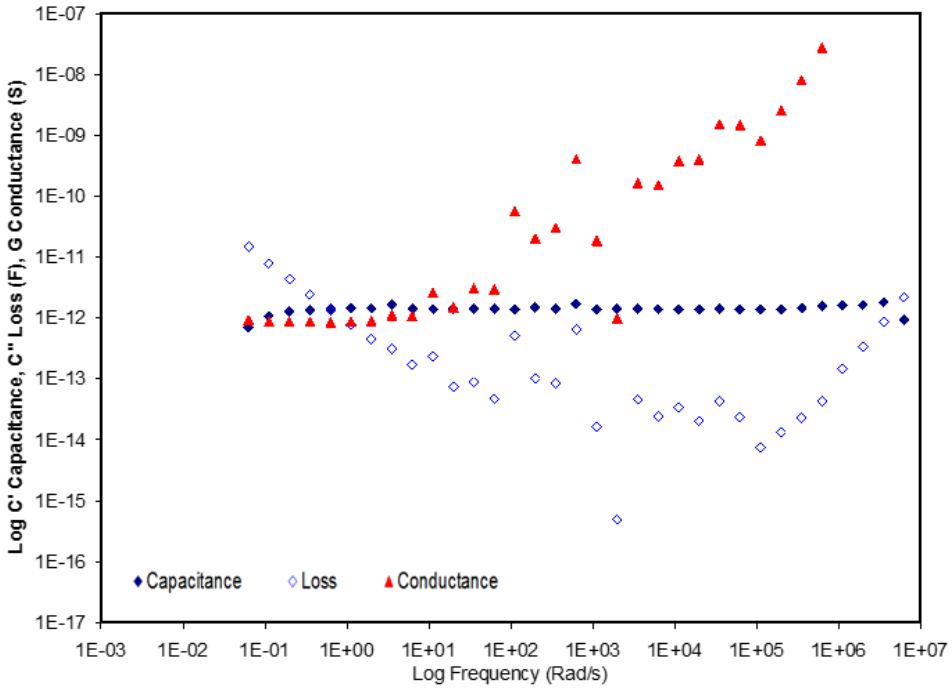

Figure 5-21 Response of soya bean oil using 1 V applied ac voltage and 5.0 ± 0.5 mm electrode spacing

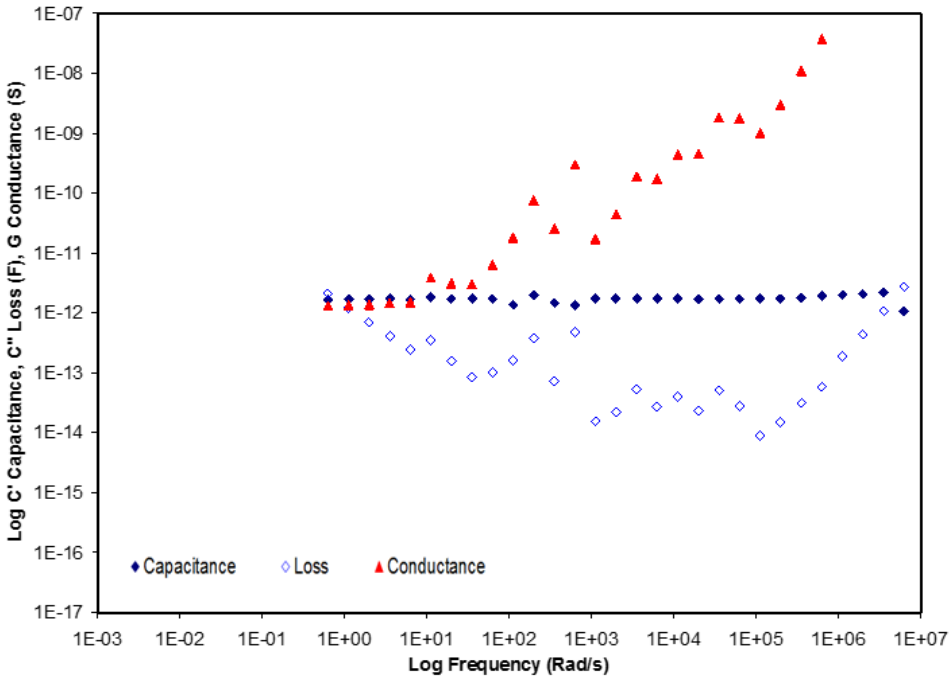

Figure 5-22 Response of castor oil using 1 V applied ac voltage and 5.0 ± 0.5 mm electrode spacing.

5.5 Hysteresis Effect of the Frequency Sweep

The samples were measured repeatedly to determine reproducibility. Two methods were used, high to low frequency sweep followed by a low to high frequency sweep and a repeated frequency sweep in the same direction. Although the responses from consecutive frequency sweep measurements initially appeared to reproducible for the individual samples, there were notable changes in the magnitude of conductance, and the frequency at which the barrier charging commenced when responses where plotted on the same chart.

5.5.1 High to Low and Reversed Frequency Sweeps – IPM

When a new sample was loaded it was initially examined using a high to low frequency sweep to ensure that there are no cell configuration issues or that the sample is free of any apparent contamination. The sample measurement was re-started but beginning at L1, low frequency 10^{-4} Hz and sweeping to 10^{+6} Hz, reversing the direction of the frequency sweep H2 high 10^{+6} Hz, to low 10^{-4} Hz, then repeating the low to high frequency sweep L3. It should be noted that the measurement of a single point at 10^{-4} Hz over 24 hours to complete.

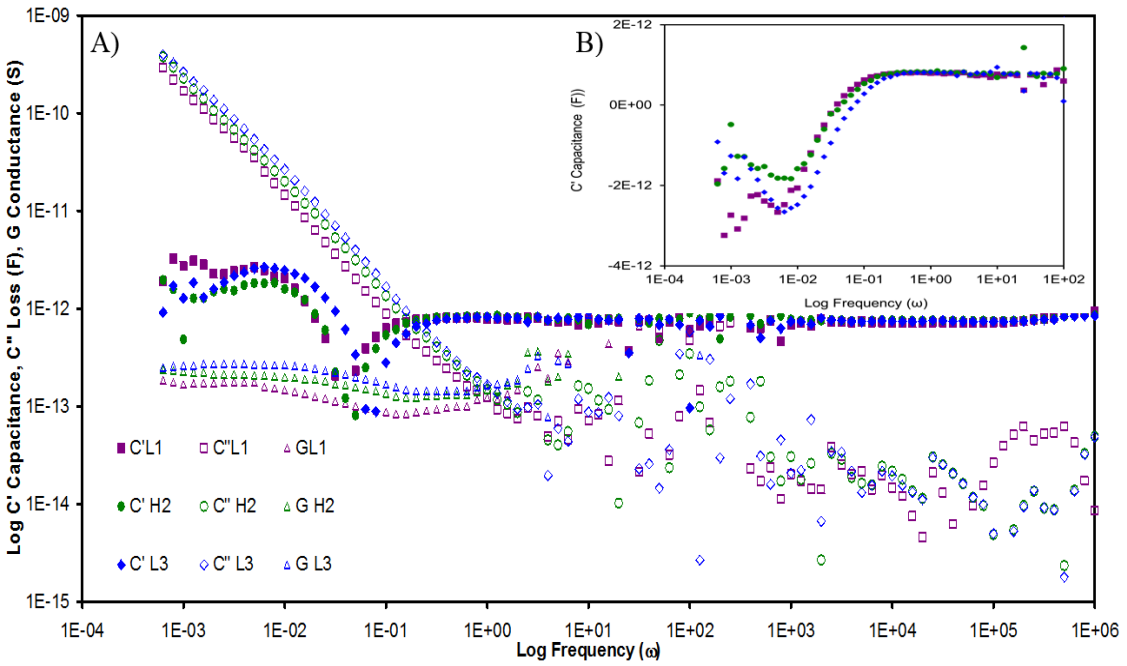

Figure 5-23 A) Consecutive frequency sweeps measurements of IPM from low to high (L1), high to low (H2), then low to high (L3) again. The magnitude of the conductance increased with each measurement sweep below the intracluster characteristic frequency. Insert B) shows the decrease in magnitude of the capacitance below the cross over frequency.

IPM showed little evidence of hysteresis in the bulk capacitance for frequencies above ω=0.1 (Figure 5-23). Below this frequency, which coincides with onset of the conductance associated with barrier charging, the capacitance showed a decrease in magnitude with successive frequency sweeps whilst the conductance showed an increase in magnitude with each sweep cycle. This suggests a build-up of mobile charges an interface boundary coinciding with stored charges being released. Note the same sample was measured repeatedly over a period of one month with each of the frequency sweep cycles (10 points per decade 10^{-4} Hz to 10^{+6} Hz) taking over 147 hours (6 days) to be completed.

5.5.2 High to Low and Reversed Frequency Sweeps – Water

Unlike IPM, water shows a magnitude increase in both the capacitance and conductance in the bulk frequency range with repeated measuring of the same sample (Figure 5-24).

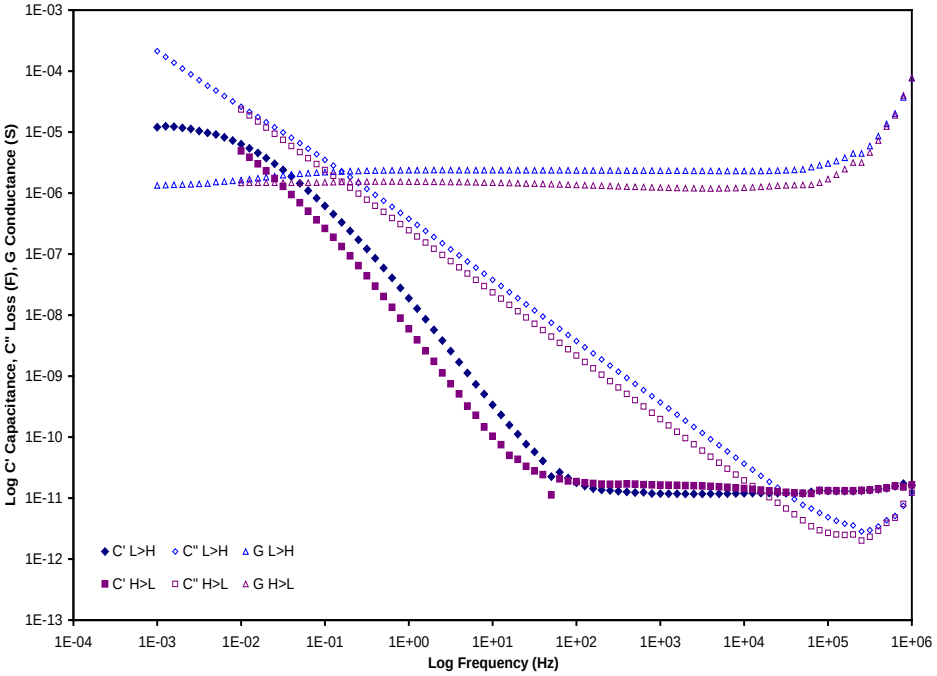

Figure 5-24 Water- consecutive frequency sweeps high>low (H>L) then from low>high (L>H) frequency.

The L > H frequency sweep appears to enable a more ordered structure to be established between the water clusters at higher frequencies which has provided an easier path for charge transport across the clusters. The response of second of the consecutive frequency sweeps has an index n=0.32 compared to n=0.23 for the first frequency sweep hence confirming the increase in structural order between measurement. Estimates for the barrier thickness indicates that a thinner layer was formed for the H>L frequency cycle.

5.5.3 Consecutive Frequency Sweeps

PG exhibited increases in the magnitude of the bulk capacitance however the bulk conductance is unaffected by this cycling. The barrier region appears to be unaffected by the repeated measurements but the Maxwell-Wagner dispersion begins at higher frequencies whilst retaining a gradient $\omega^{(2-n)} = 1.59$ (Figure 5-25).

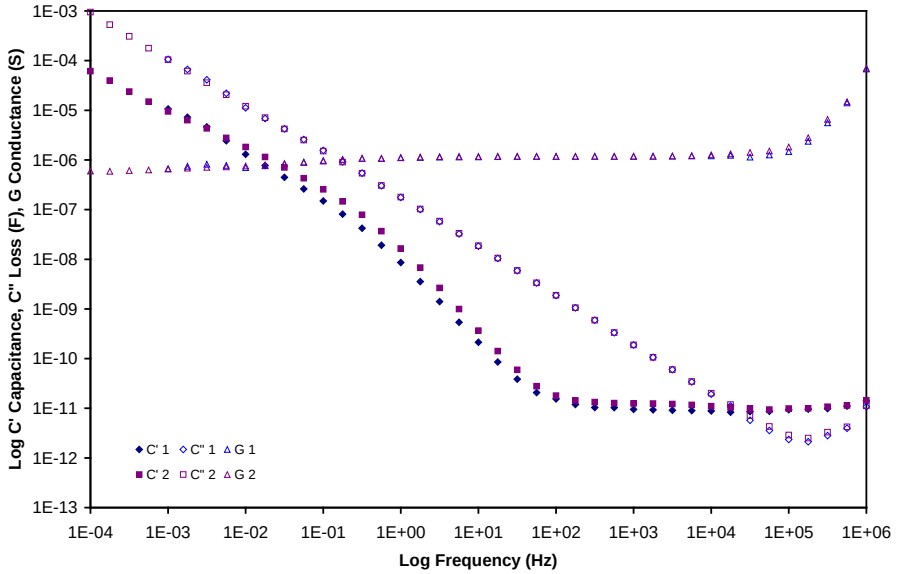

Figure 5-25 PG - consecutive frequency sweeps high>low frequency

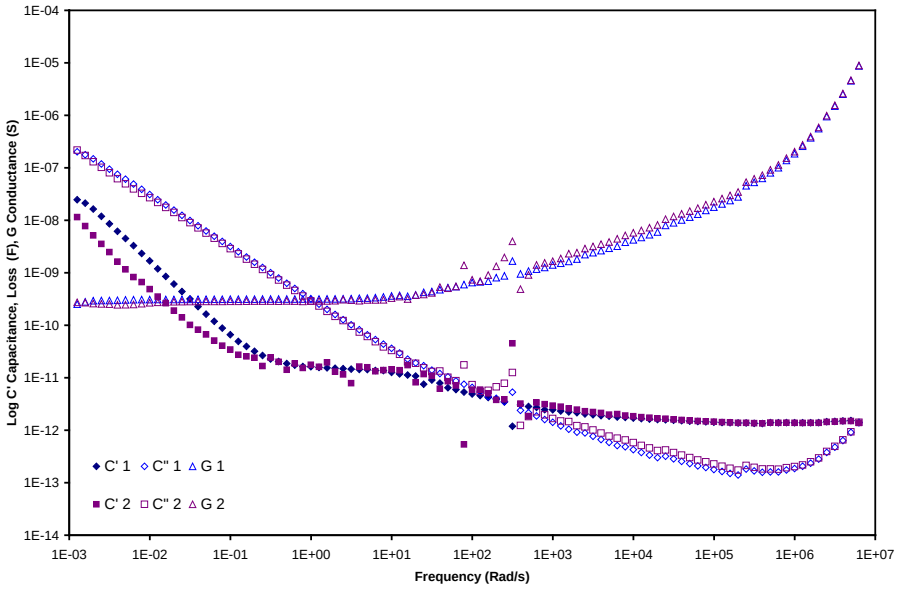

Figure 5-26 AOT consecutive frequency sweeps low>high

AOT exhibited an increase in the magnitude of the conductance for frequencies above the intra cluster cross over point. The transition to the intermediate capacitance plateau from high frequency becomes more diffusive and both the loss and capacitance and

attain a gradient of 0.5 over a frequency range of 1.2 decades on a log frequency scale. At frequencies below the intra cluster cross over, the Maxwell-Wagner dispersion of the capacitance moves to lower frequencies whilst the conductance remains relatively unchanged.

5.6 General Discussion

The characteristic properties of response of the individual components have been listed in Table 5-1. Table 5-1 contains bulk and barrier properties of the individual components which have been extracted or extrapolated (in the case for the barrier charging relaxation frequency) from the experimental data shown in Figure 5-1 to Figure 5-22.

Figure 5-27 to Figure 5-32 display capacitance, loss and conductance responses of the main components used in this study together with that of ternary microemulsion AOT:IPM:H_2O 20:60:20 and the three component non microemulsion composition E200:IPM: H_2O 30:40:30 for comparison. It can be seen that magnitude of the responses of the polar components to the applied field are relatively large when compared to the surfactant or the oil. Their presence in a sample would be expected to be dominant in the bulk response. The oils exhibits relatively small magnitudes in the capacitance hence would be expected to dominate if a series capacitance configuration were to be adopted with respect to the electrodes or interface between clusters.

The response of all the components exhibit dc or quasi-dc conductance (frequency independent) at low frequency typically < 1 Hz which is a common feature of dielectric materials. The dc conduction transports charges across the sample but is blocked by the electrode or internal interfaces. The existence of a charge barrier is evidenced by a large Maxwell-Wagner dispersion in the capacitance as the frequency of the ac field is reduced to zero. Such a response is characteristic of a single dipole (circuit comprised of a resistor and capacitor in series) with a relaxation time equivalent to the inverse of the frequency at which the barrier capacitance intersects the conductance G/ω.

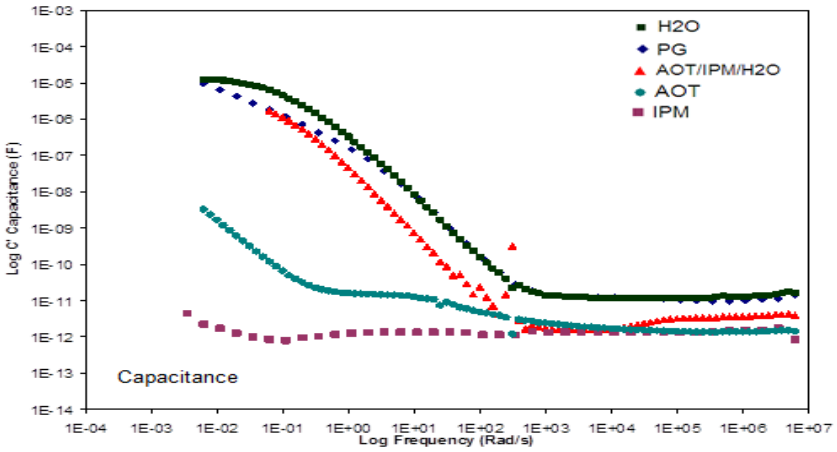

Figure 5-27 Capacitance response of individual components with the ternary composition AOT:IPM:H_2O 20:60:20 for comparison.

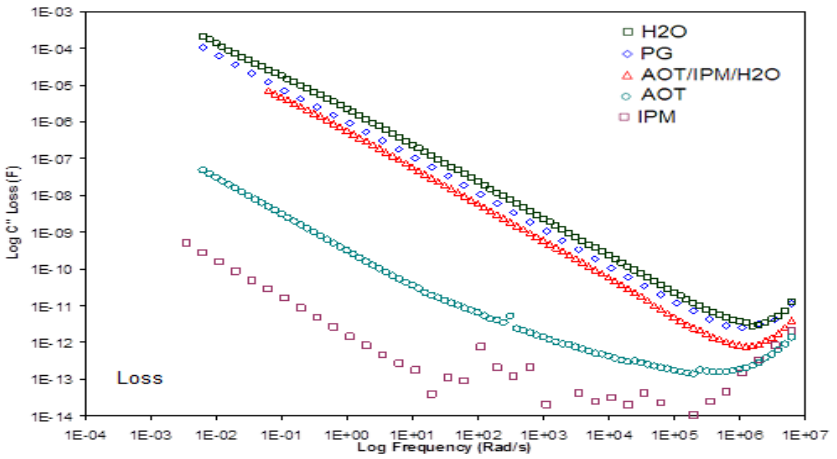

Figure 5-28 Loss response of individual components with the ternary composition AOT:IPM:H_2O 20:60:20 for comparison.

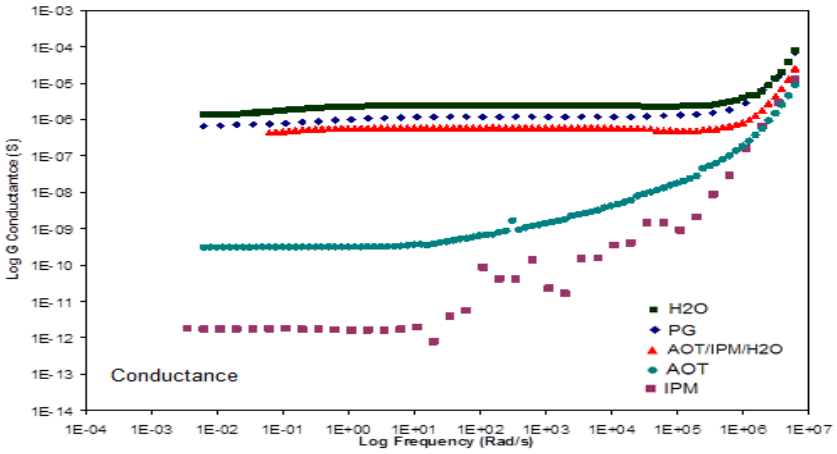

Figure 5-29 Conductance response of individual components with the ternary composition AOT:IPM:H_2O 20:60:20 for comparison

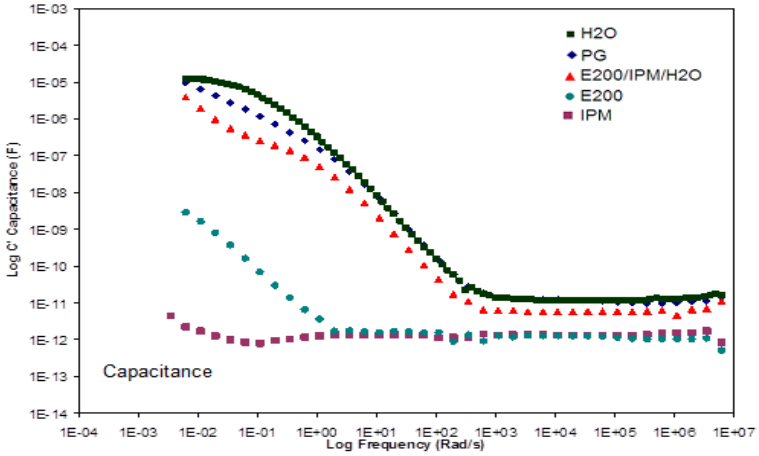

Figure 5-30 Capacitance response of individual components with the ternary composition E200:IPM: H_2O 30:40:30 for comparison

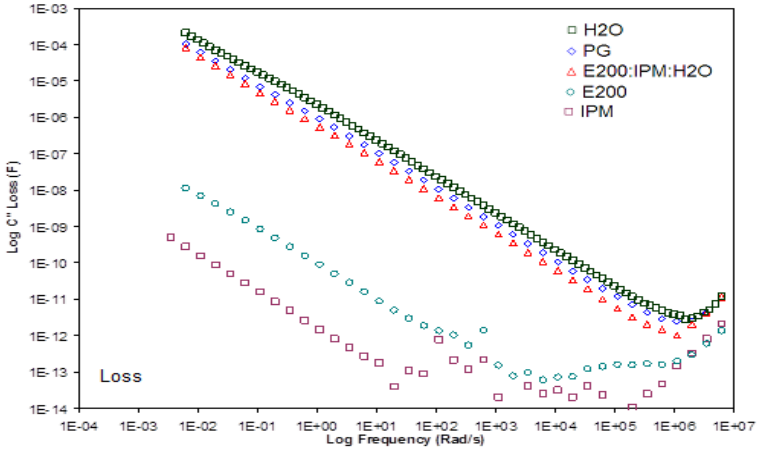

Figure 5-31 Loss response of individual components with the ternary composition E200:IPM:H_2O 30:40:30 for comparison

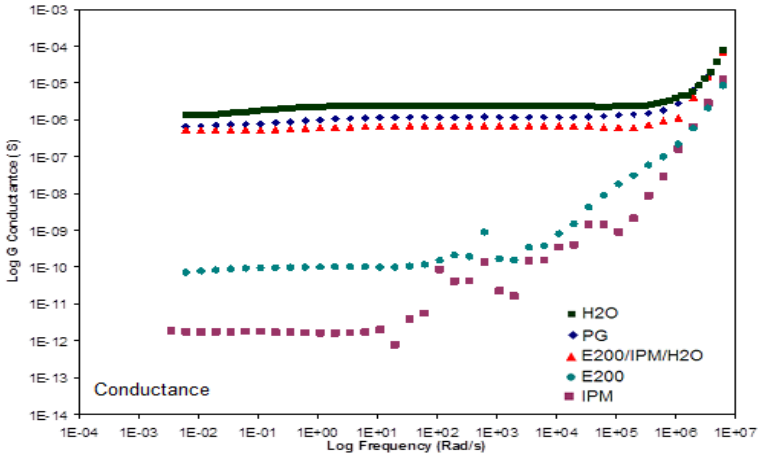

Figure 5-32 Conductance response of individual components with the ternary composition E200:IPM:H_2O 30:40:30 for comparison

The properties of the individual components and empty cell have been presented in Figure 5-33 to Figure 5-36 for comparison. The magnitudes of the properties are variable and are dependent upon the geometry of the measuring cell, as whilst the area of the electrodes remains constant, the electrode spacing is variable due to the flexible nature of the platinum wire electrodes (described in section 3.4.1). It is necessary when reviewing changes in magnitudes of the response, and frequency ranges where the responses features occur for different samples, to be mindful that the electrode spacing "d" may deviate from the spacing value measure prior to sealing the sample cell.

The magnitudes of the responses of the polar components and the ionic surfactants are greater than that of the apolar materials as expected (Figure 5-33). The rate of exchange of charges τ_1 within the cluster was found to be faster for polar and mixtures containing water (Figure 5-34), water being the fastest whilst soya oil being the slowest.

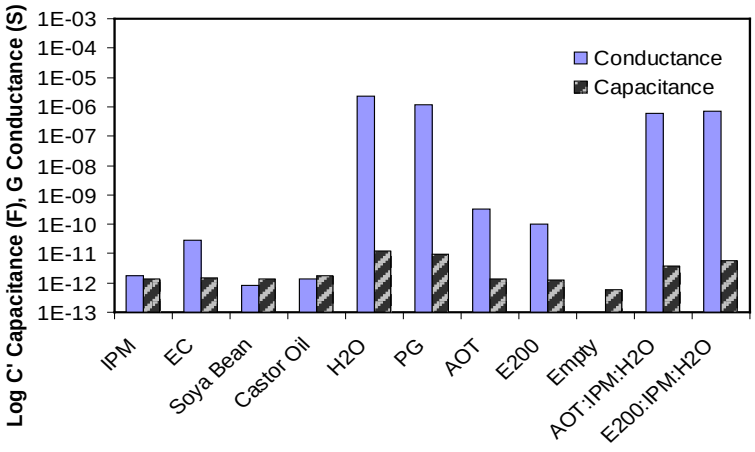

Figure 5-33 Bulk capacitance and conductance for individual components and the empty small cell.

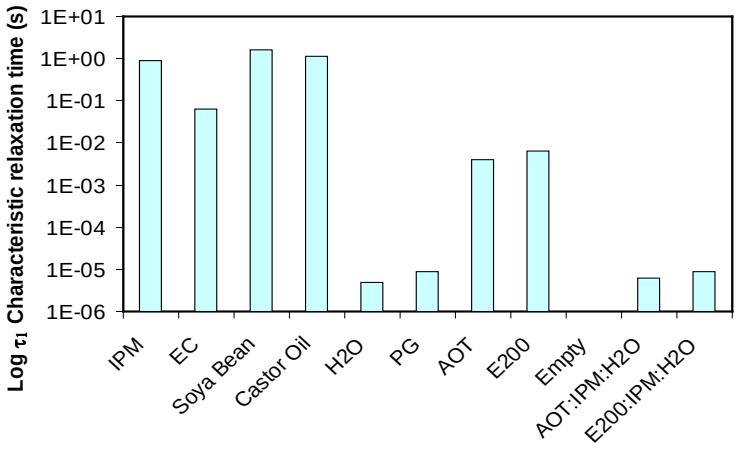

Figure 5-34 High frequency intracluster relaxation time for individual components.

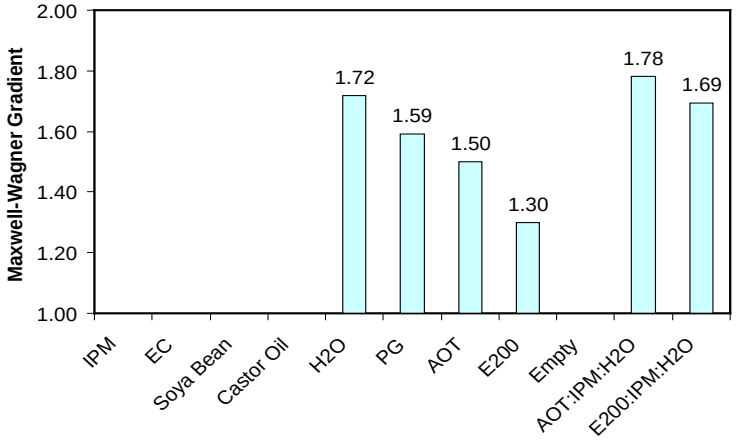

Figure 5-35 Maxwell-Wagner gradients $\omega^{-(2-n)}$ of the dispersion in the capacitance for the individual components and the empty cell. The dispersion of the oils IPM, EC, soya bean and castor oil were not visible with the available frequency range.

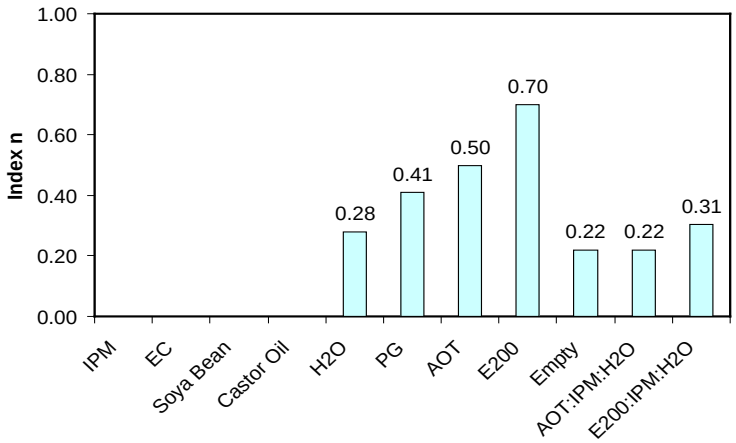

Figure 5-36 Cluster bound index n for individual components and the empty cell.

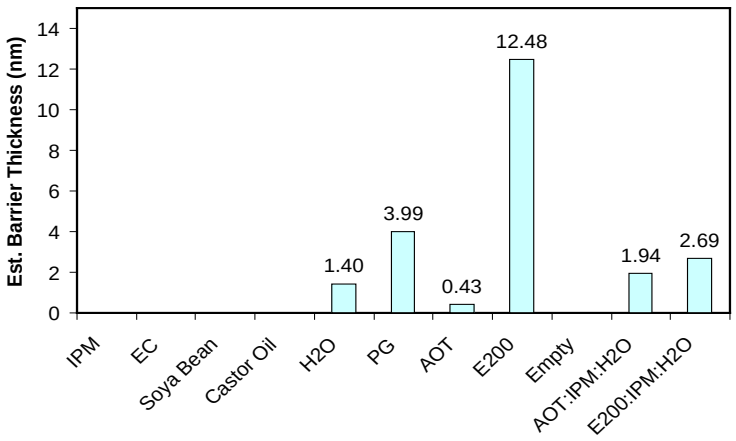

Figure 5-37 Estimated thickness of barrier visible within the available frequency range for individual components.

5.6.1 Voltage Variation and Electrode Spacing

The individual components IPM and deionised water produce bulk capacitance that are largely insensitive or uniformly insensitive to changes in the applied ac voltage in the range 0.05 to 1.00 V. The surfactant AOT in its solid form displayed a voltage sensitivity for frequencies lower that the cross over point where the capacitance and loss components are equal. This voltage sensitivity is assumed to be due to polarisation of the ionic head group and the dissociation of the sodium counter-ion.

The conductance of the water is significantly greater than that of AOT and IPM hence its presence in an unbound state is expected to dominate the dielectric response of a reverse microemulsion. If the water is bound within an aggregate, it is expected to contribute to the magnitude of the conductance response over a range of frequencies.

The magnitude of the response of the sample capacitance and conductance changes with magnitude of the cell constant. Generally if the electrode separation of the cell were decreased, then the magnitude of the response increased.

5.6.2 Hysteresis

It was noted that when the sample measurement was repeated but reversing the sequence of the ac frequency sweep, either or both the bulk and barrier responses varied in magnitude for the individual components. If a material contains only dipoles and no mobile charges, then high to low or the reverse frequency sweep responses are expected to be reproducible. The induced or permanent dipoles will relax and return to their original position and orientation once the driving ac field is removed. If however, the material contains charges these will move away from their ion/counterion and migrate to new locations by hopping from site to site in local clusters (refer to section 2 (Figure 2-9 a2) and (Figure 2-9 b2)). When the ac field is removed, the hopping charge will recombine with the nearest site hence the overall charge of the cluster will be net zero although the charge will not have returned to its original randomised location within the cluster. In addition, the final position of the charges will be in a location that is more favourable for conduction. Hence when the cycle is repeated, the charge species migration to the oppositely signed electrode will recommence from this new but macroscopically more ordered location. Consequently the magnitude conductance and possibly the capacitance will increase with each frequency sweep.

One consequence of the hysteresis described above is the development of the interface or electrode barrier layer is more pronounced when a frequency sweep is started from the lower frequencies if the sample contains mobile charges. The reason for the difference is sweeping from low to high frequencies allows more time for a more charges to move through the bulk medium and establish an ordered barrier structure before the frequency of the applied voltage is stepped up to the next frequency. Once at the higher frequency there is less time for the charges to relax before it is driven to the opposite electrode.

A second consequence is the impact on the characteristic relaxation times, which is dependent on the crossover of the capacitance and loss. If the magnitude of either of capacitance or the conductance changes, then the characteristic relaxation time will either become faster or slower (see the response of water Table 5-1).

5.6.3 Anomalous Negative Capacitance and Conductance Increase

The IPM displayed an anomalous negative capacitance and increase in the magnitude of the conductance as the frequency decreased over a limited range. Three possible explanations for the unusual feature were considered. Either the unusual response was due to an artefact of the measuring equipment configuration, contamination or else it was a characteristic of IPM.

Possible instrumentation issues due to the dielectric interface and the sample measuring cell were ruled out as both components were temporarily replaced with the Solartron 1296 dielectric interface and Solartron 12962A, and 12964A room temperature and liquid sample holders. Measurements made using this experimental set-up reproduced the anomalous increase in conductance and a reduction in the magnitude of the capacitance. However the capacitance did not become negative. This response was consistent with results obtained from the default equipment configuration as varying the cell geometry A/d (area/spacing) produced less negative response as the A/d ratio increases in magnitude. The 1255A FRA generator could not be ruled out as a possible cause of the anomalous negative capacitance as this instrument was a common component of all the dielectric measurements conducted in this study.

Sample contamination was ruled out by dismantling and cleaning the sample cell then flushing the sample cell with the fresh IPM prior to reloading it with more oil for measurement. In addition new batches of IPM were procured and tested to ensure the measured response was consistent between each batch, which it was.

When compared to IPM, EC produced a similar response hence it was assumed the anomalous response was a characteristic feature of the oils, possibly due to the presence of the single COO^- carbonyl group. The unsaturated C=O bond is classified as a polar bond [Jonscher 1983] and has a permanent dipole moment of 2.3 D (Debye=$3x10^{29}$ Cm) which is larger than that of water at 1.84 D and that the re-orientation polarisation is 534$Å^3$ for a static electric field of 10^7 Vm^{-1}, is approximately 450 times greater than the average induced polarisation at 1.2 $Å^3$. The reason for the induced re-orientation polarisation's greater contribution to the total polarisation is that the bond's ability to follow the applied electric field is restricted in structured liquids and solids hence making the effect of induced polarisation stronger.

It was noted that Craig [Craig *et al.* 1993] observed a similar negative capacitance response when measuring the oily surfactant, Labrafil M2125 CS (also known as linoleoyl macrogolgyceride). The authors assumed this feature to be noise however the capacitance can be seen to be decreasing before becoming negative for one decade in the log frequency range 1 Hz to 10^{+1} Hz (Figure 5-38). This response is consistent with that obtained for the oils IPM and EC in this present study. It should be noted that a single carbonyl group is also present in the Labrafil M21215 CS structure, arising from the linoleic acid based element.

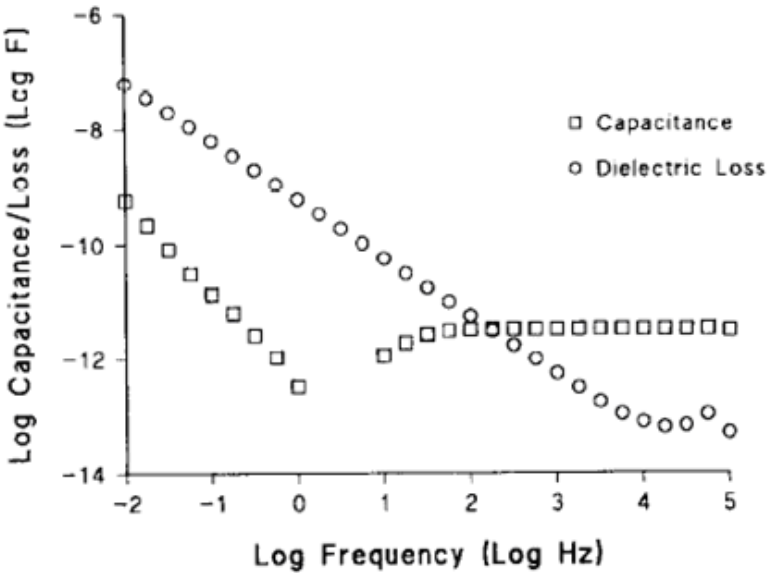

Figure 5-38 Dielectric response of Labrafil M2125 CS (exhibiting negative capacitance in the frequency range 1 Hz to 10 Hz) [reproduced from Craig *et al.* 1993]

In a study of the impact of the carbonyl group location of the ester bond on the interfacial properties of sugar based surfactants, Razafindralambo *et al.* (2009) concluded the close proximity of the C=O group to sugar molecules in sugar based surfactants increased the adsorption rate at the air-water interface. This view concurs with the conclusion in the present study that the presence the carbonyl group enables the continuous medium and the aggregates to undergo structural changes that enable ions to be transported more readily.

5.6.4 Potential Sample Contamination

Whilst investigating possible sources of the negative capacitance observed in IPM and EC, the response of the commercial detergent, Decon 90 and solvent ethanol used to clean the dismantled measuring cell were obtained. Figure 5-39, Figure 5-40 and Figure 5-41 show the typical responses for Decon 90, ethanol, and the contaminant free empty cell respectively. The magnitude of the bulk capacitance response of Decon 90 at 10^{-8} F is four orders of magnitude greater than of AOT, IPM and E200 and three orders of magnitude greater water and PG (Table 5-1). The response of the cleaned empty cell was measured before each new sample was added and compared to Figure 5-41 to confirm the cell is free from contaminants before adding samples for measurement.

It should be noted that the response of Decon 90 was such that FRA generator was overload for all applied ac voltages above 0.10 V with an electrode spacing of 5 mm.

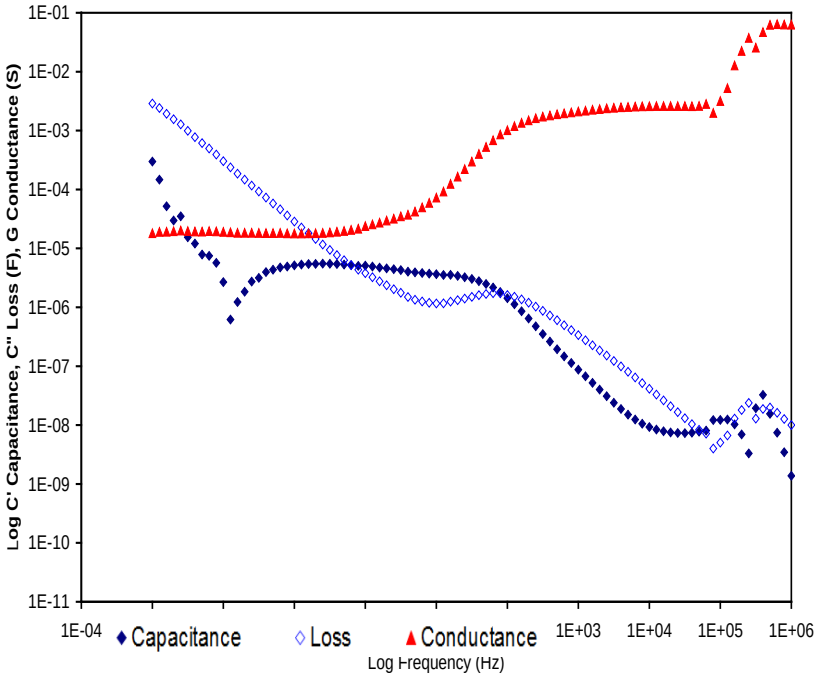

Figure 5-39 Decon 90 measured with 0.1 V applied voltage and 5 mm spacing.

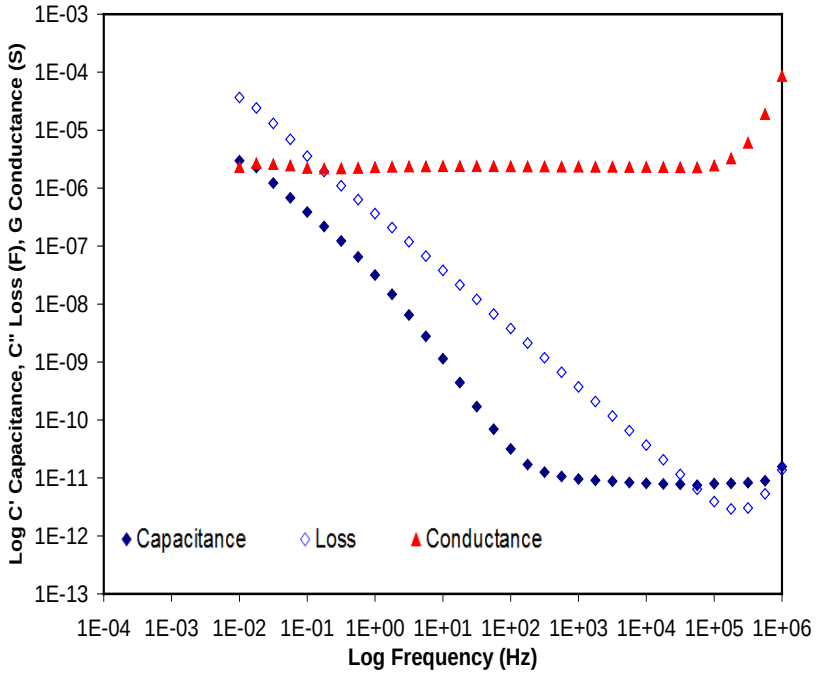

Figure 5-40 Ethanol – solvent used in the cleaning of the sample cell and electrodes measured with 1.0 V applied A/C voltage.

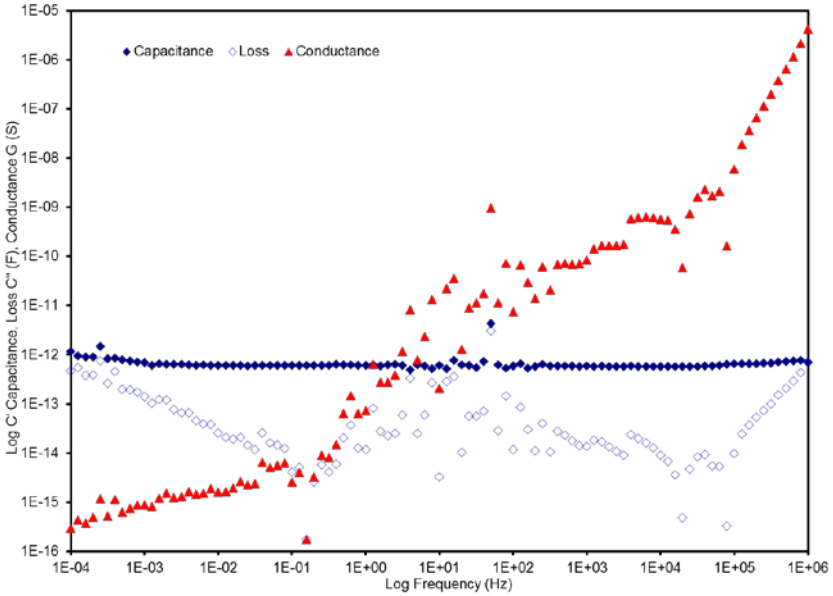

Figure 5-41 Response of the empty cell measured using 1.0 V applied A/C voltage.

5.7 Conclusion

Low frequency dielectric spectroscopy is a useful technique for examining the dielectric behaviour of both polar and apolar materials. Comparing the responses obtained for each of the materials and analysing the data using an appropriate model provides information on the structural arrangements of local clusters as well as the efficiency of the energy transport process.

One of the most striking observations is the ability of low frequency dielectric spectroscopy to detect the reorientation of the carbonyl dipolar groups in the esters. The corresponding structural rearrangements in the medium are evidenced by the frequency dependent increase in the magnitude of the conductance, and subsequent reduction in the magnitude of the capacitance as stored charge is released and the transport of charge increases.

Changes in the geometry of the measuring cell and environmental conditions can have an impact on the both the magnitude and shape of the dielectric response. Special attention is needed when setting the electrode spacing for a series of measurements on different samples if it is important to make a direct comparison between the responses. Similarly materials suspected of containing mobile charges are likely to suffer from hysteresis when measured repeatedly. Hence results selected for comparison when a

series of measurement have been made on a range of samples need to be matched i.e. the first measurement for each of the samples as no individual spectral response can be taken as an absolute representation.

5.8 Further work

It is recommended that a more detailed study on the low frequency properties of oils used in the formation of w/o microemulsions be carried out. Particular attention to the ester based or compounds synthesised using these esters as they feature amongst a number of excipients that have been classified as topological penetration enhancers [Mortazavi and Aboofazeli 2003, Singh *et al.* 2005].

It is also recommended that further analysis of the raw response data be conducted to determine if the observed anomalous negative capacitance data points could be associated with the switching of reference capacitors of the 1255a FRA ranging array.

Chapter 6

Dielectric Characterisation of the Surfactant Dispersed in Oil

6. Dielectric Characterisation of the Surfactant Dispersed in Oil

6.1 Introduction

The objective of this series of investigations is to determine whether low frequency dielectric spectroscopy can be used to detect variations based on changes in the compositions of [Surf]/[Oil] surfactant and oil used to prepare reverse microemulsions. No water will be added to sample compositions in this study, and all material will used as received from the suppliers.

6.2 Characterisation of AOT Dispersed in IPM

The dielectric response of the anhydrous, two component oil continuous phase systems comprised of, isopropyl myristate (IPM) oil and sodium bis(2-ethylhexyl) sulfosuccinate (AOT) anionic surfactant were measured at room temperature using the frequency sweep technique. Although the samples are categorised as anhydrous as no water was added, it is acknowledge that AOT used as supplied reported as containing 2% bound water.

All systems measured had a clear, single phase appearance and exhibited no birefringence when examined using plane polarised light prior to, or post, dielectric measurements. These compositions are classified as L2 phase and form the basis of a w/o microemulsion.

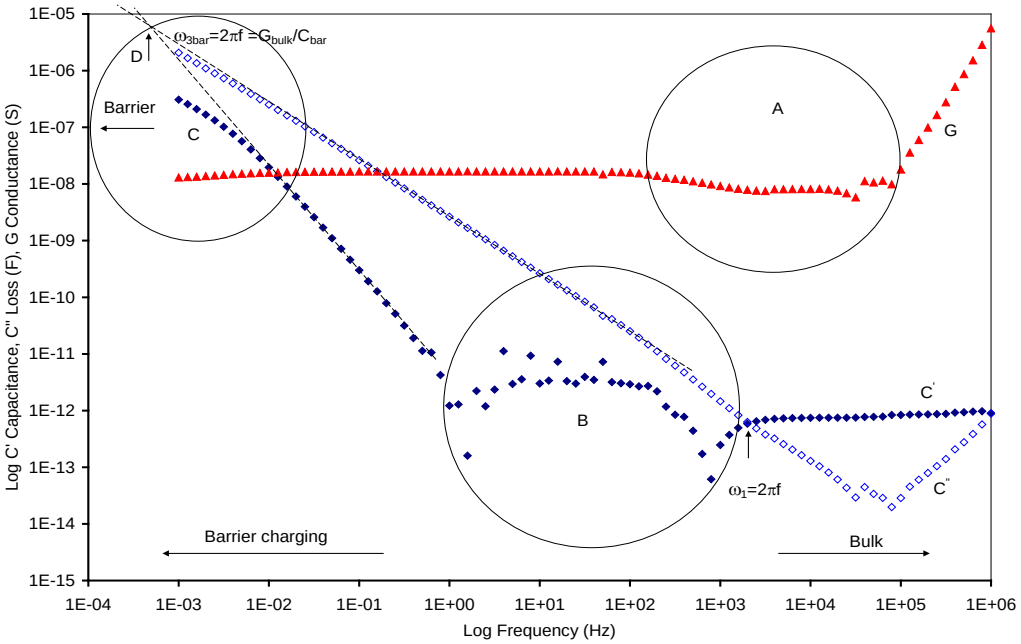

Figure 6-1 Characteristic response for dual component AOT/IPM= 30:70, single phase sample the loss ◊, conductance ▲ and capacitance ♦ components.

When examined using dielectric spectroscopy, the various mixtures of these L2 phase systems displayed two characteristic features that are not usually observed in dielectric materials, see for example Figure 6-1 regions A and B. Figure 6-1 shows the relaxation response for sample composition 30:70 AOT:IPM by percentage weight (molar ratio, [AOT]/[IPM]=0.2607) and the features displayed are representative of the dielectric responses obtained for the reverse micellar compositions tested and listed in Table 4-1

The characteristic feature in region A in Figure 6-1 is a small but anomalous increase in the magnitude of the conductance in the frequency range 10^{+4} Hz to 10 Hz and is enlarged and re-plotted in Figure 6-2. Feature B in Figure 6-1 shows an anomalous change to negative values of the capacitance over a frequency range of 10^{+3} Hz to 1 Hz and is re-plotted using a lin/log scale in Figure 6-3.

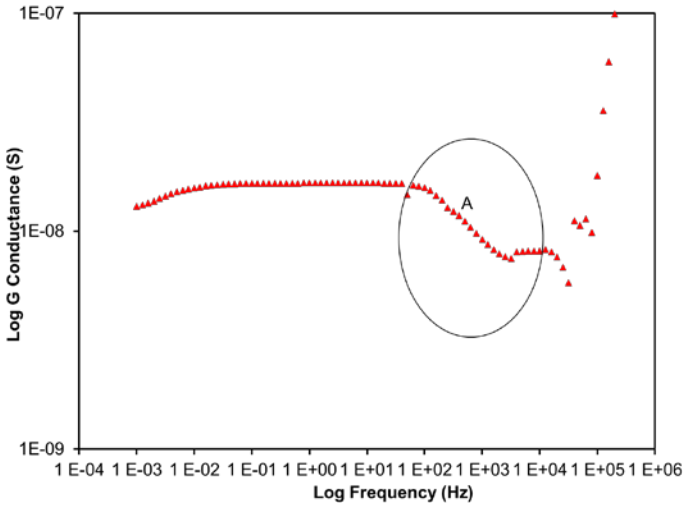

Figure 6-2 Ringed area A is an anomalous increase in conductance ▲ response for dual component (AOT/IPM= 30:70) single phase sample.

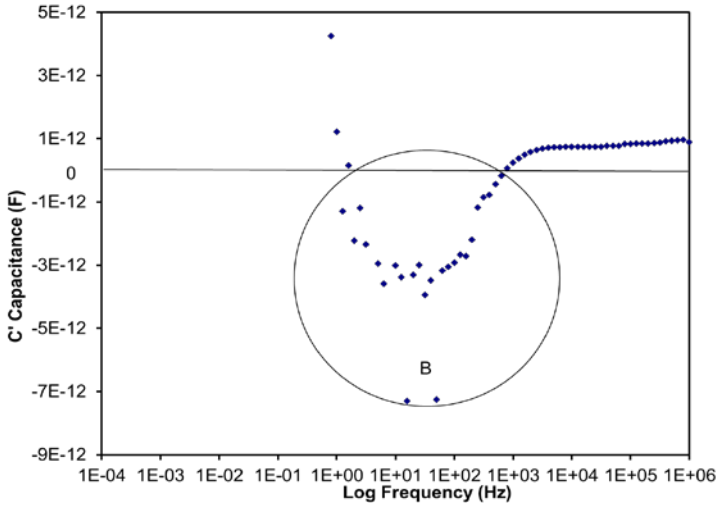

Figure 6-3 The ringed area B from Figure 6-1 is re-plotted using a lin/log scale to show the transition from normal to negative capacitance over a range of two decades of log frequency.

The net capacitance becomes negative in response to the anomalous increase in conductance. The magnitude of the conductance during a frequency sweep is expected to either be constant or decrease as the frequency of the applied electric field between parallel electrodes is reduced to zero in a closed system. This is due to the migration and build-up of charges at the interfaces consequently blocking the conducting paths [Debye] and [Jonscher 1983]. Hence the physical mechanism responsible for the increase in conductance and the negative capacitance is of interest. It is noted that similar characteristics are observed in oil/surfactant systems under study and with samples of pure IPM (Figure 5-23), where these anomalous features occur at frequencies less than 10^{-1} Hz.

The dispersion spectra of the AOT/IPM reverse L2 systems also showed characteristics attributable to intracluster relaxation of charges bound to a cluster at frequencies greater than 10^{+3} Hz (ω_1 Figure 6-1), with charge transport resulting in the charging of a barrier layer at frequencies below 10^{+3} Hz, and a barrier blocking the charge flow at frequencies less than 10^{-2} Hz (region C Figure 6-1). The barrier layer is not fully developed in the frequency range displayed in Figure 6-1. However the magnitude of the magnitude of the barrier capacitance C_{bar} and characteristic frequency can be approximated by extrapolating the straight line gradient of the capacitance and corresponding loss components of the dispersing Maxwell-Wagner process until they intersect see dashed lines, Figure 6-1D then reading the frequency $\omega_{bar} = 2\pi f_{bar}$ and magnitude of the intersection.

6.2.1 Summary of Macroscopic Observations

The dielectric response for a range of anhydrous compositions with percentage weight ratios of AOT:IPM ranging from 0.2:99.8 to 25:75 were measured and compared to the response obtained for 30:70. To aid the visual analysis the dielectric response of the individual loss, conductance and capacitance components of the complex capacitance of AOT:IPM compositions 0.2:99.8, 1:99, 5:95, 10:90, 15:85, 20:80, 25:75, 30:70 are displayed in Figure 6-4 to Figure 6-6. It can be seen that samples displaying large magnitudes of bulk conductance and dispersing capacitances corresponds to the largest AOT %w/w, and the smaller magnitudes to samples with little or no surfactant.

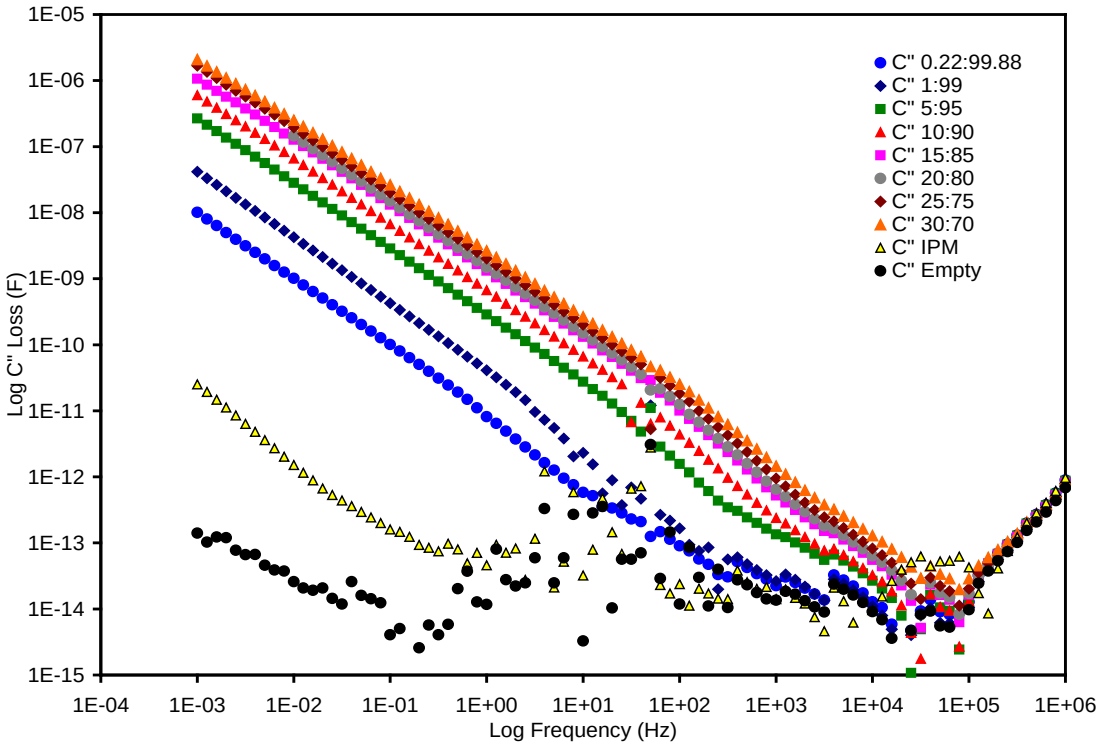

Figure 6-4 Loss components for percentage weight ratios of AOT:IPM 0.2:99.8, 1:99, 5:95, 10:90, 15:85, 20:80, 25:75, 30:70. The response of pure IPM and the empty cell is also shown for comparison.

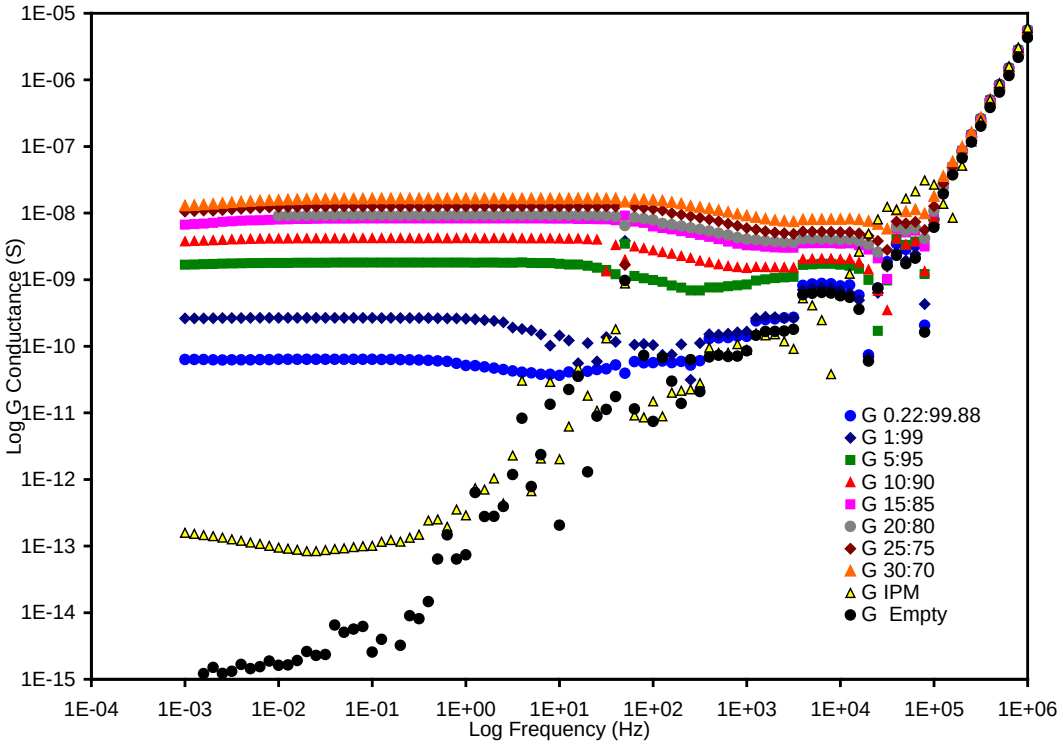

Figure 6-5 Conductance response for percentage weight ratios of AOT:IPM 0.2:99.8, 1:99, 5:95, 10:90, 15:85, 20:80, 25:75, 30:70. The response of pure IPM and the empty cell is also shown for comparison.

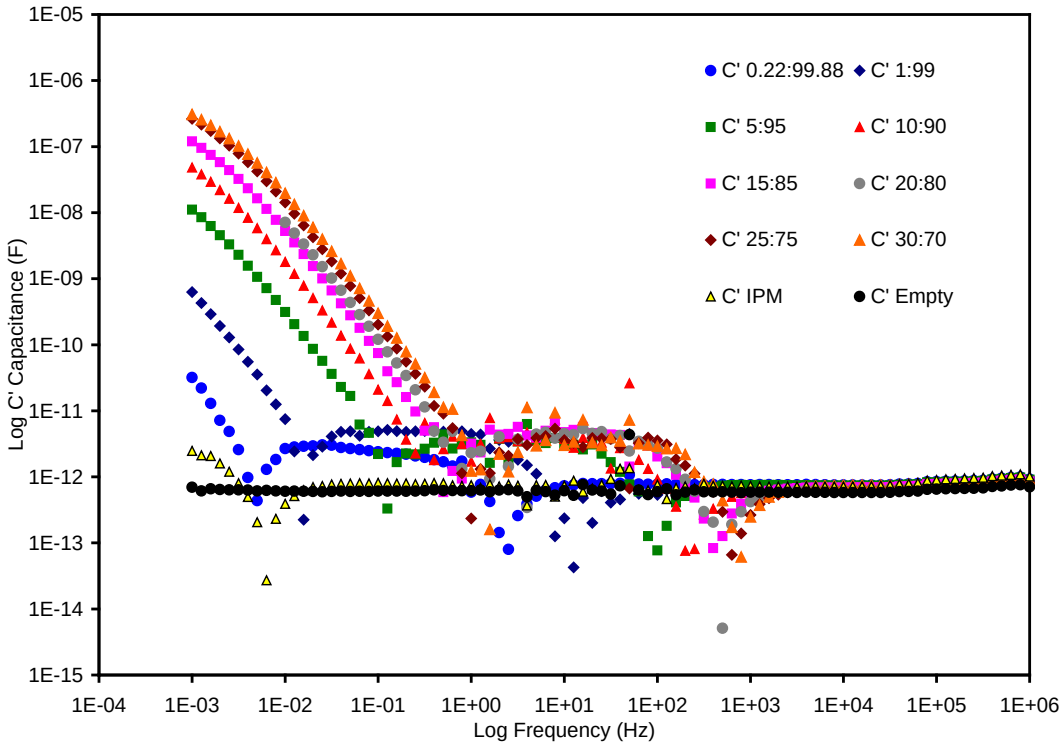

Figure 6-6 Capacitance response for percentage weight ratios of AOT:IPM 0.2:99.8, 1:99, 5:95, 10:90, 15:85, 20:80, 25:75, 30:70. The response of pure IPM and the empty cell is also shown for comparison.

6.2.1.1 Bulk Phase

As the concentration of AOT increases, the characteristic intracluster crossover frequency moves to higher frequencies indicating the mixture is polarised more easily for higher concentrations of AOT. The intracluster characteristic response time, $\tau_{1,}$ was found to have a linear dependence on the molar ratio [AOT]/[IPM] and is plotted using log/lin axis in Figure 6-7.

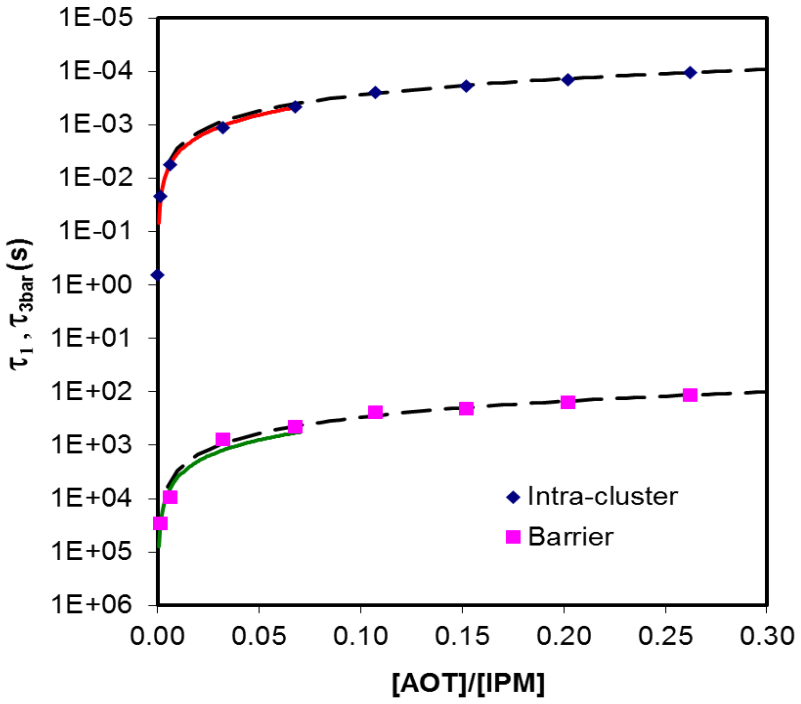

Figure 6-7 Log/lin plot relaxation times for ♦$\tau_{1,}$ intracluster and ■τ_{3bar} barrier charging processes for a range of AOT/IPM molar ratios. The dashed lines are calculated linear fit for the rate of polarisation with increase in the molar ratio of [AOT/IPM].

It was noted that for molar ratios below [AOT]/[IPM]=0.06 (<10% AOT by weight) the characteristic rate of polarisation is proportional to a gradient of 34.5μs per molar ratio [AOT]/[IPM]$^{-1}$. Above the molar ratio [AOT]/[IPM]=0.06, the characteristic rate of polarisation increases and is proportional to a gradient 28.0 μs per molar ratio [AOT]/[IPM]$^{-1}$. Hence the rate of increase the polarisation of the bulk mixture due to the percentage weight of added AOT is approximately 23% faster above an approximate transition molar ratio greater than [AOT]/[IPM]=0.06. The linear relationship suggests that the size of the clusters of oil molecules which form the bulk phase are reducing as more surfactant molecules are available to disrupt the permanent dipole-dipole bonds within the IPM oil (Figure 6-8). The consequence of smaller clusters is that they are able to be polarised more easily at higher frequencies.

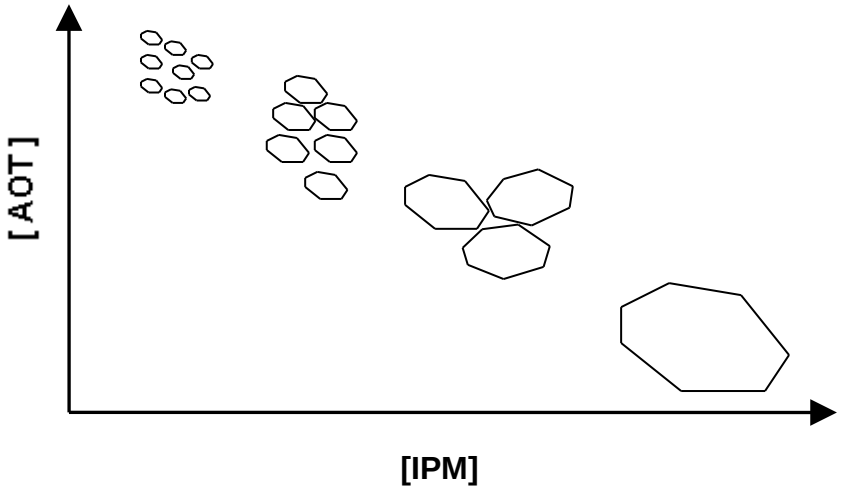

Figure 6-8 Schematic representation of the reduction in size of the clusters of IPM molecules as the concentration of [AOT] is increased implied from the linear decrease in the intracluster relaxation times with [AOT]/[IPM].

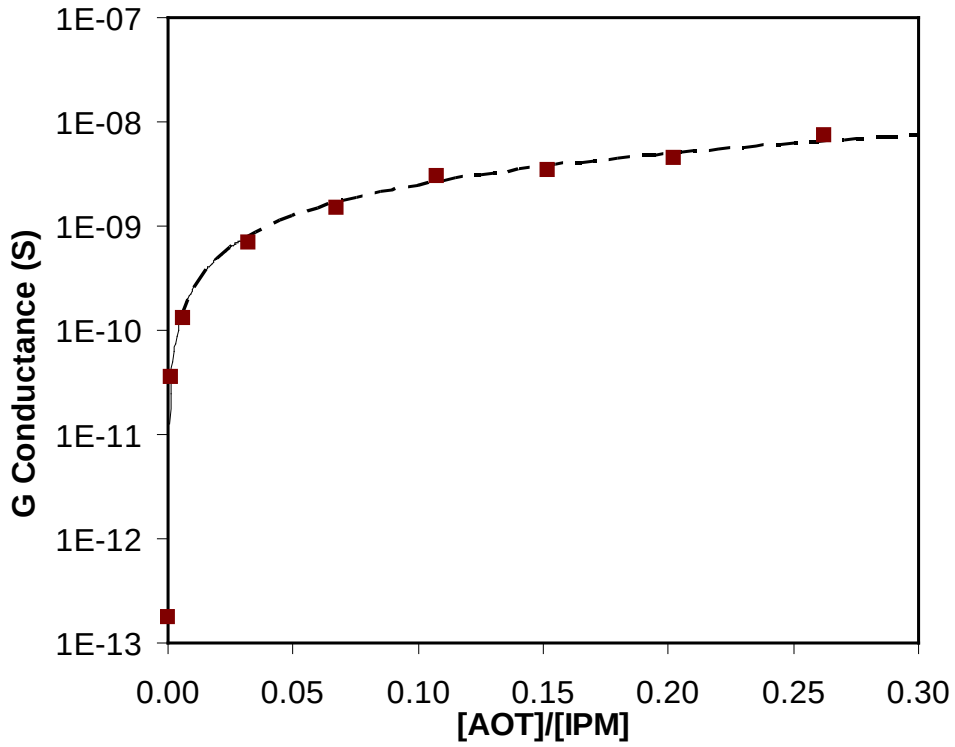

Figure 6-9 Log/lin of the increase in bulk conductance as the concentration of solubilised AOT increases. The dashed line is the calculated linear model with a gradient of 2.5×10^{-8} S +/- 0.25×10^{-8} S.

The magnitude of the bulk conductance has also been observed to increase linearly as the [AOT]/[IPM] molar ratio increases (Figure 6-9) with a rate of increase 0.025 μS per molar ratio $[AOT]/[IPM]^{-1}$. This result could be attributed to an increase in mobile charge carriers which are able to hop across and between local clusters more readily as more sites are available. An approximate value for the conductance due to the molar

ratio [AOT]/[IPM] is $1.43x10^{+5}$ S and is obtained by dividing out the constant contribution due to that of the bulk magnitude of pure IPM 0.17 pS. Using an electrode spacing of d = 5 mm yields an IPM conductivity σ_{IPM} = Gd/A of magnitude 35 pSm^{-1}. An estimate for the conductivity of $2.86x10^{+7}$ Sm^{-1} for the molar ratio range 0<[AOT]/[IPM]<0.30 is obtained and plotted in Figure 6-10. The electrical conductivity of sodium is $2.08x10^{+7}$ Sm^{-1} hence it is likely that the Na^{+} cation has dissociated from the AOT head group and is largely responsible for the magnitude observed conductance.

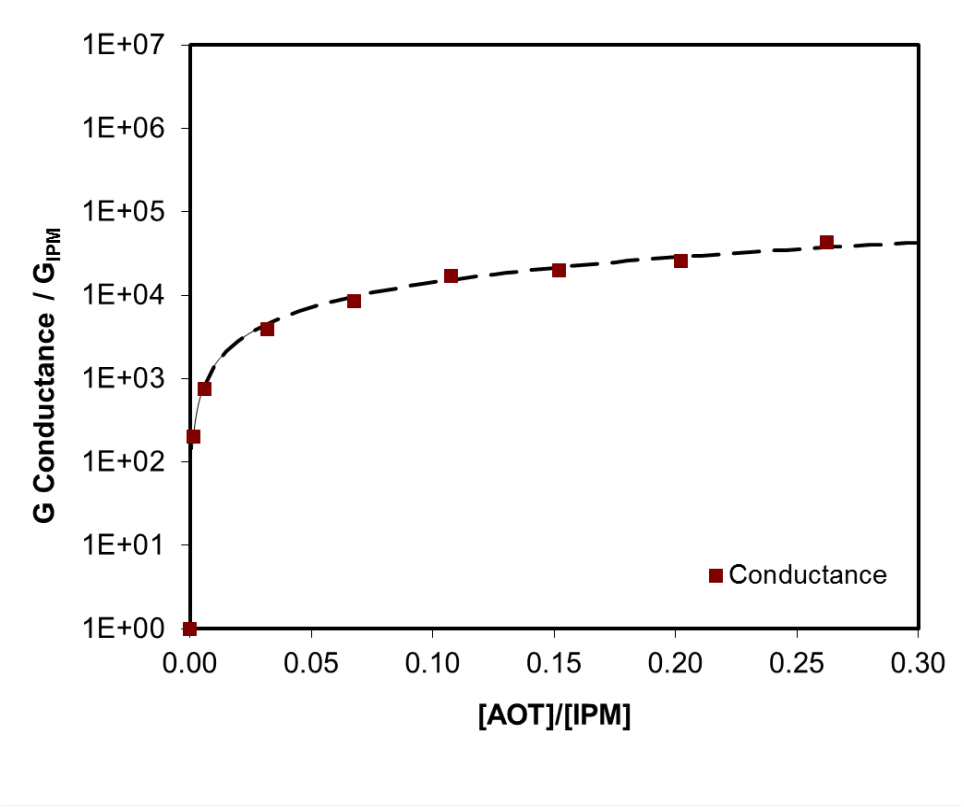

Figure 6-10 Log/lin plot of the increase in bulk conductance as the concentration of solubilised AOT increases, normalised with respect to pure IPM. The dashed line is the calculated linear fit with a gradient of $1.43x10^{+5}$ S.

6.2.1.2 Barrier Charging

The fully developed barrier response was outside of the available frequency measuring range for these anhydrous samples, hence it was necessary to extrapolate the Maxwell-Wagner dispersion to lower frequencies to obtain an estimate of the characteristic barrier frequency for the crossover of the loss and capacitance components. The characteristic barrier charging response time, τ_3, and the magnitude of the barrier capacitance were then derived using Equation 6.1. The magnitude of τ_3 was also found to vary linearly with increase in the molar ratio of [AOT]/[IPM] (Figure 6-7). The characteristic rate of polarisation is proportional to a gradient of 30 s per molar ratio $[AOT]/[IPM]^{-1}$ for [AOT]/[IPM] > 0.006 and 45 s per molar ratio $[AOT]/[IPM]^{-1}$ for [AOT]/[IPM]<0.006.

$$\omega_3 = \omega_{bar} = \frac{G_{bulk}}{C_{bar}} = \frac{1}{\tau_3} \qquad \text{Eqn. 6-1}$$

The values of the Maxwell-Wagner (2-n) index n for the molar ratio [AOT]/[IPM] are plotted in Figure 6-11. The low values of 'n' indicates that the structure of the clusters are well ordered.

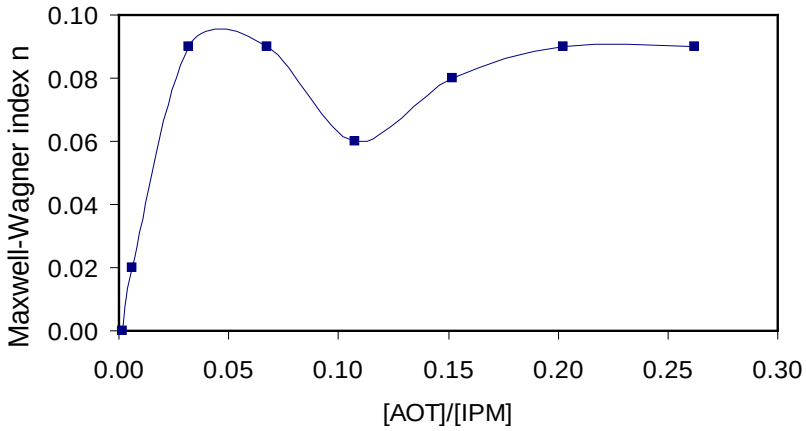

Figure 6-11 Intracluster index n measure of order within the cluster as the molar ratio is increased.

6.2.1.3 Anomalous Bulk-Barrier Transition

The frequency at which the anomalous capacitance and conductance features occurs, increase as more surfactant is added to the IPM. Table 6-1 and Table 6-2 list the frequency range of the anomalous conductance and capacitance respectively as the percentage weight of AOT added to IPM is increased.

The features are deemed to begin at the upper end of the frequency scale. The start and end frequencies of the anomalous conductance increase and negative capacitance features are plotted in Figure 6-12 and Figure 6-13 using a log/lin scale. There is a linear frequency rate increase as the molar ratio increases (freq/([AOT]/[IPM]) for both the conductance and the capacitance features. However, in the case for the conductance, the upper frequency of the start of the anomalous feature departs from the linear relationship with a gradient of 11 KHz (Figure 6-12 dash-dot line B) and becomes constant at approximately 3 KHz for molar ratios [AOT]/[IPM]>0.1 (dashed line A Figure 6-12). This departure from the linear relationship frequency/molar ratio relationship (freq/([AOT]/[IPM]) appears to be due to the dielectric response being either saturated or becomes masked (Figure 6-1 regions A), by the instrumentation effects of the 50Ω BNC lead connecting the sample to the frequency response analyser. The BNC lead is known to respond in 100 kHz to 10 MHz frequency range [Sorichetti and Matteo 2007].

For lower concentrations of added AOT, molar ratio [AOT]/[IPM]<0.1 (dashed line B Figure 6-12), the response of the sample dominates over the BNC connector and a linear relationship is observed.

Table 6-1 Frequency trend at which the conductance begins to increase as percentage weight ratio of AOT:IPM ranging from 0 to 30:70

AOT:IPM (%w/w)	$\frac{[AOT]}{[IPM]}$	Conductance increase start Frequency (Hz)	Conductance increase end Frequency (Hz)
0.1:99.9	0.0006	6.31	$6.31x10^{-2}$
0.2:99.8	0.0014	$1.00x10^{1}$	$6.31x10^{-3}$
1:99	0.0061	$3.16x10^{1}$	$3.16x10^{-3}$
5:95	0.0320	$3.16x10^{2}$	3.98
10:90	0.0676	$1.00x10^{3}$	1.26
15:85	0.1074	$3.16x10^{3}$	3.16
20:80	0.1521	$3.16x10^{+3}$	2.00
25:75	0.2028	$3.16x10^{+3}$	3.98
30:70	0.2607	$3.16x10^{+3}$	10.00

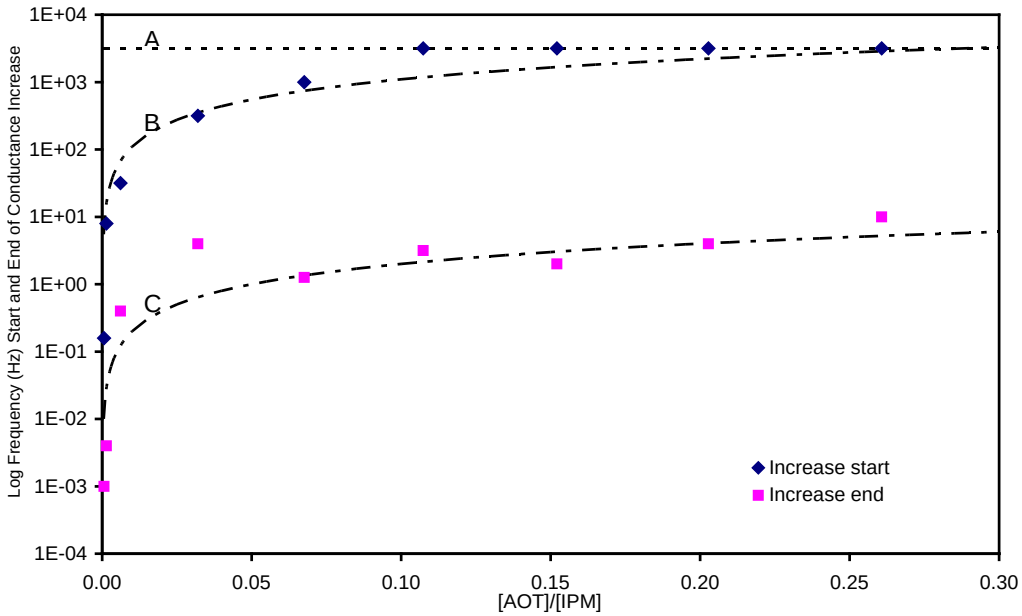

Figure 6-12 Frequency at which the anomalous increase in the bulk conductance G begins ♦ and ends ■ for each molar ratio [AOT]/[IPM]. Dotted line A is constant frequency 3.16 KHz and dashed lines B and C are calculated linear fits with gradients 11.0 KHz and 20.00 Hz per molar ratio [AOT]/[IPM].

The linear relationship for the lower frequency end of the anomalous conductance increase (dashed line C Figure 6-12) has a gradient of 20 Hz per molar ratio [AOT]/[IPM] and is not impacted by the BNC lead impedance.

Table 6-2 Frequency trend at which the anomalous negative capacitance begins and ends as a % w/w ratio of AOT:IPM ranging from 0 to 30:70

AOT:IPM (%w/w)	$\frac{[AOT]}{[IPM]}$	Negative C' Start Frequency (Hz)	Negative C' End Frequency (Hz)
0.1:99.9	0.0006	1.26	7.94×10^{-3}
0.2:99.8	0.0014	2.51	3.98×10^{-3}
1:99	0.0061	20.00	2.00×10^{-3}
5:95	0.0320	$1.00 \times 10^{+2}$	1.26×10^{-1}
10:90	0.0676	$2.00 \times 10^{+2}$	3.98×10^{-1}
15:85	0.1074	$3.98 \times 10^{+2}$	5.01×10^{-1}
20:80	0.1521	$5.01 \times 10^{+2}$	7.94×10^{-1}
25:75	0.2028	$7.94 \times 10^{+2}$	1.00
30:70	0.2607	$7.94 \times 10^{+2}$	2.00

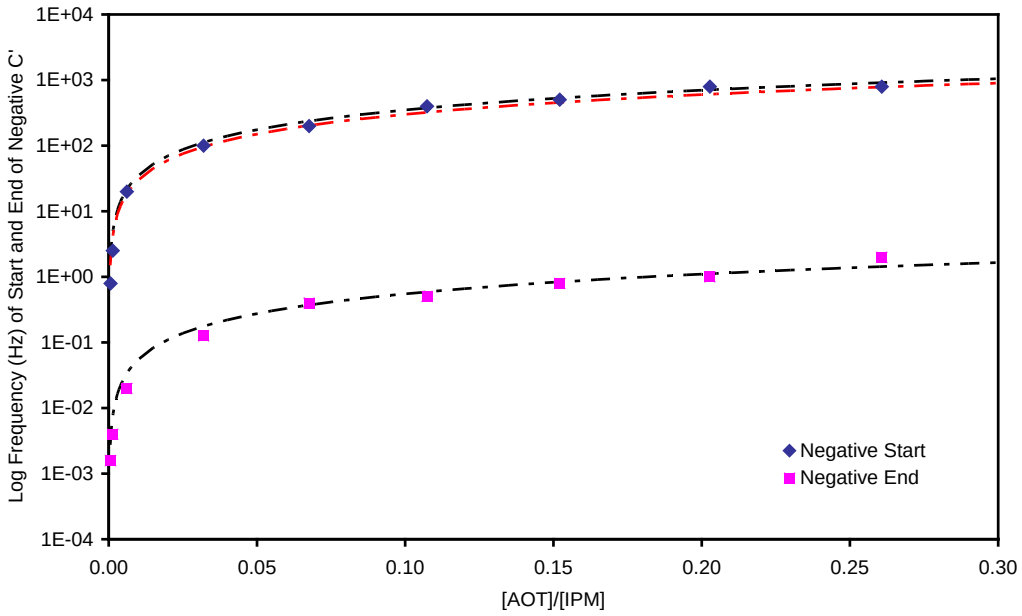

Figure 6-13 Frequency at which the anomalous dispersion in the capacitance C′ begins ♦ and ends ■ for each molar ratio AOT:IPM. The feature appears at higher frequencies as the molar ratio of AOT increases. Dashed lines are calculated linear fit with gradients Hz/[AOT]/[IPM] = $3.5x10^3$ for [AOT]/[IPM] <0.1, $3.0x10^3$ for [AOT]/[IPM] >0.1 and 5.5 for the start and end of the feature.

The anomalous negative capacitance feature exhibits a linear move to higher frequencies as [AOT]/[IPM] is increased (Figure 6-13). The feature begins close to the characteristic intracluster relaxation frequency ω_1 Figure 6-1, however, there is a change in the gradient Hz/[AOT]/[IPM]=$3.5x10^{+3}$ for [AOT]/[IPM]<0.1 to $3.0x10^{+3}$ for [AOT]/[IPM]>0.1. The lower frequency end of the anomalous negative capacitance gradient was found to be Hz/[AOT]/[IPM] = 5.5 Hz.

Variations in shape, magnitude and onset frequency of the characteristic of the loss and real components of the complex capacitance with changes to the molar ratio compositions [AOT]/[IPM] were examined at selected spot frequencies. The selected frequencies associated with bulk, barrier and transition loss characteristics are listed in Table 6-3 and plotted in Figure 6-14. Figure 6-14 shows linear increase trends in the as the molar ratio [AOT]/[IPM] increases. The response transition frequency range, 0.1 KHz to 1 KHz, exhibits two linear rates of change to the loss, above and below [AOT]/[IPM]=0.06.

Table 6-3 Magnitude of the loss component at selected frequencies for molar ratios of [AOT]/[IPM] ranging from 0 to 0.26

AOT:IPM (%w/w)	[AOT] / [IPM]	Magnitude of Loss C″ (F) at Spot Frequencies				
		10^{-2} (Hz)	1 (Hz)	10^{+2} (Hz)	10^{+3} (Hz)	10^{+4} (Hz)
0:100	0	4.85×10^{-12}	5.51×10^{-14}	1.82×10^{-14}	3.08×10^{-14}	1.15×10^{-14}
1:99	0.0061	5.74×10^{-9}	5.47×10^{-11}	2.28×10^{-13}	1.35×10^{-13}	1.29×10^{-14}
5:95	0.0320	2.38×10^{-8}	2.87×10^{-10}	1.57×10^{-12}	2.38×10^{-13}	2.67×10^{-14}
10:90	0.0676	6.62×10^{-8}	6.70×10^{-10}	4.39×10^{-12}	5.22×10^{-13}	3.24×10^{-14}
15:85	0.1074	1.27×10^{-7}	1.32×10^{-9}	1.00×10^{-11}	6.71×10^{-13}	5.52×10^{-14}
20:80	0.1521	1.49×10^{-7}	1.53×10^{-9}	1.30×10^{-11}	9.48×10^{-13}	6.54×10^{-14}
25:75	0.2028	1.95×10^{-7}	2.01×10^{-9}	1.83×10^{-11}	1.47×10^{-12}	8.24×10^{-14}
30:70	0.2607	2.57×10^{-7}	2.66×10^{-9}	2.53×10^{-11}	3.08×10^{-14}	1.64×10^{-13}
Gradient (F/([AOT]/[IPM])		1.00×10^{-6}	1.10×10^{-8}	9.5×10^{-11} 5.0×10^{-11}	4.75×10^{-12} 3.75×10^{-12}	5.0×10^{-13}

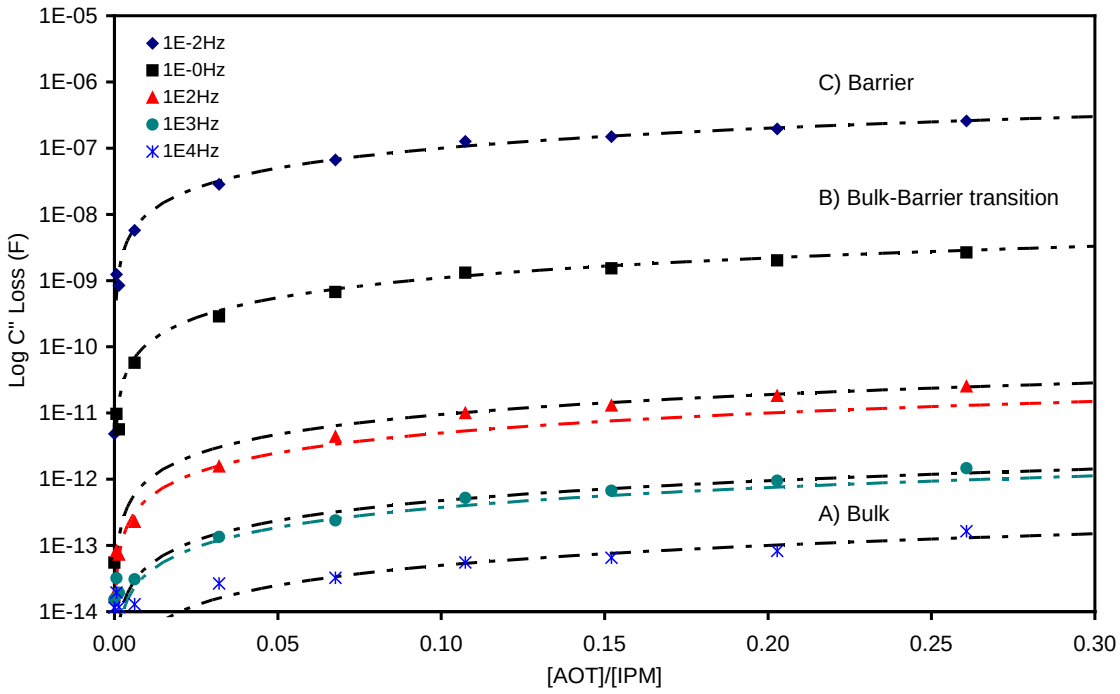

Figure 6-14 The Magnitude of the loss component at frequency, f=0.01 Hz ♦, 1 Hz ■, 100 Hz ▲, 1000 Hz ●, 10000 Hz* for each ratio of AOT and IPM. The conductivity of the sample increase as the [AOT]/[IPM] molar ratio increases.

The observed transition between bulk and barrier characteristics of the real component of the capacitance are listed in Table 6-4 and displayed in Figure 6-15 where the magnitude of the capacitance is plotted for selected frequencies for each molar ratio.

The frequency region associated with the transition between the bulk to barrier response, is plotted using a linear scale on the second vertical axis as the value of the capacitance becomes negative within this frequency range. The magnitude of the bulk capacitance remains relatively constant for all compositions at frequencies $f \geq 10^{+4}$ Hz. As the frequency is reduced to 10^{+3} Hz the magnitude of the capacitance begins to decrease as the concentration of AOT increases. However the characteristic response in the frequency range above 10^{+3} Hz can still be considered to be that of the bulk continuous medium. The magnitude of the capacitance exhibits larger increases as the concentration of AOT increases, at frequencies below 10^{-2} Hz. The response in this frequency region is characteristic of the charging of a barrier layer and as the concentration of surfactant increases, the barrier charging response moves to higher frequencies and increases in magnitude. The charging of the barrier and the increase in conductance shows that charges are mobile and move with greater ease. The characteristic relaxation response time of the barrier becomes faster as the molar concentration of [AOT] increases.

Table 6-4 Magnitude of the capacitance component at selected frequencies for molar ratios of [AOT]/[IPM] ranging from 0 to 0.26

AOT:IPM	[AOT]	Magnitude of Loss C′ (F) at Spot Frequencies				
(%w/w)	[IPM]	10^{-2} (Hz)	1 (Hz)	10^{+2} (Hz)	10^{+3} (Hz)	10^{+4} (Hz)
0:100	0	-3.31×10^{-12}	-1.06×10^{-12}	7.13×10^{-13}	6.94×10^{-13}	6.91×10^{-13}
1:99	0.0061	8.71×10^{-12}	-4.08×10^{-12}	6.43×10^{-13}	6.64×10^{-13}	6.66×10^{-13}
5:95	0.0320	3.13×10^{-10}	-3.31×10^{-12}	7.70×10^{-14}	7.52×10^{-13}	7.38×10^{-14}
10:90	0.0676	1.79×10^{-9}	-1.70×10^{-12}	-9.13×10^{-13}	5.92×10^{-13}	6.59×10^{-13}
15:85	0.1074	5.26×10^{-9}	-3.18×10^{-12}	-2.03×10^{-12}	5.08×10^{-13}	6.94×10^{-13}
20:80	0.1521	8.87×10^{-9}	-2.95×10^{-12}	-2.80×10^{-12}	4.09×10^{-13}	6.43×10^{-13}
25:75	0.2028	1.43×10^{-8}	2.35×10^{-13}	-3.55×10^{-12}	2.65×10^{-13}	6.57×10^{-13}
30:70	0.2607	1.97×10^{-8}	1.22×10^{-12}	-2.92×10^{-12}	2.47×10^{-13}	7.44×10^{-13}

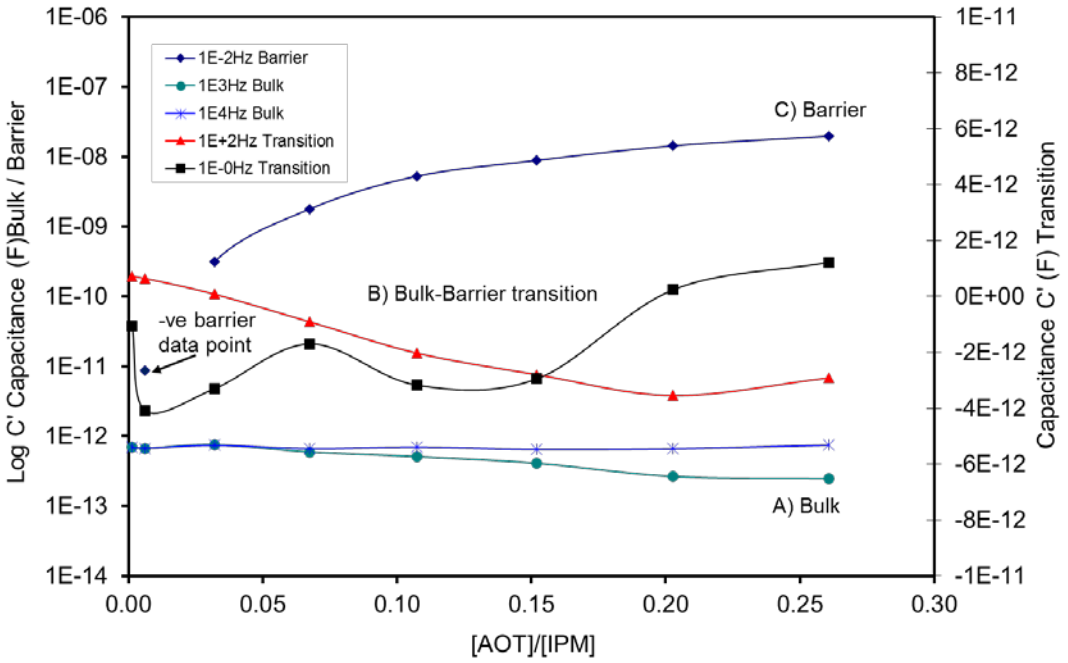

Figure 6-15 The magnitude of the capacitance component at selected frequencies, f=0.01 Hz ♦, 1 Hz ■, 100 Hz ▲, 1000 Hz ●, 10000 Hz* for molar ratio AOT/IPM ranging from 0 to 0.26.

The transition between the bulk and barrier response occurs in the frequency range 100 Hz ≥ f ≥ 1 Hz. The capacitance decreases from a small but positive magnitude to a negative value as the concentration of the surfactant increases for selected frequencies around 10^{+2} Hz. The value of the capacitance returns to a positive value as the frequency is reduced to 1 Hz and as the response behaviour moves from transition to that of a barrier charging response.

6.2.2 Analysis of Characteristic Response Using Normalisation

The effect of increasing the concentration of AOT dispersed in IPM was further examined by normalising the response of the dual component series using Maxwell-Wagner dispersion of composition AOT:IPM 30:70 weight ratios as the loci. This composition was selected as the characteristic features common to all the samples were centrally located within the available measuring frequency range. Table 6-5 contains the magnitude shifts in frequency required to normalise the dual component compositions and are plotted in Figure 6-16 using a lin/log scale.

Table 6-5 Frequency shift normalisation values

Components Percentage by weight			[Surfactant] /[Oil]	Magnitude shift relative to composition *	Normalised from *
AOT%	IPM%	H_2O%	[AOT]/ [IPM]	Frequency Δ (Hz)	Frequency (Hz)
0.225	99.771	0.005	0.0014	265	30.0
0.986	98.993	0.020	0.0062	61	13.0
4.896	95.005	0.100	0.032	10	79.4
9.810	89.990	0.200	0.0677	4	199.0
14.707	84.993	0.300	0.1074	2	397.0
19.603	79.997	0.400	0.1521	1.63	662.0
24.457	75.044	0.499	0.2023	1.2	662.0
*29.532	69.865	0.603	0.2624	1	794.0

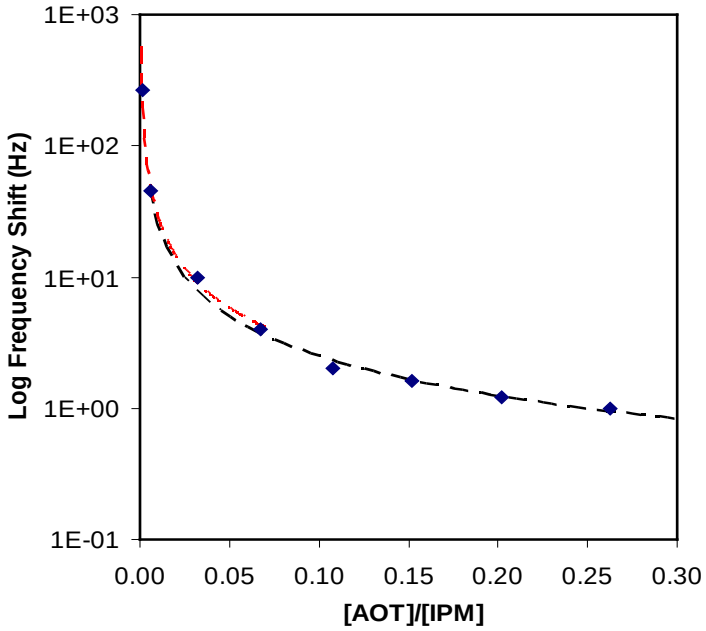

Figure 6-16 Log/linear plot of the Δ shift in frequency required to normalise the response as the ratio of surfactant to oil increases and has a gradient $2.5x10^{-01}$ for ratios above [AOT]/[IPM]= 0.06.

For frequencies above the characteristic intracluster relaxation frequency $2x10^{+3}$ Hz, the bulk polarisation processes appear to be become increasingly independent of the surfactant concentration, indicating the bulk response property is due to IPM (Figure 6-17). However, below the characteristic intracluster frequency ω_1 Figure 6-1, the response of the dual component compositions are dependent upon the frequencies of the applied ac field. The normalised anomalous negative capacitance is re-plotted on a lin/log scale and displayed in Figure 6-18. It can be seen that there are differences in

the magnitude of the negative capacitance with AOT increasing concentration, and a stepped pattern is evident.

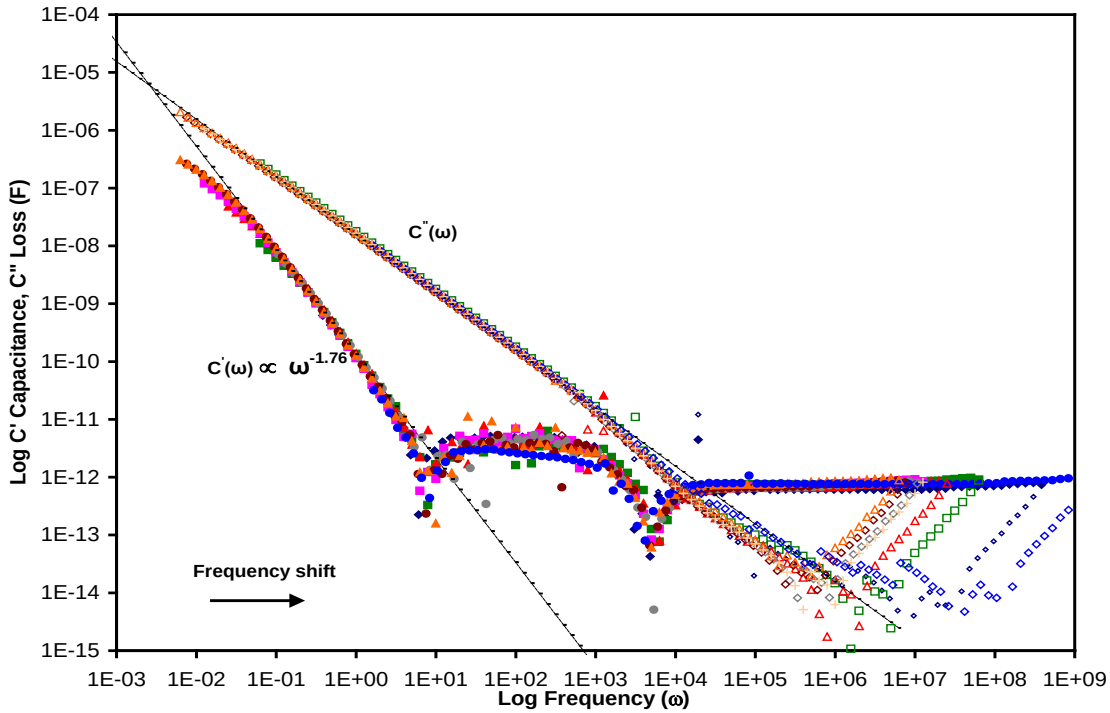

Figure 6-17 AOT/IPM normalised data from Table 6-5 with respect to composition AOT:IPM = 30:70. All compositions are shifted to higher frequencies.

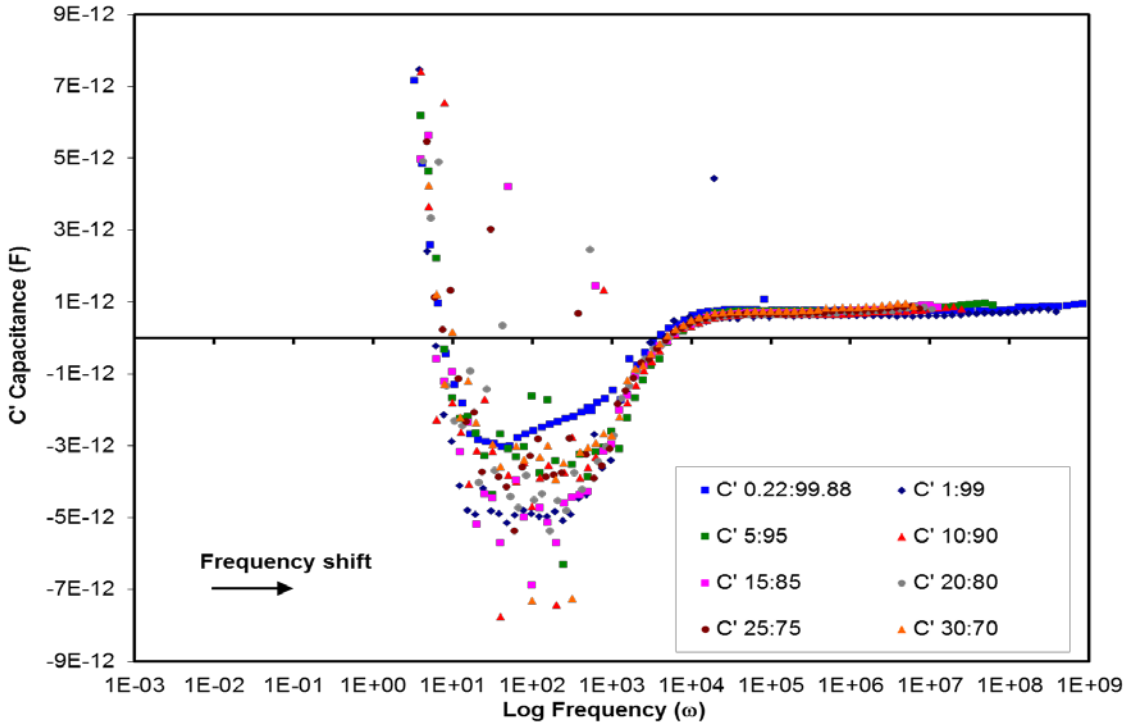

Figure 6-18 Negative capacitance response for percentage weight ratios of AOT:IPM 0.2:99.8, 1:99, 5:95, 10:90, 15:85, 20:80, 25:75, 30:70.

6.3 Effect of Varying the Electrode Spacing

The effect of applying variable field strength was investigated by changing the electrode separation whilst maintaining a fixed voltage. It was noted that varying the cell geometry in this way resulted in unexpected variations in the anomalous but characteristic features such as the breadth of the frequency range and magnitude of the negative capacitance feature see Figure 6-1B. A comparison of composition molar ratio [AOT]/[IPM] = 0.15 for electrode separations of 2 mm and 5 mm is displayed in Figure 6-19. The variation of the characteristic response features of the sample with respect to the electrode separation as the frequency is stepped form high to low frequency did not appear to be uniform. The differences are listed in Table 6-6.

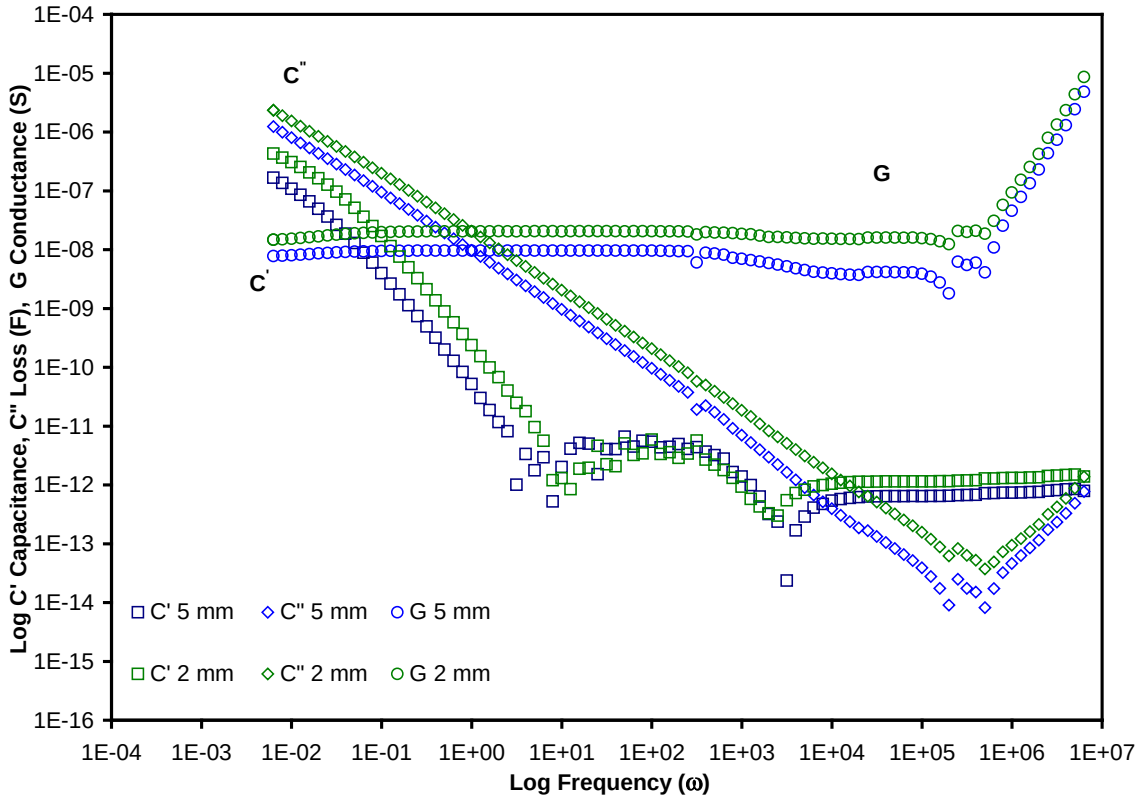

Figure 6-19 AOT:IPM = 20:80 % w/w dielectric response for electrode spacing of 2 mm and 5 mm.

Comparisons of the magnitude changes in the bulk and barrier capacitance and conductance as well as the frequency shift for the intracluster and Maxwell-Wagner barrier charging process, indicated that the polarisation processes were affected differently by the magnitude of the electric field or cell geometry.

Decreasing the electrode separation resulted in the barrier charging process moving to a higher frequency since the charges have a smaller distance to travel to the electrode of

opposite polarity. An examination of the anomalous negative capacitance indicates that the feature approaches a minimum negative value.

Table 6-6 Impact of electrode spacing on the response for AOT/IPM

Parameter / Feature		Electrode Separation		Ratio
		d1 2.0 ± 0.5 (mm)	d2 5.0 ± 0.5 (mm)	d1/d2
C_∞	(F)	$1.20x10^{-12}$	$6.51x10^{-13}$	1.84
Negative C start	(ω)	$1.99x10^{+3}$	$3.15x10^{+3}$	0.63
Negative C end	(ω)	7.91	3.96	2.00
Log frequency width of negative capacitance	Log (ω)	2.40	2.90	0.83
G_∞	(S)	$1.51x10^{-8}$	$3.71x10^{-9}$	4.07
G_{bulk}	(S)	$2.06x10^{-8}$	$9.63x10^{-9}$	2.14
ω_1	(ω)	$1.25x10^{+4}$	$7.91x10^{+3}$	1.58
Frequency G_∞	(ω)	$1.99x10^{+4}$	$1.99x10^{+4}$	1.00
Frequency G_{bulk}	(ω)	$9.96x10^{+1}$	$4.99x10^{+1}$	2.00
Log frequency width of conductance increase	Log (ω)	2.30	2.60	0.88
Log frequency lag between start of G increment and negative C	Log (ω)	1.00	0.8	1.25
Maxwell-Wagner capacitance gradient	+/- 0.01	-1.94	-1.94	1.00
Maxwell-Wagner loss gradient	+/- 0.02	-1.00	-1.00	1.00
Normalisation Frequency shift for Maxwell-Wagner dispersion		1.00	2.18	na
ω_{3bar}	(ω)	$7.94\ x10^{-3}$	$3.98x10^{-3}$	1.99
C_{bar}	(F)	$2.58x10^{-6}$	$2.42x10^{-6}$	1.07

6.3.1 Normalising the Maxwell-Wagner Barrier Charging Feature

Normalising with respect to the barrier charging response feature by frequency shifting the measurement response of 5 mm with respect to the 2 mm sample shows, in the Maxwell-Wagner dispersion frequency region the magnitude of the loss component and consequently the conductance is not impacted by cell geometry (Figure 6-20). The negative capacitance and corresponding increase in conductance features cannot be superimposed when the data is normalised with respect to the barrier charging process. The negative capacitance feature spans a larger frequency range for electrode separation of 5 mm than that of the 2 mm separation and extends to lower frequencies. The characteristic barrier charging frequency of the 2 mm response was approximately twice that of the 5 mm response.

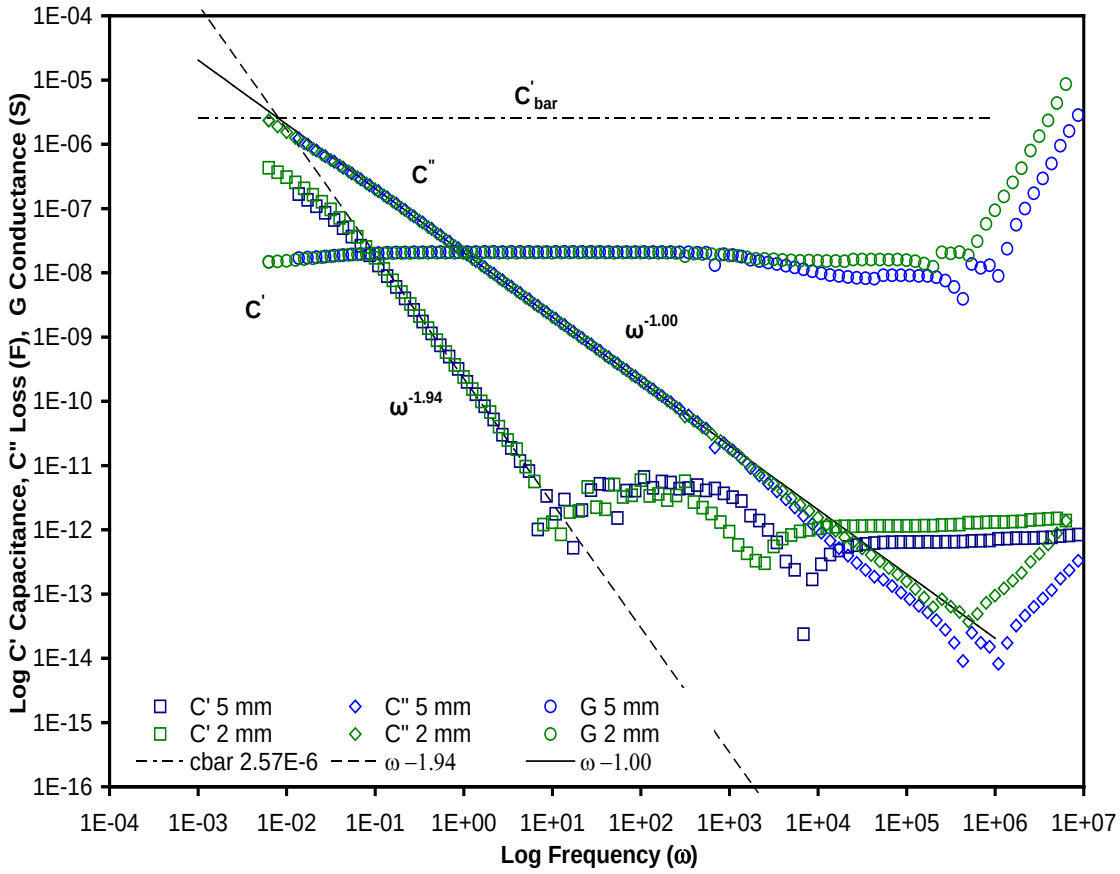

Figure 6-20 Normalised plot for AOT:IPM = 20:80 electrode spacing of 2 mm and 5 mm. Data from 5 mm results frequency shifted by a factor of 2.18 to normalised the Maxwell-Wagner dispersion in the capacitance.

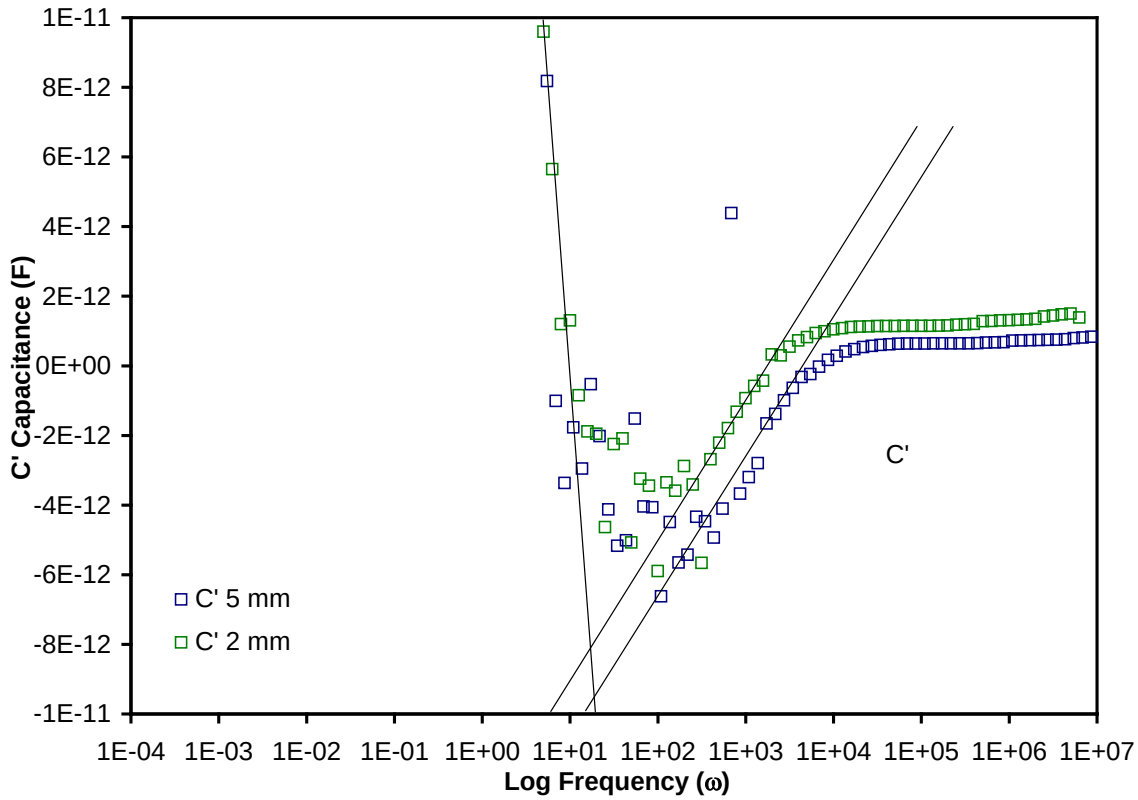

Figure 6-21 Log/lin normalised plot for anomalous negative capacitance for AOT:IPM = 20:80 electrode spacing of 2 mm and 5 mm. Data from 5 mm results frequency shifted by a factor of 2.18 to normalised the Maxwell-Wagner dispersion in the capacitance.

An examination of the Maxwell-Wagner normalised anomalous negative capacitance shown in Figure 6-18 and Figure 6-21 suggested that there are three polarisation processes which contribute to the feature. Firstly a positive bulk phase capacitance process which dominates the response for frequencies above the characteristic intracluster response frequency ω_1; a second positive barrier charging capacitance which begins to dominate the response at frequencies below ω_1 over a visible frequency range of 6-7 decades; and third a negative or depletion capacitance which is dominant at frequencies immediately below ω_1 and over a log frequency range of 2-3 decades. It is evident from Figure 6-21 that the magnitude of the barrier charging process begins to dominate the anomalous feature as the lower frequency part of the response is normalised with the Maxwell-Wagner process.

6.3.2 Normalising the Bulk Capacitance Feature

Normalising the data with respect to the magnitude of the bulk capacitance response shows changes in the magnitude of the bulk capacitance and loss component associated with the barrier charging loss are directly proportional to one another (Figure 6-22). The Maxwell-Wagner dispersion of the capacitance and the transition anomalous negative capacitance and corresponding increase in conductance features cannot be superimposed by normalising this data with respect to the magnitude of bulk capacitance.

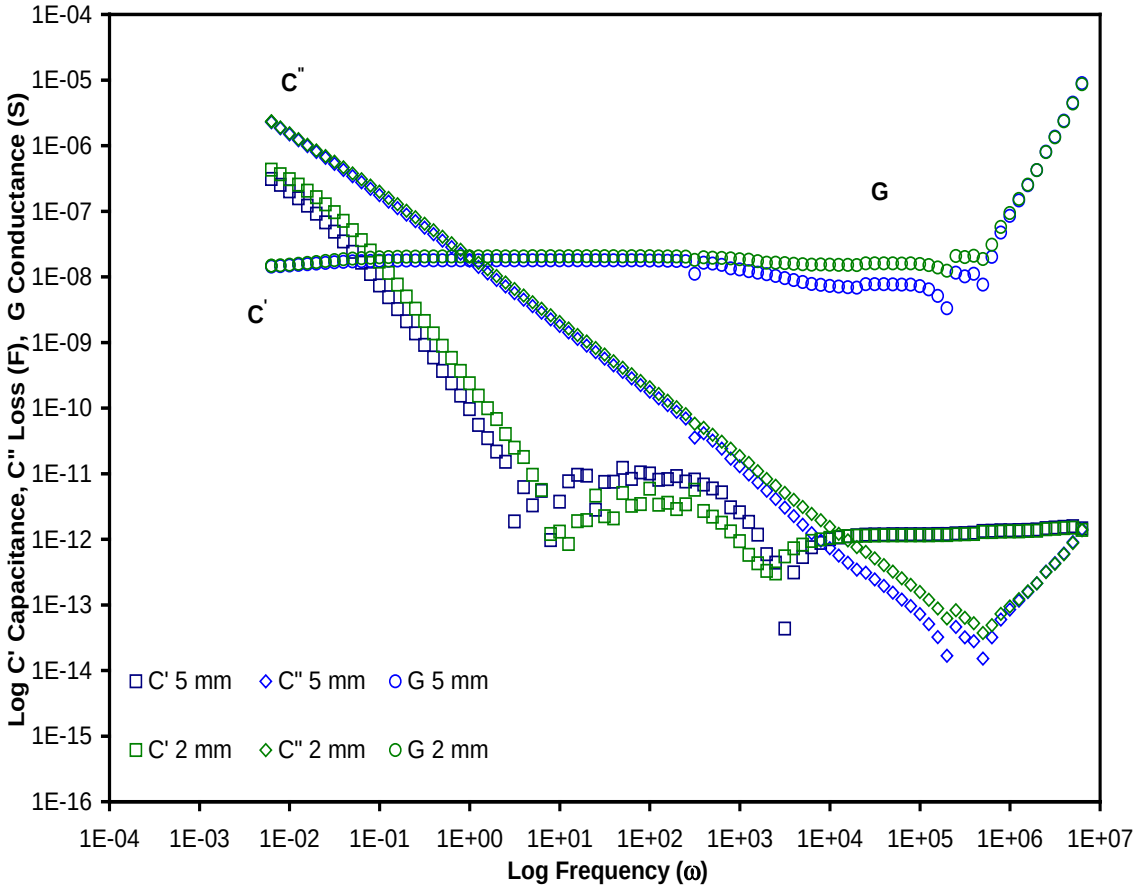

Figure 6-22 Normalised plot for AOT:IPM = 20:80 electrode spacing of 2 mm and 5 mm. Magnitude of the capacitance data from 5 mm results shifted by a factor of 1.85 to normalised the bulk capacitance C'.

6.3.3 Normalising the Bulk Conductance Feature

Normalising the data with respect to the bulk conductance response shows, changes in the magnitude of the bulk/ transition conductance and capacitance associated with the Maxwell-Wagner barrier charging dispersion are directly proportional to one another (Figure 6-23). The Maxwell-Wagner dispersion, the anomalous negative capacitance and corresponding increase in conductance transition features cannot be superimposed by normalising this data with respect to the magnitude of bulk conductance. However examination of the dispersing Maxwell-Wagner capacitance shows a relatively small difference in magnitude with the 5 mm response being the smaller value.

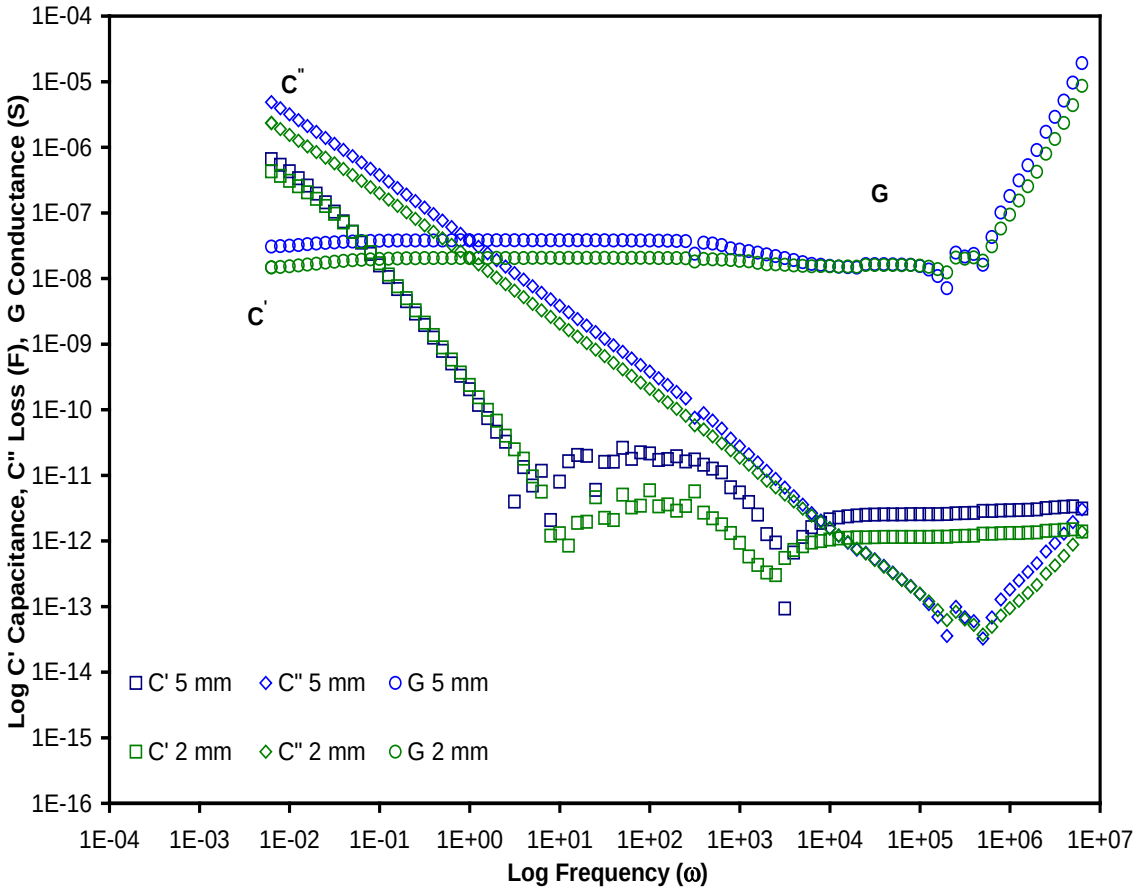

Figure 6-23 Normalised plot for AOT:IPM = 20:80 electrode spacing of 2 mm and 5 mm. Magnitude of the conductance data from 5 mm results shifted by a factor of 3.95 to normalised the bulk conductance G.

6.4 Effect of Varying the Magnitude of the Applied Voltage

The effect of the applied electric field strength on the sample was examined by using the ac voltage sweep technique for selected frequencies with constant electrode spacing. Figure 6-24 shows the response of sample AOT:IPM 30:70 for applied ac voltages of 1.0 V and 0.2 V. The development of the barrier characteristics (frequency $\omega<10^{-1}$) region is clearly affected by the strength of the ac field and shows a clear difference in both shape and magnitude for the two different voltages measured. There are also differences in the magnitude of the anomalous negative capacitance with the 0.2 V applied ac voltage being the most negative in value and also the noisiest.

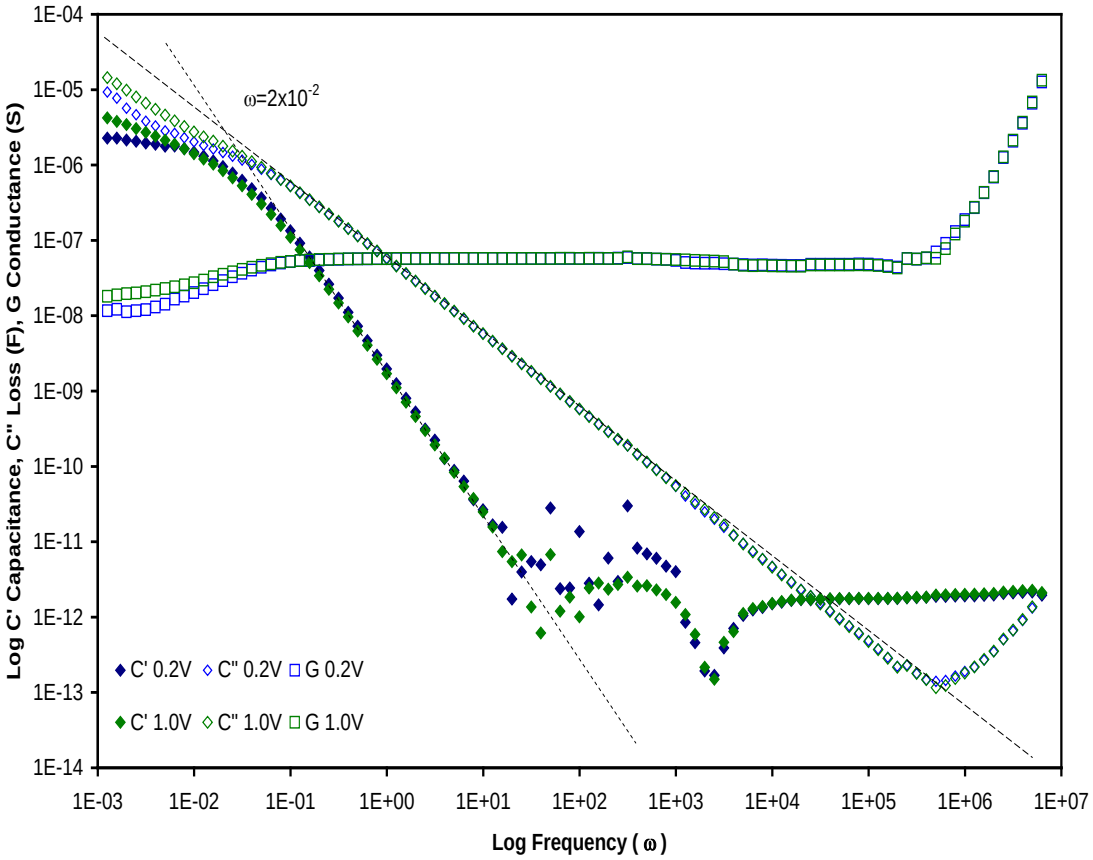

Figure 6-24 Plot for AOT:IPM = 30:70 % w/w, applied ac voltage 0.2 and 1.0 V. The magnitude of the 0.2 V conductance is less than the 1.0 V data in the barrier region and the anomalous negative capacitance is more negative for the 0.2 V data.

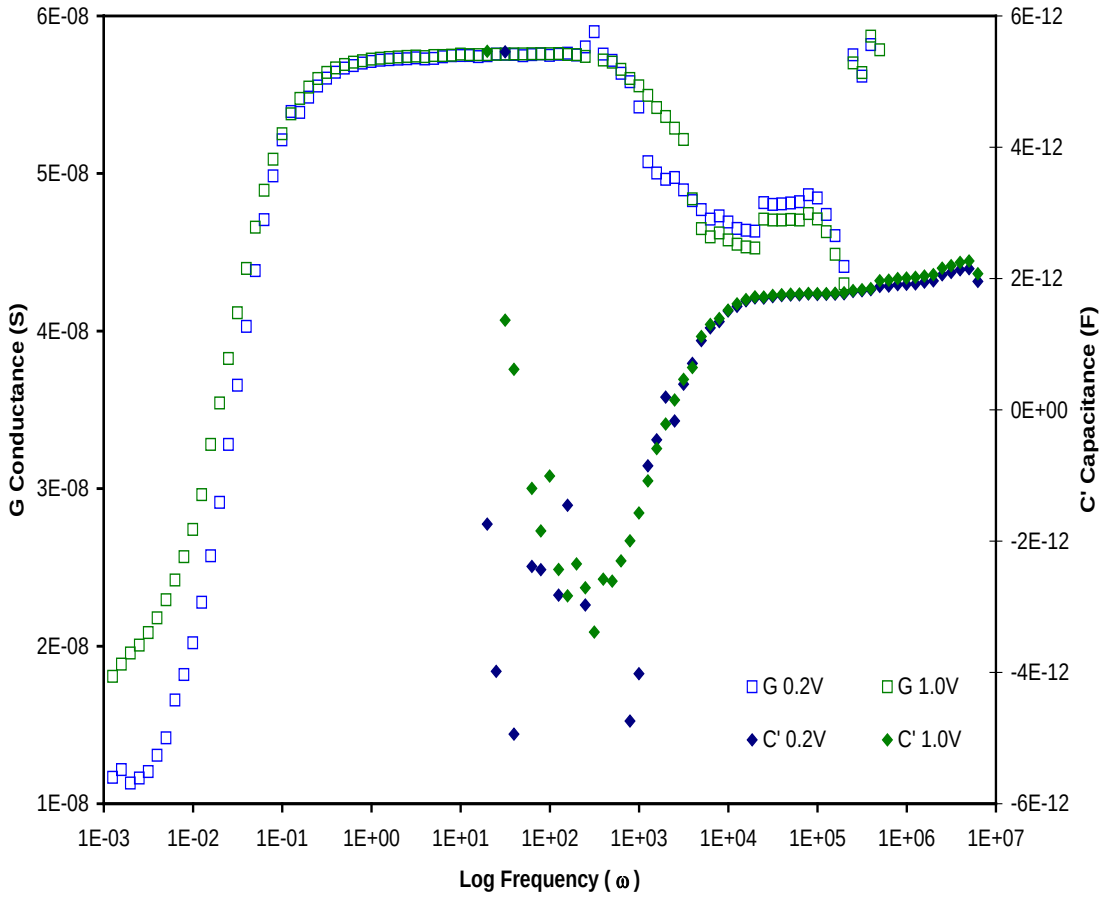

Figure 6-25 Lin/log plot of AOT:IPM = 30:70 % w/w, applied ac voltage 0.2 V and 1.0 V.

Re-plotting the conductance and the capacitance on a lin/log scale Figure 6-25 shows a variation in the bulk-barrier transition frequency region. The magnitude of the 0.2 V conductance is less than the 1.0 V data in the barrier region and the anomalous negative capacitance is more negative for the 0.2 V data whilst a variation in the conductance magnitude can be seen in the bulk-barrier transition region $10^{+2} < \omega < 10^{+5}$.

The effect of varying the applied ac voltage on the bulk-barrier transition frequency region is displayed in Figure 6-26 and Figure 6-27 where the voltage sweep is stepped from 0.05 V to 1.50 V for a selected frequency. The conductance can be seen to undergo two stepped increases in magnitude whist the capacitance experiences an equivalent stepped decrease in magnitude. The stored capacitance charges are reduced or released whist the charge flow or conductance increases. The magnitude increase/decrease in conductance/capacitance remains constant over a voltage range that is frequency dependent. It can be seen that as the frequency is increased towards the

bulk intracluster frequency region, the step transition becomes less sensitive to voltage increments.

A)

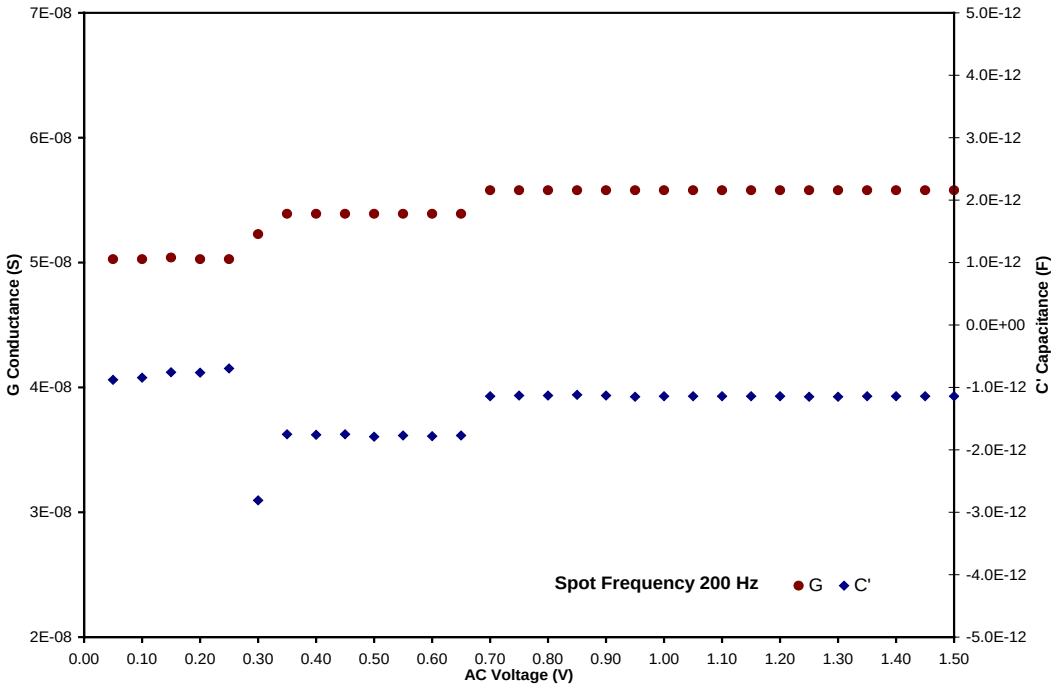

B)

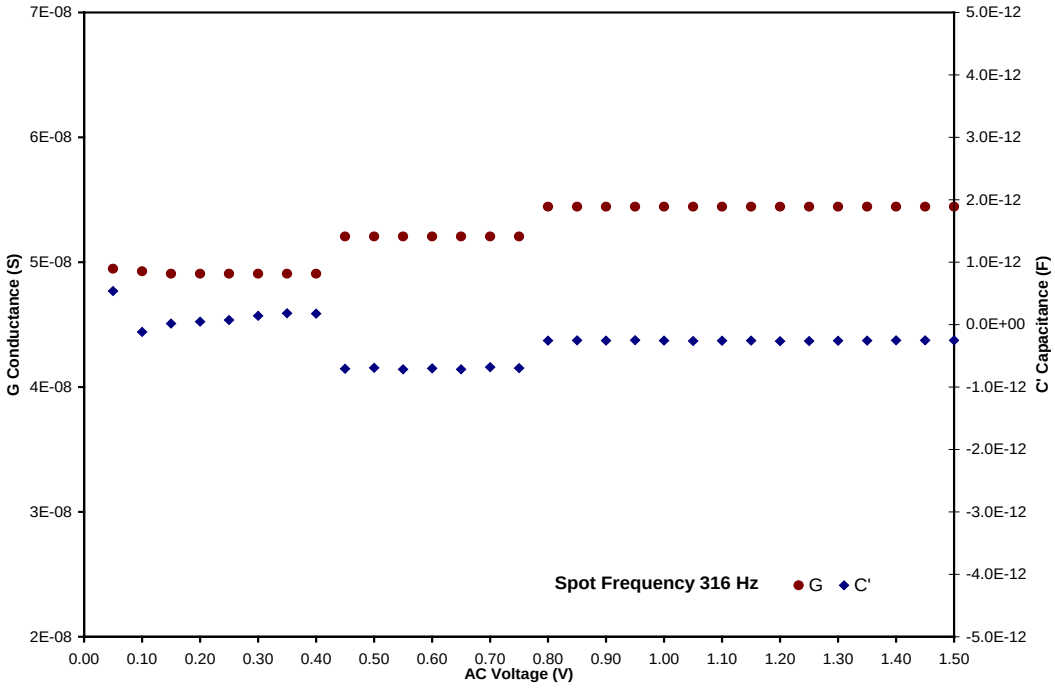

Figure 6-26 Lin/lin plot of AOT:IPM = 30:70 % w/w, applied ac voltage 0.05 V and 1.5 V for frequencies 200 Hz (A) and 316 Hz (B)

A)

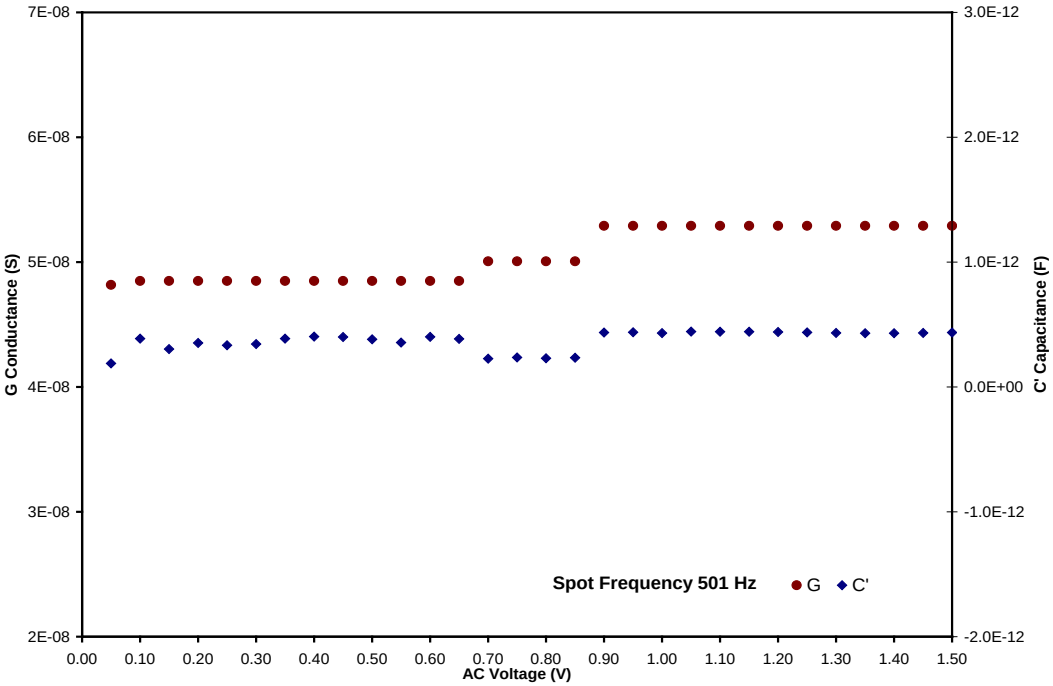

B)

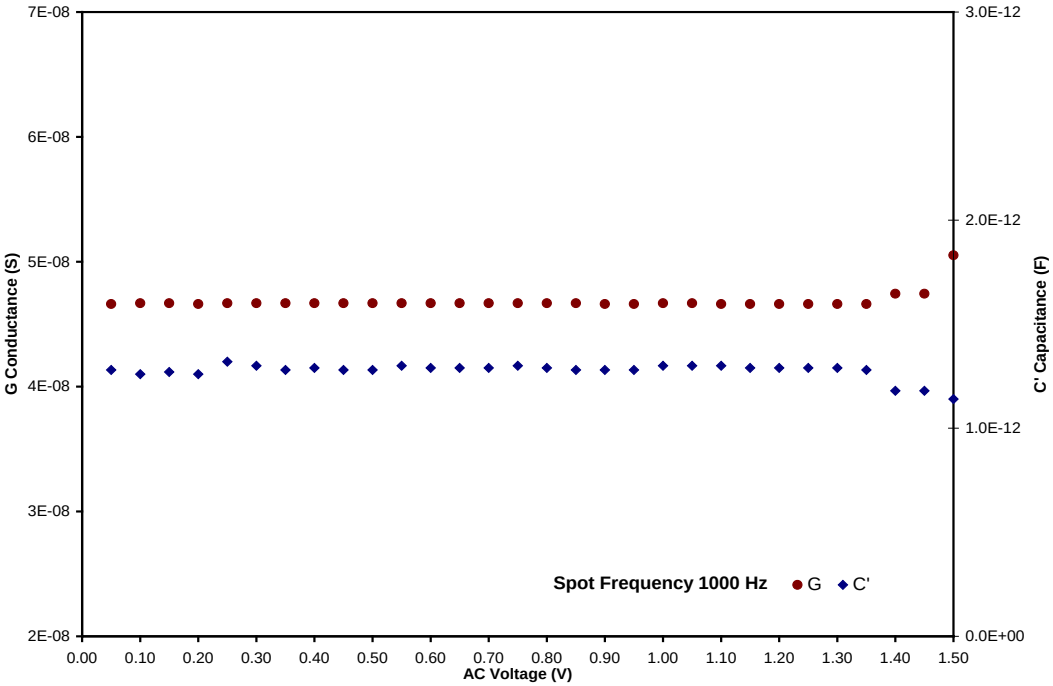

Figure 6-27 Lin/lin plot of AOT:IPM = 30:70 % w/w, applied ac voltage 0.05 V and 1.5 V for frequencies 501 Hz (A) and 1000 Hz (B)

6.4.1 Co- Voltage/Frequency Structural State Transitions

The anomalous negative capacitance region also exhibited stepped transitions in magnitude when examined using the frequency sweep method and applying spot ac voltages in the range 0.05 to 1.00 V using increments of 0.01 V. The cell geometry was adjusted to increase the field strength by reducing the electrode space to approximately 1 mm. Responses of sample composition [AOT]/[IPM] =0.1/99.9 for applied voltages of 0.39 V, 0.40 V, 0.42 V, 084 V are shown in Figure 6-28 to Figure 6-31. Evidence of similar step transitions were however apparent in all of the anhydrous compositions examined.

As the voltage is increased from 0.39 to 0.40 V, the anomalous negative capacitance exhibited a stepped increase in magnitude i.e. becoming less negative for frequencies below 1 Hz. The conductance experienced a corresponding step decrease in magnitude for the same frequency range. Further increases in the applied voltage magnitude resulted in additional capacitance datum point making the step transition increase as the frequency increase Figure 6-30 and Figure 6-31.

Further indications of frequency dependence of the state transitions have been observed in Figure 6-18 i.e. the plot of the normalised negative capacitance for all anhydrous concentration ratios. The magnitude of the negative capacitance appears to have 3 levels. The lowest and most negative level corresponds to AOT % w/w 1, 15, 20; the middle level ratios of AOT % w/w 5, 10, 25, 30 and highest and least negative capacitance; AOT % w/w ~ 0.2.

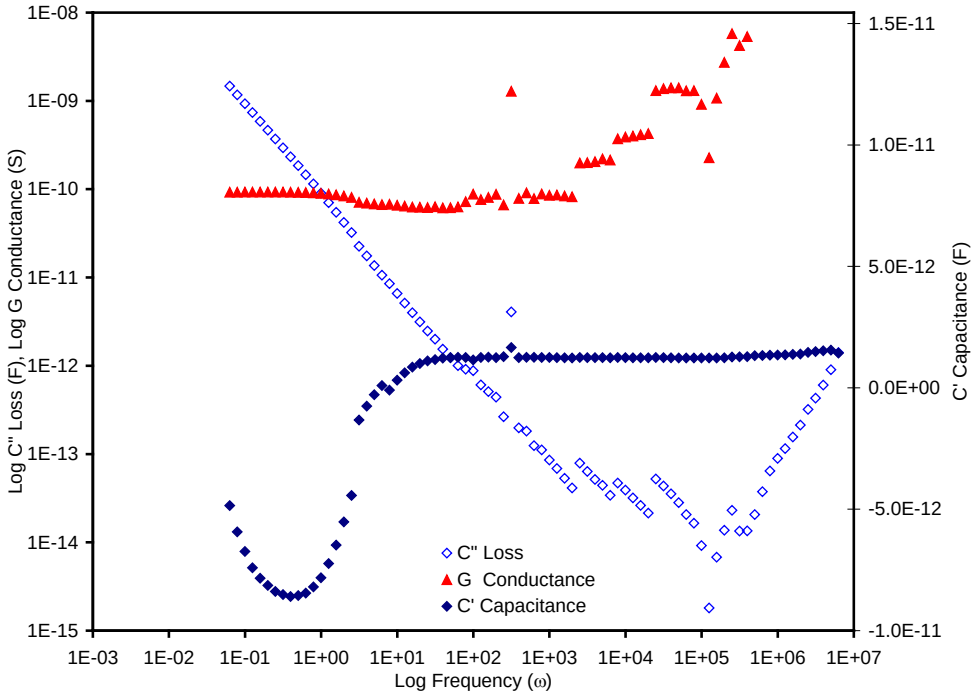

Figure 6-28 AOT:IPM = 0.1:99.9 response measured with 0.39 V ac.

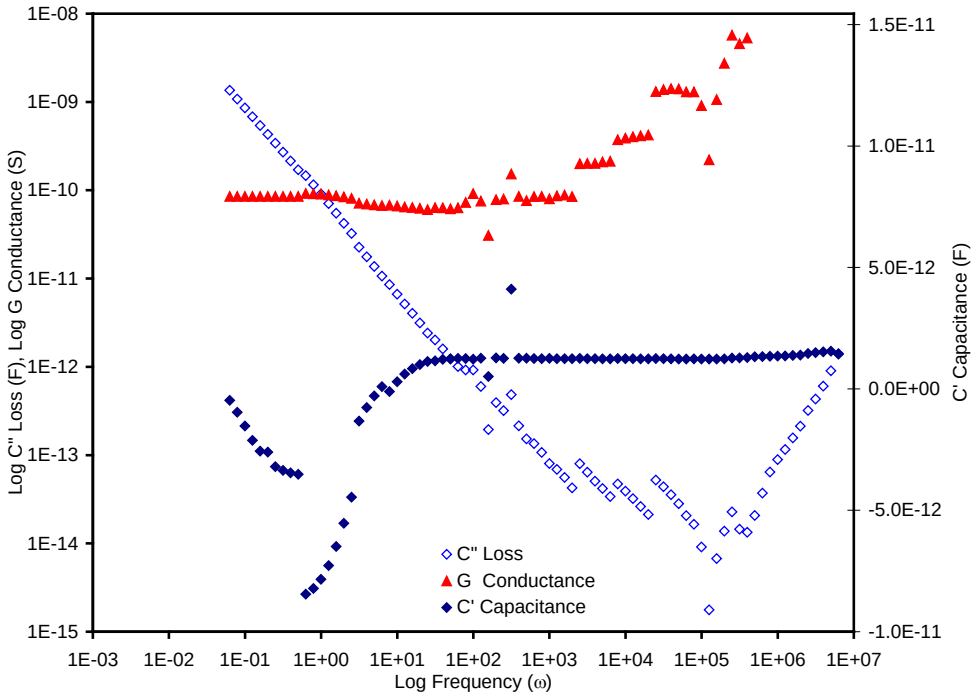

Figure 6-29 AOT:IPM = 0.1:99.9 response measured with 0.40 V ac showing a step increase in capacitance for frequencies below ω=0.628 Rad/s

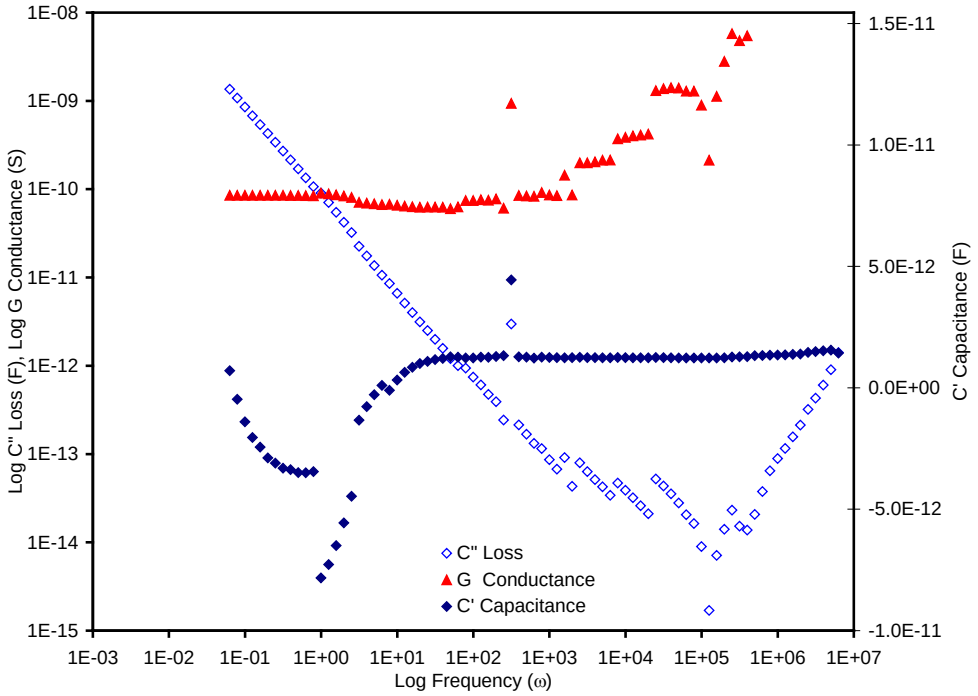

Figure 6-30 AOT:IPM = 0.1:99.9 response measured with 0.42 V ac showing a step increase in capacitance for frequencies below 0.99 Rad/s

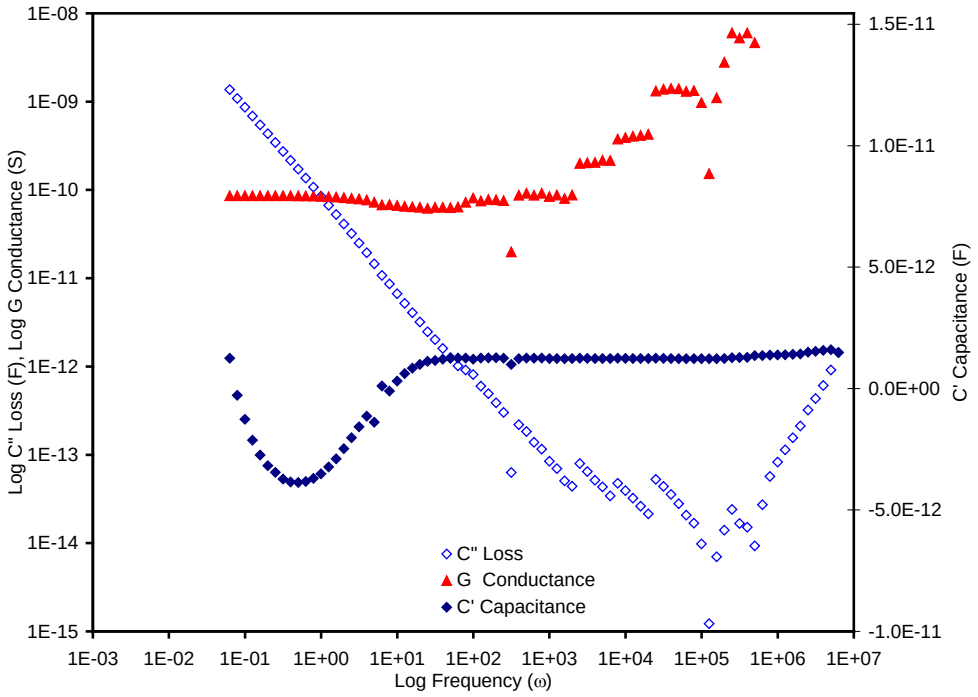

Figure 6-31 AOT:IPM = 0.1:99.9 response measured with 0.84 V ac.

6.5 Intercluster Quasi-dc Index p

The value of intercluster index p is plotted in Figure 6-32 and provides an indication of the efficiency of the charge transfer between clusters. A value of p = 1 would indicate that a charge was completely free of its cluster and hence dc conduction would occur. The relatively high values derived 0.6 < "p" < 1 indicates that the charges are fairly mobile but are still effectively bound to their original clusters.

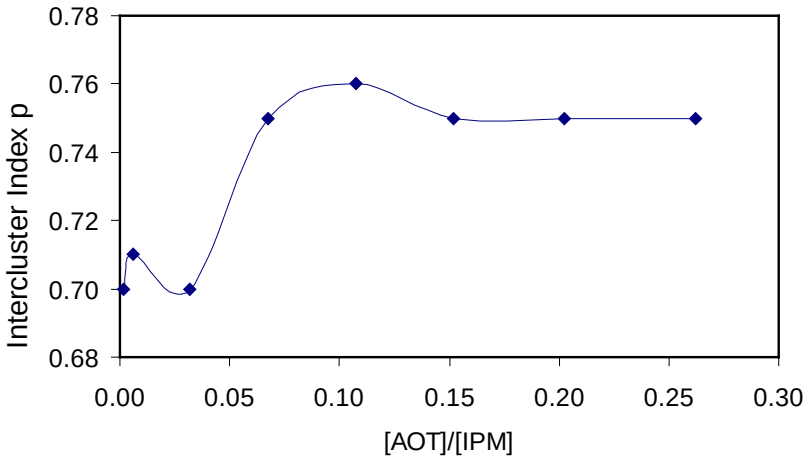

Figure 6-32 Intercluster index p measure of the efficiency of charge transfer between clusters as the molar ratio is increased.

6.6 Modelling of AOT/IPM Dielectric Response

The dielectric spectra obtained for two component composition contain features that were common across the weight ratio sets examined. Re-presenting the data from a typical log frequency response in the form of an impedance plot where the imaginary component of the complex impedance Z" is plotted on the Y axis whilst the real component Z' is plotted on the X axis (Z"/Z'). Figure 6-33 displays two approximate semi-circles which are indicative of the sample exhibiting a bulk-barrier series circuit configuration [Jonscher 1983]. The bulk response appears largely unaffected by the change in magnitude of the applied ac voltage whilst the magnitude of the barrier response decreases as the applied voltage increases.

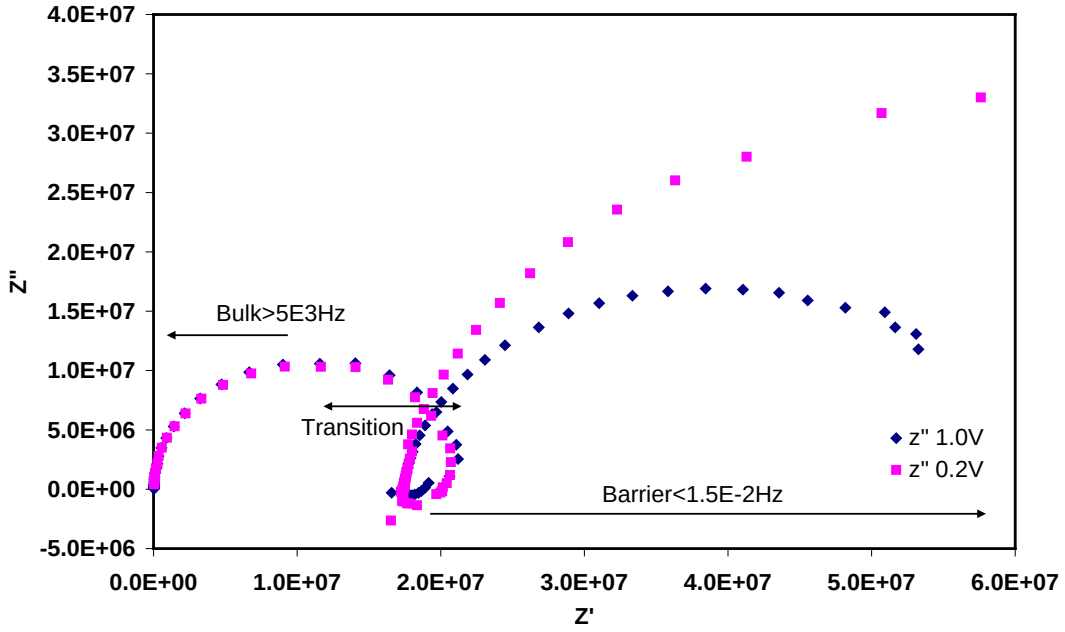

Figure 6-33 Lin/lin impedance plot of AOT:IPM = 30:70, 0.2 V and 1.0 V ac applied voltage.

The characteristic response features can be represented as a series pair of electric circuits comprised of bulk or macroscopic conductance in parallel with bulk capacitance which are in series with a dispersive barrier capacitance. The model for this circuit when seeded with appropriate parameters can provide information on features which may be just on the edge of the measuring capabilities of the equipment. The plot of modelled data in Figure 6-34 shows three points where the capacitance and loss components cross over. The frequencies ($\omega_j = 1/\tau_j$, j = 1, 2, 3 and τ_j are characteristic times) at which the crossovers occur are characteristic of the sample and the conditions under which they being measured. The corresponding characteristic times have been attributed to the relaxation of the material within a particle or charges bound to a cluster,

τ_1; the relaxation of a barrier between particles or for charges to move between clusters, τ_2; the Maxwell-Wagner process which is associated with the transport of charges within clusters which are blocked by the capacitance of the barriers, τ_3 (Hill and Cooper [1992]).

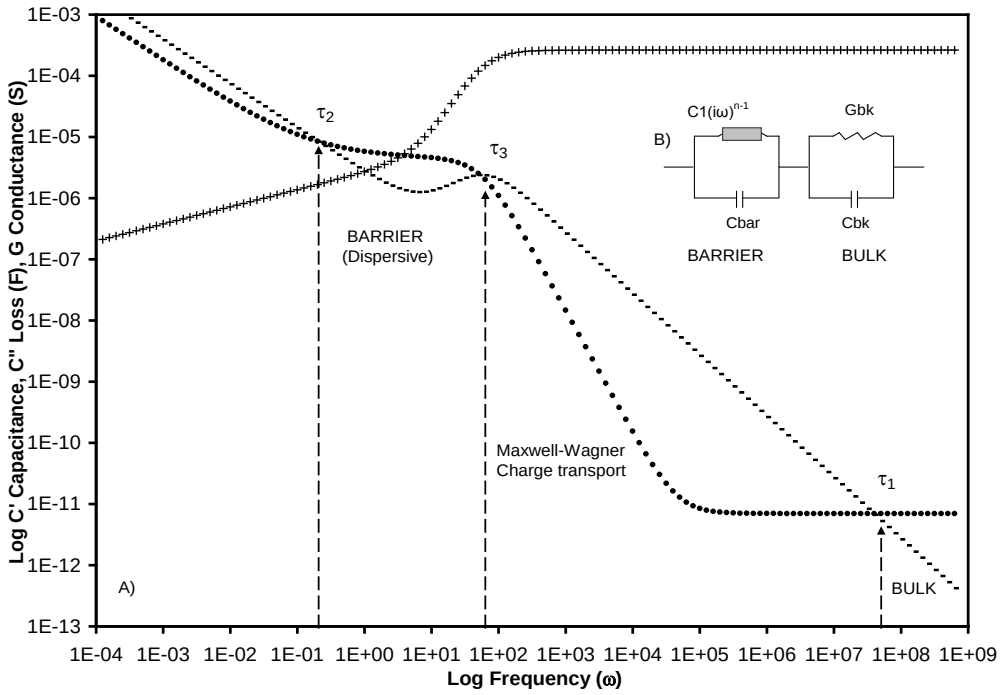

Figure 6-34 A) Plot of modelled bulk- dispersive barrier series circuit insert B) using parameters which generate characteristic relaxation features intracluster τ_1, barrier, τ_3, and intercluster, τ_2.

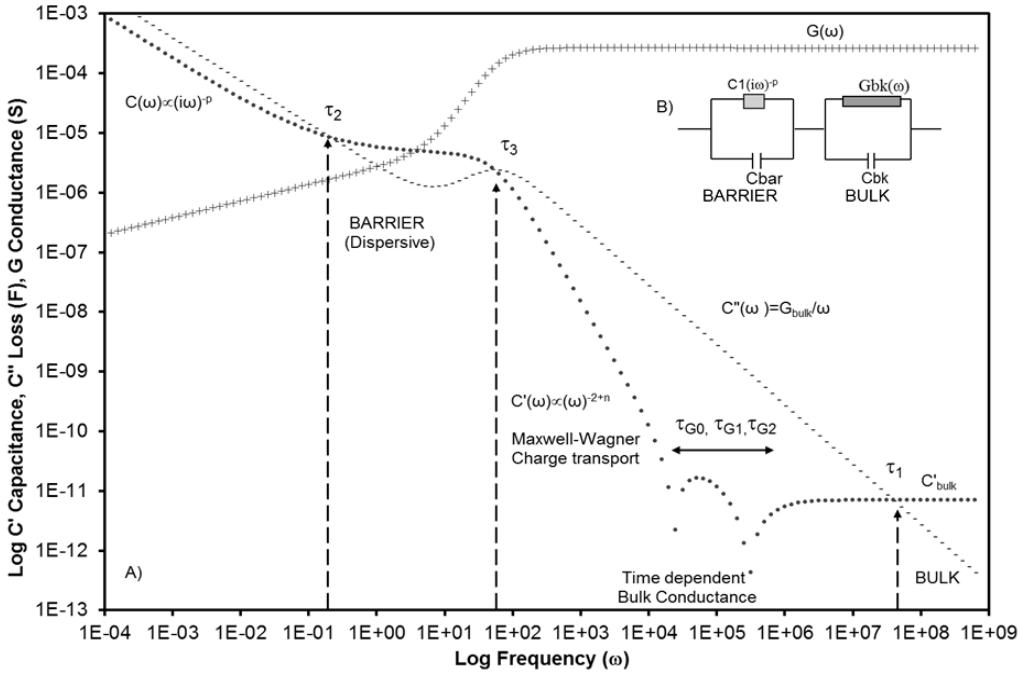

Figure 6-35 A) Plot of modelled bulk- dispersive barrier series circuit with a time dependent bulk conductance element inset B) using parameters which generate the anomalous time dependent conductance (with characteristic times τ_{G0}, τ_{G1} and τ_{G2}), negative capacitance and the characteristic relaxation times for intracluster, τ_1, barrier, τ_3, and intercluster, τ_3, features.

The experimental spectral results contained an anomalous negative capacitance and small increase in conductance in the bulk region of the response as the ac frequency $\omega > 0$ (Figure 6-2 and Figure 6-3). It was determined from the electrode spacing and voltage variation that this response was due to the overlapping of the barrier charging process and capacitance depletion process assumed to be due to structural changes at the boundaries of the clusters of the IPM molecules in the bulk phase. The circuit described above (Figure 6-34B) cannot produce either of the anomalous features as the structural changes require the bulk conductance element to have frequency dependent characteristics in order for the bulk capacitance to decrease to negative values. Hence the circuit model for the anomalous response depicted in Figure 6-35B is modelled using the quasi-dc Dissado-Hill (DH) power law cluster model discussed in sections 2.5 and 2.6 and a replacing the constant bulk conductance element with a frequency dependent term. Fishman *et al.* [1979] and Dissado [1990] reported such sign changes in capacitance of squid axons and other animal tissue and used a linearised frequency dependent conductance term to model voltage dependent structural changes in biological cell membranes (Equation 2-28) above (i.e. gating or the opening and closing of pores) which either allowed or blocked the passage of sodium or potassium ions into or out of a cell.

The parameters used to model the anhydrous compositions are detailed in Table 6-7. An example of the experimental data modelled for ratio AOT:IPM =30:70 is displayed in Figure 6-36. The goodness of fit for this curve fit model, adapted to include linearised frequency dependent conductance term which is used to model the behaviour of an active membrane structure, and confirms the concept; that the carbonyl structures in the IPM molecule are able to form boundaries which restructure themselves with a frequency that is dependent on the size of the clusters, which in turn is linearly dependent upon the molar ratio of [AOT]/[IPM]

Relaxation times for the characteristic features include intracluster, time dependent conductance increments and barrier charging, derived from the model, and are detailed in Table 6-8. The relaxation times associated with the frequency dependent conductance increment appear to be linearly related to the molar ratio [AOT]/[IPM] of

two of the constant conductance increments. The third conductance increment does not exhibit the same linear trend, see Figure 6-37.

Table 6-7 AOT/IPM Dissado-Hill cluster model adapted to include linearised bulk conductance parameters

			Barrier parameter			Bulk parameters				
[AOT]/ [IPM]	% AOT by weight	Effective permittivity ε_r	Barrier Capacitance Cbar (μF)	Index ω^{-p} p	Barrier Magnitude (μF)	C(∞) (pF)	G_∞ (nS)	ΔG_0 (nS)	ΔG_1 (nS)	ΔG_2 (nS)
0	0	3.25								
0.0014	0.2	3.25	1.85	0.70	0.04	0.760	0.0354	0.0124	0.135	0.0024
0.0061	1.0	3.30	3.30	0.71	0.08	0.690	0.690	0.230	0.130	0.014
0.0320	5.0	3.33	1.30	0.70	0.10	0.773	0.690	0.590	0.396	0.124
0.0678	10.0	3.42	1.80	0.75	0.09	0.680	1.50	0.900	0.128	0.530
0.1074	15.0	3.50	1.89	0.76	0.11	0.729	3.00	4.20	1.05	0
0.1521	20.0	3.58	1.87	0.75	0.10	0.651	3.47	0.770	4.70	0.700
0.2023	25.0	3.66	1.87	0.75	0.10	0.661	4.55	2.77	4.76	0.620
0.2624	30.0	3.75	1.80	0.75	1.50	0.775	7.51	1.20	2.60	5.210

Table 6-8 AOT/IPM Characteristic relaxation times and bulk conductance increment

[AOT]/ [IPM]	Time dependent bulk conductance increments			Bulk conductance		Intra cluster relaxation	Barrier charging	Index n $\omega^{-(2-n)}$	Index p ω^{-p}	Est. barrier thickness
	τ_{G0} (μs)	$\tau_{G\,1}$ (μs)	$\tau_{G\,2}$ (μs)	G_0 (nS)	G_∞ (nS)	τ_1 (μs)	τ_3 (s)	n ±0.02	p ±0.02	d_{bar} (nm)
0										
0.00140	200,000	66,700	58,800	0.0638	0.0354	21,500.00	29,700	-0.04	0.70	1.85
0.00609	26,300	14,300	14,300	0.364	0.690	5,660.00	9,290	0.02	0.71	0.94
0.03199	4,000	4,000	1,140	1.80	0.690	1,120.00	778	0.09	0.70	2.60
0.06767	2,000	1,250	1,250	4.21	1.50	453.00	449	0.09	0.75	1.74
0.10741	1,110	345	345	8.29	3.00	243.00	244	0.06	0.76	1.81
0.15212	1,330	769	100	9.63	3.47	188.00	204	0.08	0.75	1.68
0.20231	800	439	40	12.70	4.55	145.00	155	0.09	0.75	1.74
0.26240	633	400	400	16.60	7.51	10.30	118	0.09	0.75	1.25

A)

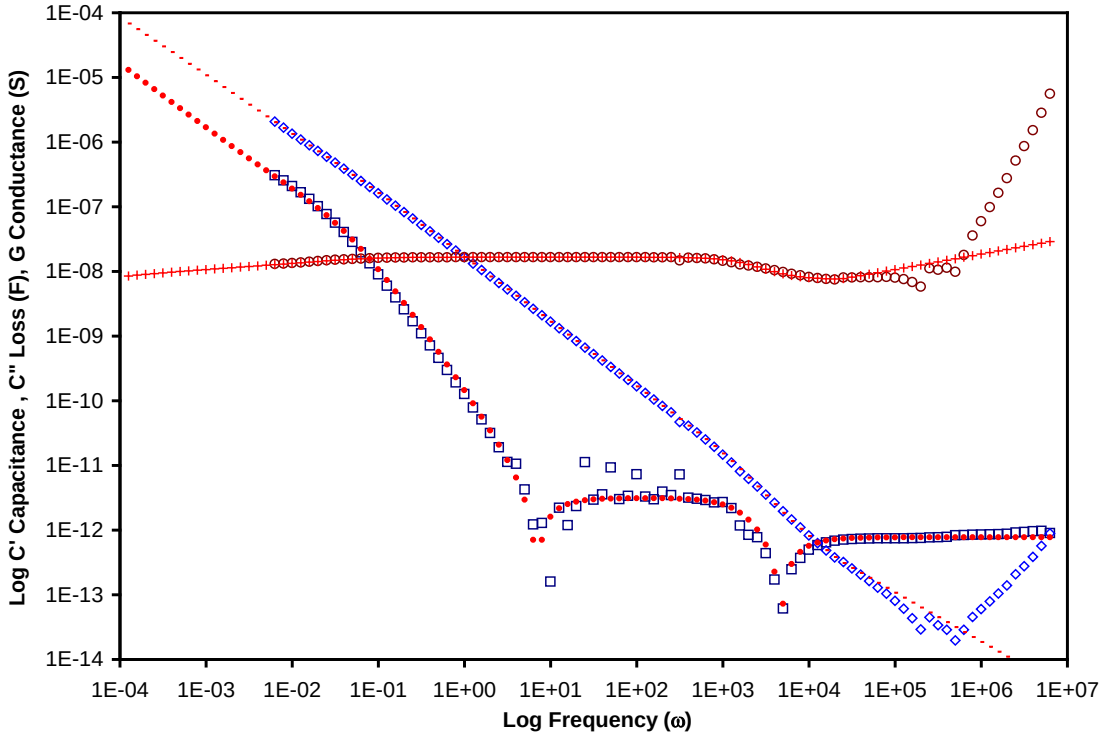

B)

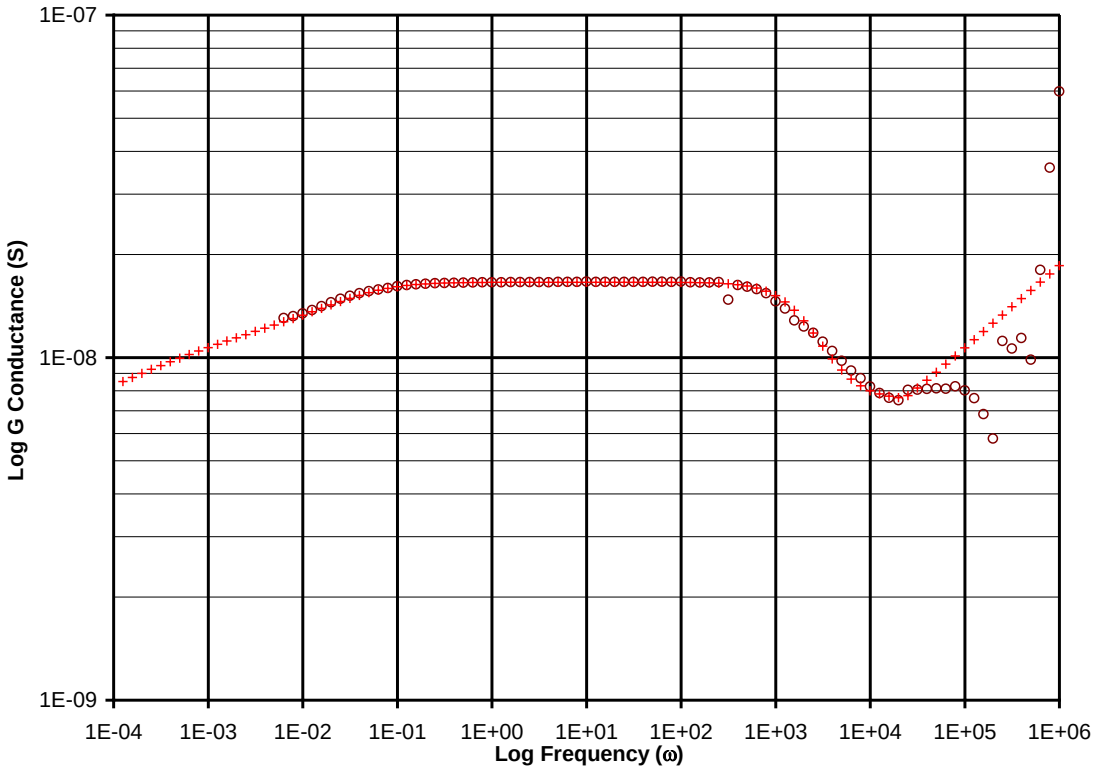

Figure 6-36 (A) Experimental data for AOT:IPM = 30:70 modelled using the adapted frequency dependent QDC-DH model. (B) Model fit for the anomalous conductance increase.

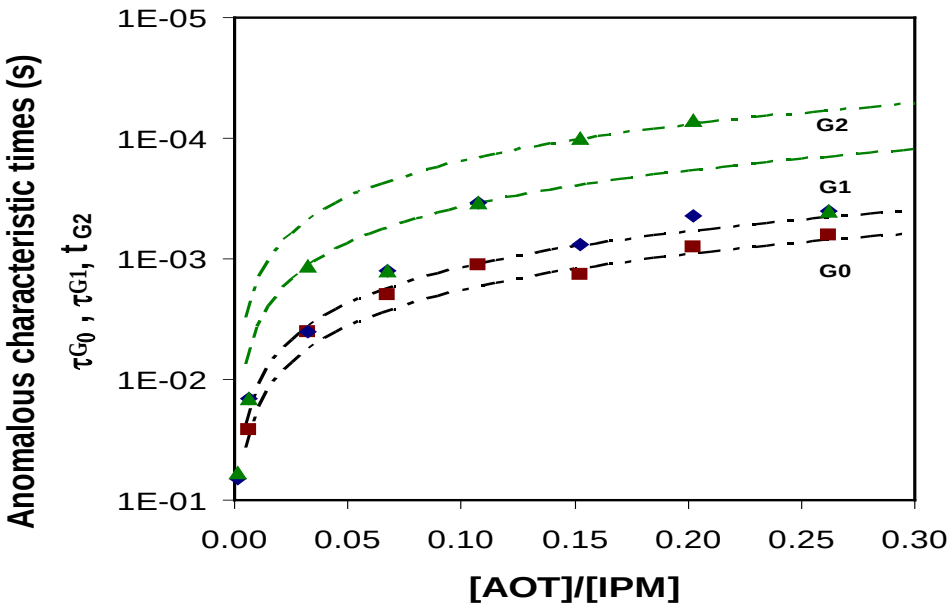

Figure 6-37 Log /lin plot of characteristic times for the frequency dependent bulk conductance increase with decreasing frequency. ■τ_{G0}, ♦τ_{G1}, and ▲ τ_{G2}

Table 6-9 AOT:IPM = 20:80 DH cluster model parameters for electrode spacing 2 mm and 5 mm

		Electrode Separation		Ratio
Parameter		2.0 ± 0.5 (mm)	5± 0.5 (mm)	5 (mm)/2 (mm)
C_∞	(F)	1.20×10^{-12}	6.51×10^{-13}	1.84
G_∞	(S)	1.51×10^{-8}	3.47×10^{-9}	4.35
G_0	(S)	2.06×10^{-8}	9.64×10^{-9}	2.14
ΔG0	(S)	2.30×10^{-9}	7.70×10^{-10}	2.99
ΔG1	(S)	1.60×10^{-9}	4.70×10^{-9}	0.34
ΔG2	(S)	1.60×10^{-9}	7.00×10^{-10}	2.29
C_{bar}	(F)	1.80×10^{-6}	1.80×10^{-6}	1.00
B		1.30×10^{-7}	9.00×10^{-8}	1.44
P		0.77	0.77	1.00
ω_{G0}	(Rad/s)	$1.26\times10^{+3}$	$7.50\times10^{+2}$	1.68
ω_{G1}	(Rad/s)	$1.26\times10^{+3}$	$1.30\times10^{+3}$	0.97
ω_{G2}	(Rad/s)	$1.26\times10^{+3}$	$9.96\times10^{+3}$	0.13
ω_1	(Rad/s)	$1.26\times10^{+4}$	$5.33\times10^{+3}$	2.36
ω_3	(Rad/s)	1.07×10^{-2}	5.10×10^{-3}	2.09

The frequency adapted DH cluster model was also used to examine the impact of varying the electrode separation for a single sample. Table 6-9 and Table 6-10 contain the parameter values required to model AOT:IPM = 20:80 ratio while the modelled data is superimposed on the experimental response data and plotted in Figure 6-38.

Table 6-10 AOT:IPM = 20:80 characteristic relaxation times for electrode spacing 2 mm and 5 mm

		Electrode Separation		
Parameter		2.0 ± 0.5 (mm)	5± 0.5 (mm)	5 (mm)/2 (mm)
τ_{G0}	(s)	$7.94x10^{-4}$	$1.33x10^{-3}$	0.60
τ_{G1}	(s)	$7.94x10^{-4}$	$7.69x10^{-4}$	1.03
τ_{G2}	(s)	$7.94x10^{-4}$	$1.00x10^{-4}$	7.90
τ_1	(s)	$7.95\ x10^{-5}$	$1.88x10^{-4}$	0.42
τ_3	(s)	$9.37\ x10^{+1}$	$1.96x10^{+2}$	0.48
Log(ΔFreq) Negative capacitance		2.102	3.00	0.70

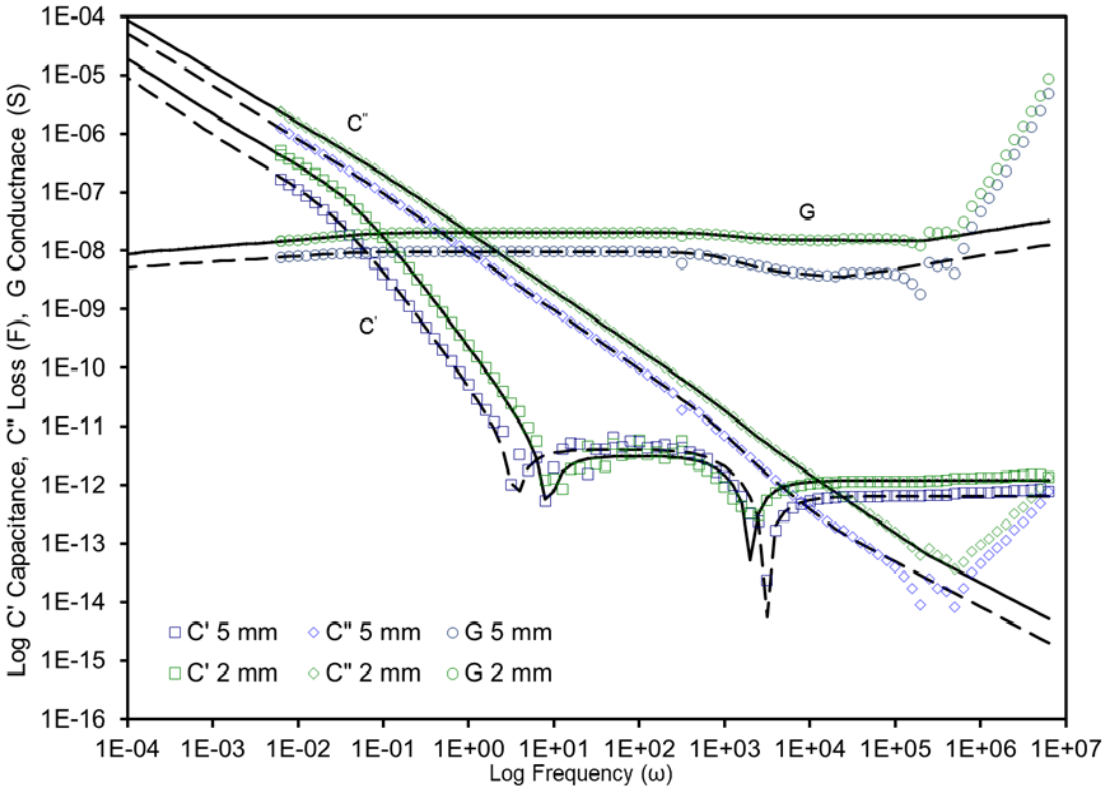

Figure 6-38 AOT:IPM = 20:80 for electrode spacing 2 mm and 5 mm. Dashed and continuous lines are curve fit for 5 mm and 2 mm respectively

6.7 Discussion

6.7.1 Curve Fitting the anomalous Negative Capacitance and Conductance Increase

An increase in the magnitude of conductance was observed for all composition ratios containing IPM and AOT. Although the magnitude of the conductance increase is relatively small (ΔG approximate 1.76 greater than G_∞) the occurrence of this increase is indicative of a structural change which results in an increase in the transfer of charges through the sample, which is dependent on the frequency of the applied ac field. The magnitude of the conductance response normally decreases as the frequency of the applied ac field is reduced to zero. This is due to a build-up of a barrier layer at the electrodes or interfaces which consequently reduces or blocks charge transport. Hence it is unusual to observe an increase in the conductance magnitude as the frequency $\omega \rightarrow 0$.

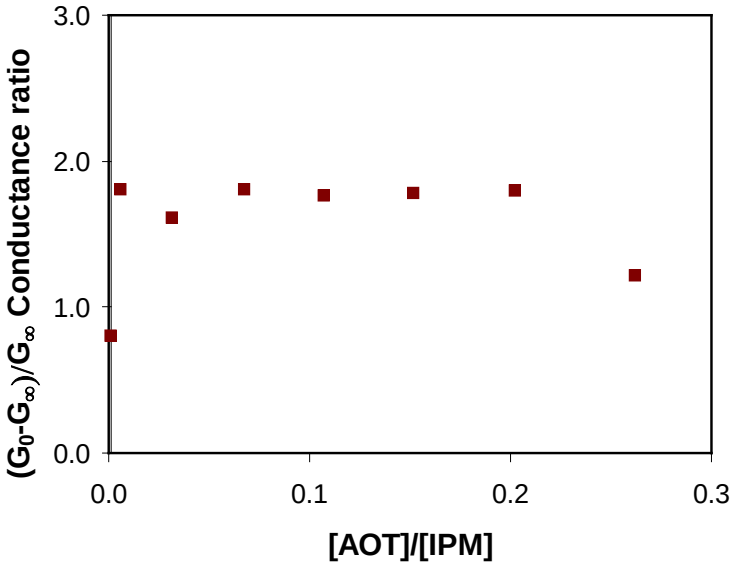

Figure 6-39 Ratio of the conductance increase to the minimum conductance

A second and very striking feature in the response is the occurrence of negative values in the capacitance over a frequency range of 10^{+3} Hz to 1 Hz (region A Figure 6-1 and Figure 6-3). Capacitance is the storage of charges and the values are positive for the majority of materials. Negative values can occur when additional charges are introduced to the sample by way of the electrode or via structural changes which enable previously trapped charges to flow through the sample i.e. an increase in conductance resulting in the capacitor or charge reservoir being discharged or depleted.

The total value of the capacitance in this frequency region is a sum of the negative capacitance due to the time dependent conductance and the positive contribution due to the charging of the barrier layer process. Hence the total capacitance is only negative if the magnitude of the time dependent conductance component is greater than the sum of the bulk and the interface charging capacitance C_{bulk} - $\tau_0 G_0$. The maximum negative amplitude is $G_0 = G(\omega_{low}) - G(\omega_{high})$. The bulk capacitance is proportional to the area of the sample "A" and inversely proportional to the electrode separation "d". Hence if the electrode separation is reduced or the area increased the maximum negative capacitance may be prevented from being achieved. To illustrate this the magnitude of bulk capacitance C_∞ modelled for composition AOT:IPM=30:70 has been altered from 0.0775 pF to 0.775 pF, 7.75pF, 77.5 pF and plotted in Figure 6-40 A, B, C and D respectively.

Reducing the area/spacing A/d ratio by one order of magnitude from C_∞ 0.775 pF (measured value) causes the net capacitance to become more negative Figure 6-40 a) C_∞ = 0.0775 pF relative to Figure 6-40 b) C_∞ = 0.775 pF. Increasing the A/d ratio by one order of magnitude Figure 6-40 c) C_∞ = 7.75 pF causes the capacitance to show a reduction in magnitude but it does not become negative. Increasing the A/d ratio by two orders of magnitude C_∞ = 77.5 pF Figure 6-40 d), eliminates the appearance of the net reduction in magnitude of the capacitance. Note the conductance continues to experience an increase in magnitude however the net impact (Cbulk - τG0) is insufficient to impact a visual reduction in the real component of the complex capacitance.

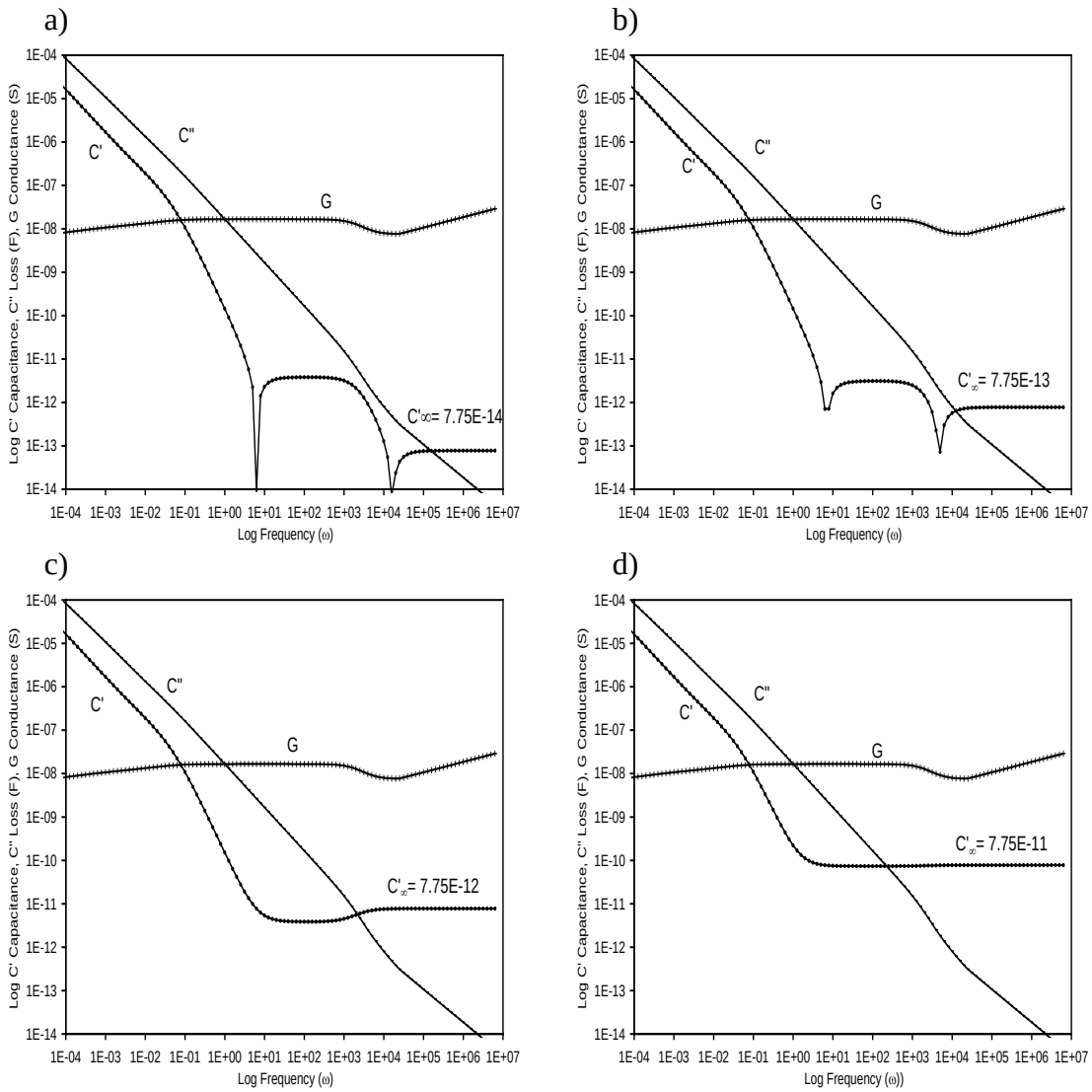

Figure 6-40 Curve fit of the effect of altering the magnitude of the high frequency capacitance C_∞ only on the magnitude of the negative capacitance. A) C_∞ = 0.0775 pF, b) C_∞ = 0.775 pF, c) C_∞ = 7.75 pF, d) C_∞ = 77.5 pF.

6.7.2 Maxwell-Wagner Interface Barrier Structure

The large dispersion of the capacitance Figure 6-1 region C is consistent with the build-up of charges at an interface forming a thin barrier layer. This is evidenced by the onset of a reduction in the magnitude of the conductance Figure 6-36B and relatively high magnitude of the barrier capacitance when compared to the bulk capacitance Figure 6-36A. Examining the structure of the barrier layer in microscopically homogeneous systems can provide information on the properties of the system. However we have a bulk and a dispersed phase hence it is only possible to obtain an approximation. If one assumes the sample composition has an effective permittivity (estimate of the polarisability) made up of the percentage ratios by weight of the constituents an

estimate of the barrier thickness can be obtained from the ratios of the bulk and the barrier capacitances.

$$\varepsilon_{eff} = (\varepsilon_{rAOT} * AOT\%) + (\varepsilon_{rIPM} * IPM\%) + (\varepsilon_{rH_2O} * H_2O\%) \quad \text{Eqn. 6-2}$$

$$d_{bar} = \frac{C_{bulk}}{C_{bar}} * \frac{\varepsilon_{effbar}}{\varepsilon_{bulk}} d_{bulk} \quad \text{Eqn. 6-3}$$

It should be noted that the surfactant is assumed to have 2% water as supplied by the manufacturer. The relative permittivity values of AOT, IPM and water 3.2, 3.25 and 78.9 respectively listed in Table 4-1 were used to calculate the effective permittivity of each composition.

The estimates for the barrier thickness ranges from 1 nm to 3 nm with an average of 1.70 nm +/- 0.05 nm. This suggests that the barrier layer does not contain micelles or microemulsion aggregates as particle sizing carried on these samples did not detect any particles. However Zulauf and Eicke [1979] observed particles with a Stokes radius r_h = 1.5 nm +/- 0.03 nm (3 nm diameter) for anhydrous samples comprised of AOT and isooctane. This radius was invariant upon changes to the concentration of the surfactant in the range $8x10^{-3}$mol to $2x10^{-2}$mol.

Light scattering studies (chapter 4) did not detect any aggregates for mixtures of IPM:AOT:H2O samples containing less than W_0 =[H2O]/[AOT]< 10. No water was added to the samples in this study hence it is more likely that the barrier is comprised of a single layer of AOT and IPM molecules.

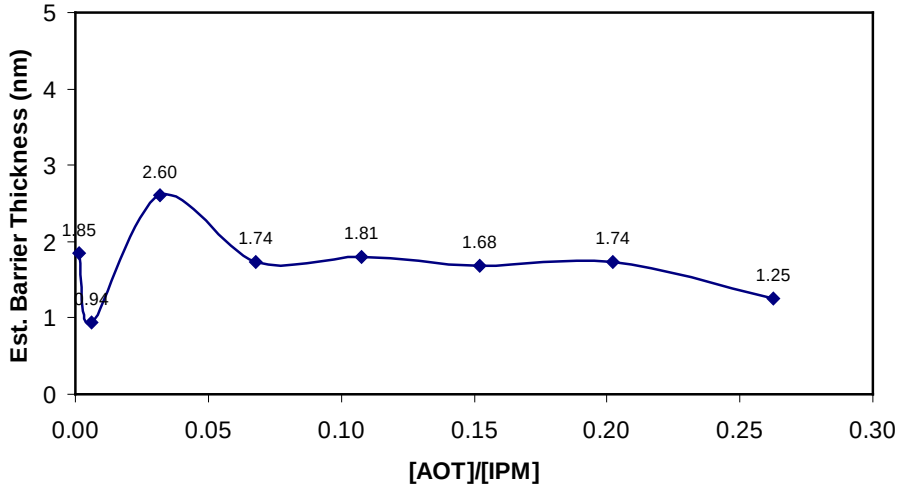

Figure 6-41 Estimated barrier thickness of anhydrous mixtures of varying ratios of AOT and IPM.

6.7.3 Normalising Features Subject to Electrode Spacing Variation

Normalising the responses of the same sample but with different electrode spacing has shown that although the bulk capacitance and barrier conductance can be aligned Figure 6-22, the anomalous conductance and capacitance features as well as the barrier charging capacitance cannot. The nature of the variation in the dielectric response with changes in electrode separation or cell geometry makes it inappropriate to use the geometrically independent permittivity, ε, or susceptibility,χ to present the experimental data if comparing responses on a series of different samples unless the geometrical cell configuration can be controlled to high precision. However curve fitting frequency adapted DH cluster model capacitance term $C' = C_{bulk} - \tau_0 G_0$ confirms the normalisation observation regarding impact of changing the electrode spacing on the commencement and magnitude of the dispersing Maxwell-Wagner feature.

6.7.4 Step Transition Co-Voltage and Frequency Variation

The co-voltage frequency dependent stepped transitions changes to the magnitude of the capacitance is thought to be due to the changes in the orientation of the carbonyl group within the structure configuration of the bulk continuous phase IPM oil clusters. Such changes to structure are usually dependent upon changes in temperature however this does not appear to be the case for the oil IPM or compositions that contain the oil as all measurements were conducted at room temperature. Dissado describes such fluctuations in the configuration of molecular systems which contain permanent dipoles where there is no change to the heat content [Dissado 2006]. The permanent dipoles within these condensed systems do not respond to the an applied electric field individually, but instead interact with one another resulting in a number of local dipoles responding as a group or cluster. Hence the dipoles not considered to be simply local but isolated elements embedded within the material matrix moving in a fixed local field, but are an integral part of the matrix whose dynamics are described by the Gibbs free energy G = H-TS of the whole ensemble, where H, T and S are enthalpy, temperature and entropy. This concept accounted for the many experimental situations in which changes occur in the magnitude of the dielectric susceptibility ($\chi_0 \propto C_0$), were independent of temperature.

Figure 6-26 (a) and (b) for example show a discrete step transition decrease then a small step transition increase in the magnitude of the capacitance as the magnitude of the applied voltage is increased. These discrete transitions can be accommodated by introducing the Kirkwood correlation factor "g" into expression $\chi 0 \propto Ng\mu^2$, which links the dielectric increment $\chi 0$ and the permanent dipole moment μ where $1 < g < 1$ or $g = 1$. The value of g and associated dipole orientations are listed in Table 6-11. Gilani *et al.* [2003] described correlated dipoles molecules, $g > 1$ as having the dipole perpendicular to the long molecular axis, and anti-correlated dipole molecules, $g < 1$ as being ellipsoidal in shape where the dipole orientation is parallel to the longest axis. The introduction of the Kirkwood correlation factor provides a mechanism to enable the dielectric increment to increase or decrease depending on the favoured orientation of the permanent dipoles. However the explanation does not address the transition due to the magnitude of the electric field.

Table 6-11 Kirkwood correlation factor value and correlation description

g		Description
>1	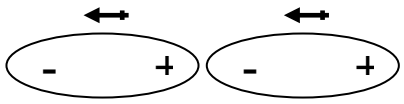	Correlated – dipoles aligned head to tail in the same direction and can result in an increase in the dielectric increment
<1	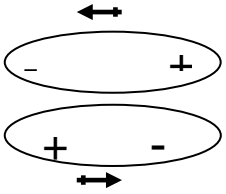	Anti-correlated – parallel pairs of dipoles are aligned in opposite directions and can result in decrease in the dielectric increment
=1	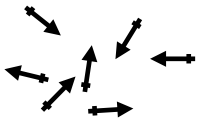	Uncorrelated – dipoles randomly orientated

The permanent dipoles interacting with an electric field are able to adopt two or more local favoured orientations which, enables them to achieve a lower energy status in the presence of the applied electric field. Orientation changes to one dipole will inevitably

alter the molecular interactions around the dipole which in turn will replicate and travel through the local cluster in condensed systems. The magnitude of the applied field E, will cause the dipole to favour one orientation over another and will change the potential energy difference between alternate orientations $2\Delta x$ to $2(\Delta x - \mu E)$ leading to the dielectric increment $\chi 0 \propto N g \mu^2 \propto (\mu^2 / k_B T) x \exp(-2(\Delta x - \mu E) / k_B T)$.

6.7.5 Active Membrane Characteristics

The anomalous negative capacitance and increasing conductance features were first observed in the 100% IPM sample and were thought to be attributed to the oil undergoing a structural change. However this structural response feature moves to higher frequencies due to interactions with the added surfactant. This behaviour is not unexpected as the surfactant breaks the bonds between the oil molecules hence reducing the sizes of the clusters or local group of IPM molecules. The smaller clusters of IPM are consequently able to respond to a more rapidly changing applied electric field.

The anomalous negative capacitance feature lies between the bulk and barrier charging processes on a frequency scale (Figure 6-1B). This suggests that the structures responding in this frequency range are located on the exterior or at boundaries of the clusters since the intracluster relation time describes polarisation inside a cluster. Hence as the frequency of the ac field is reduced then larger entities are able to respond. This type anomalous dielectric response has been observed from biological tissue, for example squid axon, when measuring the response to sodium and potassium ions passing to or from the interior of a cell via the cell membrane (Fishman *et al.* [1979]). Hence one can postulate that a structure or structures within the IPM are behaving like a cell membrane which, dependent upon conditions, undergoes structure changes to allow the passage of ions into or out of a cell

6.8 Conclusion

The low frequency dielectric spectroscopy technique is able to detect changes in sizes of clusters of bulk phase of the IPM oil as the concentration of the dispersed phase surfactant AOT is varied by tracking changes to the intracluster relaxation time.

The technique is also able to detect changes in the orientation of the carbonyl permanent dipole in ester. The reorientation of these dipoles results in a structural change in the boundaries of the clusters which enables charges to flow more easily. This reorientation process is non-linear process and requires a linearised circuit element used in the modelling of excited biological cell membranes to model this response. This indicates that the choice of the bulk phase is plays a significant role in the ability of an oil/water/ surfactant mixture to form reverse micelles and microemulsion aggregates.

Chapter 7

Dielectric Characterisation of Ternary Systems

7. Dielectric Characterisation of 20% w/w AOT, IPM and H_2O Ternary Systems

7.1 Introduction

The primary objective of this study was to determine if the low frequency dielectric spectroscopy could be used to detect properties of microemulsions and micellar systems. Comparative analysis of the dielectric responses of the anhydrous samples comprised of surfactant AOT and oil IPM, reported in section 6 showed bulk, anomalous conductance increase, negative capacitance and the barrier features shifting to higher frequencies as the molar ratio of [AOT]/[IPM] increased under the same measuring conditions. It was anticipated that the addition of water to the mixture would increase polarisability of the samples potentially shifting the dielectric responses of the features of interest previously outside of the measuring range of the dielectric instrument into view.

The dielectric response of the anhydrous composition AOT:IPM 30:70 (see Figure 6-1) was relatively free of noise and both the bulk and barrier charging characteristic response features were located with the frequency measuring range 10^{-4} Hz to 10^{+6} Hz. However the magnitude of the conductance response for this 30% AOT anhydrous sample appeared to be at an upper limit at higher frequencies, becoming partially obscured by the impedance of the BNC leads connecting the sample to the dielectric instruments. Adding water to this composition would be likely to push the bulk response further towards and beyond the upper limit of the measuring frequency range (Appendix A).

Compositions containing 5% AOT by weight produced responses where the barrier region was not observed within the frequency measuring range. Although the adding water to the baseline 5% w/w AOT sample would be expected to shift the overall response to higher frequencies, it was anticipated that all frequency sweep measurements would need to extend to 10^{-4} Hz taking up to 24 hours for each point response to be measured. Hence the AOT:IPM 20:80 percentage weight ratio response being more centrally located within the available frequency range, was selected as the base line for a series of measurements to determine the effect upon the dielectric response of increasing the percentage weight ratio of water to AOT. For example, the dielectric responses of the anhydrous percentage weight ratio composition AOT:IPM

20:80, 0% w/w added water and the microemulsion composition AOT:IPM:H_2O 20:64:16 % w/w are shown in Figure 7-1.

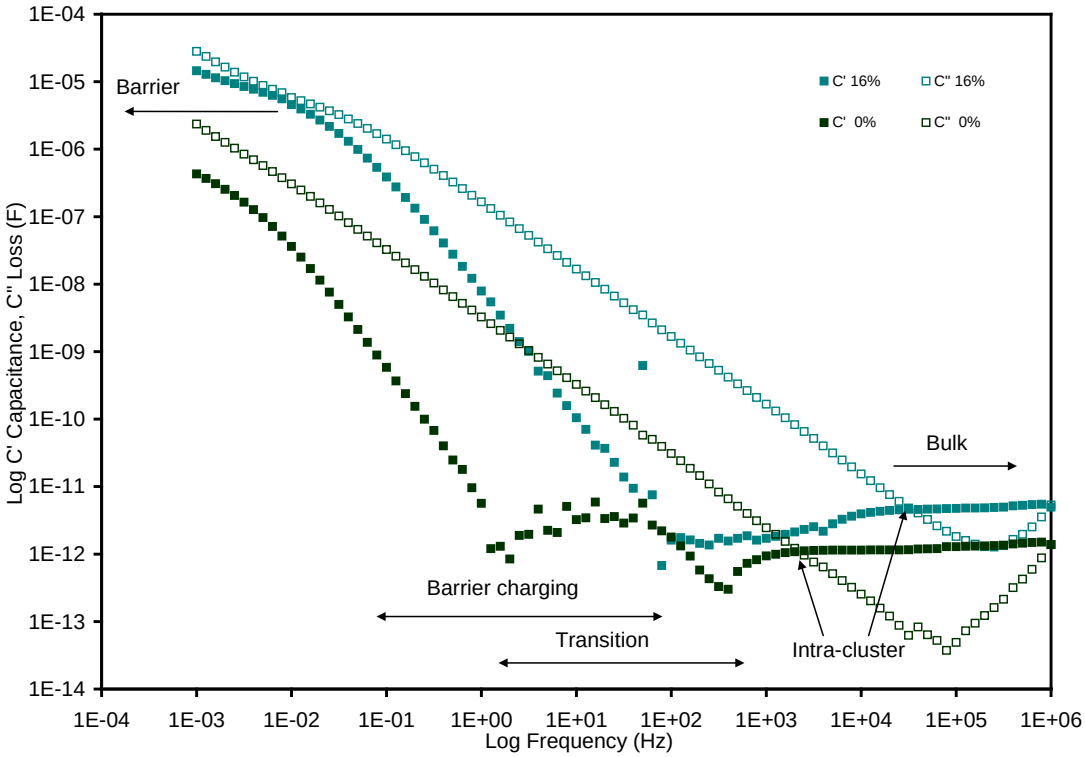

Figure 7-1 Baseline composition IPM 80% w/w, AOT 20% w/w displayed with IPM 64%, w/w AOT 20% w/w and H2O 16%.w/w

Particle sizing of the 16% w/w added water composition IPM:AOT:H_2O, was found to contain aggregates of radius size 15.7 nm (chapter 4). The barrier feature of the complex response is well developed and lies within the lower limits of the frequency range. Although the bulk characteristics feature occurs at a higher frequency, it is still within the upper limit of the measuring frequency range.

The measurements reported for this series were carried out using 0.25 V applied ac voltage and electrode spacing set to approximately 2 mm. This experimental configuration was chosen because the lower the magnitude of the applied voltage, the more apparent the magnitude of the barrier capacitance became; and increasing the magnitude of the applied voltage only appeared to reduce the noisy response in the anomalous transition frequency range.

The complex capacitance response of the hydrated IPM, AOT 20% w/w sample series is presented side by side in Figure 7-2 for visual comparison. The side by side complex

impedance Z(ω) plots for the same series are displayed in Figure 7-3, and shows the overlapping the high frequency bulk response and the lower frequency barrier response. The complex impedance was obtained by converting the complex capacitance to complex impedance Z(ω) using equation 7-1.

$$Z(\omega) = \frac{1}{i\omega C(\omega)} \qquad \text{Eqn. 7-1}$$

$$Z(\omega) = Z'(\omega) - iZ''(\omega)$$

$$Z'(\omega) = \frac{C''}{\omega\left(C'^2 + C''^2\right)} \text{ and } Z''(\omega) = \frac{-C'}{\omega\left(C'^2 + C''^2\right)}$$

The impedance plots shows that the sample responses do conform to bulk-barrier series pair of parallel conductance and capacitance components; where the higher frequency bulk response corresponds to the first semi-circle on the real Z' axis and the barrier response corresponds to the second semi-circle on the Z' axis [Jonscher 1983]. The impedance plots also shows that the dielectric response of the bulk and barrier overlap, and this overlap is consistent with the frequency range of the anomalous negative capacitance and conductance increase features.

It was noticed the shape of both the anomalous feature and the barrier response varied visually in both the complex capacitance and impedance plots (Figure 7-2 and Figure 7-3). Hence the frequency range dependent response of bulk, anomalous, barrier charging and barrier features for sample IPM:AOT:H_2O, 62:20:18 % w/w ratio with applied voltage 0.05< V< 1.00, were plotted separately in Figure 7-4 A, complex capacitance, B complex impedance to Figure 7-7 A, complex capacitance, B complex impedance respectively. It was anticipated that variations in the barrier response would be more apparent in a complex impedance plot.

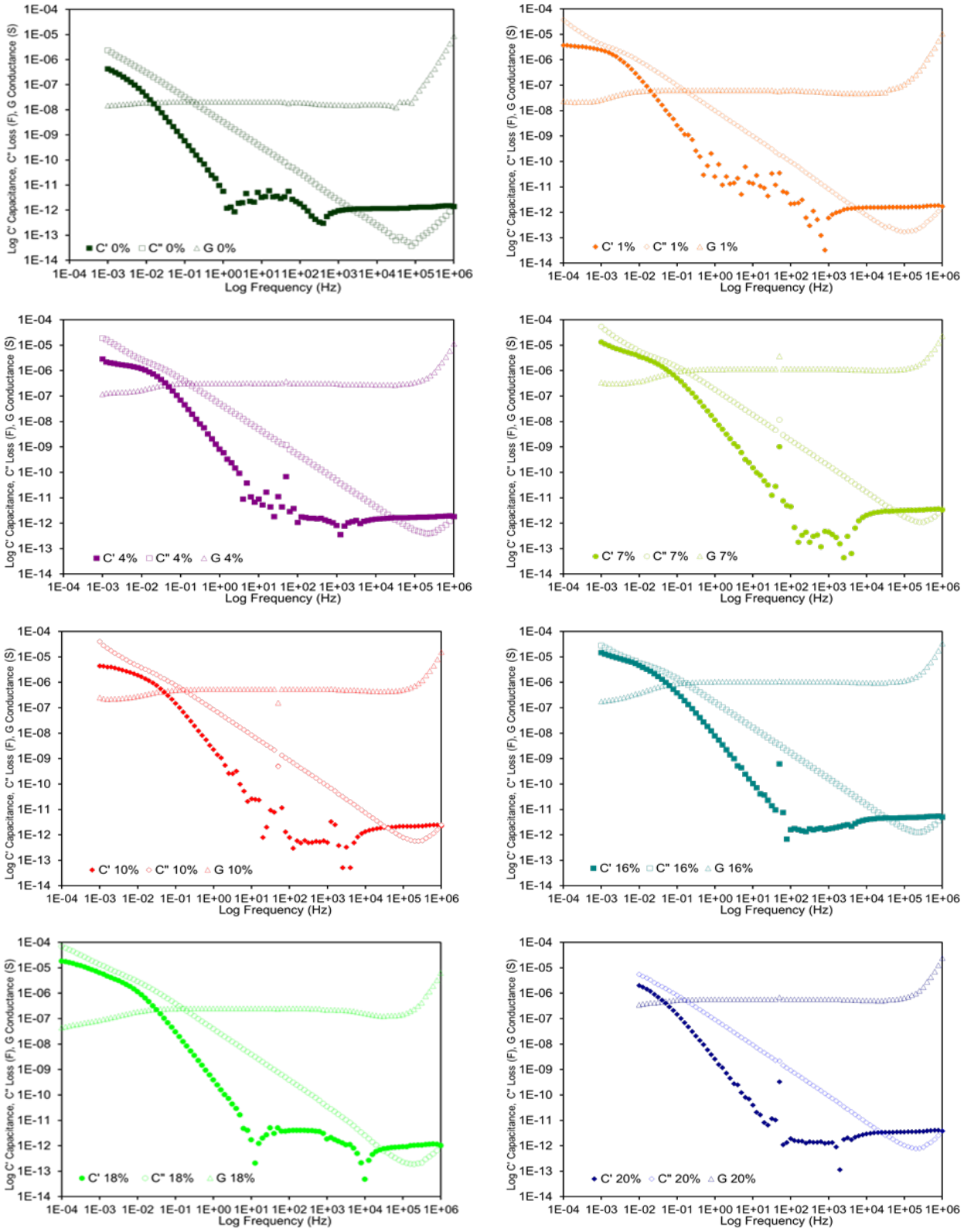

Figure 7-2 Log/log dielectric response of micellar and microemulsion samples comprised of 0% to 20% water, AOT 20% w/w and IPM.

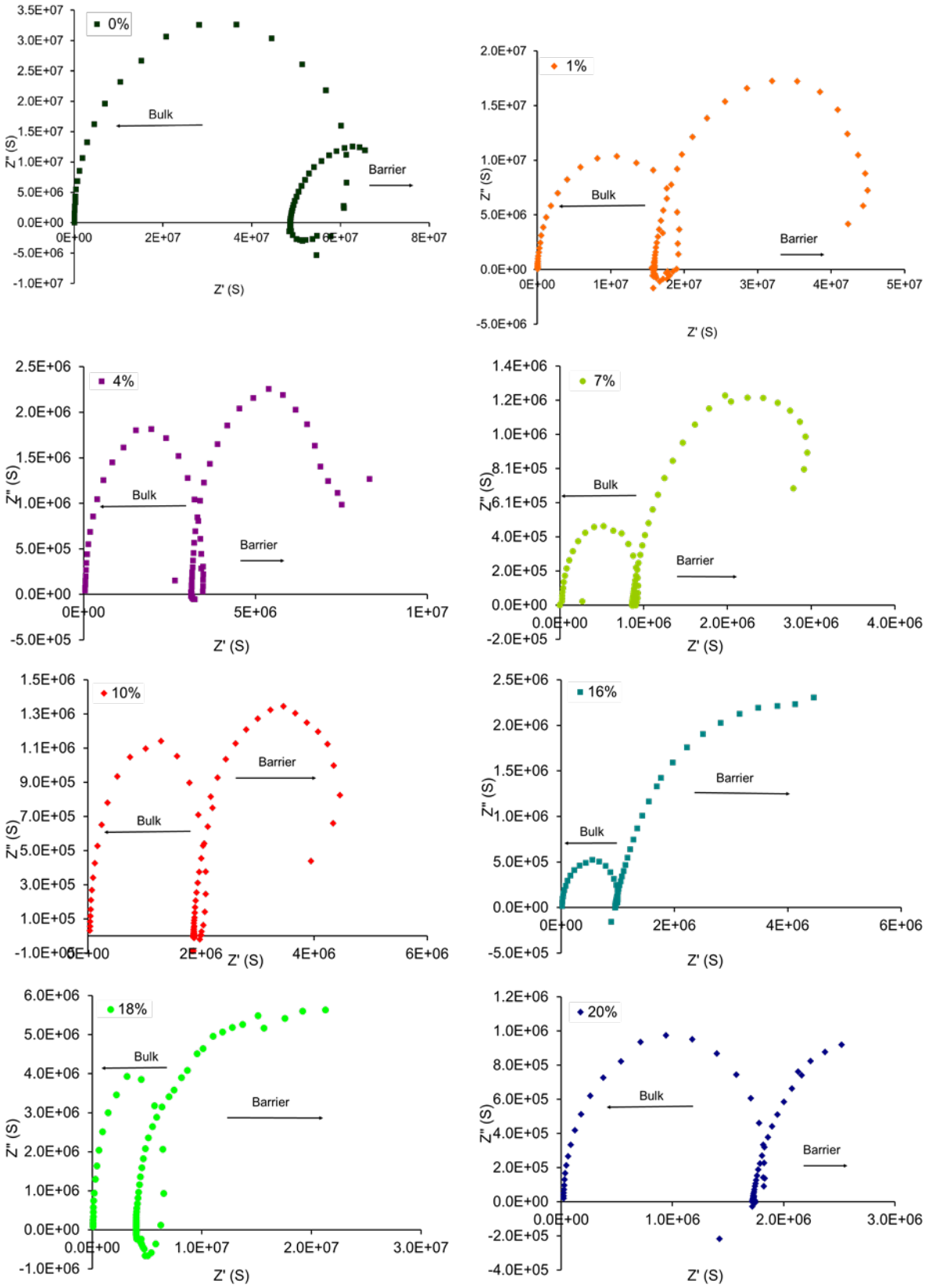

Figure 7-3 Linear impedance plot for compositions, IPM, water 0% to 20% w/w with AOT fixed at 20% w/w. Indicating the bulk-barrier series

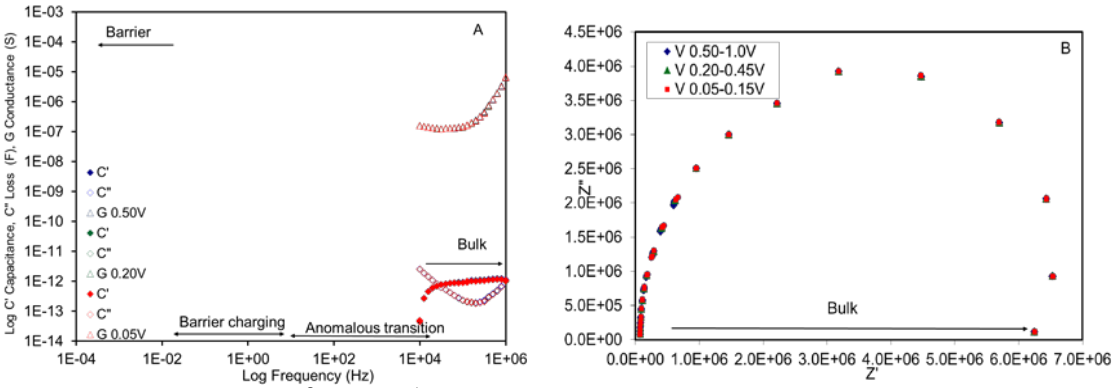

Figure 7-4 Bulk response 10^6 Hz to 10^4 Hz A) Complex capacitance and B) impedance plots of IPM 62% w/w, AOT 20% w/w and H_2O 18% w/w for 0.05 V to 1.00 V applied ac voltage

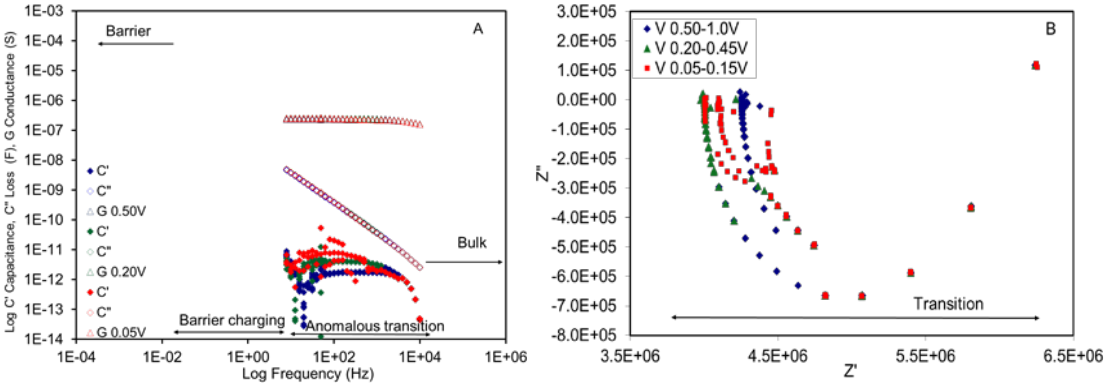

Figure 7-5 Anomalous transition response 10^4 Hz to 7.9 Hz, A) Complex capacitance and B) impedance plots of IPM 62% w/w, AOT 20% w/w and H_2O 18% w/w for 0.05 V to 1.00 V applied ac voltage.

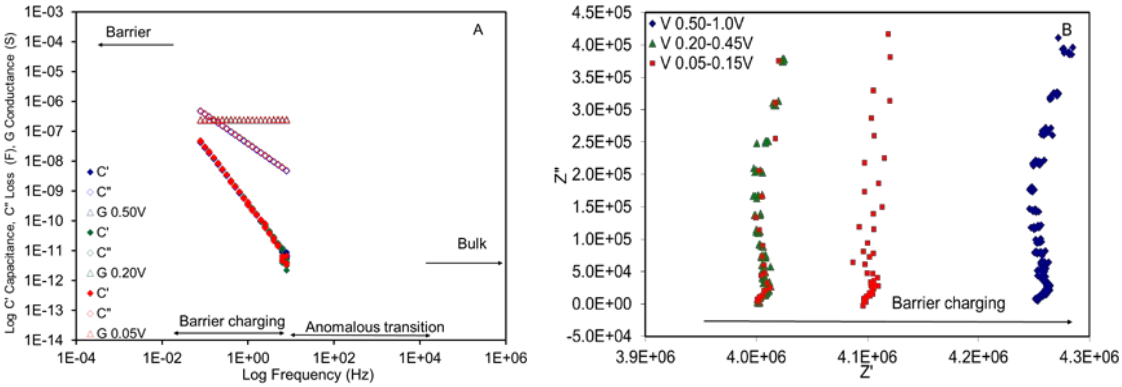

Figure 7-6 Barrier charging response 7.9 Hz to 7.9 10^{-2} Hz, A) Complex capacitance and B) impedance plots of IPM 62% w/w, AOT 20% w/w and H_2O 18% w/w for 0.05 V to 1.00 V applied ac voltage.

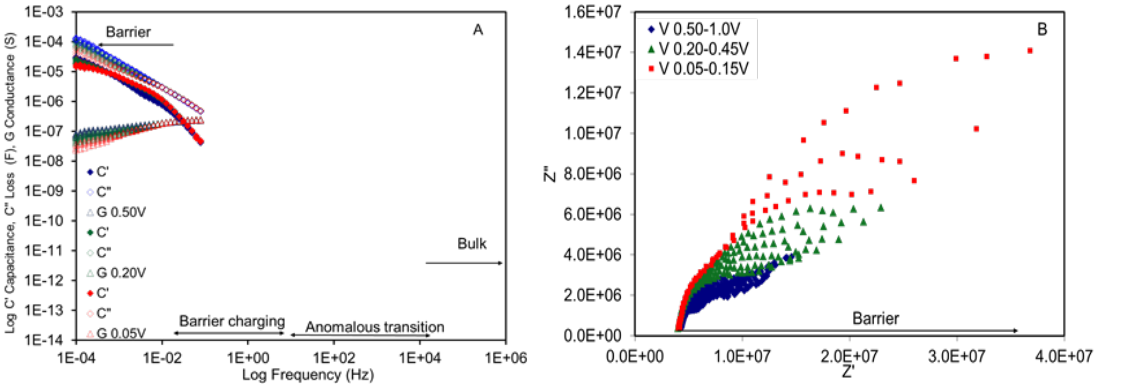

Figure 7-7 Barrier response 7.9 10^{-2} Hz to 10^{-4} Hz, A) Complex capacitance and B) impedance plots of IPM 62% w/w, AOT 20% w/w and H_2O 18% w/w for 0.05 V to 1.00 V applied ac voltage.

7.2 Analysis of the AOT 20% w/w, IPM Hydrated Series Responses

Particle sizing results reported in chapter 4 showed that only compositions with molar ratios $W_0=[H_2O]/[AOT] \geq 10$ contained any microemulsion aggregates, with diameters ranging between 10 nm and 30 nm. To determine if there were any discernable differences in the dielectric response of, compositions known to contain w/o microemulsion aggregates and those which did not; ternary w/o microemulsion comprised of AOT 20% w/w, IPM and added water ranging from 1% to 20% w/w were examined. Figure 7-8 shows the capacitance A, loss B and conductance C response for the hydrated samples. As the percentage weight of water was increased to 16%, the bulk capacitance and conductance response increased in magnitude. The dielectric response of the anhydrous composition IPM:AOT, IPM 80% w/w and AOT 20% w/w is also plotted in Figure 7-8 to show relative changes as the percentage of added water is increased.

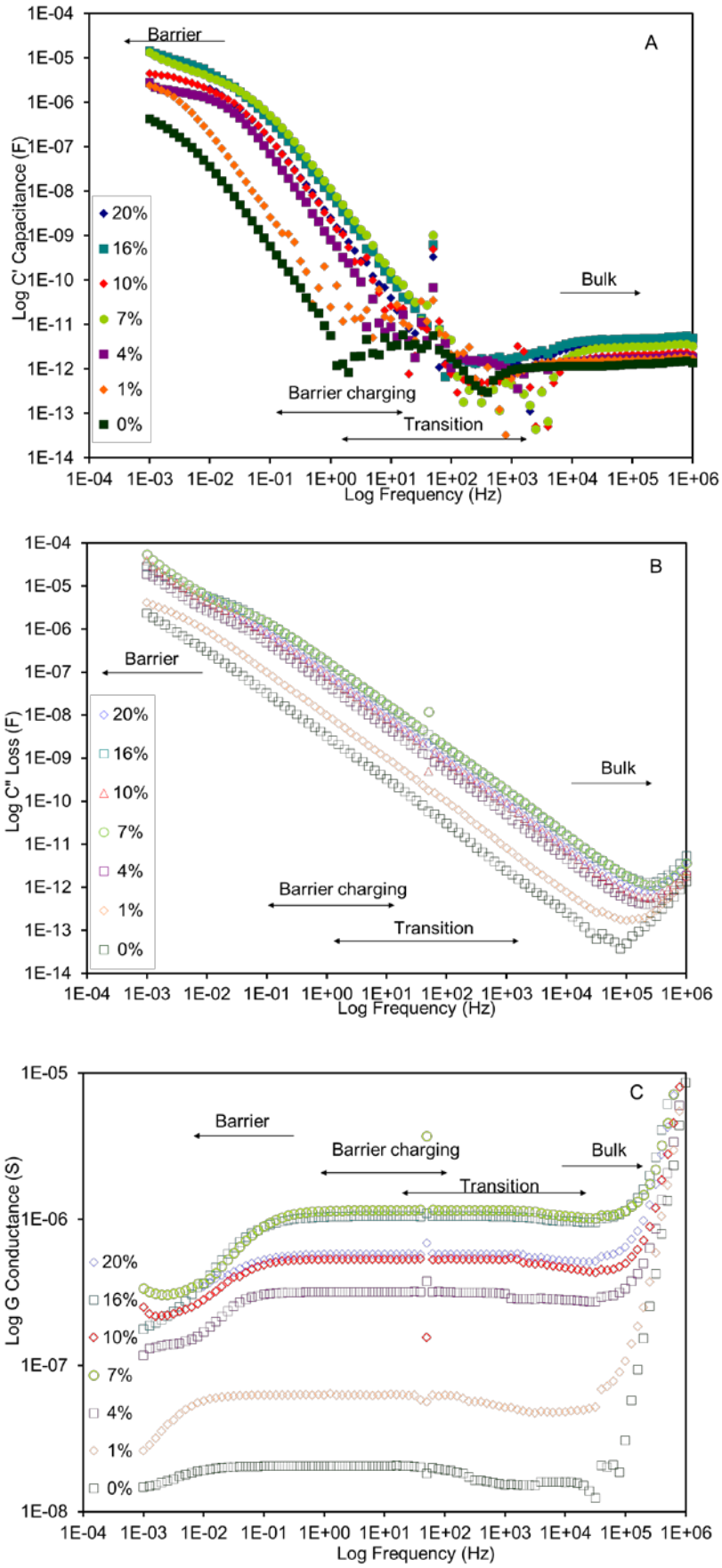

Figure 7-8 A) Real component C', B) loss component C", C) conductance component G for the AOT 20% w/w, IPM series containing added water ranging from 0% to 20% w/w.

7.3 Bulk properties of Ternary 20% w/w AOT, IPM and Water Systems

7.3.1 Bulk Capacitance

The bulk properties of the series were analysed and compared by eliminating magnitude variations due to differences in the cell geometry ratio area/spacing (A/d). The permittivity ε=C'*d/A property was obtained by dividing the measured sample bulk capacitance by the bulk capacitance of the empty cell measured prior to the cell being filled with a sample. It should be noted that due to the design of the measuring cell that less than 50% of the platinum electrodes are available to be immersed in the sample (Figure 7-9B). Hence only the portion of the electrode that is immersed in the sample is used to derive the permittivity and conductivity values.

$$C_{cell} = \varepsilon_0 \left(\varepsilon_{Teflon} \frac{A_{Teflon}}{d_{Teflon}} + \varepsilon_{air} * \frac{A_{airgap}}{d_{airgap}} \right) \quad \text{Eqn. 7-2}$$

$$\varepsilon_{eff} = (\varepsilon_{rAOT} * AOT\%) + (\varepsilon_{rIPM} * IPM\%) + (\varepsilon_{rH_2O} * H_2O\%) \quad \text{Eqn. 7-3}$$

$$C_{Total} = \varepsilon_0 \left(\varepsilon_{Teflon} \frac{A_{Teflon}}{d_{Teflon}} + \varepsilon_{air} * \frac{A_{airgap}}{d_{airgap}} + \varepsilon_{sample} * \frac{A_{sample}}{d_{sample}} \right) \quad \text{Eqn. 7-4}$$

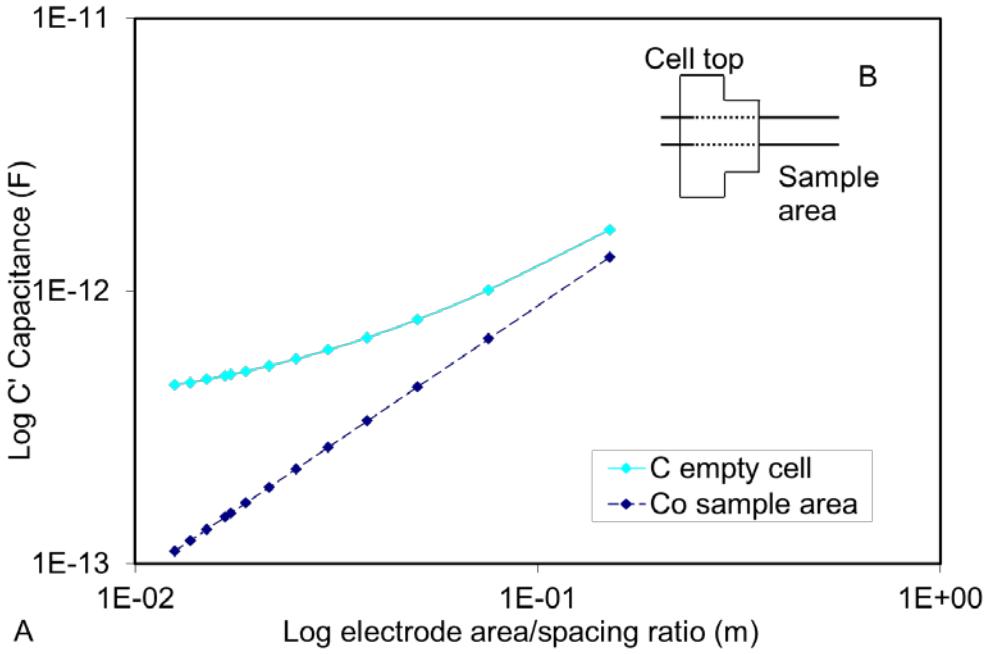

Figure 7-9 Estimates of the bulk capacitance for the empty cell and electrode area available to be immersed in the sample.

The relative permittivity values ε_{Teflon} =2.2 and ε_{air}=1 of the empty cell components, were applied to equation 7-2 to obtain estimates for the bulk capacitance of, the empty cell and that of the sample area for a range of electrode area/spacing ratios. The estimates are plotted in Figure 7-9.

Estimates of the effective permittivity for each measured sample composition were calculated using equation 7-3. It should be noted that although no water was added to the baseline composition AOT:IPM 20:80 w/w and the AOT used as supplied by Fluka, contained approximately 2% water w/w. Hence the baseline sample is assumed to contain a fixed molar ratio of water to surfactant W_0= [H2O]/[AOT] =0.493.

The effective permittivities and the derived cell constant were inserted into equation 7-4 to obtain values for the sample geometry area/spacing (A_{sample}/d_{sample}) which reproduce the measured bulk capacitance for each sample composition listed in Table 7-1. The total effective bulk capacitance calculated using the parallel capacitance configuration $C' = C_{cell} + C_{0sample}*\varepsilon_{eff}$ are plotted using a log-lin scale in Figure 7-10, together with the measured bulk capacitance, permittivities and the cell geometry ratio A/d (m).

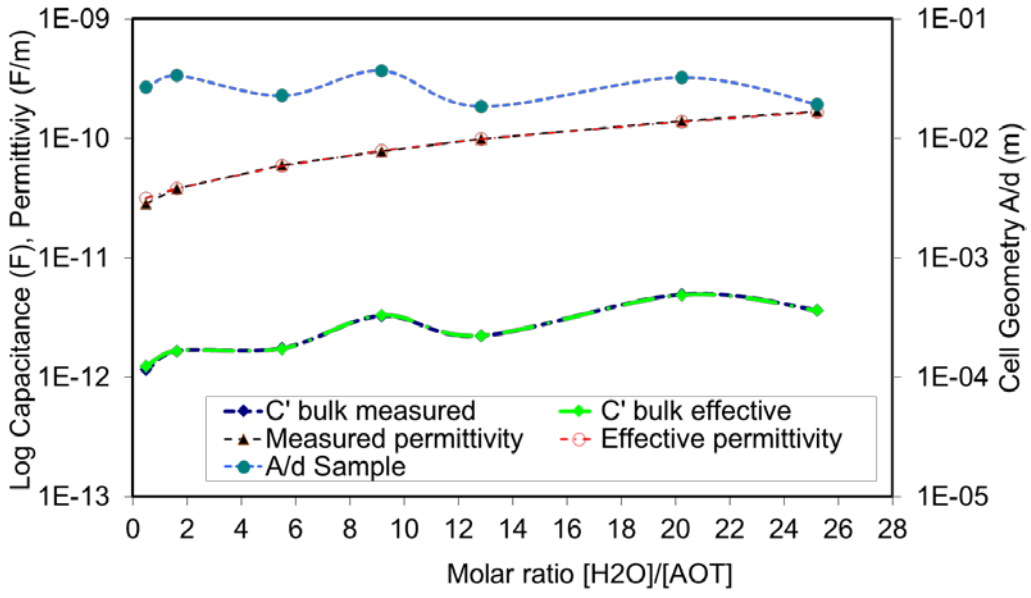

Figure 7-10 Bulk capacitance measured response and estimated using the effective permittivities of IPM:AOT:H_2O samples with molar ratio 0<[H_2O]/[AOT]<30. Sample electrode Area/spacing A/d (m) ratio shown for each sample composition.

Table 7-1 Effective and measured relative permittivities of AOT 20% w/w for $0<W_0<26$

Percentage water	W_0= [water]/[AOT]	$\varepsilon_{r\ effective}$	Electrode area /spacing (m)	$C'_{effective}$ (pF)	$C'_{measured}$ (pF)
0	0.493	3.58	0.0267	1.24	1.25
1	1.632	4.28	0.0336	1.67	1.67
4	5.504	6.65	0.0228	1.74	1.76
7	9.167	8.92	0.0363	3.30	3.28
10	12.832	11.15	0.0186	2.23	2.23
16	20.234	15.70	0.0323	4.89	4.95
20	25.221	18.73	0.0194	3.61	3.66

7.3.2 Bulk Conductance and Conductivity

Analysis of the measured bulk response showed the conductance exhibited an anomalous increase in magnitude as the frequency of the applied field was decreased from 10^{+6} Hz to 10^{-4} Hz for all compositions in the 20% AOT w/w series. Consequently, two bulk conductance magnitudes are reported, labelled G_{inf} at the upper end of the frequency range and G_{trans}, the increased conductance magnitude which was observed as the frequency ω of the applied field decreased below $\omega<10^{+3}$. The bulk conductivity $\sigma=G*d/A$ property was calculated and used to determine the bulk geometry independent characteristics of the hydrated series. Table 7-2 contains a list of conductance and conductivity response as the molar ratio is varied between $0<W_0<26$. The measured conductance and derived conductivity properties are plotted in Figure 7-11 and Figure 7-12.

The magnitude of the bulk and transition conductivity was found to increase linearly with a gradient of 3.5 μS/m and 4.0 μS/m as the molar ratio W_0 increased in the range $1<W_0<9$ shown in Figure 7-11. Above $W_0=9$ the conductivity becomes relatively constant and attained an average value of σ_{inf} 26.5 μS/m +/- 2.21 μS/m and σ_{trans} 30.8 μS/m +/- 1.75 μS/m for the bulk high frequency and post transition bulk responses. The ratio of the bulk conductivity to molar ratio σ/W_0 –■- plotted in Figure 7-12 shows a peak around $W_0= 9$, which is the ratio associated with the number of added water molecules that are able to contribute to the bulk conductivity.

Table 7-2 Conductance and conductivity AOT 20% w/w for $0<W_0<26$

		Molar ratio W_0=[water]/[AOT]						
		0.493	1.632	5.504	9.167	12.832	20.234	25.221
Percentage water		0	1	4	7	10	16	20
[AOT]	(mmol)	1.575	1.575	1.573	1.575	1.574	1.576	1.571
Electrode A/d	(m)	0.027	0.034	0.023	0.036	0.019	0.032	0.019
G_{inf}	(μS)	0.012	0.045	0.274	1.020	0.434	0.915	0.518
σ_{inf}	(μS/m)	0.461	1.33	12.0	27.7	23.3	28.3	26.5
σ_{inf}/W_0	(μS/m)	0.94	0.87	2.18	3.03	1.82	1.4	1.05
G_{trans}	(μS)	0.022	0.063	0.319	1.180	0.535	1.050	0.581
σ_{trans}	(μS/m)	0.814	1.88	14.00	32.10	28.80	32.50	30.00
σ_{trans}/W_0	(μS/m)	1.65	1.15	2.54	3.50	2.24	1.61	1.19
$\sigma_{trans}/\sigma_{inf}$		1.76	1.41	1.16	1.15	1.23	1.14	1.13

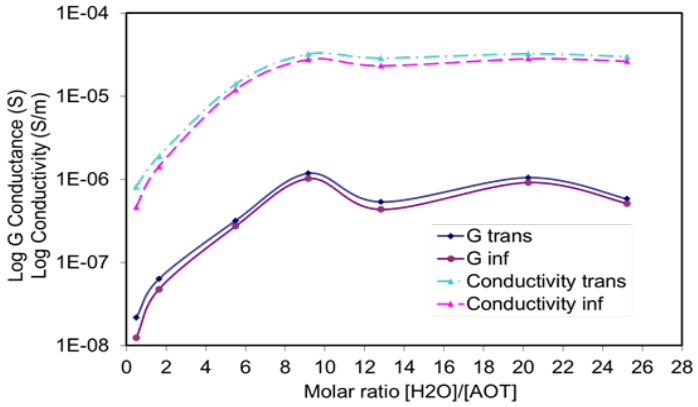

Figure 7-11 Variation in bulk conductivity and conductance G as the molar ratio W_0=[H_2O]/[AOT] increases.

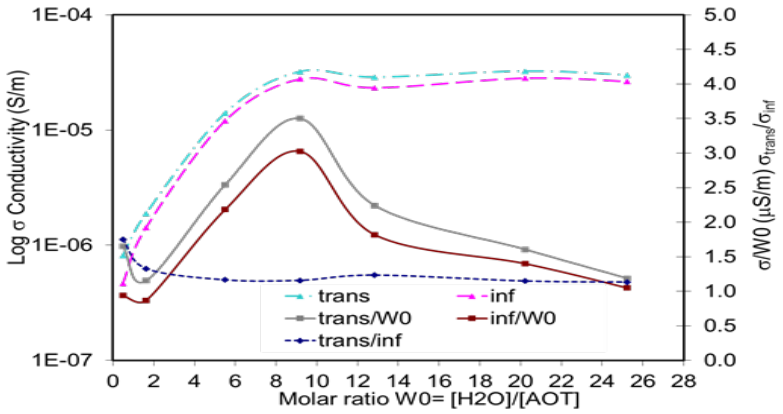

Figure 7-12 Log-lin plot of the variation in bulk conductivity σ trans▲, inf▲ as the molar ratio W_0=[H_2O]/[AOT] increases. Lin-lin plot of the variation ratio of conductivity σ/W_0 trans σ/W_0■ inf σ/W_0 ■ and ratio of the transition and bulk conductivities $\sigma_{trans}/\sigma_{inf}$.

The magnitude of the conductivity of water derived from the values reported in Table 5-1 is of the order of 330 μS/m. Hence assuming 7% added water equates to an increase in conductivity of approximately 23 μS/m, it would appear that the water added water up to W_0=9 is unbound and readily able to contribute to the conductivity response.

The magnitude of the conductivity falls when $W_0 > 9$ indicating there is a reduction in the number of free and mobile water molecules that are able to participate in the bulk conductivity as more water is added. Hence it is assumed that the additional water is locked within the microemulsion aggregates.

No microemulsion aggregates were observed below W_0=10 using light scattering particle size technique (probe wave length= 677 nm, section 4 Table 4-4). Hence the increase in conductivity with hydration was probably due to the small micellar aggregates and the added unbound water disrupting the dipolar bonds between the IPM-IPM and AOT molecules hence enabling the population of mobile ions Na^+ and AOT^- monomers to flow more freely. In the molar ratio range $10 \leq W_0 \leq 26$ aggregates were observed with diameter sizes increasing from 10 nm to 30 nm as more water was added to ratios of W_0<26. The change from conductivity increasing linearly W_0<9 to a relatively constant conductivity for W_0>9 indicates that a structure change has taken place between compositions around W_0=9. Water added above W_0>9 was not available to contribute to the bulk conductivity. All additional water added is assumed to be bound or contained within the microemulsion aggregates which, begin to swell as more water is added. There are lager but fewer aggregates as there is a fixed concentration of [AOT]=1.57 mmol, and the lager aggregates respond more slowly to the applied ac field.

7.3.3 Bulk Intracluster Characteristic Relaxation Times

The characteristic bulk intracluster relaxation time τ_1 is equal to $\tau_{bulk}=RC=C'_{bulk}/G_{bulk}$. The value of τ_1 can also be obtained from the reciprocal of frequency ω^{-1} at which the real and imaginary components of the complex capacitance crossover. However the occurrence of the anomalous increase in the magnitude of the bulk conductance results in intracluster relaxation times that vary over an average of 0.16 decades on a log frequency scale for each sample.

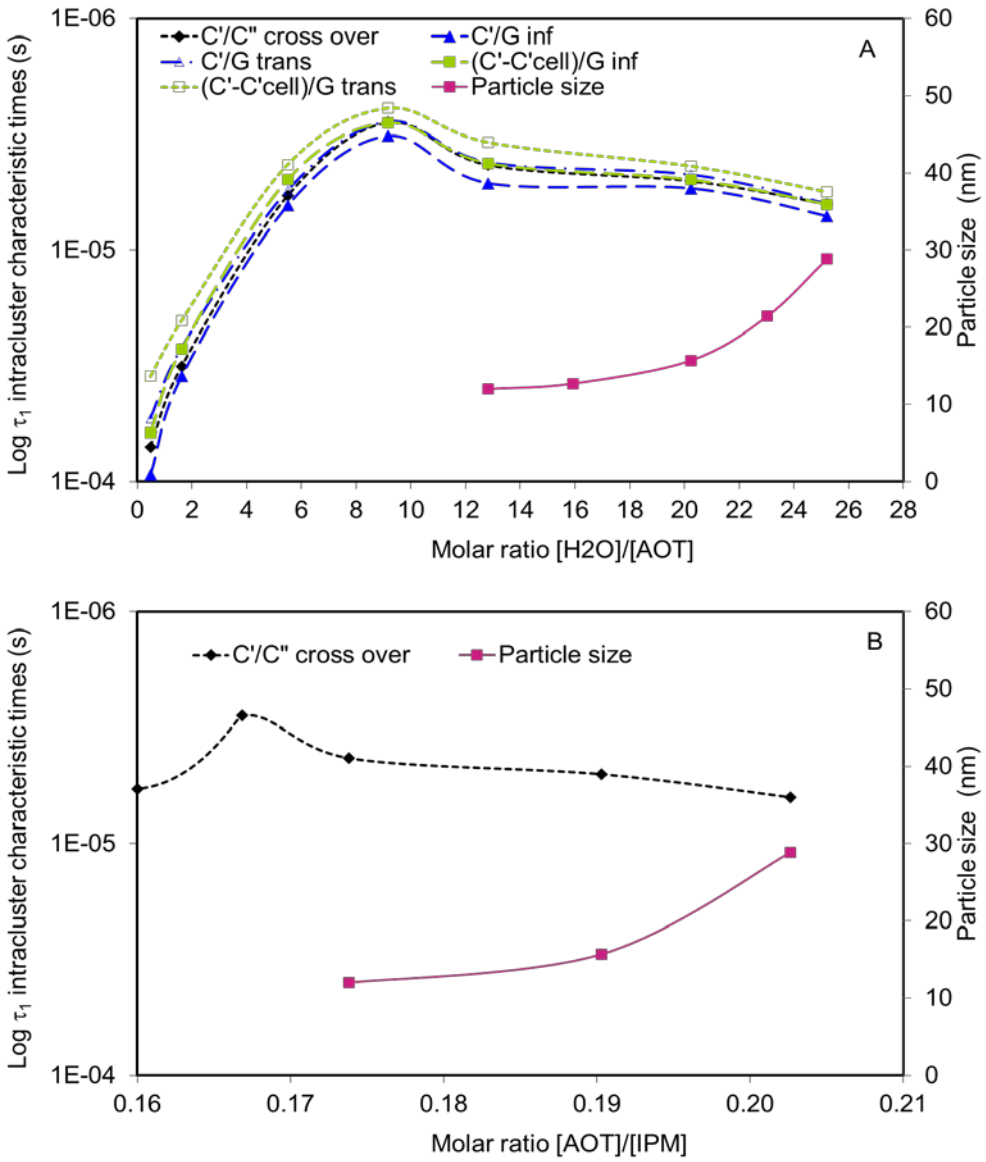

Figure 7-13 A) Variation in characteristic intracluster and post transition relaxation times as the molar ratio W_0=[H_2O]/[AOT] increases. B) Variation in characteristic intracluster relaxation time as [IPM] decreases. The radius of the aggregates are plotted on the right vertical axis.

The characteristic times are plotted in Figure 7-13A for increasing W_0 and B for increasing [AOT]/[IPM] molar ratio and listed in Table 7-3, show the measured cross over response times of the capacitance and loss components C'/C" ♦, the bulk and transition conductance response times for the sample with cell C'/G_{inf} ▲, C'/G_{trans} Δ, and derived sample only response ■ $(C'-C'_{cell})/G_{inf}$, $(C'-C'_{cell})/G_{trans}$ □.

The fastest response observed in the intracluster process occurs in the region where the molar ratio W_0=9, with relaxation times ranging from 2.4 μs < τ_1 < 3.2 μs. The characteristic intracluster response times observed for samples containing

microemulsion aggregates $9<W_0<26$, range between 4.2 μs $<\tau_{1Sinf}<$ 6.4 μs and 3.4 μs $<\tau_{1Strans}<$ 5.6 μs. The intracluster relaxation time τ_1 slows down as the aggregate swells as W_0 increases from $W_0= 9$ to $W_0=26$, and takes 1.75 to 2 times longer to relax than sample without any detected aggregates. The aggregates swell not only pooling of water in the interior, but by adding more AOT, either by a process of aggregate coalescence or via AOT monomers joining existing aggregates. The consequence of the swelling process is there are fewer but larger aggregates which leaves fewer particles available to interrupt the bulk cluster continuum of IPM molecules (see Figure 1-13).

Eicke *et al.* (1989) and Bourrel and Schechter (1988) reported relaxation times associated with the τ_1 monomers joining and leaving microemulsion aggregates and τ_2 the complete break down or dissociation of an aggregate, where τ_1 was of the order of 0.1 μs and τ_2 1 ms. Hence at molar ratio $W_0=9$, aggregates are able to form most quickly.

Table 7-3 Characteristic intracluster relaxation times τ_1 AOT 20% w/w for $0<W_0<26$

Percentage added water	W_0 =[water] /[AOT]	[AOT] (mmol)	[AOT] /[IPM]	τ_1 (μs)	τ_{1inf} (μs)	τ_{1trans} (μs)	τ_{1inf_sample} (μs)	τ_{1tran_sample} (μs)
				C'/C"	C'/ G_{inf}	C'/ G_{trans}	(C'- C'$_{cell}$) / G_{inf}	(C'- C'$_{cell}$)/ G_{trans}
0	0.493	1.575	0	70.60	93.40	53.40	61.35	35.10
1	1.632	1.575	0.0016	31.70	35.10	26.40	26.74	20.10
4	5.504	1.573	0.160	5.83	6.42	5.52	4.97	4.27
7	9.167	1.575	0.167	2.81	3.22	2.78	2.83	2.44
10	12.832	1.574	0.174	4.29	5.14	4.17	4.22	3.43
16	20.234	1.576	0.190	5.04	5.41	4.71	4.98	4.34
20	25.221	1.571	0.203	6.34	7.13	6.30	6.36	5.62

The values of the observed cross over characteristic relaxation time $\tau_{1C'/C"}$ ♦ plotted in Figure 7-13, lies between those which are due to the bulk and transition processes. Hence the cross over relaxation time $\tau_{1C'/C"}$ for these samples is an overlapping of the relaxation processes which are dominated by the bulk conductance G_{inf} and the by the transition conductance G_{trans}. The magnitudes of the differences transition and cross over response times are smaller than those of bulk and cross over response times, indicating that the transition process dominates the intracluster relaxation process in this frequency region.

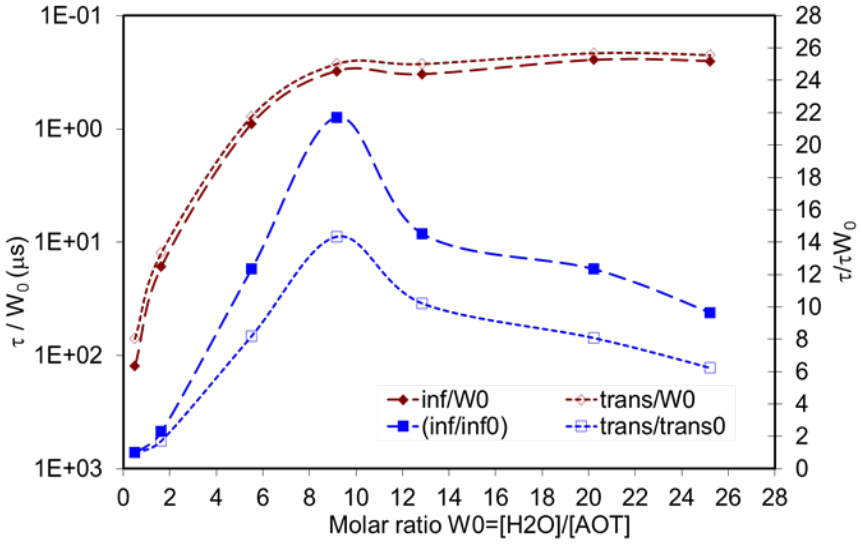

Figure 7-14 Ratio of intracluster relaxation times and molar ratio log τ/W_0 (μs) bulk ♦ and transition ◊ and linear ratio of intracluster and post transition relaxation times $\tau/\tau_{W0=0}$ bulk ■ and transition □ as the molar ratio W_0 increases.

Table 7-4 Ratio intracluster relaxation times τ_1 and molar ratios W_0 for samples IPM, AOT 20% w/w for $0<W_0<26$

Percentage added water	W_0 =[water] /[AOT]	[AOT] (mmol)	τ_{inf}/W_0 (μs)	τ_{trans}/W_0 (μs)	τ_{inf}/τ_{infW0}	$\tau_{trans}/\tau t_{transW0}$
0	0.4934	1.575	124.35	71.05	1.00	1.00
1	1.6321	1.575	16.38	12.34	2.29	1.74
4	5.5038	1.573	0.90	0.78	12.34	8.21
7	9.1668	1.575	0.31	0.27	21.71	14.35
10	12.8323	1.574	0.33	0.27	14.53	10.23
16	20.2335	1.576	0.25	0.21	12.33	8.09
20	25.2206	1.571	0.25	0.22	9.65	6.24

The impact on the relaxation time of adding water whilst keeping the molar fraction of surfactant fixed at [AOT]=1.57 mmol is shown in Figure 7-14 and data listed in Table 7-4. The ratio of relaxation time and molar ratio τ/W_0 bulk ♦ and transition ◊ responses, are plotted using log-lin scale and shows that after the fastest response is attained around $W_0=9$, τ/W_0 remains relatively constant as W_0 increases to $W_0=26$. This indicates above the molar ratio $W_0=9$ additional water has the same τ/W_0 impact on the intracluster relaxation times i.e. the rate of reduction in τ_1=C'/C" is proportional to the growth in the size of aggregates for molar ratios $W_0>9$. Hence the intracluster relaxation times reported for the series can be directly attributed to the microemulsion aggregates.

Comparison of the intracluster time ratio $\tau/\tau_{W0=0}$ bulk ■ and transition □ responses are plotted using a lin-lin scale in Figure 7-14, where $\tau_{W0=0}$ is the relaxation time for sample $W_0=0$ with no added water. The bulk response time for the anhydrous sample $W_0=0$ is 21.7 times slower than that peak response time which occurs around $W_0=9$, whilst anhydrous response is 14.4 times slower than the equivalent ratio for the transition process.

Thompson and Gierasch (1984), using the near infrared technique reported the presence of tightly bound water in aggregates with low levels of hydration with a small pool of free water increasing in size as the levels of hydration increased to $W_0=8.3$. Below

W_0=10, no microemulsion aggregates are observed (particle sizing wavelength λ= 677 nm) hence the faster response times can be attributed to the presence of smaller micellar aggregates < 10 nm or mobile ions not bound within the micelle. It is reminded that the intracluster relaxation times τ_1 reported in section 5 of IPM τ_{1IPM}=8.9 s, solid AOT τ_{1AOT}=4 ms and deionised water, 5 μs <τ_{1water} < 10 μs. Hence the responses of composites rather than the responses of the individual components is being observed.

7.4 Anomalous Bulk – Barrier Transition Properties of 20% w/w AOT, IPM and Water Ternary Systems

As with the anhydrous compositions examined in chapter 6, the hydrated samples continue to exhibit decreases in the magnitude of the capacitance down to negative values as the response moves from that of the bulk through a transition to that of the barrier charging process. The development of the barrier is apparent from 1% w/w water capacitance Figure 7-2 and conductance Figure 7-8 in the frequency range less than 10^{-1} Hz.

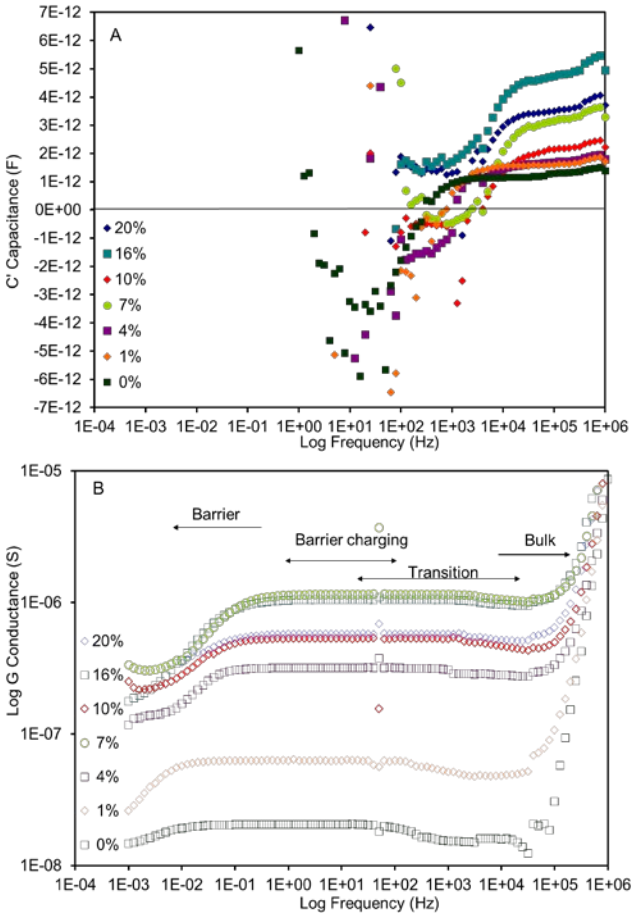

Figure 7-15 A) Anomalous negative capacitance and corresponding B) conductance increase for Ternary systems comprised of AOT 20% w/w, IPM and water.

The negative capacitance feature in the frequency range 1 Hz < frequency < 10^{+4} Hz is re-presented in Figure 7-15A using a lin/log scale and increased conductance in Figure 7-15B. Again it is assumed that IPM is responsible for this anomalous response as discussed in chapters 5 & 6. However the presence of the added water has shifted the anomalous feature to a higher frequency range than that of the anhydrous sample. This indicates that the structure of IPM bulk continuum is being broken into smaller cluster groups by the water impacting the covalent bonding, and the smaller clusters groups of IPM or the IPM shells of the reverse micellar aggregates are able to respond to applied electric field at higher frequencies.

7.5 Barrier Response

7.5.1 Barrier Response to Increasing Hydration

The complex capacitance response of the IPM, 20% AOT hydrated series Figure 7-2 shows the presence of the barrier feature. However the shape of the barrier region varied with no apparent trend, but in response to the strength of the applied ac field. The complex impedance plots of the same series Figure 7-3, show overlapping of the barrier and the bulk response which coincides with the anomalous negative capacitance feature.

Table 7-5 Maxwell-Wagner and loss and low frequency intercluster index for IPM, AOT 20% and $0 < W_0 < 26$ hydrated samples.

Molar ratio	H_2O	Dispersion indexes			Loss		
W_0=[H2O]/[AOT]	%	ω^{-p} p	$\omega^{(n-2)}$ (n-2)	ω^{-n} n_{MW}	ω^{-n} n_{low}	$\omega^{-n'}$ n'_{high}	$\omega^{-n\sim}$ $n^{\sim}_{trans}$
0.493	0	0.77	-1.95	0.05	-1	-1.01	-1.04
1.632	1	0.67	-1.95	0.05	-1	-1.03	-1.03
5.504	4	0.79	-1.95	0.05	-1	-1	-1.02
9.167	7	0.69	-1.86	0.14	-1	-1	-1.05
12.832	10	0.77	-1.88	0.12	-1	-1.01	-1.06
20.234	16	0.70	-1.84	0.16	-1	-1	-1.05
25.221	20	0.72	-1.86	0.14	-1	-1	-1.04

The gradients of the Maxwell-Wagner barrier charging feature and the gradients of the associated loss components of the samples $0<W_0< 26$ displayed in Figure 7-2 are listed in Table 7-5 and are plotted in Figure 7-16 A and B.

The magnitude of the Maxwell-Wagner index shows the efficiency of charge transfer through the barrier. When the Maxwell-Wagner index n=0 the barrier is 100% effective and no charge leaks through hence charge transport is blocked. The charge blocking effectiveness is most efficient when the molar ratio $W_0 <6$. There is a reduction in the effectiveness of the barrier in the range $6<W_0<10$ where micelles transition to microemulsion aggregates. The efficiency of charge transport achieves and average of 14% (n=0.14) for samples containing microemulsion aggregates whilst samples containing micellar aggregates have an average efficiency of 5%.

The gradient of the loss component n_{low} of the dispersing Maxwell-Wagner feature which occurs at frequencies below that of the anomalous negative capacitance transition frequency region, have a value of -1. However in the transition frequency range associated with the anomalous negative values for the real component of the complex capacitance, the loss components has gradients whose values range $-1.06 < n^{\sim}_{trans} < -1.00$. The modulus loss index is expected to approximately 1 and not expected to exceed 1 as the bulk conductance=loss * frequency (ω) of the system is constant and reduces when blocked by a barrier as the frequency of the applied fields reduces towards zero. A loss gradient exceeding unity suggest structural changes to the system which allows previously screened charges to flow, or charges are added from outside the system. The gradient of loss component for frequencies above the anomalous transition frequency range n'_{high} generally have a value of -1 where the frequency of the boundary between the high frequency intracluster and the anomalous negative capacitance feature response are clearly identifiable.

The dispersion index p of the barrier response was obtained applying the bulk and barrier parameters listed in Table 7-6 and Table 7-7 to the curve fitting model adapted to include the bulk conductance frequency dependant term for each of the samples $0<W_0<26$ are listed in Table 7-5 and plotted in Figure 7-16 C. All the index p values were greater than 0.6 hence all the samples exhibit low frequency quasi-dc response.

All of the samples have mobile charges that are free to hop to charge site within the local cluster group, but these charges are not free to move to neighbouring clusters.

A

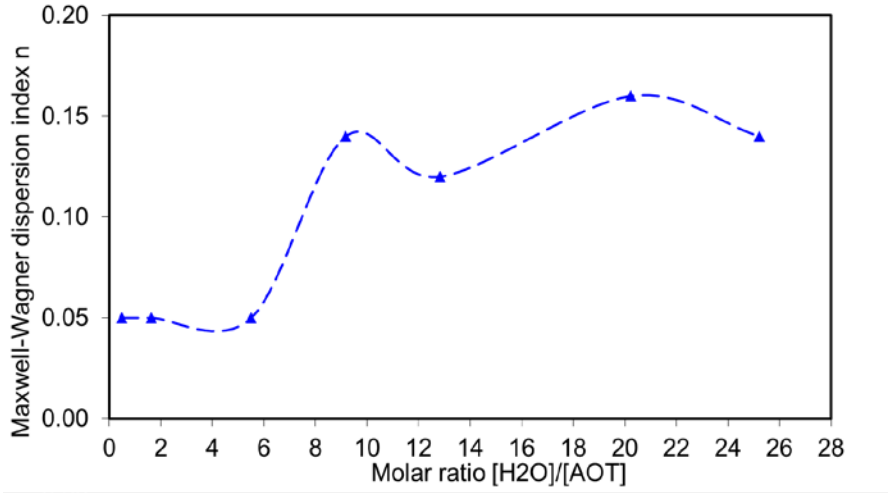

B

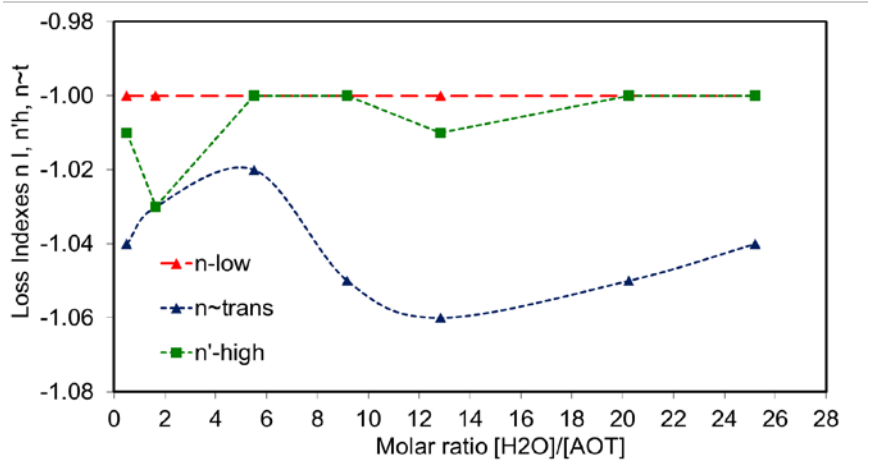

C

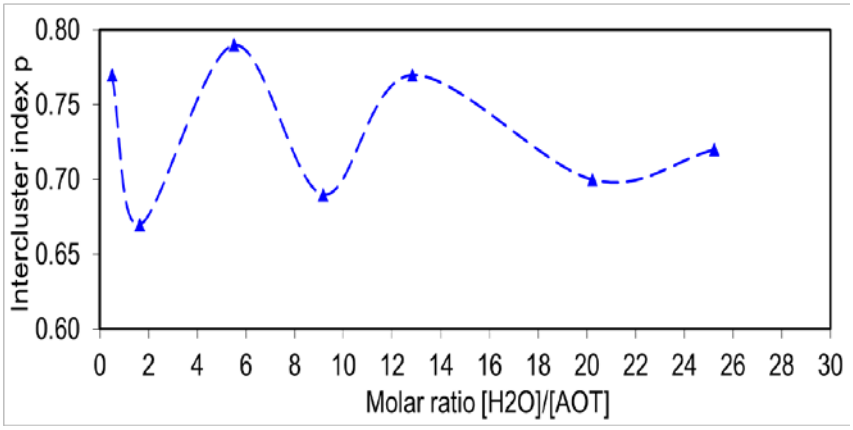

Figure 7-16 A) Maxwell-Wagner 'n' and B) loss indexes 'n_{low}', 'n_{high}' and 'n'_{trans}', C) low frequency 'p' indexes for water 0% to 20% w/w with AOT fixed at 20% w/w.

Table 7-6 Dissado-Hill cluster model parameters for a range of [H_2O]/[AOT] molar ratios compositions

Molar ratio	Barrier parameter			Bulk parameters				
[H2O]/ [AOT]	Barrier Capacitance Cbar (μF)	Index ω^{-p} p	Barrier Magnitude (μF)	C(∞) (pF)	G∞ (nS)	ΔG_0 (nS)	ΔG_1 (nS)	ΔG_2 (nS)
0.493	1.80	0.77	0.130	1.20	15.10	2.30	1.60	1.60
1.632	4.40	0.67	0.400	1.60	44.50	3.10	8.00	5.10
5.504	3.20	0.79	0.700	1.81	274.00	6.00	15.00	4.00
9.167	3.40	0.69	4.00	3.40	1020.0	30.00	50.00	80.00
12.832	4.20	0.77	1.40	2.20	447.00	110.00		33.00
20.234	3.80	0.70	3.20	5.30	915.00	100.00	83.00	2.00
25.221	4.80	0.72	1.10	1.06	126.00	10.00		90.00

Table 7-7 Characteristic relaxation times and bulk conductance frequency dependant times for a range of [H_2O]/[AOT] molar ratios compositions

Molar ratio W_0	Time dependent bulk conductance increments (μs)			Bulk conductance (μS)		Intracluster Relaxation time (μs)	Barrier charging time τ_3 (s)
[H_2O]/ [AOT]	τ_{G0}	τ_{G1}	τ_{G2}	G_0	G_∞	τ_1	τ_{3bar}
0.493	794.00	794.00	794.00	0.021	0.0151	70.60	93.70
1.632	345.00	200.00	112.00	0.0607	0.0445	31.70	88.50
5.504	40.00	20.00	40.00	0.299	0.0274	5.83	14.50
9.167	14.30	24.10	9.09	1.18	1.0200	2.81	4.20
12.832	20.80	-	11.10	0.590	0.4470	4.29	9.95
20.234	10.00	33.30	100.00	1.10	0.9150	5.04	4.42
25.221	26.70	-	26.70	0.226	0.1260	6.34	8.85

The barrier charging relaxation times $C_{bar}/G_{bulk}= \tau_3$ listed in Table 7-7 are plotted in Figure 7-17. As with the conductance responses previously reported for this series, the barrier charging process is fastest at 4.2 s around W_0=9 and tends to an average rate of 7.4 s for molar ratios W_0>9.

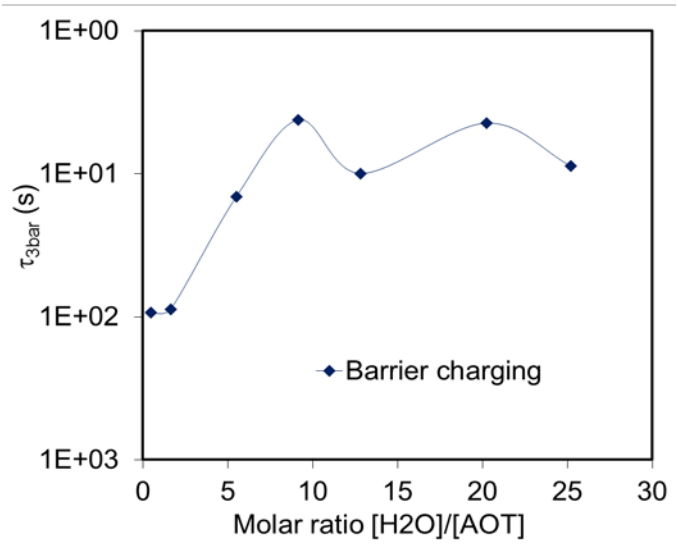

Figure 7-17 Relaxation time of barrier charging elements as the molar ratio $[H_2O]/[AOT]$ increases

7.5.2 Estimating Barrier Thickness in Response to Increasing Hydration

The Maxwell-Wagner barrier charging dispersion of these hydrated samples extends of 3 decades on a log frequency scale, and characteristic crossover frequency ω_3 is separated from the intracluster characteristic crossover frequency ω_1 by 6-7 decades on a log frequency scale (Table 7-8).

In order to obtain estimates for the barrier capacitance C'_{bar} and barrier thickness it is necessary for the both the Maxwell-Wagner dispersion and the intracluster crossover to be visible within the measuring frequency range.

The shape, frequency location and magnitude of the barrier capacitance C'_{bar} varied in response strength of the applied ac field. The magnitude of bulk capacitance C'_{bulk} was insensitive to the voltage changes, but sensitive to the changes to the electrode spacing. Being unable to certain that the measured electrode spacing has not altered whilst connect the sample to the FRA, order of magnitude estimates we can obtained for the barrier thickness, assuming the permittivities of the barrier layer and the bulk are the same. The bulk-barrier dielectric increment for all the samples listed in Table 7-8 gives an estimate for the barrier thickness of the order of 10^{-6} time's thinner that the electrode spacing, which itself was of the order of 10^{-3} m. This gives an overall thickness of the order of 10^{-9} m for the barriers of samples containing microemulsion aggregates and those that do not.

Table 7-8 Dielectric increment and dispersion interval of hydrated samples IPM and AOT 20% w/w for $0<W_0<26$

		Molar ratio W_0=[water]/[AOT]						
		0.493	1.632	5.504	9.167	12.832	20.234	25.221
Percentage water		0	1	4	7	10	16	20
C'_{bulk}/C'_{bar}	($x10^{-6}$)	0.34	0.32	0.42	0.69	0.40	0.91	0.48
ω_1/ω_3	($x10^{6}$)	1.97	2.52	2.00	1.58	2.51	1.00	2.00
Electrode spacing	m	0.003	0.003	0.003	0.003	0.003	0.003	0.004

7.5.3 Effects of Varying the Applied ac voltage on the Barrier

It was determined that the anomalous capacitance feature previously attributed to the IPM oil was affected by the magnitude of the bulk capacitance. This was confirmed via curve fitting to be coupled to the barrier response. It was noted that the shape of the barrier response varied as the strength of the applied field E=Voltage/ Electrode spacing E=V/d V/m was altered. Hence analysis of the impact of varying the magnitude of the applied ac field on one sample composition was carried out.

A sample comprised of IPM, AOT 20% w/w and water 18% w/w containing microemulsion aggregates 20.7 nm radius was measured with applied ac voltage range $0.05<V<1.00$ and frequency sweep 10^{-4} Hz through to 10^{6} Hz. Varying the magnitude of the applied electric field by fixing the geometry of the sample cell and changing the magnitude of the applied voltage showed; the magnitude and shape of the barrier response were affected by the field strength Figure 7-18A. The impedance plot Figure 7-18B also showed the lower magnitude of the applied field, the more effective the barrier was in blocking and reducing the magnitude the conductance which is expected.

The anomalous negative capacitance feature was also affected by varying the magnitude of the applied voltage strength Figure 7-18A. The three magnitude step changes appeared to coincide with three applied ac voltage ranges, 0.05 to 0.15 V, 0.2 to 0.45 V and 0.50 to 1.00 V. One voltage setting taken from each step of the anomalous negative capacitance is plotted in Figure 7-19. It can be seen in Figure 7-19A that the lowest voltage range 0.05-0.15 V ■, produce the greatest negative values for the anomalous

capacitance feature, whilst the 0.50 to 1.00 V ♦, produces the least negative capacitance values for the feature.

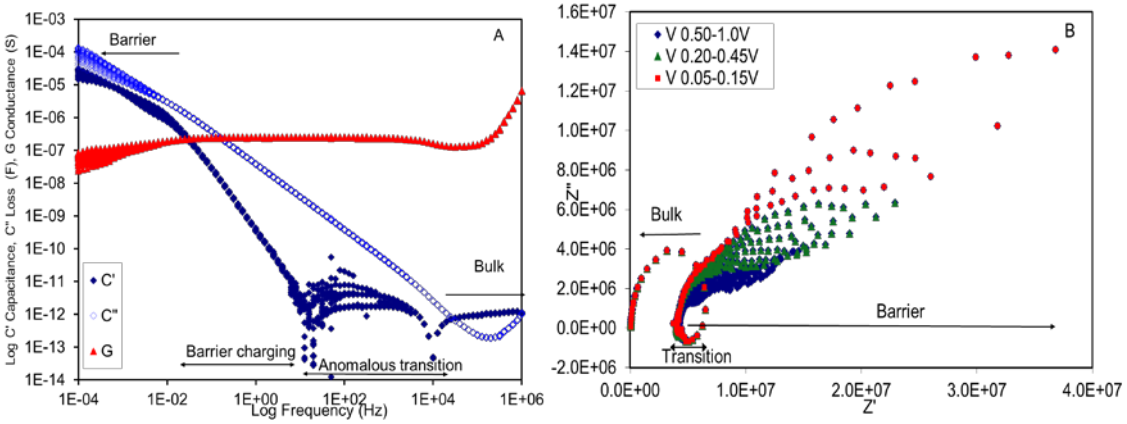

Figure 7-18 A) Complex capacitance and B) Complex impedance plot of response from IPM 62% w/w, AOT 20% w/w and H_2O 18% w/w for 0.05 V to 1.00 V applied ac voltage.

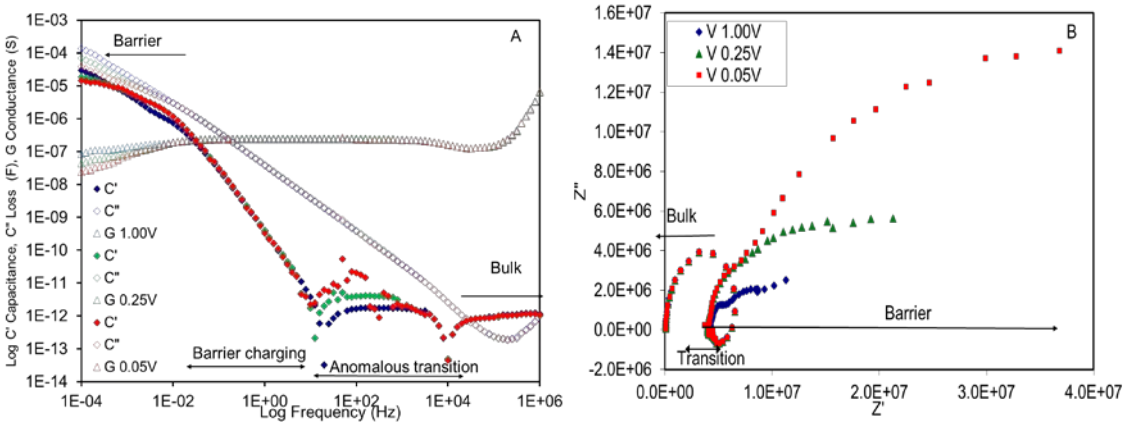

Figure 7-19 A) Complex capacitance and B) Complex impedance plot of response from IPM 62% w/w, AOT 20% w/w and H_2O 18% w/w for 0.05 V, 0.25 and 1.00 V applied ac voltage.

Although the magnitude step changes in the anomalous negative capacitance initially appeared to occur at specific voltage magnitudes for the anomalous feature frequency range, examination of the conductance and negative capacitance at spot frequencies with the anomalous frequency range for voltages ranging from 0.05 to 1.00 V showed this was not the case. Figure 7-20 A to C show three step conductance magnitude for the frequency points 12.58 Hz, 100 Hz and 1000 Hz, as the applied voltage is increased from 0.05 to 1.00 V. Figure 7-20 D which is close to the bulk cross over frequency, shows very small step changes in the magnitude of the conductance at a frequency of 10^4 Hz, below which the capacitance becomes negative.

An examination of the barrier conductance response of Figure 7-4 C showed indications that an anomalous increase in conductance occurred for the samples with 7% and 10% added water around the frequency region 10^{-3} Hz. However this barrier anomalous conductance magnitude increase was not observed for the response of the other samples in the series. However Figure 7-21 shows the impact of variations in the magnitude the applied electric field on the both the capacitance and conductance response in the barrier frequency range 10^{-4} Hz to $7.9x10^{-2}$ Hz.

The response of the IPM:AOT:H_20 62:20:18 percentage ratio w/w sample was curve fitted to analyse the impact on the barrier response due varying the applied ac field. The parameter used to fit the measured response are listed in Table 7-9, and the corresponding bulk and barrier relaxation times are listed Table 7-10.

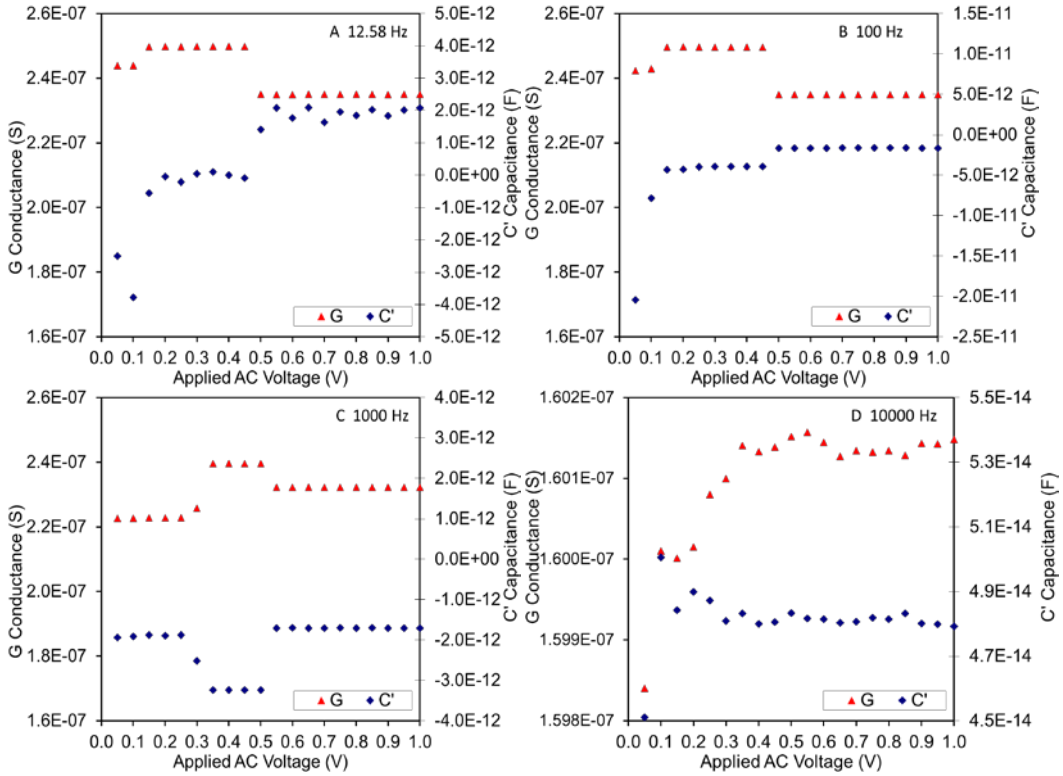

Figure 7-20 Linear Conductance G and Capacitance C, response of IPM 62% w/w, AOT 20% w/w and H_2O 18% w/w for 0.05 V to 1.00 V applied ac voltage at 12.58 Hz, 10^2 Hz, 10^3 Hz and 10^4 Hz.

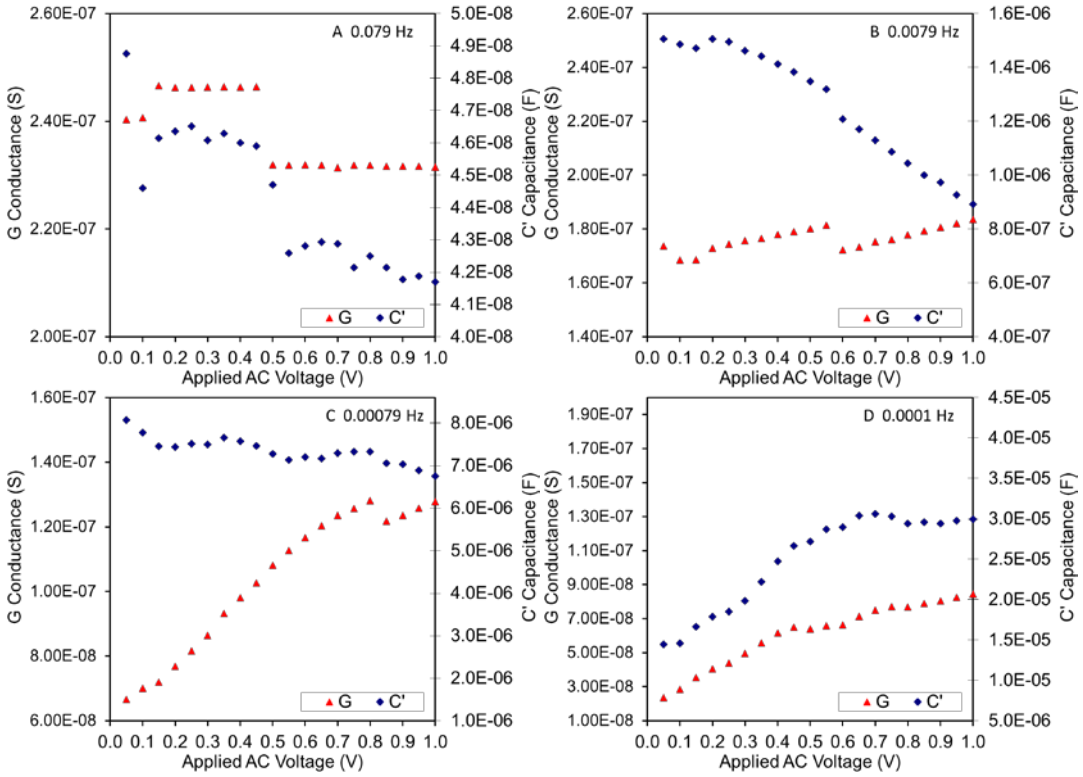

Figure 7-21 Linear Conductance G and Capacitance C, response of IPM 62% w/w, AOT 20% w/w and H_2O 18% w/w for 0.05 V to 1.00 V applied ac voltage at $7.9x10^{-2}$ Hz, $7.9x10^{-3}$ Hz, $7.9x10^{-4}$ Hz and 10^{-4} Hz.

Table 7-9 Model parameters for sample responses IPM, AOT 20% H2O 18% for applied ac voltage 0.05 V to 1.00 V

	Bulk Parameters								Barrier Parameters		
AC Voltage (V)	C_{inf} (pF)	G_{inf} (μS)	G0 (μS)	G1 (μS)	G2 (μS)	ω_{G0} (kRad/s)	ω_{G1} (kRad/s)	ω_{G2} (kRad/s)	Cb (μF)	B (μ)	p
0.05	0.92	0.13	0.25	0.22	0.23	2.50	9.00	45.00	3.40	0.65	0.59
0.10	0.92	0.13	0.25	0.22	0.22	3.00	43.00	45.00	3.60	0.75	0.60
0.15	0.92	0.13	0.25	0.22	0.22	9.00	30.00	70.00	4.00	0.80	0.62
0.20	0.92	0.13	0.25	0.22	0.22	8.00	30.00	50.00	4.00	0.85	0.63
0.25	0.92	0.13	0.25	0.22	0.22	9.00	30.00	50.00	3.60	0.65	0.67
0.30	0.92	0.13	0.25	0.22	0.22	9.50	30.00	60.00	3.40	0.70	0.68
0.35	0.92	0.13	0.25	0.22	0.22	9.50	30.00	60.00	5.00	0.85	0.67
0.40	0.92	0.13	0.25	0.22	0.22	9.50	30.00	60.00	3.40	0.70	0.68
0.45	0.92	0.13	0.25	0.22	0.22	10.00	30.00	50.00	3.60	0.90	0.69
0.50	0.92	0.13	0.24	0.24	0.22	3.90	13.00	35.00	2.90	1.10	0.68
0.55	0.92	0.13	0.24	0.23	0.19	29.00	35.00	48.00	3.90	1.30	0.66
0.60	0.92	0.13	0.24	0.23	0.19	29.00	35.00	46.00	2.90	1.35	0.66
0.65	0.92	0.13	0.24	0.23	0.19	29.00	35.00	46.00	3.20	1.60	0.64
0.70	0.92	0.13	0.24	0.23	0.19	29.00	35.00	46.00	2.90	1.25	0.67
0.75	0.92	0.13	0.24	0.23	0.19	29.00	35.00	46.00	3.20	1.40	0.67
0.80	0.92	0.13	0.24	0.23	0.19	29.00	35.00	46.00	2.90	1.00	0.67
0.85	0.92	0.13	0.24	0.23	0.19	29.00	35.00	50.00	3.90	1.10	0.72
0.90	0.92	0.13	0.24	0.23	0.19	29.00	35.00	46.00	2.90	0.90	0.73
0.95	0.92	0.13	0.24	0.23	0.19	29.00	35.00	46.00	3.50	1.00	0.72
1.00	0.92	0.13	0.24	0.21	0.22	29.00	35.00	50.00	4.00	1.20	0.72

Table 7-10 Model bulk and barrier response times for sample responses IPM, AOT 20% H2O 18% for applied ac voltage 0.05 V to 1.00 V

	Bulk				Barrier			
AC Voltage (V)	τ_{inf} (μs)	τ_{G0} (μs)	τ_{G1} (μs)	τ_{G2} (μs)	τ_{bar_inf} (s)	τ_{G0bar} (s)	τ_{G1bar} (s)	τ_{G2bar} (s)
0.05	7.39	400.00	111.11	22.22	32.40	16.53	18.08	17.92
0.10	7.39	333.33	23.26	22.22	34.80	17.76	19.42	19.51
0.15	7.39	111.11	33.33	14.29	38.40	19.20	21.43	21.52
0.20	7.39	125.00	33.33	20.00	38.80	19.40	21.65	21.75
0.25	7.39	111.11	33.33	20.00	34.00	17.00	18.97	19.06
0.30	7.39	105.26	33.33	16.67	32.80	16.40	18.30	18.39
0.35	7.39	105.26	33.33	16.67	46.80	23.40	26.12	26.23
0.40	7.39	105.26	33.33	16.67	32.80	16.40	18.30	18.39
0.45	7.39	100.00	33.33	20.00	36.00	18.00	20.09	20.18
0.50	7.39	256.41	76.92	28.57	32.00	17.02	16.46	18.35
0.55	7.39	34.48	28.57	20.83	41.60	22.13	22.51	26.80
0.60	7.39	34.48	28.57	21.74	34.00	18.09	18.40	21.91
0.65	7.39	34.48	28.57	21.74	38.40	20.43	20.78	24.74
0.70	7.39	34.48	28.57	21.74	33.20	17.66	17.97	21.39
0.75	7.39	34.48	28.57	21.74	36.80	19.57	19.91	23.71
0.80	7.39	34.48	28.57	21.74	31.20	16.60	16.88	20.10
0.85	7.39	34.48	28.57	20.00	40.00	21.28	21.65	25.77
0.90	7.39	34.48	28.57	21.74	30.40	16.17	16.45	19.59
0.95	7.39	34.48	28.57	21.74	36.00	19.15	19.48	23.20
1.00	7.39	34.48	28.57	20.00	41.60	22.13	24.64	24.07

In addition to being affected by the frequency dependent bulk conductance components, the barrier shape, magnitude and characteristic Maxwell-Wagner cross over frequency were dependent on three parameters. The C_b constant barrier capacitance, and both the magnitude B and the index p of the universal complex barrier capacitor $B(i\omega)^{-p}$. Figure 7-22A shows the changes in magnitudes of parameters used to curve fit the barrier for responses with applied ac voltages ranging from 0.05 to 1.00 V. Figure 7-22B shows the bulk relaxation times associated with bulk G_{inf} and the transition frequency dependent conductance G_0, G_1 and G_2. The transition response times display three steps as the voltage is increased from 0.05 to 1.00 V, which are consistent with the steps shown in Figure 7-20.

Figure 7-22C shows the changes in magnitudes of the bulk conductance and barrier capacitance as the ac voltages is increased from 0.05 to 1.0 V. Calculating the barrier charging relaxation time results in τ_3 = 15.9 s for the voltage range, despite the visual changes to the shape of the capacitance below and prior to the extrapolated C'/C" crossover frequency.

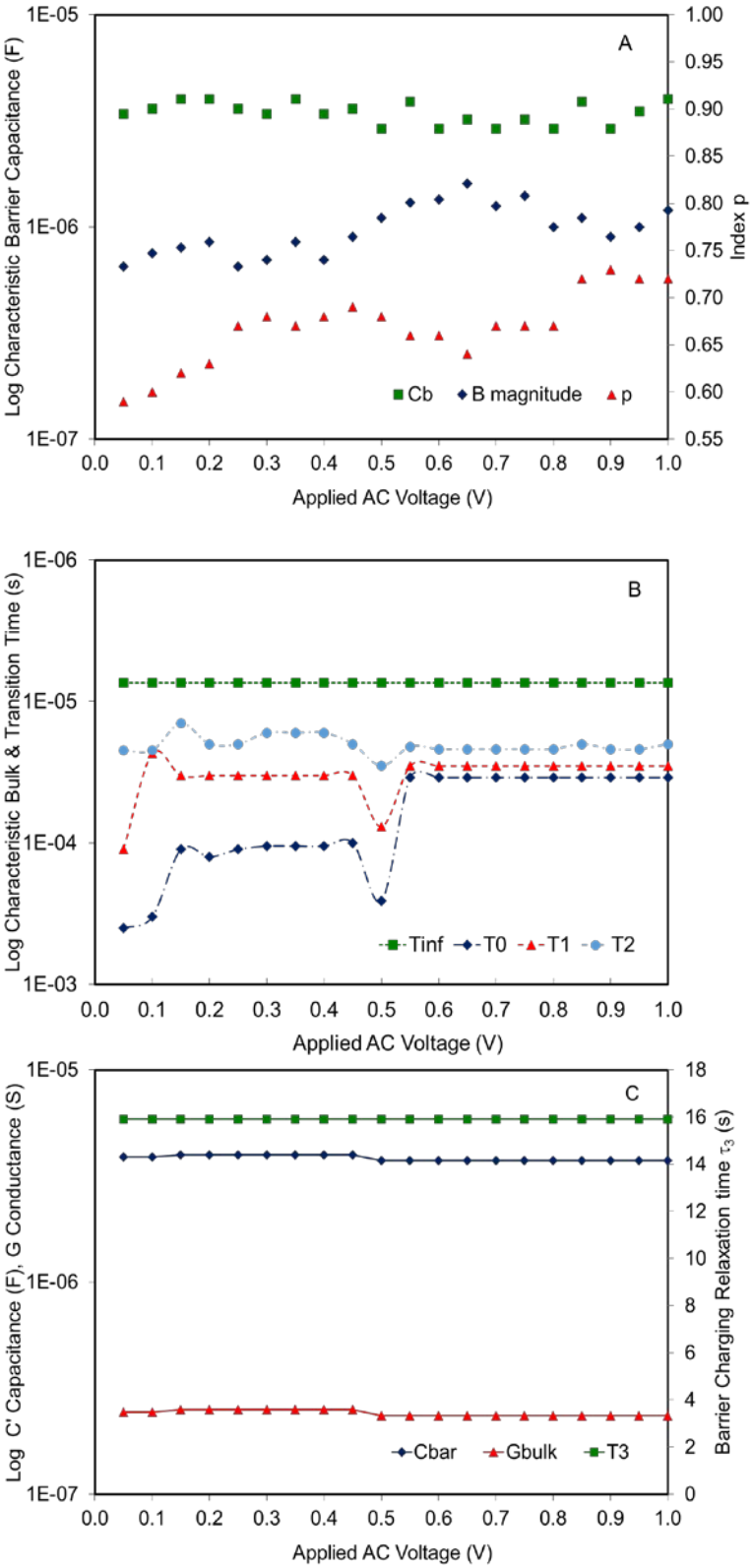

Figure 7-22 A) Index p and capacitance magnitudes of the universal barrier capacitance $B(i\omega)^{-p}$. B) fitted bulk relaxation times C) Observed variations in the magnitude of cross over bulk conductance and barrier capacitance as the applied ac voltage is increased for sample IPM:AOT:H2O percentage ratio 62:20:18.

7.6 Effects on the Barrier Response of Adding 1% w//w Na Salicylate to the Water Phase

The magnitude of the barrier capacitance of the microemulsions AOT:IPM:H_2O comprised of 20% w/w AOT with added water up 20% w/w varied due to the both the magnitude of the applied ac voltage and the spacing of the electrodes of the sample holder. When 1% w/w Na salicylate was solubilised in water to form the composition AOT 20% IPM 70% H20 9 % drug 1%, the barrier response showed more distinct changes to the shape.

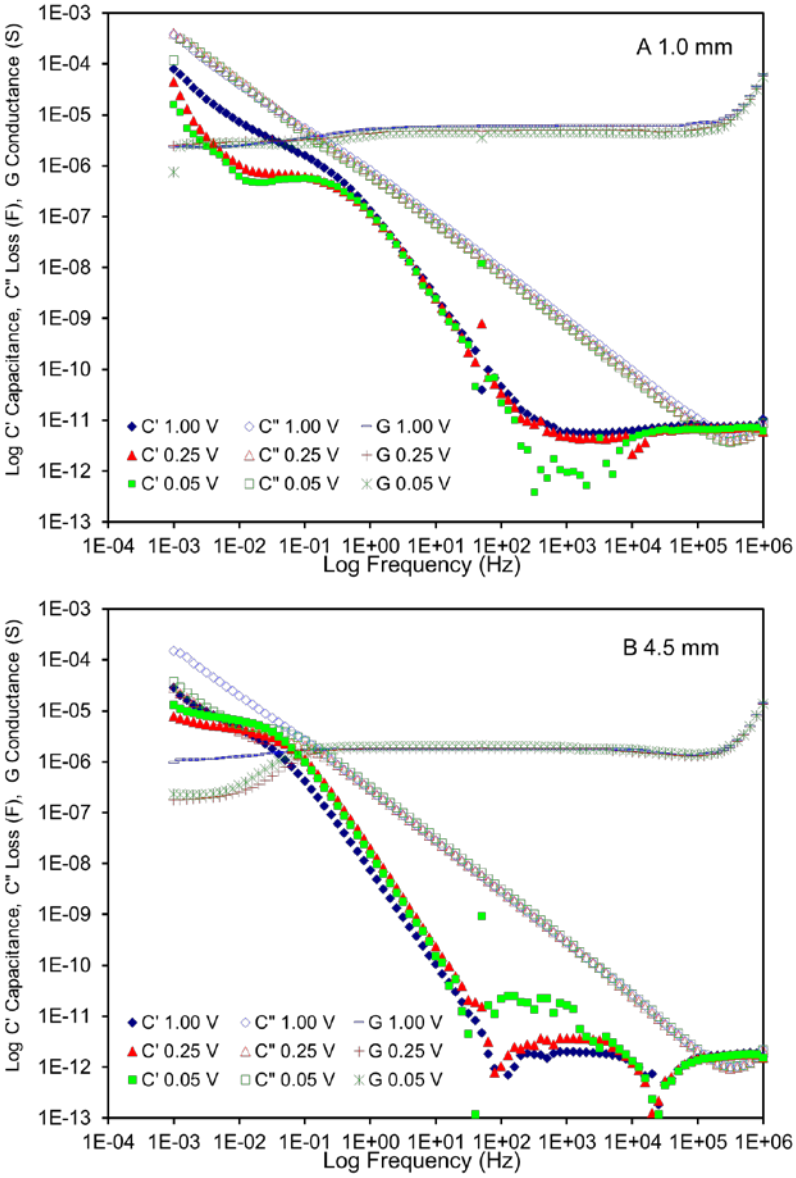

Figure 7-23 Response of quaternary sample IPM:AOT:H2O: Na Salicylate % w/w ratio 70:20:9:1 measured with A) 1 mm and B) 4.5 mm electrode spacing.

Measurements made with the wider electrode spacing 4.5 mm, the barrier showed evidence of diffusion as the gradient of capacitance changed from the MW dispersion

gradient -1.92 to -0.5 in the barrier through to p = - 0.75 below the barrier cross over frequency ω_2=4.99x10^{-2} rad/s. When electrode spacing was reduced to 1 mm, the barrier capacitance and loss components are separate. Although the magnitude of the conductance is reduced at the barrier, the charges are able to flow.

Table 7-11 Barrier charging and barrier relaxation times for sample containing 1% w/w Na salicylate measured using 0.25 V ac applied voltage

		Electrode Spacing		
		1mm	4.5mm	No drug
		0.25 V	0.25 V	0.25 V
Bulk				
Frequency ω_1	(Mrad/s)	0.79	0.13	0.233
Relaxation time τ_1	(μS)	1.26	7.94	4.29
Capacitance C'inf	(pF)	7.05	1.80	2.20
Conductance G_{bulk}	(μS)	27.33	1.78	0.447
Barrier Charging				
Frequency ω_3	(rad/s)	1.58	0.32	0.101
Relaxation time τ_3	(s)	0.63	3.16	9.95
Capacitance C'	(μF)	17.30	5.62	5.02
Conductance G_{bulk}	(μS)	27.33	1.78	0.43
MW index $\omega^{-(2-n)}$		-1.85	-1.92	-1.88
Barrier				
Frequency ω_2	(μrad/s)	628	49,900	
Relaxation time τ_2	(ks)	1.59	0.02	
Capacitance C'	(μF)	4,100	5	
Conductance $G_{barrier}$	(μS)	2.57	0.23	
Index p			-0.75	-0.77
Dielectric increment				
C'_{bulk}/C'_{bar}	(x10^{-6})	0.41	0.32	0.40
ω_1/ω_3	(x10^{6})	0.50	0.41	2.31

There are significant differences in the visual appearance of barrier for samples containing Na salicylate and the barrier thickness is still 10^{-6} thinner than the electrode spacing. However as Na salicylate is soluble in water, it is expected that it should be largely reside within the water pools in the interior of the microemulsion aggregate, and given its ionic nature in proximity to headgroups of the surfactants. The appearance of the barrier response suggest that the solute is located at the interface or boundary between aggregates. If we were to assume that the permittivities of the barrier and the bulk were the same then the thickness of the barrier ranges from 0.8 nm to 1.5 nm for samples containing Na salicylate. However the estimated bulk conductivities of the sample containing Na salicylate is approximate twice that of the sample without. Hence it would appear that Na salicylate or the sodium ions are dispersed in the bulk-intracluster phase and is contributing to the bulk polarisation response.

7.7 Discussion

7.7.1 IPM – AOT Association Prior to Microemulsion Aggregate Formation

From a dielectric perspective the bulk continuum of the IPM system is comprised of interacting clusters of IPM molecules whose individual molecules are interacting with a local group of neighbouring IPM molecules (Figure 2-11). These clusters of IPM molecules in turn are interacting with local groups of IPM clusters. This clustering is scaled with the fractal structure scaling to larger and larger interacting groups of what they would see as local cluster groups.

The introduction of the anionic surfactant AOT interferes with group and breaks up the large clusters of IPM into smaller clusters (Figure 6-8) and this is evidenced by the migration of the intracluster crossover of the capacitance C’ and loss C” components moving to higher frequencies. However the anomalous conductance increase and negative capacitance features which was observed only in the individual oil components IPM Figure 5-9 and ethyl caprylate Figure 5-19 at frequencies below ω=1 rad/s, migrated higher frequencies linearly with increasing [AOT]/[IPM] molar ratio. If the AOT was simply dispersed in the bulk IPM and not strongly interacting, then one would expect the magnitudes of the capacitance of their individual responses to add at the frequency at which they occur, and the response of the IPM anomalous features would be masked by that of AOT. However as the anomalous features moved to higher

frequencies relative to the intracluster characteristic frequency with increasing molar ratio [AOT]/[IPM] it would be reasonable to assume that a parallel rather than serial coupling configuration of the AOT and IPM exists on the boundaries of the local clusters. These cluster groups continue to reduce in size once water is added for W_0=[H2O]/[AOT] <9. The shape and size of the cluster cannot be determined solely using dielectric spectroscopy.

7.7.2 Bulk - Intracluster Relaxation and Cluster Sizing

The characteristic intracluster response time τ_1 of the ternary IPM:AOT:H_2O compositions increased linearly with molar ratio until W_0>9. For molar ratios W_0<9, the intracluster response time τ_1 decreased with increasing W_0. Particle sizing techniques confirm the presence of microemulsion aggregates radii ranging from 12 to 30 nm for samples with 9< W_0<26. Hence combining the particle sizing and low frequency dielectric spectroscopy analysis techniques it was possible to confirm that slowing down in the intracluster time τ_1 for W_0>9 was directly related to the increasing size of the microemulsion aggregate.

In the molar ratio range 0< W_0<9 the intracluster relaxation time increase at linear rate to its fastest for W_0=9.2 with τ_1 = 2.8 ms. No microemulsion aggregates were observed below W_0=10 using light scattering particle size technique (probe wave length= 677 nm, section 4 Table 4-4). Hence the relaxation time around W_0=9.2 was probably due to the presence of small micellar aggregates. Based on the difference on the response times from increasing to decreasing on either side of W_0=9, it is reasonable to assume AOT/IPM cluster undergoes structural transition from large amorphous interacting structures that collapses into the spherical body as the AOT headgroup is hydrated. The smallest particles detected using the Brookhaven Instruments Particle Sizer on an aged sample of AOT:IPM:H2O W_0=12.832 was 7.6 nm. Any micelles present must be smaller than this value.

7.7.3 Barrier – Interface Thickness estimation

Despite measurement of the electrode spacing prior to attaching the sample cell to the FRA, it was not possible to confirm that the electrode spacing had not changed once the FRA terminals were connected to the sample measuring cell.

Estimates of the barrier thickness were obtained by using the dielectric increment between the bulk capacitance C_{inf}, and the barrier capacitance C_{bar}. C_{inf}/C_{bar} provided an order of magnitude difference between the capacitance due to the electrode spacing and the magnitude of the capacitance following a dispersion. Table 7-8 list the dielectric increments for the hydrated sample series. Assuming the permittivities of the barrier and the bulk are the same, then the interface layer was of the order of 10^{-7} thinner than the electrode spacing of the sample cell. Using estimates of around 3- 4 mm for the electrode, an estimated barrier thickness of 1 nm for $W_0<2$ and a thickness ranging from 2 to 3 nm for $5.5 <W_0 < 26$. The length of an AOT molecule is around 3.25 nm, headgroup 1.75 nm and tails 1.5 nm [El Seoud 1984]. Hence the barrier interface appears to be that of the boundary between AOT/IPM clusters groups $W_0 < 9$ or between microemulsion aggregates $W_0 >9$.

7.7.4 Location of the Na Salicylate

The dielectric response microemulsions containing the solute sodium Salicylate were examined. However as no measurements were made of the individual compound or of it being dissolved in water, hence only the observation from one composition will be discussed. 1% w/w Na salicylate was solubilised in 9 % w/w water resulting in 10% w/w polar component in the IPM:AOT:H2O:NaS 70:20:9:1 % w/w composition.

The dielectric response from this sample showed a significant change to the shape of the barrier when compared to the W_0=12.83 microemulsion with no solute. The magnitude bulk conductivity was estimated as 2.19 times larger than a sample without the solute. This indicates that the sodium ions from the solute were located within the interior of the microemulsion aggregate. Estimates of the barrier thickness ranged between 1 – 1.5 nm, assuming the permittivities of the bulk and the barrier are the same. However from the appearance of the barrier Figure 7-23 this assumptions is unlikely to be correct as it would appear that the solute is sited at the interface boundary of the aggregate, whilst the dissociated positive sodium ion is located within water core of microemulsion

aggregate (Figure 1-17C) contributing to the increase in the conductivity of the aggregate response.

7.7.5 IPM Permanent Dipole State Transition Gating Characteristics

The weakly conducting IPM showed evidence of state changes which resulted in anomalous magnitude increase in the conductance and magnitude decrease in capacitance components of the frequency sweep dielectric response. The anomalous response took place in the frequency range between the intracluster ω_1 and the barrier charging dispersion ω_3 responses hence placing the characteristic feature at the interface boundary. The quasi-dc Dissado-Hill cluster model was adapted to include linearised bulk frequency dependant conductance $G(\omega)$ terms in parallel with the bulk conductance, both in series with a leaky universal capacitor term and was used to curve fit the experimental data (Figure 5-18).

The inclusion of the linearised conductance terms in the curve fit model, mirrored the approach taken by Fishman *et al.* (1979) and Dissado (1990) to analyse similar magnitude changes to conductance and capacitance response of biological tissue, membrane and squid axions for example. The tissue membrane exposed to conditions such as small variations in electric field strength, the addition solutions contain various concentrations of sodium and potassium ions showed evidence of membrane pores opening closing or structure realignments. The structural changes allowed ions to travel through the channels opened and the flow of ions continued until a new equilibrium on either side of the membrane was established which triggered membrane structure realignment (gating) which closed the channel.

The anomalous response was observed for both esters oils IPM and ethyl caprylate, but not observed with the other oil, surfactant and polar components examined. The anomalous response continued to be observed in dual component samples, but at higher frequencies ranges when the surfactants in the study, E200, Brij 97 and AOT were dispersed in IPM. A review of the literature [Razafindralambo 2009] suggested the ester carbonyl group C=O and the permanent 2.3 D dipole [Dissado 2006] may have been the source of the anomalous response features. Gilani *et al.* [2003] description of correlated and anti-correlated dipoles was found to be compatible with the observed step changes in the response of the anomalous conductance increase and the capacitance

decrease to negative values. In order for the magnitude of the capacitance to decrease stored or blocked charges must be released. This can be achieved if a channel is opened in the barrier at frequencies and / or electric fields specific strengths. If a local cluster group of IPM and the individual IPM dipoles on the boundaries of local the group exist in one of the 3 Kirkwood correlation states described in Table 6-11 changes, then channels allowing charges to be released and flow can be opened.

When IPM is joined with AOT at the interface between clusters as determined from, the frequency response position of the anomalous feature and the shifting the feature to higher frequencies with increasing [AOT]/[[IPM], the local cluster group sizes reduce. However as the larger clusters are not detected by particle scattering, it is assumed the AOT/IPM form film like structures on at the boundaries of the clusters (Figure 7-24). As the hydration of the AOT headgroup increases $0<W_0 < 9$ the response of the anomalous feature rapidly moves to higher frequencies indicating the cluster size shrinking to point where small spherical structures can be formed around $W_0=9$. It is probable that the small micelles reported by authors are also present, but due to their small size are only detectable beyond the upper frequency limit of the low frequency FRA.

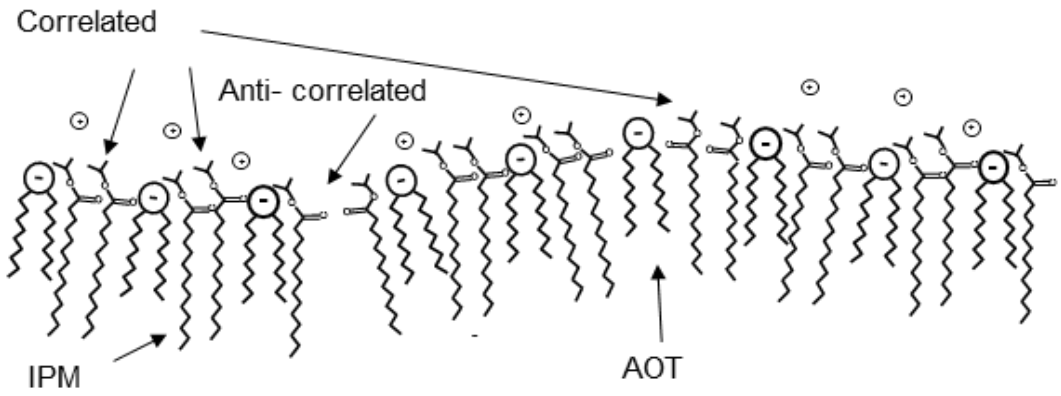

Figure 7-24 Pictorial representation of AOT-IPM structure with the IPM carbonyl group adopting both anti correlated and correlated configurations.

Above $W_0=9$ the reduction in the intracluster relaxation time with the light scattering confirmation of the presence microemulsion aggregates, the gating process corresponding to the anomalous response continues. Indicating the oil IPM contributes to the stabilities and life time of the microemulsion aggregate.

7.8 Conclusion

The dielectric technique was able to detect changes in magnitude of the conductivity and the speeding then slowing down of the characteristic intracluster relaxation as samples transitioned from one expected to contain micelle aggregates to one which contained microemulsion aggregates.

The use of the low frequency dielectric spectroscopy technique combined with particle sizing is a good method of examining complex condensed microemulsion systems without the need to either dilute or change components to aid the probing technique.

7.9 Further Work

Initial dielectric response obtained for the quaternary system comprise of AOT:IPM:H2O: Na salicylate 20:55:13.5:1.5 showed the fully developed barrier response τ_2=8 s, barrier charging t3=0.02 s however the τ_1 intracluster cross over was beyond the upper limit of the FRA but was modelled and found to be 0.01 μs. It is recommended that AOT 25% w/w ternary and quaternary series be examined using dielectric spectroscopy and particle sizing techniques to catalogue the micelle / microemulsion transition and the characteristics of the barrier layer.

It is recommended that impact of cooling reverse microemulsion, ternary, dual and individual component samples to domestic refridgeration temperatures be investigated. It is anticipated that features which respond at frequencies outside the 10^{+6} Hz range of the 1255A FRA /CDI configuration may be brought into range by the lowering of the temperature of the samples under investigation.

It is also recommended that the individual response both ester and non ester based oils be obtain under a range of field strengths before obtaining the responses from dual component systems comprised of surfactants known to be capable of forming reverse microemulsions solubilised in the oils. Appendix C shows a side by side comparison of the response the indivual ester oil components IPM and ethyl caprylate, and the same oils with 10% AOT surfactant dispersed in the oils.

Chapter 8

Conclusion

8. Conclusion

8.1 Individual Components

Low frequency dielectric spectroscopy is a useful technique for examining the dielectric behaviour of both polar and apolar materials. Comparing the responses obtained for each of the individual components, and analysing the data using an appropriate model, provides information on the structural arrangements of local clusters as well as the efficiency of the energy transport process.

Changes in the geometry of the measuring cell and environmental conditions can have an impact on the both the magnitude and shape of the dielectric response. Special attention is needed when setting the electrode spacing for a series of measurements on different samples if it is important to make a direct comparison between the responses. Similarly, materials suspected of containing mobile charges are likely to suffer from hysteresis when measured repeatedly. Hence results selected for comparison from series of measurements, made on a range of samples need to be matched, i.e. the first measurement for each of the samples as no individual spectral response can be taken as an absolute representation.

8.2 Annomalous Negative Capacitance and the Ester Carbonyl Group

Two of the oils, Isopropyl myristate (IPM) and Ethyl caprylate (EC) examined in this study showed evidence of capacitance gradually decreasing to negative values whilst the conductance simultaneously increased in magnitude. Examination of the log/log plots of the complex capacitance as well as the data files showed that there was a gradual decrease in the magnitude of response of the capacitance as the frequency of the applied field was reduced for a log frequency scale range of more than a decade prior to the capacitance becoming negative. When the surfactant AOT was dispersed in the oils, the appearance of the negative capacitance moved the higher frequencies.

Both IPM and EC are single chained ester oils which have a carbonyl COO^- group that contains a permanent dipole. It is reasonable to assume that the observed negative capacitance with corresponding increases in conductances is due to response of the carbonyl groups. Hence it may be therefore concluded that the low frequency dielectric spectroscopy technique is able to detect changes in the orientation of the carbonyl permanent dipole in ester. The reorientation of these dipoles results in a structural

change in the boundaries of the cluster groups of the oils, which enables charges to flow more easily. This reorientation process is non-linear process and requires a linearised circuit element used in the modelling of excited biological cell membranes to model this response. This indicates that the choice of the bulk phase is plays a significant role in the ability of an oil/water/ surfactant mixture to form reverse micelles and microemulsion aggregates.

8.3 Dual Component Compositions

The low frequency dielectric spectroscopy technique is able to detect changes in the composition of dual component samples comprised of bulk phase IPM oil with varying concentrations of surfactant AOT dispersed within the oil phase. The characteristic negative capacitance feature which is observed in the individual IPM samples, move linearly to higher frequencies as the concentration of the dispersed surfactant is increased. The migration of the anomalous negative capacitance to higher frequencies suggests that interacting groups of clusters of IPM have been disrupted and broken into progressively smaller groups as the concentration of dispersed surfactant increase. Hence the low frequency dielectric spectroscopy technique is able to track relative changes in sizes of clusters of bulk phase of the IPM oil by, tracking changes to the intracluster relaxation time τ_1 as the concentration of the dispersed phase surfactant AOT is varied.

8.3 Ternary Compositions and Reverse Microemulsions

The dielectric technique was able to detect changes in magnitude of the conductivity and the speeding up then slowing down of the characteristic intracluster relaxation τ_1 as samples transitioned from one expected to contain micelle aggregates to one which contained microemulsion aggregates.

The use of the low frequency dielectric spectroscopy technique combined with particle sizing is a good method of examining complex condensed microemulsion systems without the need to either dilute or change components to aid the probing technique.

8.4 Selection of Electrodes

A pair of brass disc electrodes were used to conduct a small series of dielectric measurments on a range of samples comprised of the oil IPM, surfactant AOT and

water or propylene glycol PG. Although each full cycle measurement took approximate 2 hours, the brass electrodes were found to have a copper coloured appearance after the same sample was measured repeatedly (Appendix D, Figure D-1(E). Examination of the complex response showed an anomalus changed in the shape of the barrier region circled Appendix D, Figure D-1(A-D) with each measuring cycle. It was assumed that the brass electrode was reacting with the dispersed AOT, hence the electrode was unsuitable for use with the samples in this study.

Chapter 9

References

9. References

Aboofazeli, R.; The formation and characterisation of phospholipids microemulsions; PhD Thesis, (1994); Chelsea Department of Pharmacy, Kings College London

Abramowitz, M.; Stegun, I.A.; *Handbook of Mathematical Functions* (1972) Dover Publications , **1020**,72,74

Aniansson, E.A.G.; Wall, S.N.; Almgren, M.; Hoffmann, H.; Kielmann, I.; Ubricht, W.; Zana, R.; Tondre C.; Theory of the kinetics of micellar equilibria and quantitative interpretation of chemical relaxation studies of micellar solutions of ionic surfactants; *J. Physical Chemistry*, (1976) **80**, 905-922

Antalek, B.; Williams, A. J.; Texter J.; Feldman Y.; Garti, N.; Microstructure analysis at the percolation threshold in reverse microemulsions; *Colloids and Surfaces A: Physicochemical and Engineering Aspects* (1997) vol **128**, 1-11

Antalek, B.; Williams; A. J., Texter, J.; Feldman, Y.; Garti, N.; Microstructure analysis at the percolation threshold in reverse microemulsions; *Col and Surf A: Physicochemical and Engineering Aspects* (1997) **128**, 1- 11

Barlow, D.J.; Lawrence, M.J.; Zuberi, T.; Zuberi, S.; Small-angle neutron scattering studies on the nature of the incorporation of polar oils into aggregates of N,N-dimethyldodecylamine-N-oxide.; (2000) *Langmuir*, **16**, 10398-10403

Barnadas-Rodreguez, R.; Estelrich, J.; Photophysical changes of Pyranine induced by surfactants: Evidence of premicellar aggregates; J. Phys. Chem.. B (2009) **113**, 1972-1982

Barsoukov, E.; Macdonald, J. R.; Impedance Spectroscopy theory, experiment and applications ;Wiley-Interscience 2nd ed. (2005), 205-226

Becher, P.; The Chemistry of Emulsifying Agents. In Emulsions Theory and Practice 2nd edition Krieger Publishing Company (1977) 209-266

Binks, B.P; Surfactant Monolayers at Oil-Water Interfaces; *Chemistry & Industry* (1993), **14**, 535-541

Bodakain, B.; Hill, R.M.; The use of Dielectric Analysis in the Examination of Coatings; *J Phys D: Appl Phys* **24** (1991),78-80

Bourrel, M. Schechter, R.S., Microemulsions and related systems, Marcel Dekker, Inc., New York and Basel, (1988).

Brinchi, L.; Germani, R.; Savelli, G.; Di Michele, A.; Onori, G.; Premicelles of cetyltrimethylammonium methanesulfonate: Spectroscopic and kinetic evidence; *Colloids and Surfaces A*: Physicochem. Eng. Aspects (2009) **336**, 75–78

Broze, G; Handbook of detergents part A: Properties, Marcel Dekker, Inc New York and Basel, (1999)

Bru, R.; Sanchez-Ferrer, A.; Garcia-Carmona, F; Kinetic models in reverse micelles; *Biochem. J.* (1995) **310**, 721-739

Chandler, D.; Interfaces and the driving force of hydrophobic assembly; (2005) *Nature*, **437**, 640-647

Chen, S.H.; Chang, S.L.; Strey, R.; Structural evolution within the one-phase region of a three-component microemulsion system: Water-n-decane- sodium bis(2-ethylhexyl) sulfosuccinate (AOT); *J. Chem. Phys*. (1990), **93**, 1907-1918

Chen, S.J.; Evans, D.F.; Ninham, B.W.; Mitchell, D.J; Blum, F.D; Pickup, S.; Curvature as a Determinant of Microstructure and Microemulsions; *J. Phys. Chem.* (1986), **90**, 842-847

Chevalier, Y; Zemb, T; The Structure of Micelles and Microemulsions; *Rep. Prog. Phys.* **53** (1990) 279-371

Cooper, J.; Hill, R.M.; Dielectric Spectroscopy of liquid lamellar phases; *J. Colloid and Interface Science*, (1996)**180**, 27-35

Craig, D.Q.M.; Livens, H. S. R.; Pitt, K.G.; Storey, D.E.; *et al*; An investigation into the physic-chemical properties of self-emulsifying systems using low frequency dielectric spectroscopy, surface tension measurements and particle size analysis; *International Journal of Pharmaceutics*, **96** (1993) 147-155

Cui, X.; Mao, S.; Liu, M.; Yuan, H.; Du, Y.; Mechanism of Surfactant Micelle Formation; *Langmuir (*2008), ***24***, 10771-10775

Danov, K. D.; Kralchevsky, P. A.; Ivanov, I. B; Equilibrium and dynamics of surfactant adsorption monolayers and thin liqid films; *Handbook of detergents part A: Properties,* Marcel Dekker, Inc New York and Basel, (1999), **82**, 303-418

Debye, P; Polar Molecules; Dover Publications: New York, (1945)

Dissado, L. A.; Dielectric Response; Springer Handbook of Electronic and Photonic Materials, (2006), Part A,187-212

Dissado, L. A.; Hill, R. M.; A Cluster approach to the structure of imperfect materials and their relaxation spectroscopy; *Proc. R. Soc. Lond A.* (1983) **390**, 131-180

Dissado, L. A.; Rowe, R.C.; Haidar, A.; Hill, R. M.; The Characterisation of Heterogeneous Gels by Means of a Dielectric Technique; J. *Collod and Interface Science* (1987) **117**, 310-324

Dissado, L. A; A fractal interpretation of the dielectric response of animal tissues; *Phys. Med. Biol.*; (1990), **35**,1487-1503

Dissado, L. A; Hill, R.M; Anomalous Low-frequency Dispersion; *J. Chem. Soc, Faraday Trans. 2*, (1984), **80**, 291-319

Dissado, L. A; Hill, R.M; Constant-phase-angle and power-law regimes in the frequency response of a general determinate fractal circuit; *Phys. Rev. B.* (1988), **37**, 3434-3439

Dissado, L. A; Hill, R.M; The fractal nature of the cluster model dielectric response functions; *J. Appl. Phys.* (1989), **66**,2511-2524

Dissado, L.A.; Ion transport through nerves and tissues*; Comments on Molecular and Cellular Biophysics*, (1987), **4**, 143-169

Drennan , C.E.; Hughes , R.J.; Reinsborough, V.C.; Soriyan, O.O.; Rate enhancement of nickel(II) complexation in dilute anionic surfactant solutions; *Can. J. Chem.* (1998), **76**, 152-157

Durbut, P. Surface Activity; Hand book of Detergents; *Surfactant Science Series*, (1999), **82**, 47-97

Eicke, H.F.; Borkovec, M.; Das-Gupta, B.; Conductivity of Water-in-Oil Microemulsions: A Quantitative Charge Fluctuation Model; *J. Phys. Chem.*, (1989) **93**, 314-317

Eicke, H.F.; Hilfiker, R.; Thomas, H.; Connectivity-Controlled Charge Transport in Water-in-Oil Microemulsions; *Chem. Phys. Lett.*, (1986) **125**, 295-298

Eicke, H.F.; Kvita, P.; Reverse Micelles and Aqueous Microphases; In: Reverse micelles – Biological and technological relevance of amphiphilic structures in apolar media, (Luisi, P.L. and Straub, B., eds.), Plenum Press, New York. (1984) 21-35

Ek, R; Hill, R.M.; Newton, J.M.; Low frequency dielectric spectroscopy characterization of microcrystalline cellulose tablets and paper; *Journal of Materials Sciences*, (1997) **32**, 4807-4814

El Seoud, O. A.; Acidities and basicities in reversed micellar systems; In: Reverse micelles – Biological and technological relevance of amphiphilic structures in apolar media, (Luisi, P.L. and Stmub, B., eds.), Plenum Press, New York. (1984) 81-93

Feldman, Y.; Kozlovich, N.; Nir, I.; Garti, N.; Dielectric spectroscopy of microemulsions; *Colloids and Surfaces A: Physicochemical and Engineering Aspects* (1997) vol **128**, 47-61

Feldman, Y.; Kozlovich, N; Nir, I; Garti, N.; Dielectric relaxation in sodium bis(2-ethylhexyl) sulfosuccinate – water – decane microemulsions near the percolation temperature threshold; (1995*) Physical review E*, **51**, 478-491

Fendler, J.H; Fendler, E.J; Prepartaion and purification of synthetic and naturally occurring surfactants; in: Catalysis in micellar and macromolecular systems; Academic Press New York San Francisco London 1975, Chapter 1, 1-16

Fishman, H.M.; Poussart, D.; Moore, L.E.; Complex Admittance of Na+ Conduction in Squid Axon; *J. Membrane Biol.* (1979), **50**, 43-63

Fletcher, P.D. I.; Howe, A. M.; Robinson, B.H.; The Kinetics of Solubilisate Exchange between Water Droplets of Water-in-oil Microemulsion; *J. Chem. Soc., Faraday Trans. 1*, (1987), **83**, 985-1006

Gilani, G.A.; Mamaghani, M.; Anbir, L.; Dipole moments and intermolecular association of some carbonyl compounds in nonpolar solvents; *J. Solu. Chem*. (2003), **32**, 625-636

Griffin, W. C; Classification of Surface Active Agents by HLB; *J. Soc Cosmet. Chem.*, (1949), **1**, 311-326

Hadgiivanova, R; Diamant, H; Premicellar aggregation of amphiphilic molecules: Aggregate lifetime and polydispersity; *J. Chem. Phys.* (2009) **130**, 114901

Hadgiivanova, R; Diamant, H; Premicellar aggregation of amphiphilic molecules; *J. Phys. Chem. B* (2007) **111**, 8854-8859

Hauser, H.; Haering, G.; Pande, A.; Luisi, P.L.; Interaction of Water with Sodium Bis(2-ethyl-1-hexyl) Sulfosucinate in Reversed Micelles; *J. Phys. Chem*, (1989) **93**, 7869-7876

Herzig, E.M.; White, K. A.; Schofield, A.B.; Poon, W.C.K.; Clegg, P.S; Bicontinuous Emulsions Stablilized Solely by Collodal Particles; *Nature Materials*, (2007) **6**, 966-971

Hill, R. M.; Cooper, J.; Characterisation of water in oil emulsions by means of dielectric spectroscopy, *J. Materials Science*, (1992) **27**, 4818-4827

Hill, R.M.; A quantified analysis of the dielectric dispersion in a simple emulsion system.; Int. *J. Pharm*, **227**, (2001) 139-148

Hill, R.M.; Beckford, E.S.; Rowe, R.C.; Jones, C.R. Dissado, L.A.; The characterisation of oil in water emulsions by means of a dielectric technique.; *J. Colloid Interface Sci*., **138** (1990) 521-533

Hill, R.M.; Cooper, J.; Dielectric Spectroscopy of Micelle Structures; *J. Colloid and Interface Science*, (1995) **174**, 24-31

Hill, R.M.; Lawrence,M. J.; Dielectric spectroscopy of Micro-Emulsions*;*

Encyclopaedia of Surface and Colloid Science (2002)

Israelachvili, J. N.; Mitchell, D. J.; Ninham, B. W.; Theory of Self-assembly of Hydrocarbon Amphiphiles into Micelles and Bilayers; *J. Chem. Soc. Faraday Trans.2*, (1976), **72**, 1525-1568

Jonscher, A.K.; Dielectric Relaxation in Solids; Chelsea Dielectric Press London; 1983

Kaler, E.W.; Billman, J.F; Fulton, J.L.; Smith, R.D; A Small Angle Neutron Scattering Study of Intermicellar Interactions in Microemulsions of AOT, Water and Near Critical Propane; *J. Phys. Chem*, (1991) **95**, 458-462

Kantaria, S; Novel Microemulsion-Based Gels: Their use with transdermal iontophoresis; PhD Thesis (1998); Chelsea Department of Pharmacy, Kings College London

Kaye, G.W.C.; Laby, T.H.; Noyes, J. G.; Phillips, G.F.; Jones, O.; Asher, J.; Kaye & Laby, Tables of Physical & Chemical Constants; 16th Edition; 1995

Langevin, D; Microemulsions and liquid crystals.; *Mol. Cryst. Liq. Cryst.*, **138** (1986) 259-305

Lawrence, M. J.; Rees, G. D.; Microemulsion-based media as novel drug delivery systems; *Adv. Drug Delivery Rev.* (2000), **45**, 89-121

Ludwig, R; Water: From Clusters to the Bulk; *Angew. Chem. Int. Ed.* (2001), **40**, 1808-1827

Luisi, P. L.; Giomini, M.; Pileni, M. P.; Robinson, B. H.; Reverse micelles as hosts for proteins and small molecules; *Biochimca et Biophysica Acta*, (1988) **947**, 209-246

Malliaris,,Angelos; Lang,,Jacques; Zana, Raoul; Dynamics of Micellar Solutions of Ionic Surfactants by Fluorescence Probing; *J. Phys. Chem.* (1986) **90**, 655-660

Martinek, K; Klyachko, N.L.; Kabanov, A.V; Khmelnitsky, Y.L.; Levahov, A.V.; Micellar enzymology: its relation to membranology; (1989) *Biochim. Biophys. Acta* **981**, 161-172

Martinsen, O.; Grimnes, S.; Schwan,H.P.; Interface phenomena and dielectric properties of biological tissue ; *Encyclopedia of Surface and Colloid Science*, (2002) 2643-2652

Mortazavi, S. A.; Aboofazeli, R.; An Investigation into the Effect of Various Penetration Enhancers on Percutaneous Absorption of Piroxicam; Ira. *J. Pharm. Res.*, (2003) **2**, 135-140

North, A. N.; Dore, J. C.; McDonald, J. A.; Robinson, B. H.; Heenan, R. K.; Howe, A. M.; Structure and Dynamics of Water-In-Oil Microemulsions Stabilised by Aerosol-OT; *Colloids and Surfaces* (1986), **19** ,21-29

Oldenhove de Guertechin, L.; Surfactant Classification; Hand book of Detergents; *Surfactant Science Series*, (1999), **82**, 7-46

Overbeek, J. Th. G; Microemulsions, a field at the border between lyophobic and lyophilic collids; *Faraday Disc. Chem. Soc.*; **65** (1978) 7-19

Pileni, M.P.; Zemb, T.; Petit, C; Solubilization By Reverse Micelles: Solute Localization and Structure Pertubation; *Chemical Physics Letters* (1985) **118**, 414-420

Pugh, J.; Chelsea Dielectric Interface User guide issue 1 circa 1988.

Razafindralambo, H.; Blecker, C.; Mezdour, S.; Deroanne, C.; Crowet, J.; Brasseur, R.; Lins, L.; Paquot, M.; Impact of the carbonyl group location of the ester bond on the interfacial properties of sugar based surfactants; *J. Phys. Chem. B.* (2009), **113**, 8872-8877

Robins, M.L., Theory for the phase behaviour of microemulsions; In Mittal, K.L. (Ed), *Micellization, Solubilisation, and microemulsions*, Vol **2** Plenum Press, New York (1977), 713-754

Rouch, J.;Safouane, A.; Tartaglia, P.; Static and dynamic light scattering studies of water –in – oil microemulsions in the critical region. Evidence of a crossover effect.; (1989) *J. Chem. Phys*., **90** 3756-3764

Ruckenstein, E.; Nagarajan, R.; Aggregation of amphiphiles in nonaqueous media; *J. Phys. Chem*, (1980) **84**, 1349-1358

Salager, J. L.; Anton, R. E; Sabatini, D. A.; Harwell, J. H.; Acosta, E. J; Tolosa, L. I.; Enhancing Solubilization in Microemulsions – State of the Art and Current Trends; *J. Surfactant and Detergents*, (2005), **8**, 3-21

Salager, J.L.; Microemulsions; *Hand book of Detergents; Surfactant Science Series*, (1999), 8**2**, 253-302

Schulman, J.H; Stoeckenius, W.; Prince, L. M.; Mechanism of formation and structure of microemulsions by electron microscopy; *J. Phys. Chem.* (1959), **63**, 1667-1680

Schwan, H.P.; Electrical Properties of Tissue and Cell Suspensions; *Adv Biol. Med Phys* (1957) **5**, 147-209

Schwan, H.P.; Linear and Nonlinear Electrode Polarization and Biological Materials; *Annals of Biomedical Eng.*, (1992) **20**, 269-288

Schwan, H.P.; Maczuk, J.; A simple Technique to control the stray field of electrolytic cells; *Review of Scientific Instruments* (1960) **31**,59-62

Scrivens, L.E.; Equilibrium Bicontinuous Structures; In Mittal, K.L. (Ed), *Micellization, Solubilisation, and Microemulsions*, Vol **2** Plenum Press, New York (1977); 877-893

Singh, B. N.; Singh, R. B.; Singh, J.; Effects of ionisation and penetration enhancers on transdermal delivery of 5-fluorouracil through excised human stratum corneum; *Int. J. Pharm.*, (2005), **298**, 98-107

Solartron Analytical 1255 Frequency Response Analyser Operating Manual (June 2001)

Sorichetti, P. A., Matteo, C. L.; Low-frequency dielectric measurements of complex fluids using high-frequency coaxial sample cells; *Measurement* (2007), **40**, 437-449

Stenius, P.; Micelles and Reverse Micelles: A Historical Overview; In: Reverse micelles – Biological and technological relevance of amphiphilic structures in apolar media, (Luisi, P.L. and Stmub, B., eds.), Plenum Press, New York. (1984) 1-19

Tanford, C.; The hydrophobic effect; J Wiley; (1973)

Thompson, K.F.; Gierasch, M.; Conformation of peptide Solubilzate in a Reverse Micelle Water pool, *J. Am. Chem. Soc.* (1984)**106**, 3684

Winsor, P. A.; Binary and multi-component solutions of amphiphilic compounds. Solubilization and the formation, structure and theoretical significance of liquid crystalline solutions; *Chem Rev*, (1968) **68**, 1-40

Winsor, P. A; Hydrotropy, solubilization, and related emulsification processes,. Part I, *Transactions of the Faraday Society*, *(*1948*),* **44**,376-399

Zettl, H.; Portnoy, Y; Gottlieb, M.; Krausch, G.; Investigation of Micelle Formation by Fluorescence Correlation Spectroscopy; *J. Phys. Chem. B* (2005) **109**, 13397-13401

Zulauf, M.; Eicke, H. F.; Inverted Micelles and Microemulsions in Ternary Systems H_2O /AOT/ Isooctane as studied by Photon Correlation Spectroscopy; *J. Phys. Chem*, (1979) **83**, 480-486

Appendix A - CDI and FRA 1255 Thresholds of Measurement

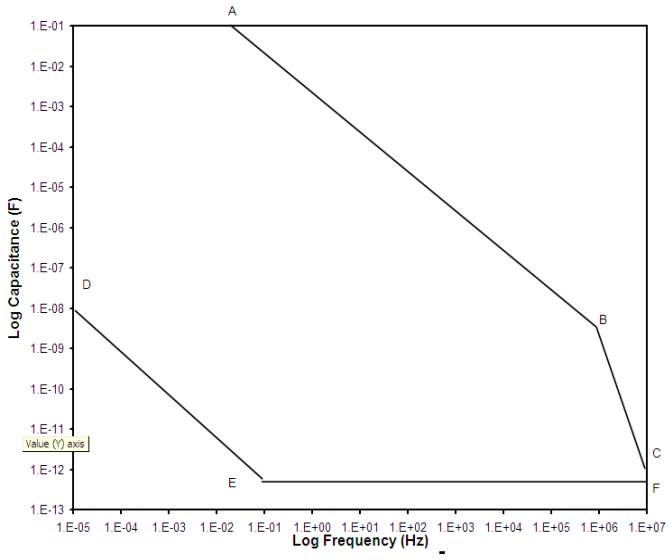

Capacitance Window

Upper threshold, line ABC.

At boundary AB the generator is loaded to 66% and boundary BC is due to high frequency limitations.

Lower threshold, line DEF

At boundary DE, the sample reactance is 5E-13 (S). Boundary EF represents the practical limit to sample capacitance of 0.5pF.

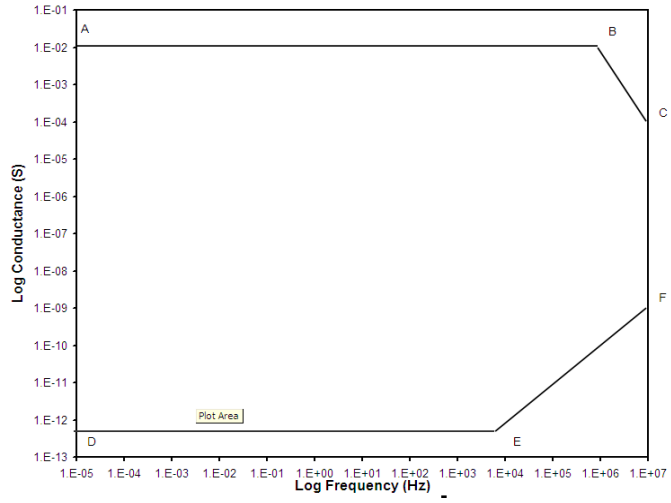

Conductance Window

Upper threshold, line ABC.

At boundary AB the generator is loaded to 66% and boundary BC is due to high frequency limitations.

Lower threshold, line DEF

At boundary DE, the sample conductance is 5E-13 (S). Boundary EF represents the high frequency limitations

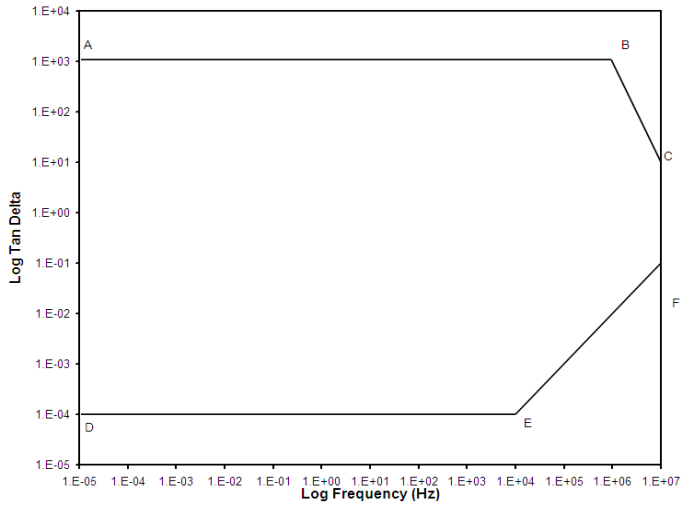

Tan Delta Window

Upper threshold, line ABC.

This represents the boundary above which the error in the discrimination of the sample capacitance may become greater than a factor of three or more.

Lower threshold, line DEF

This represents the boundary below which the error in the discrimination of the sample conductance may become greater than a factor of two or more.

Figure A-1 CDI and FRA 1255 Thresholds of Measurement for generator output 1vrms

Appendix B - Small Sample Cell Specification

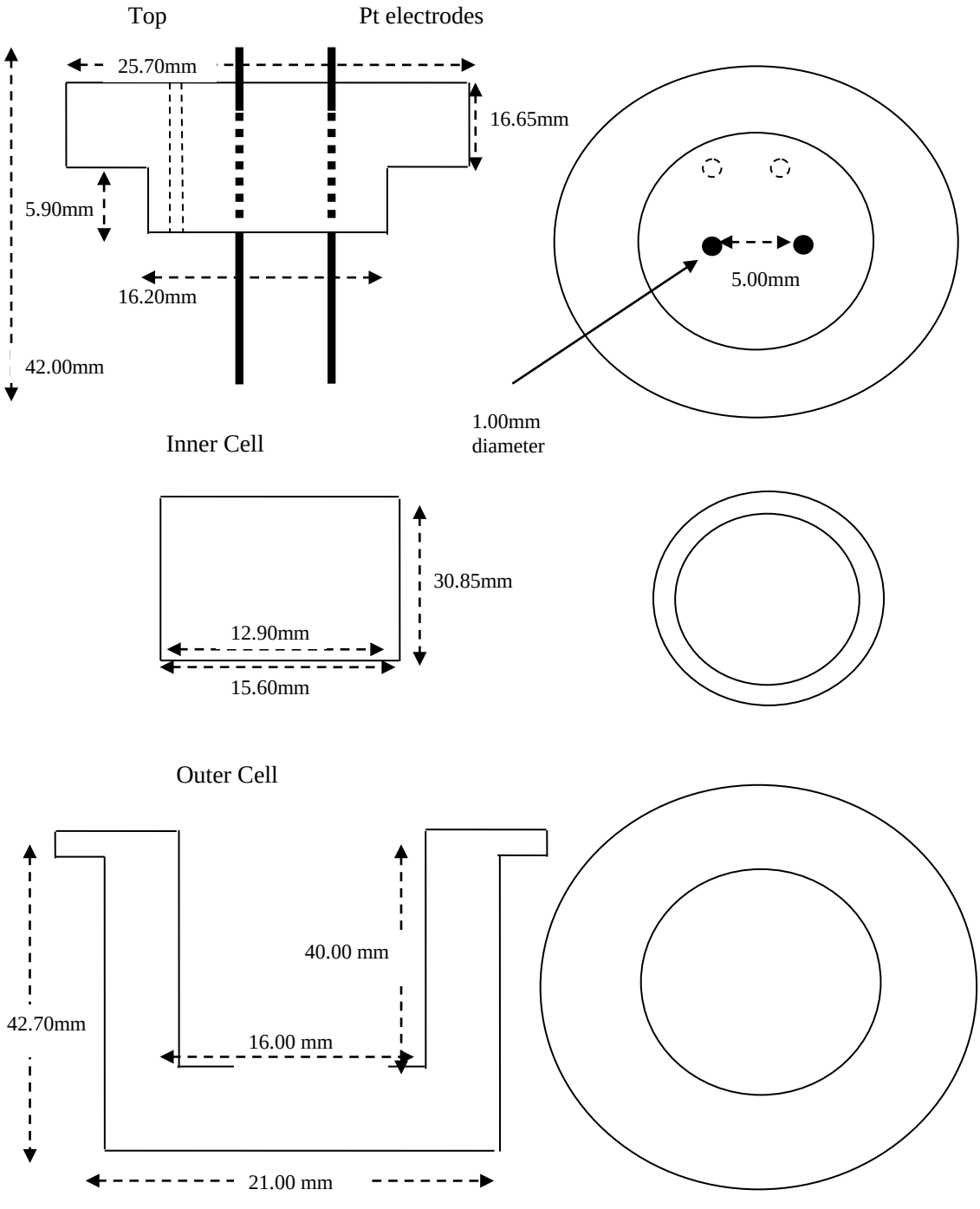

Figure B-1 Small Sample Cell Specification

Appendix C – 10% AOT Dispersed in Ethyl Caprylate

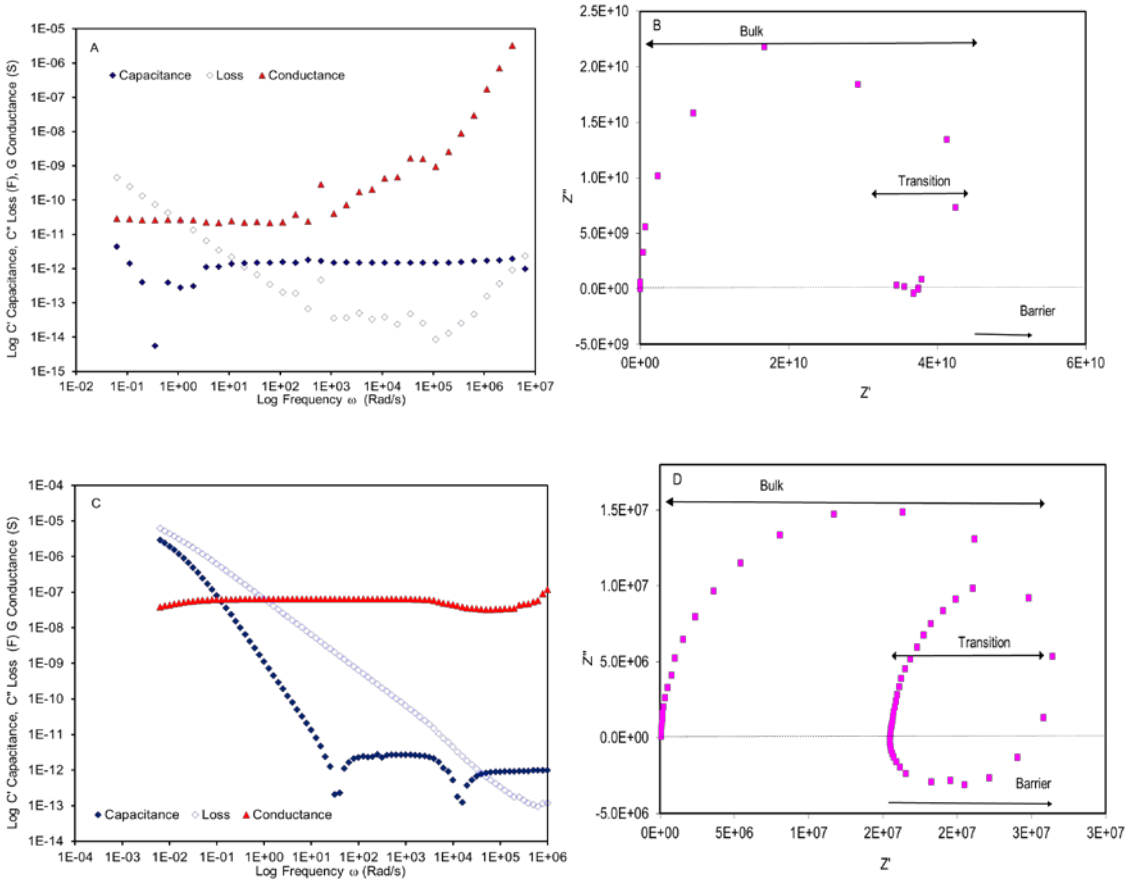

Figure C-1 (A) Complex capacitance response of 100% EC. (B) Impedence response of 100% EC. (C) Complex capacitance response of 90% EC, 10% AOT. (D) Impedence response of 90% EC, 10% AOT.

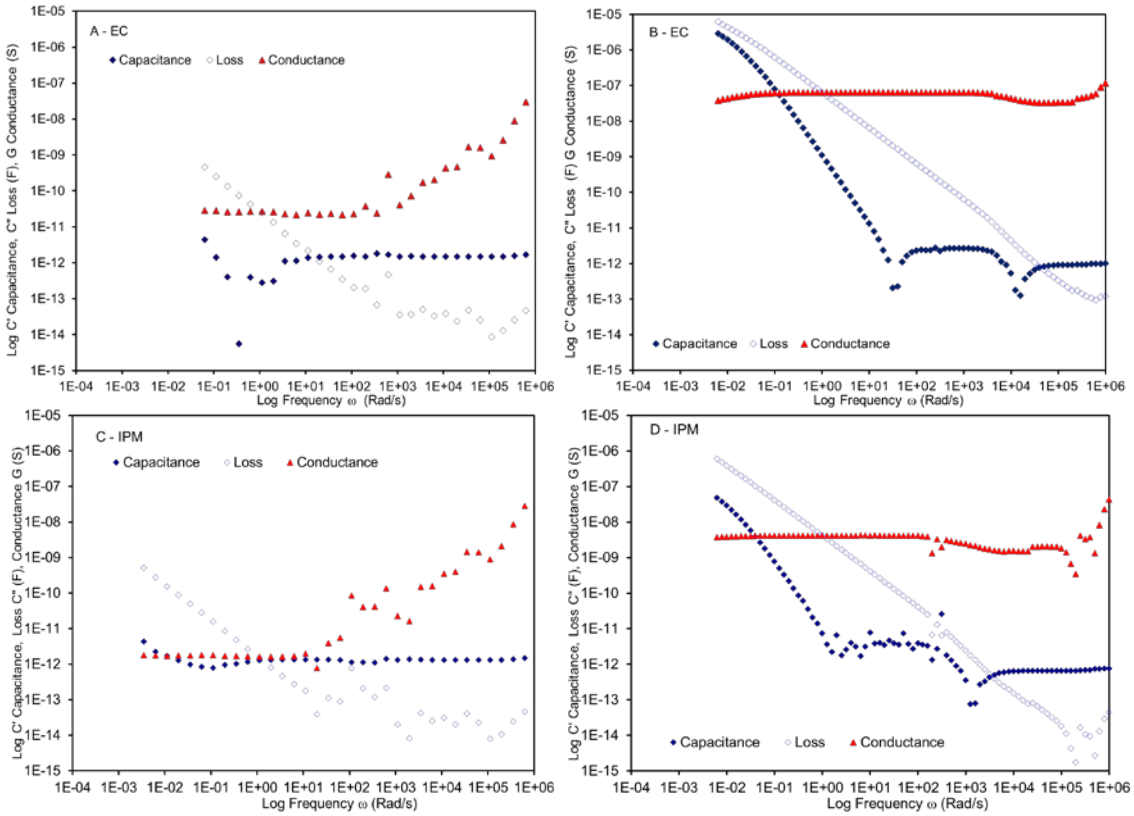

Figure C-2 IPM and EC response presented together for visual comparison. Absolute values of negative capacitance values plotted. (A) Complex capacitance response of 100% EC. (B) Complex capacitance response of 90% EC, 10% AOT. (C) Complex capacitance response of 100% IPM. (D) Impedence response of 90% IPM, 10% AOT.

Appendix D –Response of IPM, AOT, PG Sample Meassured with Brass Electrode

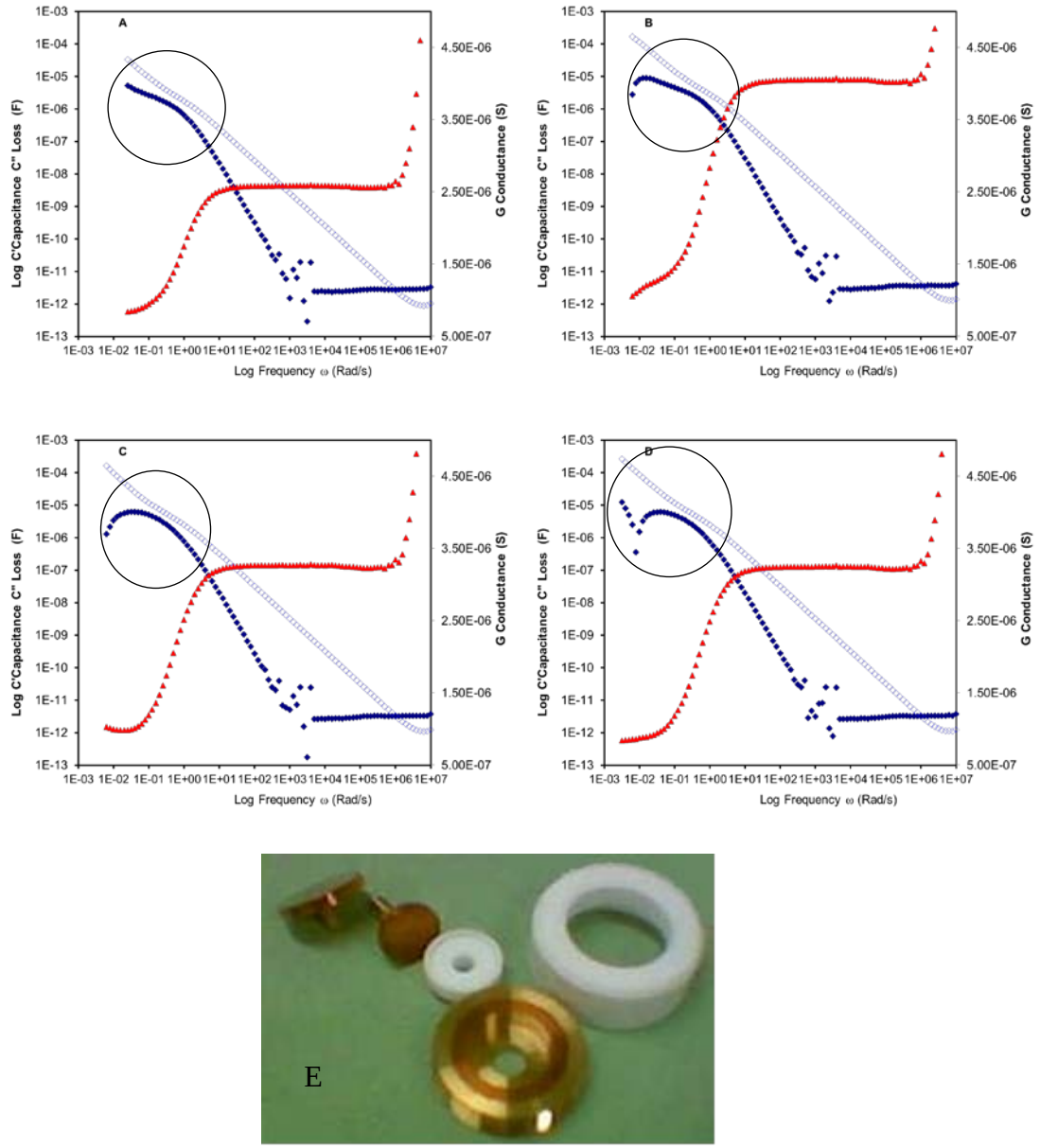

Figure D-1 Complex capacitance response of sample 70% IPM, 25% AOT, 5% PG measured using brass electrodes. (A) Electrode spacing 3.6 mm. (B), (C) & (D) Electrode spacing 3.2 mm. The shape of the barrier changed during consecutive measurements of the same sample. (E) Brass electrode appeared to be oxidised upon examination following the final measurement (D).